Electronic and structural properties of conjugated molecules at molecular hetero-interfaces and on metal surfaces

DISSERTATION

zur Erlangung des akademischen Grades
doctor rerum naturalium
(Dr. rer. nat.)
im Fach Physik

eingereicht an der
Mathematisch-Naturwissenschaftlichen Fakultät
Humboldt-Universität zu Berlin

von
Herrn Dipl.-Phys. Jens Niederhausen

Präsident der Humboldt-Universität zu Berlin:
Prof. Dr. Jan-Hendrik Olbertz

Dekan der Mathematisch-Naturwissenschaftlichen Fakultät:
Prof. Dr. Elmar Kulke

Gutachter:

1. Prof. Dr. Norbert Koch
2. Prof. Dr. Jürgen P. Rabe
3. Prof. Dr. Neal R. Armstrong

Tag der mündlichen Prüfung: 27.04.2015

Acknowledgments

I want to thank Prof. Norbert Koch, for enabling me to be part of an interesting research field and community and his kind support, Prof. Jürgen P. Rabe, for providing crucial facilities and his continuous interest in my work, Prof. Neal R. Armstrong for his immediate and motivating willingness to act as referee, as well as Prof. Saskia Fischer and Prof. Achim Peters for acting as further members of my committee.

I thank all members of my research group for substantial support, in particular Dr. Patrick Amsalem, Dr. Andreas Wilke, Christos Christodoulou, Stefanie Winkler, Raphael Schlesinger, Paul Zybarth, Dr. Ingo Salzmann, and Johannes Frisch, who helped obtaining the experimental data, as well as Dr. Georg Heimel for theoretical calculations and extensive discussions, and, last but not least, Henriette Strahl and Timo Florian for everything else.

I am much obliged to Prof. Steffen Duhm, as well as Prof. Satoshi Kera, Prof. Nobuo Ueno, Dr. Qian Xin, and Dr. Yasuo Nakayama for taking care of me in Chiba and at its University.

I thank Prof. Saw W. Hla for his support and extraordinary effort and all his group at Ohio University for their warm hospitality, moreover Yuan Zhang, Yang Li, and Heath R. Kersell for hours of STM measurements.

For support from Tübingen, I would like to thank Dr. Christoph Bürker, Dr. Takuya Hosokai, Dr. Alexander Gerlach, and Prof. Frank Schreiber.

Dr. Antje Vollmer is thanked for providing support at and around SurICat.

At my Institute, Dr. Stefan Eilers and Dr. Hendrik Glowatzki helped producing STM tips and Dr. Nicolai Severin helped understanding what those tips discovered. Prof. Stefan Kowarik, and Dr. Peter Schäfer enabled XRD-characterizations of the substrates.

Prof. Stefan Hecht, Dr. Michael Pätzel, Dr. Joachim Leistner, Jutta Schwarz, Yves Garmshausen at the chemistry department of HU as well as Ralph Rieger and Henrike Wonneberger at the MPIP provided, analyzed, and cleaned the precious organic materials.

While some of the above also provided me with friendship and meaning, I would have been lost without the support of my family, dear friends, and Saulytė. I thank you for your understanding, support, warmth and enlightenment!

Abstract

In this thesis, the electronic and structural properties of thin films of conjugated organic molecules (COMs) vacuum-deposited on metal surfaces are studied. These properties are essential for realization and optimization of device functionalities in the field of organic electronics.

Part 1 discusses two approaches for engineering the energy-level alignment (ELA), and, thereby, optimizing hole injection barriers (HIBs), at organic/metal interfaces via (over)compensation of the detrimental "push-back":

- Exploiting the peculiar ELA at chalcogen-metal bonds, shown here (with X-ray and ultraviolet photoelectron spectroscopy, UPS/XPS) for a seleno-functionalized COM that can directly be used as active material, and
- inserting electron-accepting COMs prior to deposition of active layers.

UPS shows that the latter method helps achieving a 1 eV-wide range of HIBs and that both approaches realize HIBs into the active COM as low as 0.3 eV.

Part 2 studies selected organic/organic heterostructures on metal surfaces, in order to identify the underlying mechanisms for achieving electronic equilibrium, and, in turn, to derive the ELA in these structures. These studies allow to propose that metal to overlayer charge transfer (MOCT), is responsible for achieving electronic equilibrium when such systems would not exhibit equilibrium for assumed vacuum level alignment (i.e., are Fermi-level pinned). Detailed investigations allowed a quantitative analysis of amount of transferred charges, fraction of charged molecules in the first overlayer, energy level shift induced by the concomitant electric field, and influence of the dipole-dipole repulsion on the overlayer molecular assembly.

In Part 3, metal surfaces are used as support for supramolecular architecture with polar building blocks. Scanning tunneling microscopy (STM) of a series of rod-like COMs with and without partial fluorination and with different dipole moments help disentangling the delicate balance of van der Waals forces, adsorbate-substrate registry, hydrogen bonds, and dipole-dipole interaction for sub-monolayer films physisorbed on Ag(111). For another, highly-polar COM at ca. monolayer coverage on Au(111), STM identifies four pre-annealing (those with more complex unit cells only for sufficient ripening time or induced by the STM tip) and two post-annealing phases. All phases are found to exhibit antiferroelectric unit cells. UPS evidences a preferential alignment of *multilayer molecules* via a surface potential increase larger than 1 V upon deposition.

Chalcogeno-functionalization of device relevant COMs should be straightforward. Molecular acceptors are already employed in organic light emitting diodes. Accordingly, the first part of the presented study has immediate application relevance. The results from the fundamental studies in parts 2 and 3 contribute to a better understanding of the mechanisms that control the ELA and/or morphology at organic-comprising interfaces and can be exploited to improve the design of COM chemical structures and device architectures.

Zusammenfassung

Diese Arbeit behandelt elektronische und strukturelle Eigenschaften dünner Schichten aus konjugierten organischen Molekülen (COMs), aufgebracht auf Metalloberflächen per Sublimation im Vakuum. Diese Eigenschaften sind essenziell für Funktionsrealisierung und -optimierung organischer Elektronikbauteile.

Teil 1 diskutiert zwei Ansätze zur Energieniveauanpassung (ELA) an Organik-Metall-Grenzflächen zur Einstellung der dortigen Löcherinjektionsbarrieren (HIBs) durch (Über-)Kompensation des abträglichen „Push-back"-Effekts:

- Ausnutzung der besonderen ELA bei Chalkogen-Metall-Bindungen, hier gezeigt mit Hilfe von Röntgen- und Ultraviolettphotoelektronenspektroskopie (UPS/XPS) für ein Seleno-funktionalisiertes COM, welches selbst als aktives Materials genutzt werden kann, sowie
- Einfügen von COMs mit ausgeprägtem Elektronen-Akzeptorcharakter vor dem Aufbringen der aktiven Schicht.

UPS-Messungen zeigen, dass durch letztere Methode ein 1 eV-großer HIB-Bereich zugänglich ist, sowie dass beide Ansätze HIBs von 0.3 eV ermöglichen.

Teil 2 untersucht ausgewählte organische Heterostrukturen auf Metallen, welches die Identifikation der grundlegenden Prozesse zum Erreichen des elektronischen Gleichgewichts, und damit zur ELA in solchen Strukturen erlaubt. Die Untersuchungen identifizieren einen Ladungstransfer vom Metall zur Überschicht (MOCT) als verantwortlich dafür, das System in den Gleichgewichtszustand zu überführen, wenn dieses bei angenommener Vakuumniveauanordnung nicht gegeben ist (d.h. bei Ferminiveau-Pinning). Detaillierte Untersuchungen gestatten die quantitative Analyse von transferierter Ladung, Anteil geladener Moleküle in der ersten Überschichtlage, Energieniveauverschiebung durch das entstandene elektrische Feld, sowie Einfluss der Dipol-Dipol-Abstoßung auf die molekulare Assemblierung in der Überschicht.

In Teil 3 dienen Metalloberflächen als Auflage für supramolekulare Architekturen mit polaren Bausteinen. Rastertunnelmikroskopie (STM) an einer Serie von teils partiell fluorierten, stäbchenförmigen COMs mit unterschiedlich großen Dipolmomenten ermöglicht die Entflechtung von Dipol-Dipol-Wechselwirkung, van der Waals-Kräfte, Adsorbat-Substrat-Kopplung und Wasserstoffbrückenbindung, physisorbierter Submonolagen auf Ag(111). Ein anderes, stark polares COM bildet bei Monolagenbedeckung auf Au(111), vor und nach Ausheilen, vier (hierbei solche mit komplexeren Einheitszellen nur bei ausreichender Reifungszeit oder durch die STM-Spitze induziert) bzw. zwei Phasen, alle mit antiferroelektrischer Einheitszellen. UPS-Messungen ergeben eine bevorzugte Ausrichtung der Moleküle in *Multilagen* anhand der Vergrößerung des Oberflächenpotenzials von über 1 V durch die molekulare Schicht.

Chalkogeno-Funktionalisierung von bauteilrelevanten COMs ist einfach realisierbar. Moleküle mit Akzeptorcharakter finden bereits Verwendung in organischen Leuchtdioden. Somit hat Teil 1 direkten Anwendungsbezug. Die Ergebnisse aus Teil 2 und 3 tragen zu einem grundlegenden Verständnis der ELA- und Morphologie-beeinflussenden Mechanismen an (teilweise) organischen Grenzflächen bei, und versprechen daher optimierte COMs und Bauteilarchitekturen.

Inhaltsverzeichnis

Chapter 1

Introduction

Organic electronic devices consist, to a large degree, of small molecules and/or polymers[1]. Due to strongly-bound electron-hole pairs [51], extended Wannier-Mott excitons are absent in these materials. In addition, without significant density of intrinsic free charge carriers (1 cm^{-3} [43]), band bending, which is an important phenomenon for inorganic/metal and inorganic/inorganic interfaces, is expected to occur much less prominently in the organic counterparts [141, 131, 201]. Under these assumptions, interface-related processes, like interactions upon contact formation and exciton dissociation, are largely confided to an interfacial layer that is similar to the thickness of the organic materials itself, that is, very small compared to typical layer thicknesses (> 100 nm). Since in-plane inhomogeneities are usually neglected, the interfacial layer can be visualized as a single point in energy-level diagrams (ELDs) employed when trying to make sense of macroscopic device characteristics as, e.g., current-voltage curves [152, 139, 9, 304, 233]. This is illustrated in Fig. 1.1 a).

However, strictly speaking, the term "interface dipole", which is often used to describe such a sudden potential drop in the direction orthogonal to the interface (z), is an oxymoron, since a dipole can be nonzero only if charges are separated in z, making it really an interfacial-layer dipole.[2] This rather trivial statement should stress the importance of the underlying processes occurring upon interface formation, as illustrated by the following examples.

The complex and anisotropic structure of organic molecules (as compared to atoms) makes the energy level alignment at related interfaces sensitive to microscopic details which are not encountered for interfaces comprising inorganic semiconductors. Due to the asymmetric electron distribution within the molecules, their orientation with respect to the interface significantly influences the ionization energy of organic films, and thus the energy level alignment (ELA). Notably, this also applies to non-polar molecules [57, 125, 244, 76]. For organic/metal interfaces, in particular in cases of chemisorption, the interface dipole is additionally controlled by the precise adsorption geometry of the molecule and the interaction of specific peripheral atoms with the metal

[1] This work is concerned with small molecules only.

[2] A similar argument also applies to dynamic processes. For instance, one currently favored model for the exciton dissociation at polymer hetero-interfaces is based on the (morphology-induced) potential variation along z that makes it possible for the charges to dissociate in a well-separated state, making a detrimental recombination less likely [67].

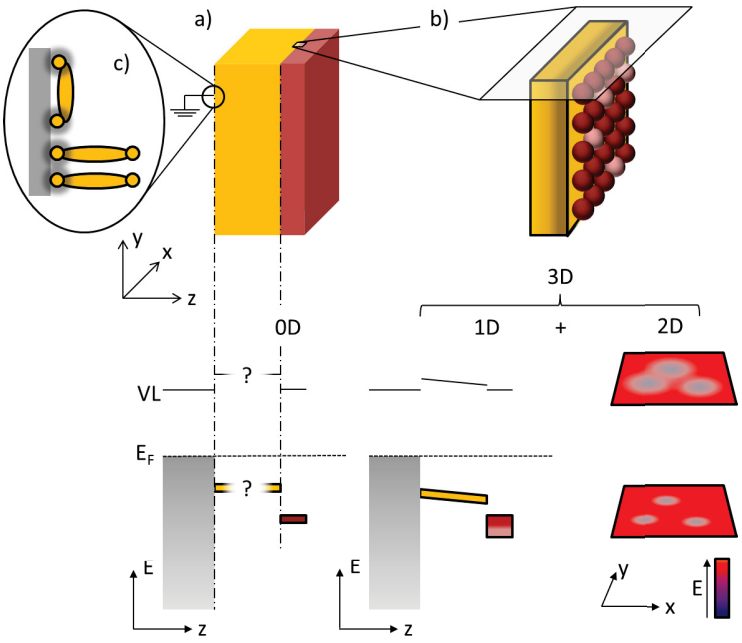

Figure 1.1: Morphology (top) and energy level diagram (ELD, bottom) for two different assessments of the same bilayer system. The ELD presents the vacuum level (VL) the Fermi-level (E_F) and the (color-coded) highest occupied molecular orbitals (HOMOs) for the two organic molecules. a): Macroscopic model neglecting the processes responsible for the energy level alignment at the interface and localizing its effect on the ELD in a single point. b): "3D model" accounting for different charge states in the interfacial layer, illustrated by individual, differently-colored molecules in the system's morphology and in-plane inhomogeneities of HOMO and vacuum level energies (only for the right material) and charge transfer invoking distant layers (illustrated for the left material). c): Illustration of chemical interactions that can occur at organic/metal interfaces and whose details depend on the adsorption geometry.

[40, 243, 121]. This is indicated in Fig. 1.1 c). In these cases, also the second molecular monolayer is often involved in the interfacial interactions via polarization or, more immediate, through open patches of a porous first-layer molecular network.

In addition to these morphology-related aspects, in-plane inhomogeneities of purely *electronic* nature can arise for *morphologically* homogenous interfacial layers[3], as can be readily estimated by the following considerations: Weakly interacting molecular systems only allow interfacial charge transfer via an integer number of charges. This results in quantized electric charge localized on nano-objects. The former implies a minimum dipole moment magnitude, while the latter translates to a large density of potential dipoles. The magnitude of the related interface dipoles in typical ELDs then prevents that all molecules participate in this process, which should result in different charge states of the interfacial molecules. Such an interfacial layer of mixed valence is illustrated in Fig. 1.1 b). Interestingly, this also depicts the expected situation in a organic field effect transistor in the "on" state.

Interfacial charge transfer, as the one mentioned just above, effectively dopes the organic materials. The generated charge carriers are not localized at the interface but are free to move about. In this case, the question arises whether the assumption of flat bands in stacked organic materials, which is often made in view of the virtual absence of intrinsic charge carriers, is still valid.

The outlined examples illustrate the complexity of organic/organic (O/O) and organic/metal (O/M) interfaces. Such microscopic details can sensitively influence processes relevant for organic electronic devices. In this work, three fundamental aspects of O/O and O/M interfaces were selected and studied with dedicated experiments. The results concern all aforementioned phenomena and, thus, have important possible applications in the control of device-relevant ELA and morphology.

The **first part** advances two concepts for optimizing the charge injection efficiency at O/M interfaces, namely *modification of the metal surface with an molecular acceptor interlayer* and *modification of the organic material via functionalization with anchor groups*. For the former, the influence of the orientation of the acceptor molecules in the interlayer on the ELA was elucidated, while for the latter the chemical situation directly at the interface as well as important characteristics of the multilayer film morphology could be resolved. The **second part** employs rational nano-architectures to elucidate the microscopic processes at play in the interfacial energy level alignment at O/O interfaces when the work function is Fermi-level pinned. In addition, important implications from a "3D"-assessment of interface energetics are given. Lastly, the **third part** sheds light on the influence of an intramolecular dipole on the molecular self-assembly and ELA at O/M interfaces.

Optimizing the energy-level alignment at organic/metal interfaces

To facilitate efficient hole transfer at O/M interfaces, low hole injection barriers (HIB) are needed [152, 163], which, when assuming vacuum-level alignment, are related to a small ionization energy (IE) of the organic material and/or a high work function (ϕ) of the metal. However when molecules are brought

[3]Strictly speaking, every molecular layer is electronically inhomogeneous. However, the potential for intramolecular inhomogeneities converges fast enough to effectively neglect them.

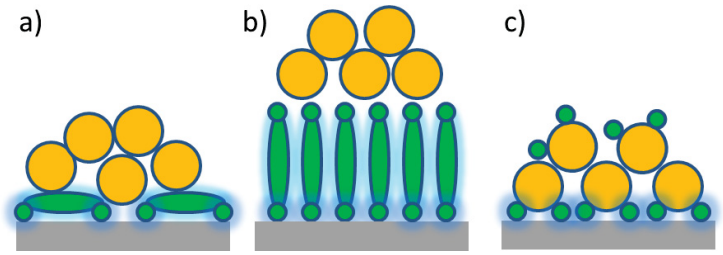

Figure 1.2: Illustration of the two employed strategies to tune the energy level alignment at O/M interfaces. a) and b): Interlayer approach. Two different interlayer orientations are shown. The green color indicates the acceptor molecules that are employed to (over)compensate the push-back effect. c): Functionalization approach. The green color symbolizes the chemical group that has the same function as the acceptor interlayers in a) and b).

into contact with clean metals, the initial metal ϕ is usually altered due to the formation of an interface dipole, which can originate from a variety of effects [142]. In the case of noble metals and physisorbed molecules without permanent dipole moment, one major contribution has been identified: The electron density spilling out into vacuum at the clean metal surface is "pushed back" by the molecules due to Pauli repulsion [152, 320]. In this case the initial metal work function is reduced and thus the HIB is significantly larger than expected from simple vacuum-level alignment.

For chemisorbed molecules, in contrast, a chemical molecule-metal interaction can further change the charge rearrangement between molecule and surface. For instance, molecular acceptors with typically large electron affinities (EAs) (and consequently also large IEs) were found to form a charge transfer complex with the metal and thus to counterbalance the push back effect [239, 165]. The organic molecules and polymers deposited onto such modified metal electrodes re-align their molecular levels with respect to the modified ϕ value [165, 239]. However, the acceptor molecules have often a low molecular weight and are thus prone to interlayer diffusion [100, 77, 5], which hinders controlled device fabrication.

An alternative approach is to combine, (i), a low IE and, (ii), the capability to mitigate the push-back at the metal electrodes in one COM. This strategy, which would eliminate the necessity for an additional interlayer, is illustrated in Fig. 1.2. Conveniently, the charge rearrangement at the O/M interface depends also on the COM chemical structure and, for example, the bonding of specific substituents to the metal surface [120]. Clearly, in order to combine the two dissimilar attributes (i) and (ii), which in the interlayer architecture are carried by donor and acceptor molecules, respectively, the semiconducting properties of the COM and its chemical bond to the metal must be electronically largely independent. This was indeed observed for selenolate- and thiolate-self-assembled monolayers (SAMs) on several coinage metal surfaces [257, 189, 3], for which the adsorption-induced charge rearrangement does not invoke the orbitals of the SAM core, and the energy-level alignment at the O/M interface is governed by an alignment of the chalcogen-derived states to the metal Fermi-level [243, 123, 121, 124].

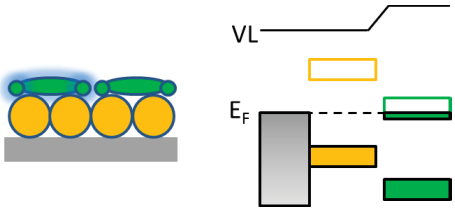

Figure 1.3: Morphology and the corresponding energy level alignment at O/O interfaces when the work function is Fermi-level pinned.

In this work, I followed both approaches. First, the effect of chalcogeno-functionalization of COMs on their energy level alignment with metal contacts was demonstrated for tetraseleno-tetracene (TSeT). The X-ray and ultraviolet photoelectron spectroscopy (XPS/UPS) results on vacuum-deposited TSeT thin films on the (111)-surfaces of coinage metals demonstrate that it is possible to combine the peculiar energy-level alignment situation of SAMs with the organic semiconductor properties of TSeT, resulting in extremely small HIBs. In addition, the photoemission experiments show that TSeT exhibits pronounced 3D island growth when deposited onto substrates kept at room temperature (RT). In contrast, by cooling the metals to 77 K (LT) during TSeT deposition, island formation is kinetically hindered, resulting in kinetically limited layering of lying-down molecules.

Next, I continued the work on the electron acceptor hexaazatriphenylene-hexanitrile (HATCN), which had been studied by B. Bröker, H. Glowatzki and others in my research group before [106, 40, 41, 105]. Their results showed that HATCN can be employed as interlayer to increase ϕ of Ag and Cu, but that its structural variability demands further attention, since it undergoes a density dependent orientation transition in the monolayer regime [40]. Notably, at this time HATCN had already started to be integrated in architectures of organic electronics devices [184, 183].

In my work, UPS was used to examine the effect of HATCN molecular orientation in interlayers on Ag(111) on the resulting charge injection barriers towards organic charge transport materials. The orientation of HATCN molecules in the interlayer is found to significantly impact the actual charge injection barriers. Moreover, the results from interlayer-modified metal electrodes are contrasted with pristine metal electrodes of the same work function, i.e., Ag *vs.* lying-HATCN/Ag and Au *vs.* standing-HATCN/Ag. This allows discussing the difference of surface electron spill-out for clean metal and interlayer-modified metal electrodes and the effect of this difference on the energy level alignment with organic semiconductors.

Role of charge transfer, dipole-dipole interactions, and electrostatics in Fermi-level pinning at molecular heterojunctions on metal surfaces

Let us assume a two-layered organic heterostructure. If the overlayer has an EA higher than ϕ of the first layer, the lowest unoccupied molecular orbital (LUMO) of the overlayer would be positioned below the occupied states of the first layer if vacuum level alignment was assumed. Contact formation is then found to give rise to an interface dipole, as illustrated in Fig. 1.3, and the work function of the system is said to be Fermi-level pinned.

Several models have been proposed to explain this process of Fermi-level alignment at organic/organic and other weakly interacting interfaces. The

charge neutrality level (CNL) model had originally been developed for strongly-interacting inorganic/metal interfaces [15, 142] and successfully employed also for more weakly-interacting organic/metal interfaces [301, 92, 22]. Notably, it asserts an induced density of interface states (IDIS) within the energy gap of the isolated organic material. These states are occupied up to the CNL, which acts as an effective Fermi-level for the organic semiconductor and partially aligns with the substrate Fermi-level. Analogously, it was proposed, that the CNL partially aligns with the CNL of the other organic material at organic heterojunctions [295, 201, 22]. However, in most cases of organic heterojunctions, no significant hybridization of the molecular orbitals is expected due to the mismatch of the molecular energy levels on either side of the interface. Indeed, other measurements showed that the interface dipole for identical O/O interfaces depends on the work function of the supporting electrode [34, 36, 33, 185], which is at variance with the CNL that only considers the energy levels at the O/O interface.

Integer charge transfer (ICT) to the overlayer was proposed as alternative idea to explain Fermi-level pinning at weakly-interacting interfaces [218, 36, 33]. In this model, the Fermi-level of the substrate is the relevant energy reference throughout all layers on top. Consequently, the notion that the charges originate from the supporting electrode had been explicitly included in the discussion of bi- or multilayered organic structures within the ICT model [36, 33, 195, 338]. The magnitude of related interface dipoles then directly translate to the fact that only a fraction of the molecules in the overlayer should become charged. However, direct evidence for such a mixed valency was still lacking when I started my work and also other implications of the ICT model were unexplored at this point: How does the inhomogeneous potential, implied by the mixed valency, influence ELA of neutral and charged molecules in the first overlayer? How do charges and differently-charged molecules arrange in this layer? Does the supporting electrode's role as counter charge for the charges in the overlayer translate to an electric field that extends over the whole layer between contact and interface [as illustrated by the slanted energy levels in Fig 1.1 b)]?

The goal of this work was to advance the understanding on how Fermi-level pinning at O/O interfaces invokes the supporting electrode and to carefully monitor concomitant electrostatic, chemical, and morphological effects in the interlayer and the first overlayer. To this end, ultra-thin organic interlayers were chosen, which should result in comparable fractions of charged and neutral interlayers. In addition, for such thin films, the whole organic heterostructure is accessible by photoelectron spectroscopy. Lastly, the morphology is favorable, since the resulting flat layers allow an accompanying scanning tunneling microscopy (STM) study and simplify the theoretical analysis.

UPS, XPS, and STM results for two material combinations will be presented. The first heterostructure employs HATCN and tris(8-hydroxyquinoline)aluminum (Alq_3). The second one comprises C_{60} and α-sexithiophene (6T). The architecture of both systems consist of a Ag(111) surface that is pre-covered with a physisorbed molecular layer (Alq_3 or 6T), on top of which a strong acceptor (HATCN or C_{60}) is deposited. In both cases, the electron acceptor has an EA higher than ϕ of the pre-covered metal substrate and the energetic situation is as sketched in 1.3.

For Alq_3/HATCN, equilibrium is found to be established via electron transfer to HATCN. The results strongly suggest that the charges that fill the HATCN

LUMO originate from the metal substrate, which will be termed metal to overlayer charge transfer, MOCT.

To derive a more generally valid and comprehensive picture of the energy levels for molecular heterojunctions in contact with a metal, C_{60} was deposited on one monolayer 6T (ML 6T) and a bilayer 6T (BL 6T) pre-covered Ag(111). Both systems exhibit MOCT, notably only involving a fraction of the C_{60} molecules within the first overlayer. The ratio of charged to neutral molecules differs markedly for both systems, demonstrating a dependence on the overlayer-to-metal distance, i.e., the thickness of the 6T spacer layer. The potential drop observed in the spacer (6T) layer as well as the energy position of the neutral C_{60} frontier levels is proposed to result from electric fields induced by the interface dipoles. This statement is further supported by classical electrostatics calculations. These findings establish a coherent picture for the energy alignment at Fermi-level pinned molecular (including organic/organic) interfaces of thin films in contact with metals. The same reasoning might also apply to cases of pinned molecular and organic heterojunctions comprising thicker layers, which was tentatively tested by applying the model to one such system that had been measured and analyzed before.

Polar molecules at organic/metal interfaces: Molecular self-assembly and energy-level alignment

Polar molecules are another means for tuning the energy level alignment at functional interfaces in (opto)electronic devices [317, 98, 52, 3, 205]. In addition, they are of interest also for other technological applications. For instance, they form the liquid crystals (LC) in LC displays [101]. Furthermore, the built-up of a giant surface potential (GSP) is observed in cases where vacuum-deposited polar molecules arrange with a preferred vertical orientation, an effect which can potentially be used to constitute the bits for organic-based memory devices [144, 143, 293, 204, 13, 228, 229, 53].

UPS readily allows accessing the macroscopic electronic parameters of such systems, like energy levels and work function. However, from this it is often not straightforward to pinpoint the actual influence of the dipole moment on the molecular arrangement in the interplay of the various intermolecular forces, since dipole-dipole interactions operate against, or cooperatively with, other short-ranged intermolecular forces like hydrogen bonds, π-π stacking, and dispersion forces [182].[4] The scanning tunneling microscopy technique, on the other hand, gives access to the electronic and geometric structure of individual molecules and the details of the molecular arrangements [308, 145, 246, 65]. In addition, STM allows monitoring the system's response when applying an electric field [112, 179, 327, 230, 50, 149, 246, 72].

In this work, the molecular self-assembly of the non-polar para-sexiphenyl (6P) was compared to a series of partly-fluorinated, and, thus, polar 6P derivatives. With low temperature-STM of low coverage films on Ag(111), the fluorinated derivatives are found to form quasi-one-dimensional rows due to hydrogen

[4]The same is also true for other macroscopic observables (e.g. derived from nuclear magnetic resonance [271, 283, 308], X-ray diffraction [283, 308, 145], differential scanning calorimetry [283, 277], optical [283, 145, 277] and scanning electron microscopy [182], or UV-Vis [182], infrared [182], and dielectric loss spectroscopy [283]).

bonds. In addition, a clear effect of the built-in dipole on the next-neighbor vertical offset along the molecular rows could be identified.

From the appearance of the 6P derivatives it was not possible to directly identify their orientation, which prevented the analysis of dipole networks in more complex two-dimensional molecular assemblies and, thus, the use of higher-coverage data for my work. The assembly in the coverage range around a full monolayer, however, is of utmost application relevance, since the first monolayer constitutes the template which determines the film growth of consecutively deposited films. In addition, for monolayer coverage the molecular assembly has to incorporate a bulk-like packing density. Accordingly, this situation much more resembles the one in relevant 3D systems like liquid crystals. For studying such higher coverage films, 9-(bis-p-tert-octylphenyl)-amino-perylene-3, 4-dicarboxy anhydride (ID28) was selected for its two very different terminal groups on either end of the perylene core, as well as its large dipole moment of 12 debye. To better predict competing intermolecular and substrate-molecule interactions, ID28 can be compared with the closely related, but non-polar molecule 3,4,9,10-perylene-tetracarboxylicacid-dianhydride (PTCDA), which has been studied extensively [284]. Four different ordered phases were observed for pristine films of ID28/Au(111), and the molecules' orientations could be identified. Formation of the three phases with larger unit cells is severely kinetically controlled and only found when the molecules are given sufficient ripening time at low coverage, or when an electric field is applied with the STM tip. Furthermore, UPS evidences a preferential alignment of ID28 molecules in multilayer films, leading to a surface potential of 1.2 eV, whose reversible partial removal by visible light irradiation was also observed.

Chapter 2

Fundamentals

The following chapter introduces the two types of materials that were used in this work, namely conjugated organic molecules[1] and metal crystals. Interactions between these materials are introduced and their impact on the energy level alignment at organic/organic (O/O) and organic/metal (O/M) interfaces is discussed. After this, the concept of Fermi-level pinning is presented. The final part addresses morphological aspects at O/O and O/M interfaces.

2.1 Conjugated organic molecules

Conjugated organic molecules (COMs) have an extended π-electron system consisting of conjugated double-bonds. Because of the weak intermolecular forces (see below), molecular solids largely retain the electronic structure of their individual entities[2]. For the same reason, charge transport is often not very efficient. In COM solids this can be mitigated by, e.g., choosing long chain-like building blocks (= polymers) or by guaranteeing a favorable next-neighbor stacking that allows the orbitals of adjacent molecules to overlap.

The energy which is required for the excitation of an electron from the highest occupied molecular orbital (HOMO) to the lowest unoccupied molecular orbital (LUMO) is called optical gap (E_{opt}). E_{opt} is $> 1.5\,\mathrm{eV}$ for most COMs. Therefore, the number of intrinsic charge carriers in a COM solid is negligible [43]. Charge carriers can be introduced by excitation with light[3], from the contacts, or by (electro-)chemical or field-effect doping.

The most important energies for organic electronics are the electron affinity (EA) and ionization energy (IE), which are defined for a COM as the energy gain when adding one electron to the LUMO and energy cost when taking out one electron from the HOMO, respectively. The energy reference is the vacuum level (VL), which in this case is the rest energy of an electron at a point infinitely far away from the COM. The energy difference between EA and IE for a COM then corresponds to taking one electron from its HOMO and adding it to the

[1] Note that in this work the term COM will be used also for the all-carbon molecule C_{60}.

[2] Chemical interaction is observed when the energy levels of two COMs in contact "match", e.g., between acceptor and donor molecules [245], which is carefully excluded in all encountered cases throughout this work and will therefore not be discussed here.

[3] However, excitation by light creates localized electron-hole pairs (Frenkel excitons), which have to be separated first to end up with free charge carriers

LUMO of another COM of the same type and is called transfer gap (E_{trans}). Due to correlation effects, E_{trans} can be larger than E_{opt} by more than 1 eV [71].

COMs combine several properties which make them ideally suited for certain (opto)electronic applications: They absorb and emit light very efficiently, can be designed virtually unrestricted, and offer the possibility to be processed at large scale and with low cost and energy.

2.2 Intermolecular forces

In the absence of strong (covalent, ionic, or metallic) bonds, intermolecular forces are dominated by the so-called van der Waals forces, whose contributions will be discussed in the following.

2.2.1 London dispersion force and Pauli repulsion

Quantum theory yields two phenomena that dominate the interaction between most neutral molecules: Firstly, the so-called London dispersion force, which is due to the dispersion interaction between molecules, proportional to their polarizabilities [80], and always attractive, and, secondly, the so-called Pauli repulsion, which is due to the exchange interaction between identical fermions and makes it unfavorable for the wave functions of electrons with the same spin to overlap. The resulting potential can often be approximated by the Lennard-Jones potential [80]

$$U(r) = Ar^{-12} - Br^{-6},$$

or the similar function

$$U(r) = A\exp(-Br) - Cr^{-6},$$

where A, B, and C are empirical constants for a given intermolecular interaction and r is the intermolecular distance. A proper theoretical description of the dispersion force is intricate, since it is due to Coulomb correlation, which is not included in the Hartree-Fock method [45, 19].

2.2.2 Electrostatic interactions due to permanent multipole moments

Obviously, molecules containing a built-in dipole interact via dipole-dipole forces (see e.g. [330]). The assessment of this interaction, however, is severely complicated by the fact that small COMs, as the ones used throughout this work, are equipped with a dipole moment by means of introducing electron withdrawing or donating groups, thereby forming intramolecular polar bonds (IPB). This means that polar COMs significant differ from ideal dipoles and contain higher order multipole moments. In addition, the IPBs, rather than the net built-in dipole of the complete COM, are most relevant for certain localized interactions (e.g. hydrogen bonds). Therefore, in the following paragraph the discussion of multipole-interactions will start from the IPB level.

Most COMs contain IPBs. For example, carbon bound to hydrogen (with the smaller electronegativity of the two) often gives a dipole moment pointing

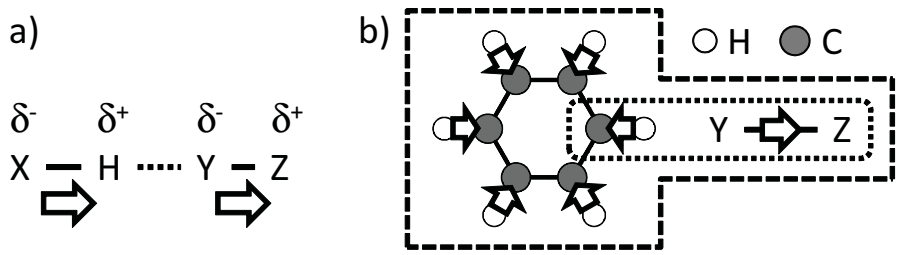

Figure 2.1: a): Illustration of a hydrogen bond on the basis of the peripheral intramolecular polar bonds (IPBs; illustrated by arrows) of two adjacent molecules only. b): Proton acceptor-organic ring system interaction (PARI). The peripheral IPBs of two adjacent molecules (dotted lines) should result in a repulsive force. In contrast, a net attractive force emerges when taking all IPBs of the ring system into account (dashed lines) [10].

towards the carbon[4], while the dipole moment points away from the carbon atom when it is bound to more electronegative atoms (e.g. fluorine, nitrogen, and oxygen). In general, the entirety of all IPBs results in a non-vanishing total permanent dipole moment. And although for molecules with inversion center the total dipole moment is zero, higher order multipole moments for these molecules due to the IPBs remain. Therefore, electrostatic forces always have to be considered when studying intermolecular interactions. The appropriate description of the respective interaction is determined by the geometry at hand: While the macroscopic multipole expansion model is suitable for large-enough distances, for which it rapidly converges and higher order terms can be neglected [296], a first principle description has to be applied for very small distances.

A good example for the latter is the hydrogen bond, as illustrated in Fig. 2.1. In its electrostatic description, the IPB-dipole between hydrogen and a more electronegative atom X attracts the IPB-dipole of a highly electronegative peripheral atom Y of another molecule (or of the same molecule in case it has a tertiary structure) [Fig. 2.1 a)]. These two dipoles will align parallel and cause an X-H$\cdots$Y bond angle of ca. 180°. The magnitude of the polarity of the X-H bond is dependent on the chemical environment of X. For instance, partial fluorination of acetylene, ethylene, ethane, and methane strengthens these molecules' hydrogen bonds to ammonia [312]. Notably, while (as shown by the just mentioned example) fluorine has a large electronegativity, it was claimed that "organic Fluorine hardly ever accepts hydrogen bonds" [81]. Moreover, for the interaction between proton acceptors and organic ring systems (PARI), it was shown that the electrostatics of the whole ring has to be taken into account [10]. The PARI can be attractive even when the two IPB-dipoles are antiparallel [Fig. 2.1 b)], the most favorable alignment in this case being Y located in between two hydrogen atoms [10].

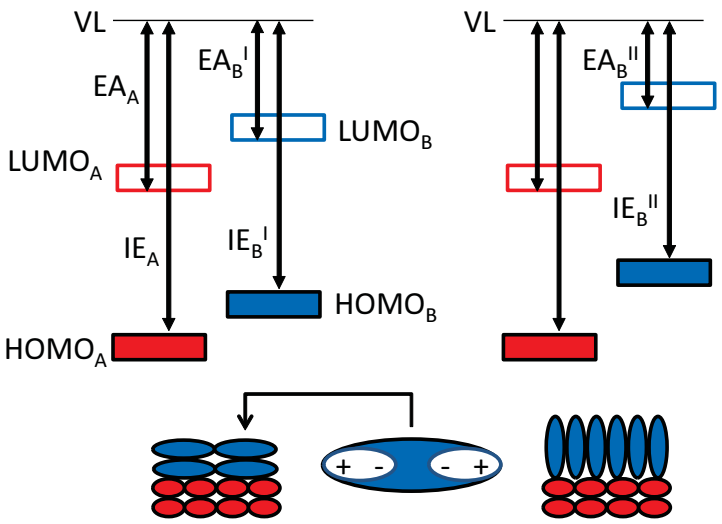

Figure 2.2: Energy level alignment (ELA) at an organic/organic interface for two different orientations of the molecules in one of the layers. The relevant intramolecular polar bonds that give rise to the shifted ELA in the two cases are shown for one magnified molecule.

2.3 Organic/organic interfaces

As mentioned above, the intermolecular interaction between two different COMs is typically only via weak van der Waals forces. If no dipole is formed during the formation of the O/O interface (e.g. due to the preferential alignment of polar COMs), the energy level alignment at O/O interfaces is given by Anderson's rule [8] according to which the individual materials simply align with their vacuum levels, as shown in Fig. 2.2.

Importantly, for COMs with an asymmetric IPB distribution (e.g. planar COMs), an electron will have to cross significantly different potential barriers when traveling from or to the COM depending on the direction of travel. This means that IE and EA of a film (and distances small compared to the in-plane film dimensions) made from such a COM depends on the orientation of the molecules, as illustrated in Fig. 2.2 [57, 125, 244, 76].

Deviation from vacuum level alignment at weakly interacting organic/organic interfaces is sometimes observed also for non-polar COMs [297, 313], which for one particular system was traced back to mutual polarization [297]. Notably, the conductive substrate, which supports and electronically connects the organic hetero-layer, is often not considered when attempting to explain the observation of such interface dipoles. Such considerations have to fail in case of Fermi-level pinning as will be discussed in section 2.7.2.

[4]However, as discussed below, for organic ring systems this is not true.

2.4 Metal crystals

For a solid, the Fermi level (E_F) separates occupied from unoccupied electronic states - the probability for a state at the energy E_F to be occupied is 1/2. For a metal, the Fermi energy is located *within* one (or more) electronic energy band(s). The corresponding electrons are delocalized over the whole crystal and can be regarded as a nearly free electron gas, which gives rise to properties such as the large electric conductivity of metals.

The work function ϕ is defined as energy difference between the vacuum level and the Fermi level. The vacuum level in this case is defined as the energy of an electron at a distance large enough to neglect the influence of the image charge in the metal, but small compared to the surface dimensions. The part of ϕ that is due to the surface will be referred to as ϕ_s. It is due to the asymmetry at the surface, with the substrate on its one, and vacuum on its other side. The electron cloud extends into vacuum, while the positive charges are localized at the cores, which creates a dipole layer at the surface, as illustrated in Fig. 2.3 a).

The asymmetry at the surface also gives rise to additional, surface-bound electronic states (so-called surface states) [280, 268, 15, 128]. In addition, the energetically most favorable arrangement of atoms at the surface can deviate from the bulk crystal structure, giving rise to surface reconstructions for which the surface atoms do not have the same crystal structure as the bulk atoms [44]. From the fcc(111) surfaces employed in this work, a reconstruction is observed only for Au(111) [44, 17].

2.5 Organic/metal interfaces

The equivalent of Anderson's rule for the interfacial energy level alignment between a metal and an organic semiconductor is the Schottky-Mott rule, which assumes that the two materials align with their respective vacuum levels, thereby neglecting all interactions at the interface. The energy barriers between the metal E_F and the energy levels of the molecular solid that are responsible for charge transport (i.e. HOMO and LUMO) are usually termed hole and electron injection barrier (HIB/EIB). In the Schottky-Mott limit, they are simply given by $|\mathrm{EA} - E_\mathrm{F}|$ and $|E_\mathrm{F} - \mathrm{IE}|$. As their name suggests, these barriers sensitively influence the charge injection efficiency, and are therefore crucial for device performance. This can be clearly seen from the Shockley formula, which described the current density, j, through a Schottky-diode [278]:

$$j = A^* T^2 \exp\left(\frac{-\mathrm{IB}}{k_\mathrm{B} T}\right)\left(\exp\left(\frac{eU_\mathrm{ext}}{n k_B T}\right) - 1\right), \tag{2.1}$$

where T is the absolute temperature, k_B Boltzmann's constant, U_ext the applied voltage, and q the charge corresponding to the respective injection barrier IB. $A^* = \frac{4\pi q m^* k_\mathrm{B}^2}{h^3}$ is the effective Richardson constant with the effective mass m* and Planck's constant h. $n = \frac{q}{k_\mathrm{B} T}\frac{\partial V}{\partial (ln j)}$ is the ideality factor.

In the following, examples will be given for frequently observed interactions at metal/organic interfaces, which in general lead to the formation of interface dipoles and, therefore, significantly alter the injection barriers.

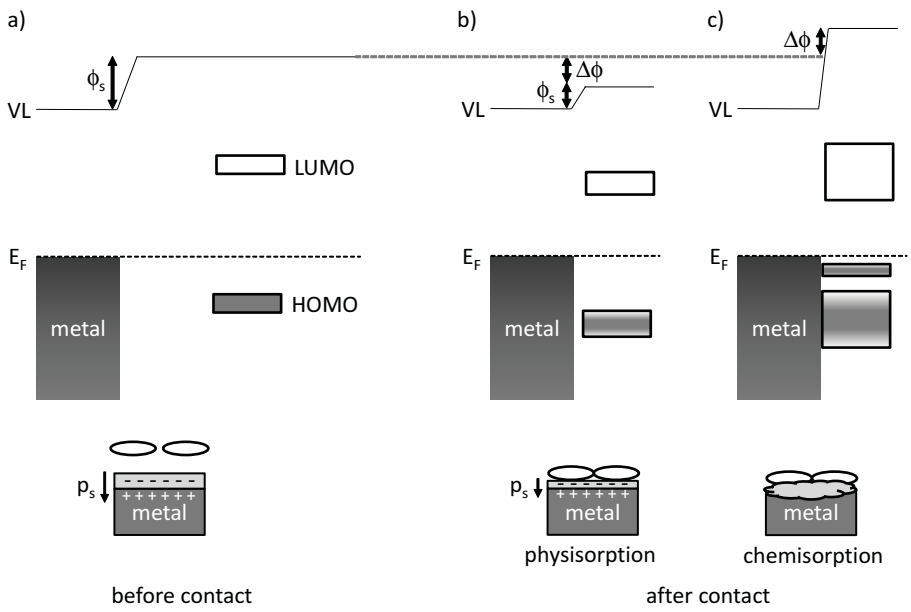

Figure 2.3: a): The organic/metal (O/M) interface before contact. The relevant energy levels are presented in the top part while the bottom part illustrates the surface charge distribution in the pristine metal substrate. b) and c): Two possible cases for the interface after contact. The models in the bottom part illustrate the push-pack effect as dominating effect for physisorbed molecules and indicate a significant charge rearrangement in the case of chemisorption by interfacial electron clouds, respectively. For physisorbed molecules, the molecular energy levels are only slightly broadened compared to the gas phase molecules. In contrast, chemisorption results in significant broadening of the molecular energy levels due to the hybridization with electronic states of the metal. Additional density of states in the HOMO-LUMO gap of the isolated molecule is observed for strong molecular-metal bonds involving specific peripheral atoms of the molecules. Note that $\Delta\phi$ for the chemisorption case was chosen as positive just as an example.

2.5.1 Physisorption and push-back effect

The weakest possible interaction between a COM and a metal surface is when only van der Waals forces are present. In this case, the adsorption process does not involve a chemical hybridization of the frontier molecular orbitals and the metal states [242, 291, 290] and is referred to as physisorption. In recent years, an increasingly accurate calculation of the adsorption energies of physisorbed molecules on metal surfaces became feasible within the framework of density functional theory. One example for the predictive power of the current models can be found in the good agreement between theory and experiment for the bonding distances of the large hydrocarbon molecule diindenoperylene on the Au(111), Ag(111), and Cu(111) surfaces, which were determined experimentally by the X-ray standing wave technique as a side project of this work [46].

When a molecule is adsorbed on a clean metal surface, the spill-out of electrons is pushed-back due to Pauli-repulsion and the surface dipole ϕ_s is decreased, as illustrated in Fig. 2.3 b). The magnitude of the push-back effect is mainly controlled by the adsorption distance [242, 291, 290]. Notably, the ϕ_s-decease depends on the initial ϕ_s. Since metals with large ϕ usually also have a large ϕ_s contribution, $\Delta\phi$ due to the push-back effect is roughly proportional to ϕ [64].

2.5.2 Chemisorption

Depending on the molecule-metal combination, chemical interactions of very different magnitude can occur at the organic/metal interface. The term weak or soft chemisorption was coined for the lower end of the spectrum, characterized by slightly decreased adsorption distances (compared to physisorption) and broadening of the molecule's energy levels [74]. Stronger interactions are often accompanied by small adsorption distances and distortions of the molecular geometry, which could in several cases be clearly related to the formation of new bonds between the metal and specific sites of the molecule (anchor groups) [120, 284, 239]. The effect of chemisorption on the density of states in the HOMO-LUMO gap is illustrated in Fig. 2.3 c).

Lastly, if metal-molecule bonds are more important than the intermolecular bonds, the molecules can break during or after the adsorption process [151, 63, 91, 328, 329].

2.5.3 Adsorption-induced intermolecular interactions

The adsorption of COMs on a metal surface can result in intermolecular forces that are not present in a bulk COM solid. One important example is the repulsion that arises between the dipoles created by an adsorption-induced charge transfer, e.g., due to the push-back effect [272] or induced by Fermi-level pinning [89]. In addition, the mutual orientation of adjacent molecules at the interface is predetermined by their adsorption geometry, which can enforce repulsion due to peripheral partial charges [303].

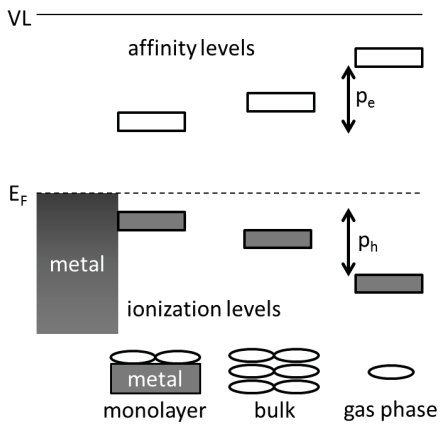

Figure 2.4: Illustration of the screening effect. When molecules are in proximity of a metal substrate or polarizable matter, an added hole (electron) is screened by the surrounding electrons, which shifts the ionization (affinity) levels by the energies p_h (p_e) [206].

2.6 Relaxation processes and renormalization of molecular electronic levels

The molecular orbitals and vibronic modes of a COM with an added hole or electron differ from the neutral system. A change in the number of electrons (induced, e.g., by charge transport in an organic electronic device or a photoelectron spectroscopy measurement) first causes a change of the electronic structure. This electronic relaxation takes place on the femtosecond timescale. Notably, the Coulomb interaction between the extra electron or hole will result in a polarization of the matter surrounding the molecule (if present). This process is called screening and stabilizes the ionization or affinity levels when compared to the corresponding gas phase levels, as illustrated in Fig. 2.4 [206]. The screening efficiency is a function of the relative permittivity of the surrounding matter, and therefore smaller for a COM surrounded by only other COMs than when located at the interface with a metal surface [131, 142, 152, 164, 331, 292].

The nuclear coordinates react to the electronic relaxation. However, the nuclear motion is significantly slower than that of the electrons. Therefore, the so-called lattice relaxation lasts on the order of 10^{-13} s [256]. Accordingly, the relaxation relevant for a given phenomenon depends on its duration.

2.7 Fermi-level pinning

The term Fermi-level pinning dates back to the middle of the 20^{th} century and was coined during the research on interfaces between metals and inorganic semiconductors. For these, a clear deviation from the Schottky-Mott rule was observed, notably in such a way that the injection barriers were only weakly dependent on the used metal. This was explained by a high density of intragap states at the interface [surface states of the semiconductor and/or new, so called metal-induced gap states (MIGS)], that become charged upon contact and thereby align the Fermi-level of semiconductor and metal at the interface [15, 142].

In the following, the concept of Fermi-level pinning will be introduced for weakly interacting interfaces. After this, O/O and O/M interfaces will be dis-

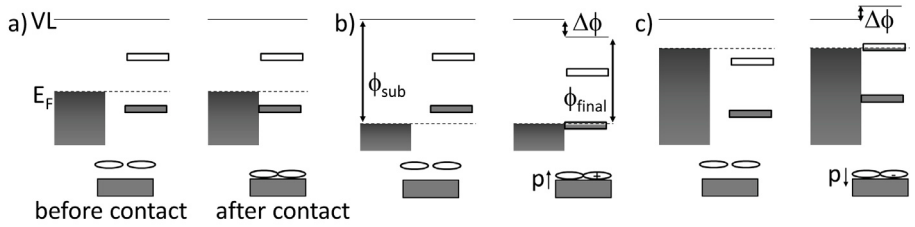

Figure 2.5: The energy levels before and after contact for weakly interacting interfaces. a): Vacuum-level alignment is compatible with the electronic equilibrium and the Schottky-Mott limit applies. b) and c): Charges flow during contact formation to guarantee electronic equilibrium. The concomitant dipole p realigns the energy levels and results in a work function after contact ϕ_{final} which is independent of the substrate work function ϕ_{sub} (Fermi-Level Pinning).

cussed.

2.7.1 Weakly-interacting interfaces

Let us assume an interface between a COM overlayer and a metallic, yet inert substrate, i.e., one that has occupied states up to E_{F} and does not interact with the COM via hybridization[5]. When drawing the energy levels for the separated materials, three situations are possible, as shown in Fig. 2.5: The work function is in between EA and IE (a), larger than IE (b) or smaller than EA (c). In case a, the energy levels will align with their vacuum levels and HIB and EIB after contact formation will be described by the Schottky-Mott limit. In this case, the work function after contact formation (ϕ_{final}) equals that of the substrate (ϕ_{sub}).

In contrast, in cases b and c, vacuum level alignment would lead to negative injection barriers and, thus, a situation out of electronic equilibrium. As a result, electrons (holes) are transferred to the COM layer, for b (c) respectively, which creates a dipole that rigidly shifts the energy levels of the overlayer. Since no electronic overlap with the substrate is assumed, integer charge transfer (ICT) by tunneling or hopping transport has to occur. The charge transfer stops once equilibrium is established. Thus, ϕ_{final} in these cases is a fixed value. It is called the positive (negative) pinning work function $\phi_{\text{pin}+}$ ($\phi_{\text{pin}-}$).

The slope parameter S relates ϕ_{final} to ϕ_{sub}

$$S = \frac{\mathrm{d}\phi_{\text{final}}}{\mathrm{d}\phi_{\text{sub}}}$$

and can be used to distinguish situations for which the Schottky-Mott limit applies ($S = 1$) from cases of Fermi-level pinning ($S = 0$, also referred to as Bardeen limit). Fig. 2.6 a) illustrates how ϕ_{final}, $\Delta\phi$, and HIB behave in the two cases.

[5]In practice, this can be a conductive polymer or a passivated inorganic substrate [36, 185], e.g., as used in this work, a metal covered with an ultra-thin COM layer

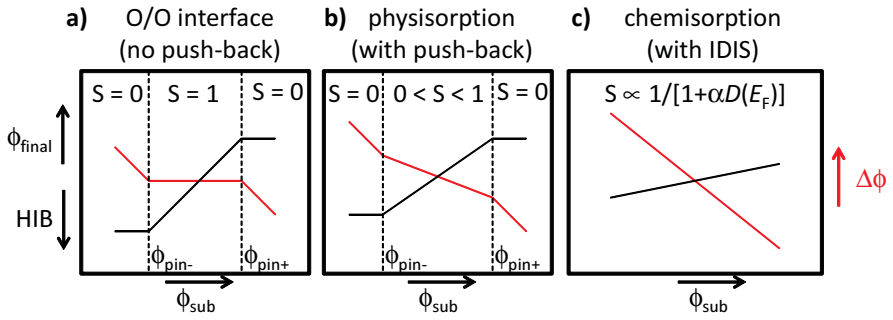

Figure 2.6: Work function after overlayer formation (ϕ_{final}), hole injection barrier between substrate and overlayer (HIB), and interface dipole ($\Delta\phi$) as function of the pristine substrate work function (ϕ_{sub}) for three cases: a): Organic-organic interfaces, where no push-back effect is observed. b): Physisorption of COMs on metals, for which the push-back effect, but no hybridization of electronic states occurs at the interface. For simplicity, the density of states for HOMO and LUMO is assumed as a delta function in a) and b). In this case, Fermi-level pinning abruptly sets in once ϕ_{sub} leaves the range defined by the critical values $\phi_{\text{pin-}}$ and $\phi_{\text{pin+}}$. c): Chemisorption, which involves an induced density of interface states (IDIS) and is described by the charge neutrality level model. See main text for details concerning the formula.

2.7.2 Organic/organic interfaces

In Sect. 2.3, isolated O/O interfaces were discussed. In relevant cases, however, at least one of the layers of the organic heterostructure is in contact with an electrode and aligns its energy levels with respect to E_{F} of the electrode. Therefore the system O/electrode needs to be considered as substrate. By doing so, we actually encounter the case of weakly interacting interfaces that was discussed in Sect. 2.7.1. Therefore, if E_{F} is located well inside the HOMO-LUMO gap, no Fermi-level pinning is expected and, as discussed in Sect. 2.3, Anderson's rule applies, which becomes the Schottky-Mott rule if we employ E_{F} as reference. In contrast, if ϕ_{sub} is $> \phi_{\text{pin+}}$ or $< \phi_{\text{pin-}}$, Fermi-level pinning is observed.

According to the picture shown in Figs. 2.5 b) and c), $\phi_{\text{pin+}}$ ($\phi_{\text{pin}-}$) simply equals IE (EA). This yields a vanishing HIB (EIB). However, in many studies finite HIBs of several tenth of an eV were observed for pinned organic overlayers. For some time, no consensus was achieved about the origin of these observations. Within the initial formulation of the ICT model, such energy differences were explained by the fact that the levels relevant for pinning are not those of the neutral molecules mapped by UPS, but those of (bi)polarons [36], which were calculated to be located at lower binding energy [186]. It was further found from electrochemical potential equilibration [29], that the pinning work functions should be independent of the Coulomb energy it takes to place a hole or electron in the COM layer, while this energy term is contained in IE and EA, respectively, which are derived from UPS (see Sect. 2.6). It was therefore argued that the energy difference between the two additionally contributes to the finite injection barriers found from UPS [29].

Later experiments of organic heterostructures, however, indeed evidenced

HIB $\approx$ 0 by UPS [195]. According to these experiments, the finite injection barriers are due to tailing intra-gap states, which are the relevant pinning levels for film thicknesses of more than ca. one monolayer, but need extra care to be resolved experimentally [195, 48, 275, 276, 191].

Interestingly, calculations predict that polarization of a first chemisorbed molecular layer can account for the $\Delta\phi$ that is required to fulfill the electrostatic equilibrium after a second, Fermi-level pinned layer is put on top [237]. This might be an alternative way for an organic heterojunction on a metal to achieve electronic equilibrium, notably without the need for a net charge transfer between any of the involved materials.

2.7.3 Organic/metal interfaces

In the case of organic/metal interfaces, the processes discussed in Sect. 2.5 have to be included. As illustrated in Fig. 2.3, for chemisorbed COMs significant density of states exists in the gap, namely the (hybridization-)induced density of interface states (IDIS) as discussed in the charge neutrality level-model [301, 92] and states due to bonds between the metal and the COM formed by specific peripheral groups of the COM. In this case, the Fermi-level pinning theory derived for Schottky contacts involving inorganic semiconductors can be applied. Therein, it was found that the slope parameter S depends on the density of states at E_F at the interface, $\mathrm{D}(E_\mathrm{F})$:

$$S = \frac{1}{1 + \alpha D(E_\mathrm{F})} \tag{2.2}$$

where α is a factor that depends on the geometry and charge densities of the two materials at the interface.

In the case of physisorption and with the metal E_F well inside the HOMO-LUMO gap of the COM, the $\mathrm{D}(E_\mathrm{F})$ is not sufficient to align the energy levels at the interface. Then $\alpha\mathrm{D}(E_\mathrm{F}) \ll 1$, $\mathrm{S} \to 1$, and the Schottky-Mott limit applies (which is just the mathematical way to express what was discussed already in Sect. 2.7.1). However, due to the push-back effect, the absence of Fermi-level pinning does not imply vacuum-level alignment.[6] In addition, due to the increasing push-back-related $\Delta\phi$ with increasing ϕ_sub (see Sect. 2.5.1), $S < 1$ is often found in these cases [Fig. 2.6 b)]. When, by varying ϕ_sub, E_F starts to overlap with HOMO or LUMO of the COM, $\mathrm{D}(E_\mathrm{F})$ increases. For a very large overlap we have $\alpha\mathrm{D}(E_\mathrm{F}) \gg 1$. Then, $\mathrm{S} \to 0$, and the work function is pinned, as shown in Fig. Fig. 2.6 b). This, again, is what was discussed in Sect. 2.7.1 with the help of Fig. 2.5 and without explicitly invoking Eq. (2.2).

2.8 Morphology at interfaces

Depending on its genesis, the interface between two materials can exhibit very different morphologies. For fundamental studies such as presented in this work, usually the formation of a planar interface by depositioning an overlayer on a flat and rigid substrate is preferred, since, amongst others, this geometry significantly simplifies the theoretical treatment. In the case of flat poly- or

[6] Note that also organic/metal oxide interfaces show a behavior that resembles the push-back effect [109, 180].

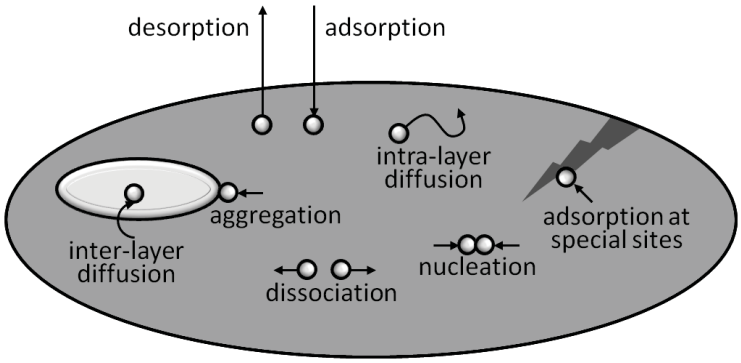

Figure 2.7: Relevant processes for COMs deposited on a surface by molecular beam epitaxy.

single-crystalline metal substrates, their surface morphology stays essentially unchanged after adsorption of molecules and only small changes can occur, like the adsorption-induced lifting or change of the surface reconstruction of Au(111) that was observed in some cases [193, 240]. For organic surfaces, however, one has to be more careful, since in-diffusion of overlayer molecules has been frequently reported [100, 77, 5]. In addition, the orientation of the molecules constituting the substrate surface might change upon overlayer formation [217, 169, 94].

In this work, all organic overlayers were prepared by molecular beam epitaxy (see Sect. 4.3.1). The formation of the resulting molecular films is complex, as illustrated in Fig. 2.7, which summarizes the relevant processes, the importance of which vary significantly as a function of, e.g., adsorbate-substrate interaction, adsorbate-adsorbate interaction, deposition rate, sample temperature, and kinetic energy of the impinging molecules.

Notably, film morphologies are often local energetic minima only, and the achievement of a global maximum is kinetically limited [172]. Annealing can be used to overcome this limitation [172, 150, 200]. Usually one distinguishes between the three growth modes shown in Fig. 2.8 a). Which one of them will be dominant depends on the surface and interface energies at play. This, in turn, allows a prediction of the film morphology for a given adsorbate-substrate combination on energetic grounds: A wetting layer usually forms if the substrate surface energy is larger than the sum of surface-adsorbate interface energy and adsorbate surface energy, while 3D-island growth prevails from the sub-monolayer on in the reverse case (the latter is usually termed Volmer-Weber growth). The same reasoning can be applied for the consecutive layers when replacing the substrate surface energy by the adsorbate surface energy and the surface-adsorbate interface energy by the adsorbate-adsorbate interface energy. This means that the slightest intermolecular attraction should lead to nucleation and island formation from the second or third[7] layer onward (Stranski-Krastanov growth). However, in some cases kinetic limitations or anisotropic intermolecular forces lead to a layer-by-layer growth also beyond the monolayer (Frank van der Merwe growth). A study that nicely shows the effect of the

[7]Sometimes the substrate-adsorbate interaction extends beyond the first layer.

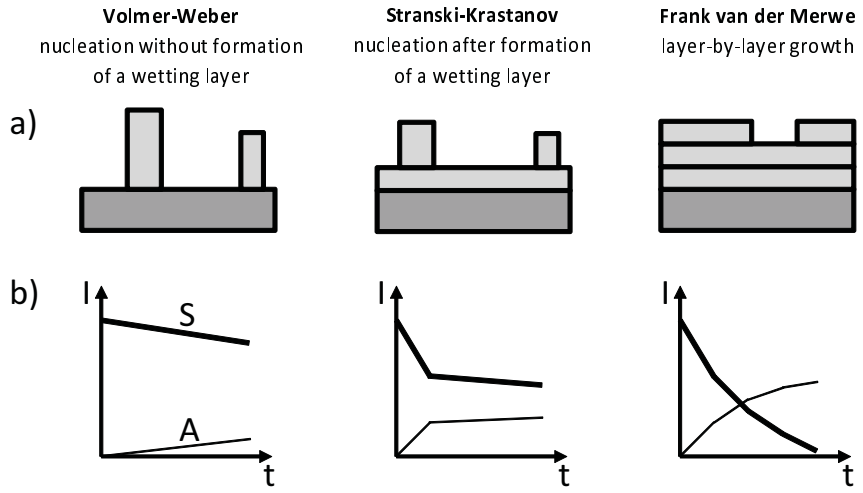

Figure 2.8: The three modes used for classifying film growth. a): The corresponding schematic real-space models (with the substrate in dark gray and the adsorbate in light gray); b): XPS intensities (I) stemming from the substrate (S) and the adsorbate (A) as function of deposition time (t) in thick and thin lines, respectively [235].

substrate-adsorbate interaction strength on the growth mode, in that it covers the whole range of growth modes for the same adsorbate, is presented in Ref. [232].

Monte-Carlo modeling and Molecular Dynamic simulations can be used to predict the morphology of a given system and account for dynamic aspects (and thus also kinetic limitations) [281, 173]. Still, due to the complexity of typical O/M and O/O interfaces and the mentioned anisotropic intermolecular forces, dedicated experiments are still an indispensable tool to elucidate interface morphologies [235, 168, 170, 169, 150, 172, 200]. Owing to its high surface sensitivity and element sensitivity, XPS [150, 200] and Auger electron spectroscopy [235] can be used for this purpose. The attenuation of photoelectrons originating from the substrate by the overlayer is described by the Beer-Lambert law (see Sect. 3.1). Therefore, comparing the intensity of core level or Auger peaks characteristic for substrate and overlayer, respectively, gives a sensitive method to infer the film growth mode [235], as illustrated in Fig. 2.8 b).

Chapter 3

Methods

Two techniques were used for obtaining the experimental results presented in this work, photoelectron spectroscopy (PES) and scanning tunneling microscopy / spectroscopy (STM/STS). The following chapter introduces the working principle of both analysis techniques and presents their respective accessible observables. At the end of the chapter, necessary details are given on how density functional theory was used to interpret some of the experimental results.

3.1 Photoelectron spectroscopy

Photoelectron spectroscopy is based on the photoelectric effect, which was discovered more than hundred years ago. Before going into the details of this process, the general working principle and setup of a PES experiment will be explained by following the way of a photoelectron from its generation to its detection.

When matter is illuminated with light of a frequency ν above a material-specific minimum value ν_{min}, electrons are emitted, while no electrons are emitted for $\nu < \nu_{\mathrm{min}}$ (except for very high intensities). The occurrence of a minimum frequency was explained by Albert Einstein, who proposed the existence of discrete wave packages, each with an energy $h\nu$, where h is Planck's constant. This model also predicted that the maximum kinetic energy of the photoelectrons should vary like ν, i.e. $E_{\mathrm{kin,max}} = h\nu - \phi$. When also accounting for the binding energy, E_{B}, of the energy level a given photoelectron originated from, its kinetic energy is given by

$$E_{\mathrm{kin}} = h\nu - \phi - E_{\mathrm{B}} \tag{3.1}$$

The highest accessible E_{B} depends on $h\nu$, and therefore on the excitation source employed.

If an electron is excited not at the very surface of the sample but in a buried layer (which in the most extreme case is a core electron that is "buried" under the atom's/molecule's electron cloud), it can get scattered by the electrons in the matter it has to traverse before reaching vacuum. This process limits the escape depth of electrons with kinetic energies relevant for PES (10 - 2000 eV) to less than 20 Å, and for $E_{\mathrm{kin}} \approx 50\,eV$ to even only a few Å (see Fig. 3.2 and, e.g., Ref. [129]). Accordingly, PES is a very surface sensitive technique.

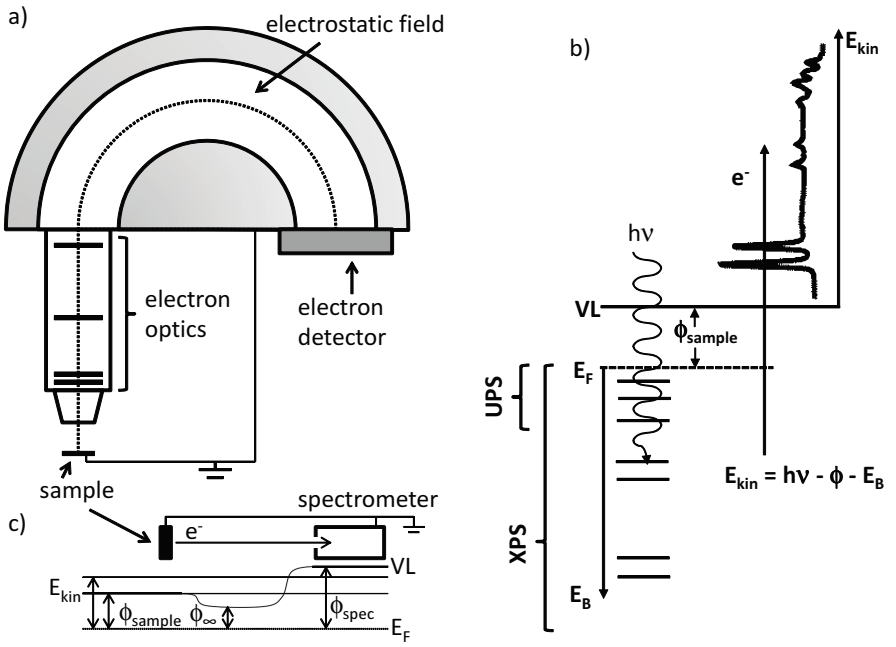

Figure 3.1: a): Hemispherical photoelectron spectrometer. The main components are described in the main text. b): Illustration of the photoelectric effect. Light of energy $h\nu$ causes an electron from within the sample to be emitted with a kinetic energy $E_{\mathrm{kin}} = h\nu - \phi - E_{\mathrm{B}}$. The energy ranges for UPS and XPS are indicated (not to scale). c): Potential map (bottom) and real space illustration (top) for an electron (from left to right) just outside of the sample, far away from sample and spectrometer, and in the spectrometer. The situation as sketched, with $\phi_{\mathrm{spec}} > \phi_{\mathrm{sample}}$ and without U_{bias} applied between sample and spectrometer, prevents ϕ_{sample} from being derivable from the SECO onset. b) and c) were adapted from [164].

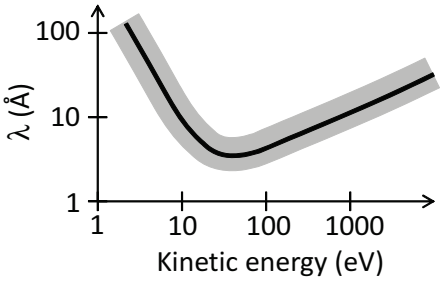

Figure 3.2: The so-called universal curve, which allows estimating the inelastic mean free path λ of the photoelectrons as a function of their kinetic energy. The gray band indicates the uncertainty of the presented fit, which was derived from experimental data obtained for various materials [258].

Nonetheless, photoelectrons from shallowly buried layers will also show up in a PES experiment. The remaining intensity of photoelectrons, I, after traveling through matter of thickness d is described by the Beer-Lambert law

$$I = I_0 e^{\frac{d}{\lambda}} \tag{3.2}$$

where I_0 is the initial photoelectron intensity and λ the inelastic mean free path[1].

Photoexcited electrons that reach the surface can escape into vacuum if their kinetic energy perpendicular to the surface is large enough to overcome the sample work function. For a periodic and flat surface, the transmission of the electrons into vacuum conserves their momentum parallel to the surface, while the momentum perpendicular to the surface is changed by the potential asymmetry between solid and vacuum.[2] This allows band mapping of a solid by angle resolved PES (ARPES) [274, 129]. The angle between the direction of travel of the liberated photoelectron and the sample surface is called take-off or emission angle.

In a PES measurement, a photoelectron spectrometer is used to detect and analyze the photoelectrons, and is thus sometimes referred to as detector or analyzer. By now, most photoelectron spectrometers follow the principle setup shown in Fig. 3.1 a). The photoelectrons first pass through a system of electron lenses, which, for example, allows optimizing the spatial or angular resolution. In addition, their kinetic energy is changed by a retarding field, so that when entering the hemispherical energy analyzer the electrons of the kinetic energy of interest now travel with the so-called pass energy E_{pass} (which means that the retarding field is changed while measuring a photoelectron spectrum). The energy resolution varies as the inverse of E_{pass}, but the transmission of photoelectrons decreases with decreasing E_{pass}, making the choice of E_{pass} usually a compromise between optimizing the two. The electrostatic field between the hemispheric plates lets pass only electrons that fulfill $E_{\text{kin}} = E_{\text{pass}}$, which are then counted by an electron detector. The result is an electron energy distribution curve as shown in 3.1 b), which, according to (3.1), directly depicts the density of states (DOS) within the probed sample.

3.1.1 Ultraviolet and X-ray photoelectron spectroscopy

With excitation energies of some eV up to several ten eV, UPS mostly probes weakly bound electrons that are shared among several atoms (the so-called valence band or valence electron region, VB). These are also the electrons that participate in chemical reactions. The spectral shape of the corresponding features in UPS therefore allows accessing these processes. In this introductory section, however, only the more-immediate aspect of deriving the energy level alignment from UPS will be discussed.

A typical UPS spectrum of a clean metal is sketched in the top part of Fig. 3.3 a). The occupied states extend up to E_{F}, which is used as origin of the binding energy scale. An example for the Fermi edge of Ag(111) measured at

[1] For electron paths close to parallel to the sample surface (i.e., for take-off angles $> 50°$), elastic scattering of photoelectrons is important and the escape depth should be used in (3.2) instead of λ [147].

[2] When assuming free photoexcited electrons within the solid, this simply reflects Snell's law [129].

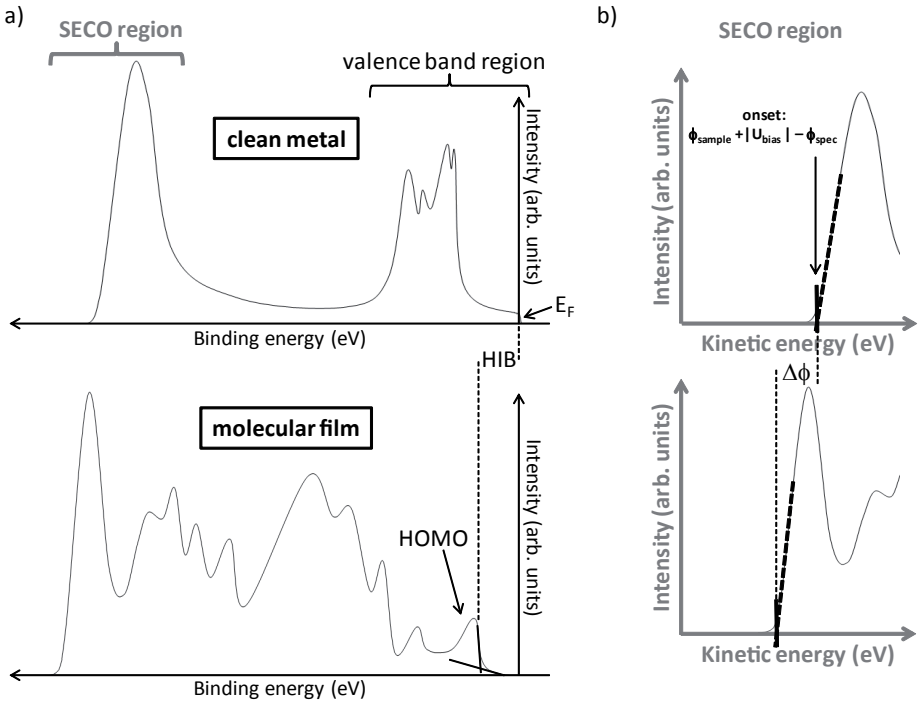

Figure 3.3: a): Sketch of UPS spectra of a clean metal (top) and after depositing a molecular film on top (bottom). The procedure for determining the low binding energy onset of emission from the HOMO (HOMO onset) is illustrated and the determination of the organic/metal HIB as energy difference between metal E_{F} and HOMO onset is depicted. b): Illustration of how plotting the SECO region as function of the kinetic energy allows determining ϕ_{sample}, when U_{bias} and ϕ_{spec} are accounted for. The SECO difference between clean metal and molecular film directly gives the interface dipole $\Delta\phi$.

BESSY with $h\nu = 35\,eV$ is shown later on in Fig. 4.3 b). Note that the energy reference is unchanged for a spectrum obtained from a molecular film, also if no DOS at E_F is observed. This allows directly determining the hole injection barrier (HIB) as energy difference between E_F and the low binding energy onset of photoelectron emission stemming from the HOMO, as illustrated in Fig. 3.3 a).

The low kinetic energy region of the spectra is shown in Fig. 3.3 b), and corresponds to the high binding energy region in 3.3 a). The cut-off is called secondary electron cut-off (SECO), since most of the intensity stems from inelastically scattered photoelectrons [cf. (3.2)], which are also called secondary electrons. The existence of a cut-off energy is due to the sample work function and its onset corresponds to photoelectrons that have $E_\mathrm{kin} = 0$ just outside of the sample. However, when sample and spectrometer are both grounded, as drawn in Fig. 3.1 a) and c) (top), the SECO will only correspond to the sample work function ϕ_sample if this is larger than the work function of the spectrometer (ϕ_spec), as illustrated in Fig. 3.1 c) (bottom). Therefore, when measuring the SECO region usually a bias voltage U_bias is applied between sample and detector in order to clear ϕ_spec. When plotting the SECO as function of E_kin and accounting for U_bias and ϕ_spec, ϕ_sample can directly be read of the graph as illustrated in Fig. 3.3 b).

X-ray photoelectron spectroscopy (XPS) is usually concerned with photoelectrons originating from more-tightly bound electrons, the so-called core levels (CL). These are strongly localized and their respective binding energies can be used as a fingerprint for the corresponding element. Accordingly, XPS allows for a quantitative analysis of the elementary composition of a given sample. Together with the high surface sensitivity described above, this means that XPS can be used to derive the growth mode of vacuum deposited overlayers (cf. Sect. 2.8).

The CL binding energies of an atom depend on the electrostatic potential it is located in. Therefore, a change of its valence, oxidation, or bond state causes a so-called chemical shift of the binding energies. In addition, an external electrostatic field also shifts the binding energies.

3.1.2 Photoexcitation

This section provides a thorough description of the photoexcitation process on theoretical grounds. It has proven valid to treat the processes on the photoelectron's way to the detector as independent of this initial photoexcitation process [129]. Therefore, the discussion of these other processes that was provided above remains valid.

In the photoelectron process, the initial state, an N electron system with wave function $\Psi^i(N)$ and Energy $E^i(N)$, is excited by a photon with energy $h\nu$, and thereby transformed into the final state described by $\Psi^f(N)$ and $E^f(N)$. The transition probability w is then given by Fermi's golden rule

$$w \propto |M_{if}|^2 \, \delta\left(E^f(N) - E^i(N) - h\nu\right)$$

where the delta-function guarantees energy conservation and M_{if} is the transition matrix element of the photoemission perturbation operator H',

$$M_{if} = \left\langle \Psi^f(N) \left| H' \right| \Psi^i(N) \right\rangle$$

If we assert that the final state consists of an ion, with $\Psi^f(N-1,k)$ and $E^f(N-1,k)$, and a photoelectron with kinetic energy E_{kin}, which originates from the energy level labeled k, the energy conservation term yields

$$E^i(N) + h\nu = E^f(N-1,k) + E_{\text{kin}} \tag{3.3}$$

Let us also define the binding energy $E_{\text{B}}(k)$ as

$$E_{\text{B}}(k) = E^f(N-1,k) - E^i(N) - \phi\,, \tag{3.4}$$

where ϕ accounts for the extra energy loss of the photoelectron when leaving the sample, thereby referencing all energies to E_{F}. Note that for PES of gas phase molecules (and sometimes also for solid materials) the vacuum level is used as reference. From combining (3.3) and (3.4) we then get:

$$E_{\text{B}}(k) = h\nu - E_{\text{kin}} - \phi\,, \tag{3.5}$$

which is equivalent to Eq. (3.1).

To make sense of PES data, it is crucial to understand the significance of $E_{\text{B}}(k)$ and to link it and the photoelectron intensity ($\propto w$) to the $\Psi(N)$ system. To this end, several approximations are usually applied. Firstly, due to their much smaller mass, it can be assumed that the electrons instantaneously adapt to a change of the nuclear coordinates. The *Born-Oppenheimer* approximation therefore asserts that the Hamiltonian does not depend on the velocity of the cores and the electronic part of Ψ can be separated from the total Ψ.

A first order approximation of $E_{\text{B}}(k)$ can be obtained by applying *Koopman*'s theorem, which assumes that the N- and $(N-1)$-electron systems consist of non-interacting electrons, and that the spatial distribution and energies of the $N-1$ remaining electrons in the $\Psi^f(N-1,k)$ system are identical to the ones of the $\Psi^i(N)$ system. With these assumptions, $E_{\text{B}}(k)$ simply equals the energy of the one-electron state $|\phi_k\rangle$ that the photoelectron was taken out of. This, however, is only a crude approximation, since correlation and final state effects are completely ignored.

Many-body-processes

A more realistic model is the so-called sudden approximation. It allows for a time evolution of $\Psi^f(N-1,k)$, but neglects any interaction between the photoelectron and the $(N-1)$-electron system [30] [however, due to energy conservation, the energy of the photoelectron is related to the final state of the $(N-1)$-electron system]. Since many-body effects are now to be included, the analysis is done by means of the second quantization, which involves introduction of annihilation and creation operators a_i and a_i^+ for an electron in a one-particle state $|\phi_i\rangle$ with energy ϵ_i, and allows writing the perturbation as

$$H' = \sum_{i,j} H'_{ij} a_i^+ a_j$$

This yields

$$w \propto \sum_{i,j} \langle\phi_f|H'|\phi_i\rangle A_{ij}\,(E_{\text{kin}} - h\nu)\,\langle\phi_j|H'|\phi_f\rangle$$

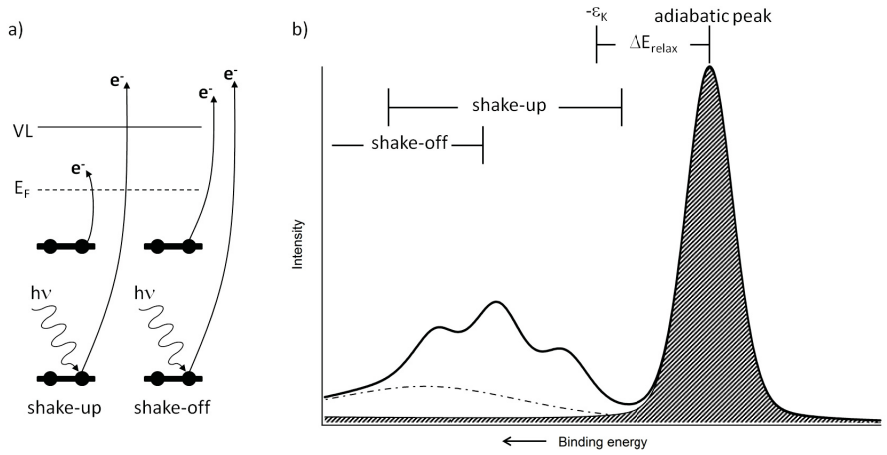

Figure 3.4: a): Illustration of two important many-body processes that decrease the kinetic energy of the primary photoelectron. b): Simulation of how many-body processes can affect the outcome of a PES experiment. ϵ_{K} is the energy of the photoelectrons initial one-electron state given by Koopman's theorem [129, 266].

with $|\phi_f\rangle$ the one-electron state of the photoelectron.

The interactions within the final state are expressed via the spectral function A_{ij}, which for the approximation of vanishing off-diagonal elements can be written as

$$A_{ii}\left(E_{\mathrm{kin}} - h\nu\right) = \sum_s |c_s|^2 \delta\left(E_{\mathrm{kin}} - h\nu + E^f(N-1,k)_s - E^i(N)\right)$$

$|c_s|^2$ gives the probability that removing an electron from state k of the initial N-electron system results in a $(N-1)$-electron system in the s^{th} excited state. In general, $|c_s|^2$ will be $\neq 0$ for all s, resulting in various peaks or a smooth background in the photoelectron spectrum, depending on the importance of correlation effects [30].

Whether the relaxation processes discussed in Sect. 2.6 are included in the photoemission process depends on their characteristic time scales. While electronic relaxation processes are included, changes due to structural relaxation, which is more than one order of magnitude slower, are usually assumed to be negligible [256].

An important process, in particular for XPS, is the excitation of a second electron in the same molecule to an unoccupied energy level during the photoexcitation process, which leaves less kinetic energy for the primary photoelectron and thus gives rise to satellite peaks at higher binding energy in the photoelectron spectrum as shown in Fig. 3.4. If the final state of the second electron is a bound state, the process is referred to as shake-up, while for an unbound final state it is called shake-off.

The energy of the final state is further influenced by vibronic transitions accompanying the primary photoexcitation. According to the *Franck-Condon* principle, the nuclear coordinates do not change during the absorption of a photon. The probability of a vibronic transition is then proportional to the

square of the overlap integral between the vibrational wave functions of initial and final state (vertical transition). Due to the strong hole-vibration coupling of COMs, the change of a COM's electronic state significantly affects its vibrational modes. Accordingly, a vertical transition into a final state with a different vibrational mode can be most likely. When assuming the COM to be initially in its vibrational ground state, the vibration satellites are given by a Poisson distribution with $I_n = S^n e^{-S}/n!$. Here, I_n is the intensity of the n^{th} vibrational mode in the final state and S is the Huang-Rhys factor for the vibrational mode [324, 111, 38]. S is a measure of the electron-vibrational coupling interaction [38].

Selection rules

In its general form, the perturbation due to light irradiation is given by

$$H' = \frac{e}{2m_e c}\left(\vec{A}\cdot\vec{p} + \vec{p}\cdot\vec{A}\right) - e\Phi + \frac{e^2}{2m_e c^2}\vec{A}\cdot\vec{A}\,,$$

where $\vec{p}$ is the momentum operator, m_e is the electron mass, and $\vec{A}$ and Φ are the vector and scalar potential, respectively. For a one-photon process and with a classical treatment of the vector potential within the sample, all terms except for $\vec{A}\cdot\vec{p}$ can be neglected. If furthermore the wavelength $\lambda = 2\pi/|\vec{k}|$ can be assumed to be large compared to the atomic dimensions, the *dipole approximation* applies and only the leading term of $\vec{A} = \vec{A_0}\exp(i\vec{k}\cdot\vec{r}) \approx \vec{A_0}$ has to be considered. H' then becomes

$$H' = \frac{e}{2m_e c}(\vec{A_0}\cdot\vec{p})$$

and the transition matrix element is given by

$$M_{if} \propto \langle\phi_f|\vec{p}|\phi_i\rangle$$

which can be rearranged by using commutator rules to yield

$$M_{if} \propto \langle\phi_f|\vec{\mu}|\phi_i\rangle$$

with the transition dipole moment $\vec{\mu} = q\vec{r}$. ϕ_i represents the bound electron in a given orbital, and ϕ_f the final state corresponding to the emitted electron. Information on the molecular orientation within a film can be obtained from the fact that M_{if} will be only non-zero if it is totally symmetric, or (for point groups with degenerate representations) contains at least one totally symmetric component, which gives rise to the so-called selection rules [274]. That said, the details of the group-theoretical treatment of the symmetry operations present in common molecules is beyond the scope of this work and it should suffice to note that the symmetry of the final states for which $M_{if} \neq 0$ is given by the direct product of the representations of ϕ_f and the dipole operator (which can be denoted by the electric field $\vec{E}$) [274]. This is illustrated in Fig. 3.5 for the point group C_{2v}, which is frequently encountered for molecules adsorbed on periodic surfaces. Accordingly, selection rules allow determining whether emission from a given orbital is allowed for a particular measurement geometry.

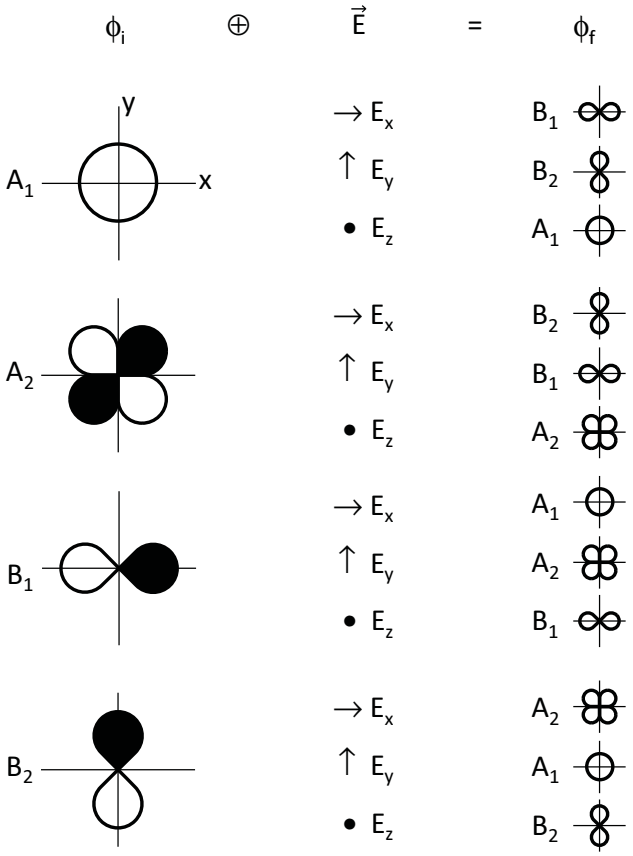

Figure 3.5: Illustration of the predictions of symmetry selection rules for the point group C_{2v} adapted from [274]. ϕ_i and ϕ_f are the initial and final state, respectively. $\vec{E}$ is the electric field polarization. A final state A_1 is allowed at any detector position. B_1 and B_2 final states are allowed in the xz- and yz-mirror plane, respectively, while they are forbidden in normal emission and in the nodal planes of the final state (the yz- and xz- mirror plane, respectively). A final state A_2 is forbidden in normal emission and in in the yz- and xz- mirror planes.

3.1.3 Line width and shape

The lower limit for the width of features in photoelectron spectra is given by the life time broadening of the probed energy levels. Inhomogeneities of the sample induce another broadening contribution, since the ionization levels of COMs sensitively depend on their orientation within the film (Sect. 2.3) and their environment (Sect. 2.6). These effects, together with the experimental resolution, decide whether the final state effects discussed in Sect. 3.1.2 are reflected in the spectra.

For thin molecular films on metals, photoelectrons stemming from the substrate are detected together with the molecular features. However, a simple simulation of such spectra by taking spectra for the respective pure systems is usually not possible due to the following reasons: Because of the interaction between molecules and metal, the N- and $(N-1)$-electron systems at the O/M interface differ from those of the two separated materials. This also means that final state effects (cf. Sect. 3.1.2) for probed molecules are different when close to the metal than for those in the molecular bulk, as was already described for the process of screening in Sect. 2.6. In addition, photoelectrons originating from the metal are diffracted by the molecular overlayer [7, 187, 102, 28, 103].

3.2 Scanning tunneling microscopy / spectroscopy

The invention of scanning tunneling microscopy (STM) dates back some 30 years [24, 25, 27, 23, 26] and STM has quickly become an indispensable technique for surface analysis [332, 246] and manipulation [246, 132]. In STM, the tunneling current I_t for an applied voltage U_t between the conductive tip and the conductive sample is employed as measurement signal. A simple formula for I_t can be derived based on the WKB approximation of the probability for an electron to penetrate a potential barrier [269]:

$$I_\mathrm{t} \propto \frac{U_\mathrm{t}}{d} e^{-2\kappa_0 d} \tag{3.6}$$

where d is the barrier width, ϕ the average work function of tip and sample, and $\kappa_0 = \sqrt{\frac{2m\phi}{\hbar^2}}$. $\phi = 4\,\mathrm{eV}$ gives $k_0 \approx 1\,\mathrm{\AA}^{-1}$, meaning that a change of d by $1\,\mathrm{\AA}$ results in an I_t change by one order of magnitude, which nicely illustrates the high sensitivity of STM.

In a more rigorous calculation by Tersoff and Hamann [285, 286] based on a formalism by Bardeen [14], I_t is shown to also depend on the DOS of the sample ρ_sample and the tip ρ_tip. For metal tips, ρ_tip can be assumed as featureless [cf. Fig. 3.6 b)], and we can write

$$I_\mathrm{t} \propto \int_0^{eU_\mathrm{t}} \rho_\mathrm{sample}(E) T(E, eU_\mathrm{t}) \mathrm{d}E$$

where $T(E, eU_\mathrm{t}) = e^{-2\kappa d}$, with $\kappa = \sqrt{\kappa_0^2 - E + \frac{eU_\mathrm{t}}{2}}$, is the transmission probability of the electron. Taking the derivative yields

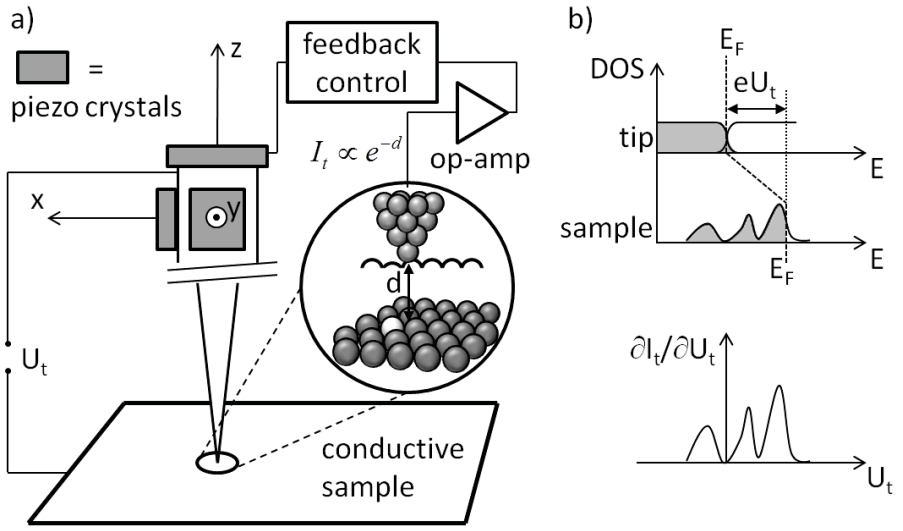

Figure 3.6: a): Principal setup of a STM: The piezoelectric actuators allow the tip to be positioned along the three spatial directions with high accuracy. The zoom depicts a favorable tip with only one atom at its end. The black line illustrates the 1D isodensity line of the electronic DOS which will be traced by the tip when in constant current mode. The one brighter surface atom depicts another element, causing a different apparent height profile than all the other atoms. b): Illustration of STS: The tip DOS is simplified as completely flat and the broadening of the $\partial I_\mathrm{t}/\partial U_\mathrm{t}$ spectrum due to the finite width of the Fermi-Dirac-distribution is neglected.

$$\frac{\mathrm{d}I_\mathrm{t}}{\mathrm{d}U_\mathrm{t}} \propto e\rho_\mathrm{sample}(eU_\mathrm{t})T(eU_\mathrm{t}, eU_\mathrm{t}) + e\int_0^{eU_\mathrm{t}} \rho_\mathrm{sample}(E)\frac{\mathrm{d}T(E, eU_\mathrm{t})}{\mathrm{d}(eU_\mathrm{t})}\mathrm{d}E$$

This relation between $\frac{\mathrm{d}I_\mathrm{t}}{\mathrm{d}U_\mathrm{t}}$ and ρ_sample is the basis of scanning tunneling spectroscopy (STS), which is illustrated in Fig. 3.6 b). To better extract the local DOS (lDOS) from the measurements, it is favorable to normalize $\frac{\mathrm{d}I_\mathrm{t}}{\mathrm{d}U_\mathrm{t}}$ by dividing by $\frac{I_\mathrm{t}}{U_\mathrm{t}}$, which gives

$$\frac{\mathrm{d}I_\mathrm{t}/\mathrm{d}U_\mathrm{t}}{I_\mathrm{t}/U_\mathrm{t}} = \frac{\rho_\mathrm{sample}(eU_\mathrm{t}) + \int_0^{eU_\mathrm{t}} \rho_\mathrm{sample}(E)/T(eU_\mathrm{t}, eU_\mathrm{t})\frac{\mathrm{d}T(E,eU_\mathrm{t})}{\mathrm{d}(eU_\mathrm{t})}\mathrm{d}E}{\frac{1}{eU_\mathrm{t}}\int_0^{eU_\mathrm{t}} \rho_\mathrm{sample}(E)\frac{T(E,eU_\mathrm{t})}{T(eU_\mathrm{t},eU_\mathrm{t})}\mathrm{d}E}$$

The advantage for this normalized version is that $T(E, eU_\mathrm{t})$ and $T(U_\mathrm{t}, eU_\mathrm{t})$ appear as ratios. Therefore, their exponential dependence on U_t and d tend to cancel [87]. Yet, all terms are approximately of the same order and and the ρ_sample signal comes with a significant background, in particular for large U_t and d [87].

As shown in Fig. 3.6 a), STM relies on piezo actuators to position the probe with high precision (ca. 1 Å in lateral and ca 0.1 Å in vertical direction with respect to the sample surface). Most STM images are taken in the constant current mode, meaning that I_t is used as feedback signal to control the z-piezo actuator such that I_t is kept constant, as illustrated in Fig. 3.6 a). According to what has been said above, a constant current image gives an isodensity plot of the electronic DOS, which, to some extent, can be interpreted as the sample's topography. For acquiring a scanning tunneling spectrum, the feedback is turned off and I_t or $\frac{\mathrm{d}I_\mathrm{t}}{\mathrm{d}U_\mathrm{t}}$ is measured as a function of U_t.

3.3 Density functional theory

For some of the organic materials, density functional theory (DFT) [45, 19] calculations on the free molecules were performed with Gaussian09 (Revision A.02) [97] using the PBE0 hybrid exchange-correlation functional [2] and a 6-31G** contracted-Gaussian basis set [119, 115]. The LANL2DZ basis set and effective core potential were used for gold [117, 302, 116].

DFT allows to determine the (ground state) occupied and virtual molecular orbitals of a given COM. Gaussian09 provides the corresponding spatial electron distribution, orbital symmetry, and energy eigenvalues.

All DFT calculations presented in this work were performed by G. Heimel, except for the 6P derivatives, which were calculated by R. Schlesinger (both Humboldt University).

Chapter 4

Materials and experimental setups

In the following, the employed substrates and COMs will be shortly described. After that, the experimental setups will be explained.

4.1 Substrates

The coinage metals gold, silver, and copper served as substrates in most presented experiments. They all form face-centered cubic crystal systems. Exclusively single crystals with a (111) orientation were used in this work. The reactiveness of Au(111), Ag(111), and Cu(111) increases in that order (from physisorption to chemisorption for many COMs), while the work functions are 5.4 eV, 4.6 eV, and 4.9 eV, respectively. Therefore, interface studies invoking these substrates can evidence trends of, e.g., the ELA as function of these two parameters. In addition, these materials are of large application relevance since they are used for contacting and wiring of electronic devices. The crystals were purchased from MaTeck GmbH (Jülich, Germany), with the exception of the gold crystal used for the measurements in Sect. 7.2, which was purchased from Surface Preparation Laboratory (Zaandam, Netherlands).

(100) p-doped silicon (Siegert Consulting, prime grade) with a native oxide layer was used as reference for a weakly interacting surface in one case only (Sect. 5.1.1). The sample was a coupon of ca. 10x10 mm^2 cut from a wafer and used as received.

4.2 Organic materials

The employed organic materials have been chosen for both, their electronic structure and the expected growth mode for films grown by molecular beam epitaxy (MBE, Sect. 4.3.1), as will be laid out in the following. In terms of morphology, sometimes a (roughly) layer-by-layer growth mode is desired, because it allows forming layered structures with defined thicknesses, which is often essential for device fabrication as well as fundamental studies. From an electronic point of view, the materials potentially used in organic electronics

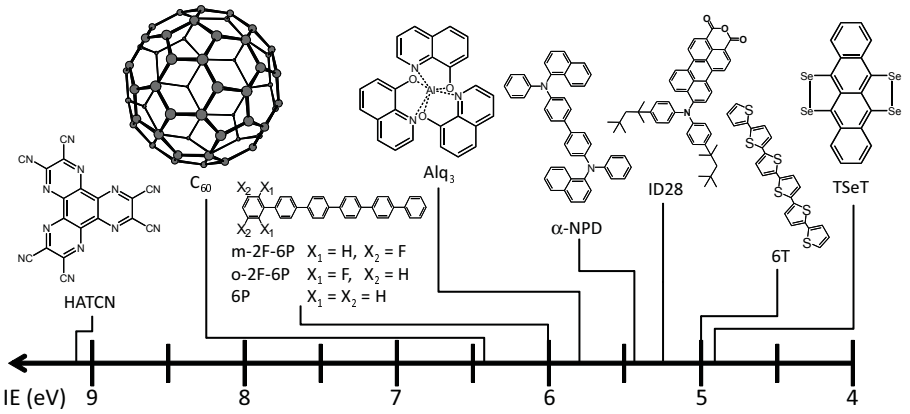

Figure 4.1: The chemical formulas and ionization energies of the organic materials used in this work. The materials are arranged with decreasing ionization energy from left to right (see main text for details).

should be good electronic conductors. In addition, the positions of their energy levels determine whether they can fulfill a particular role in an organic electronics-architecture (Sect. 5) or in a fundamental study (Sect. 6). The ionization energy gives the molecule's likelihood to act as an electron donor (the *smaller* the more likely), while its electron affinity determines whether it will accept an extra electron (the *larger* the more likely). While the transport gap is different for every material [139], in general a high EA translates into a high IE. The IE is therefore mostly sufficient to identify a molecule as more of a donor or more of an acceptor type.

4.2.1 Electron acceptor molecules

1,4,5,8,9,12-hexaazatriphenylenehexacarbonitrile (HATCN) was synthesized at the MPIP (Mainz, Germany) as strong acceptor molecule. IEs in the range of 8.95-9.35 eV were found for films of standing HATCN on Au(111), Ag(111), and Cu(111) [41].

C_{60} (buckminsterfullerene) with IE = 6.4 eV and EA = 4.0 eV was used as second acceptor molecule [309, 314]. Different than HATCN, it has an almost isotropic shape which results in a negligible orientation dependence of its IE and EA. C_{60} was purchased from Sigma-Aldrich (Taufkirchen, Germany) and used without further treatment.

4.2.2 Inert molecules

The overlayers in Sect. 5.2, the interlayers in Sect. 6, and the polar molecules employed in Sect. 7 were chosen such that they only weakly interact with the respective substrates.

Aluminum-tris(8-hydroxychinolin) (Alq_3; IE = 5.8 eV and EA = 2.2 eV) and N,N'-diphenyl-N,N'-bis(1-naphthyl)-1,1'-biphenyl-4,4'-diamine (α-NPD; IE = 5.4 eV and EA = 1.5 eV) are typical electron and hole transport materials, respectively [130, 146, 204]. Both grow layer-by-layer on many surfaces. α-

sexithiophene (IE = 5 eV) was chosen for its favorable morphology when deposited on Ag(111) [55]. In view of their energy levels and absence of reactive side-groups, all three materials are not expected to significantly interact with the studied metal surfaces. They were purchased from Sigma-Aldrich and used without further treatment.

The partly fluorinated derivatives of para-sexiphenyl (6P) were synthesized at the Department of Chemistry, Humboldt-University (Berlin, Germany). Meta-2F-6P (ortho-2F-6P) has the two hydrogen atoms at the meta (ortho) position of one terminal phenyl group substituted by fluorine, which corresponds to $X_1 = H$ and $X_2 = F$ ($X_1 = F$ and $X_2 = H$) in Fig. 4.1. Preliminary STS data of meta-2F-6P / Ag(111) indicates that the energy level alignment at the interface with Ag(111) is similar to that of the unsubstituted 6P. For the latter, physisorption was found [133, 166, 32].

9-(bis-p-tert-octylphenyl)-amino-perylene-3,4-dicarboxy anhydride (ID28) was synthesized at the MPIP (Mainz, Germany) [11]. Its IE is estimated to equal 5.6 eV from DFT calculations performed within this work and was determined experimentally to be 5.25 eV by cyclic voltammetry in dichloromethane [181].

4.2.3 Electron donor molecule

Tetraseleno-tetracene (TSeT) was synthesized already more than 50 years ago [107] and mostly studied due to its ability to form radical-cation salts, which were found to be highly conducting [265, 69]. In these salts, TSeT acts as donor, and it was shown by electrochemical measurements and calculations that the IE of tetracene indeed decreases significantly by the selenium substitution (even below that of pentacene) [336]. TSeT was chosen to test how its peripheral selenium atoms influence the organic/metal interfacial energy level alignment. It was purchased from Ambinter (Orléans, France) and purified by recrystallization in 1,2,3-trichlorobenzene in the Department of Chemistry, Humboldt-University (Berlin, Germany).

4.3 Experimental setups

The PES data was acquired with three different ultra-high vacuum (UHV) systems. The room temperature (RT) STM measurements were performed at one of them, while the low temperature (LT) STM results were acquired at a fourth UHV system. The following list gives the respective locations and an according short name in brackets. Details are listed in table 4.1

- Endstation SurICat at the synchrotron BESSY II, Germany (BESSY)
- Humboldt University, Germany (HU)
- Chiba University, Japan (Chiba)
- Ohio University, USA (OU)

Table 4.1: The UHV systems used in this work. See the main text for the meaning of the short names. The sample temperatures during preparation and measurement are given. For the PES setups, the energy resolution ΔE derived from the Fermi-edge and the bias applied during SECO measurements U_{bias} are also listed. In the Refs., additional details can be found for the respective setups.

	BESSY	HU	Chiba	OU
$\boldsymbol{T_{\mathrm{prep}}}$	20 °C	20 °C	77 K	≈ 70 K
$\boldsymbol{T_{\mathrm{meas}}}$	20 °C	20 °C	77 K - 135 °C	6 K
Methods	XPS, UPS	STM, XPS, UPS	UPS	STM
$\boldsymbol{\Delta E}$ **(meV)**	180	120	80	-
$\boldsymbol{U_{\mathrm{bias}}}$ **(V)**	-10	-10	-3	-
Refs.	[298, 41]	[105, 41]	[78]	[132, 225]

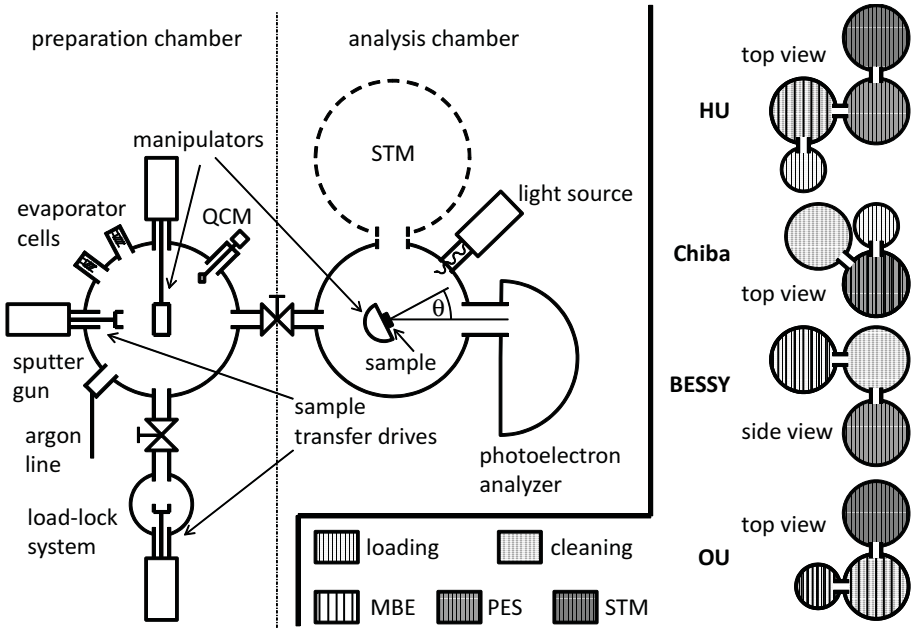

Figure 4.2: Principal setup of an UHV system consisting of interconnected preparation and analysis chambers. QCM stands for quartz crystal microbalance. Only one of the three systems used for PES was also equipped with an STM. Note that the respective actual geometries and organization slightly vary from the one depicted here. The organizations of the systems used in this work are schematically depicted in the right part of the figure. Details can be found in the references given in Tab. 4.1.

All UHV systems to a large degree follow the principle that the introduction of the sample, its preparation steps, and its analysis are located in interconnected chambers that can be isolated, as sketched in Fig. 4.2. The schematic drawings in the same figure illustrate the detailed organization of the four different systems. The experimental setup at **BESSY** consisted of interconnected MBE (base pressure $< 10^{-8}$ mbar), sample cleaning (base pressure 2^{-10} mbar), and analysis chambers (base pressure 2^{-10} mbar). At **HU**, a commercially available UHV system (Omicron) was used. In this setup, the sample preparation (base pressure $< 10^{-9}$ mbar) chamber, which is interconnected with the analysis (base pressure $< 10^{-10}$ mbar) chamber, was used for sample cleaning and MBE. In **Chiba**, MBE was performed in the analysis chamber (base pressure 4^{-10} mbar). During the experiments, the sample was cooled with liquid nitrogen, while a cooling shield ($T = 30$ K) surrounding most of the sample holder largely reduced sample surface contamination due to adsorption of residual gas. In **OU**, the load lock was also used to mount the MBE evaporation cell. The pressure in the analysis chamber (in the housing of the STM scanner) was 5^{-11} mbar.

4.3.1 Sample preparation

The substrates are first introduced into the system either via a Load-Lock system (**HU**, **Chiba**, and **OU**), or by directly placing them into the preparation chamber (**BESSY**). Silicon was used without further treatment. It was thus covered with a native oxide layer and will be referred to as SiO_x. The metal single crystals underwent repeated heating and Ar-ion sputter cycles to clean their surfaces, as described in the following. After having established a pressure of 10^{-10} - 10^{-9} mbar, Argon gas is introduced into the system, which is then ionized and accelerated by an electric field (500 V throughout this work), and finally hits the sample. This process is called sputtering and removes the topmost layer(s) of the sample. The sample surface is then heated to ca. 450 °C to evaporate the remaining contaminants and to allow the topmost substrate atoms to reconstruct into a smooth surface. In this work, heating was either done resistively by a filament in the manipulator (**BESSY**, **HU**, and **OU**) or by light irradiation of the sample surface (**Chiba**). To obtain a clean and flat surface, metal single crystals have to undergo several of such sputter/annealing cycles. Depending on the setup, the surface cleanliness and flatness were checked by the respective available techniques (XPS, UPS, and/or STM).

The molecular films are deposited onto the substrates by a process which is called molecular beam epitaxy. The materials (see Sect. 4.2) come in powders and are filled either in so-called pinhole sources, which consist of tantalum or molybdenum cases with a small opening (pinhole), or into glass crucibles. The powder is then evaporated by resistively heating the pinhole source or a filament wrapped around the glass crucible, respectively. The molecular flux is controlled by the heating power and determined with a setup described in the following and often referred to as quartz crystal microbalance (QCM). A quartz crystal is mounted such that its one surface is exposed and its resonance frequency can be measured. The resonance frequency of the quartz crystal changes when additional matter is adsorbed on its surface. This gives a measure for the mass flux, which can be translated into the coverage deposited onto the sample by MBE, given that the following conditions are fulfilled:

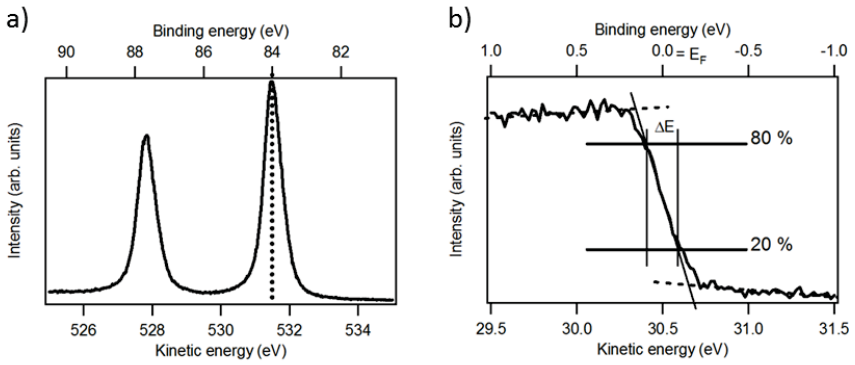

Figure 4.3: a) and b): Exemplary calibration for XPS by setting Au $4f_{7/2}$ to a binding energy of 83.96 eV and for UPS by determining E_F from the Fermi edge, respectively. The latter plot also shows how the energy resolution of the experimental setup, ΔE, can be determined.

- The sample is positioned the same as the QCM or the molecular beam profile is known.
- The angle between the surface normal of sample and QCM are identical or accounted for.
- Either the QCM measurement and the deposition are performed simultaneously, or the molecular flux is constant or its time evolution known.
- The difference in sticking coefficient [208] between quartz crystal, substrate, and substrate covered by the adsorbate is known.
- The density of the molecular film is known (as a function of thickness).

In this work, in particular the last three conditions contribute to the overall uncertainty, which is estimated to be around 10 %. The QCM readings are given as nominal coverages and where possible, were calibrated after deposition by STM or PES. All deposition rates in this work were around 1 Å per minute.

For the experiments at **Chiba**, film growth and characterization were both done in the analysis chamber to guarantee the required sample temperature of 77 K. Since this chamber is not equipped with a QCM, the rate for the evaporation source was determined beforehand in another UHV chamber. The low sample temperature during deposition will result in a somewhat higher sticking coefficient [208] compared to that of the QCM at room temperature. For the LT-STM experiments at **OU**, the pressure reading in the sample loading/MBE chamber was employed to roughly control the molecular flux. The sample was located in the cleaning chamber and the valve to the sample loading/MBE chamber was shortly opened to perform the deposition. No QCM was used and the coverages were determined from the STM results.

4.3.2 Photoelectron spectroscopy

For all spectrometers used in this work, the respective energy resolution, as determined from Fermi edge-spectra [illustrated in Fig. 4.3 b)], are listed in

Tab. 4.1, as are the respective U_{bias} used in the employed experimental setups to clear the sample work function (cf. Sect. 3.1.1).

In-house experiments at HU and Chiba

In the lab setups (**HU** and **Chiba**), ultraviolet light created by a helium discharge lamp, with the two most intense lines at 21.22 eV (HeI-α) and 40.81 eV (HeII-α), was used for UPS. X-ray radiation from an X-ray tube with Aluminum and Magnesium anode (Al K_α = 1486.6 eV and Mg K_α = 1253.6 eV, respectively) was additionally employed for XPS measurements at **HU**. Both of these light sources provide unpolarized and polychromatic light: In addition to the main HeI-α line, HeI-β and HeI-γ satellite lines exist (at 23.09 eV and 23.75 eV, and with intensities of ca. 1.8 % and 0.4 % of that of HeI-α, respectively), which stem from transitions with initial states of higher energies. For Al K_α and Mg K_α, additional lines (at ca. 9.8 eV and 8.4 eV higher energy, and with 6 % and 8 % of the primary peak intensity, respectively) exist due to the case of doubly-ionized atoms during the core-hole creation, in addition to the broad background due to bremsstrahlung.

PES measurements at **HU** were performed with a Phoibos 100 (SPECS) hemispherical electron energy analyzer. This setup allows to rotate silicon oxide foils of two different thicknesses into the UV light beam. Thereby, the UV light intensity that hits the sample can be reduced.

The UPS experiments at **Chiba** were performed with a R3000 (Scienta) hemispherical electron energy analyzer. Because of the design of this analysis chamber, the helium discharge lamp rotates together with the sample. This results in a fixed angle between the incident beam and the sample for all electron emission angles.

Synchrotron-based experiments at BESSY

The endstation chamber SurICat is connected to the beamline PM4, which is located at a dipole bending magnet of the electron storage ring. Accordingly, the synchrotron light is linearly polarized in the plane of the ring. A gold coated silicon grating with a line density of 360 lines/mm was used as monochromator and the beam entrance slit was 100 μm. Photoemission spectra were collected with the hemispherical electron energy analyzer SES 100 (Scienta). The angle between analyzer and the incident beam is fixed at 60°. This corresponds to an angle of 60° and 15° between surface normal and the incident beam for electron emission angles of 0° and 45°, respectively. All spectra were recorded angle-integrated with an acceptance angle of 10°. The energy scale was referenced to standard core level energies. We set the Au $4f_{7/2}$ peak maximum to 83.96 eV [see Fig. 3.3 a)] and [only for TSeT/Ag(111) in Sect. 5.1.1] Ag $3d_{5/2}$ to 368.21 eV [259]. The excitation energy was 620 eV for XPS and 35 eV for UPS unless stated otherwise.

4.3.3 Scanning tunneling microscopy

Room temperature measurements at HU

The RT-STM system used in this work is an variable temperature STM (Omicron). It is interconnected with the HU PES system, as indicated in Fig. 4.2,

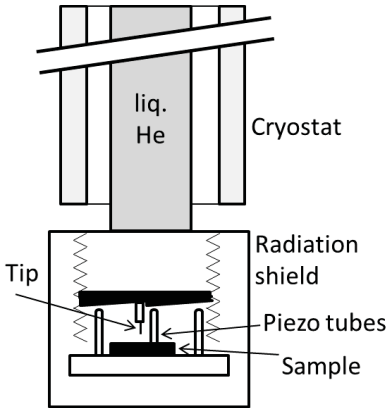

Figure 4.4: Setup of the Besocke-Beetle type STM scanner. The coarse approach is achieved in a stick-slip motion of the three outer piezo tubes, which causes a rotation of the supported disk. Due to the tilted ramp profile of the disk, this results in an approach/withdrawal of the attached tip [132, 225].

and the sample is transferred to the scanner with a wobble-stick with pincer action. The scanner is isolated from external vibrations by an eddy current dampers-system. All data was acquired at room temperature. A cut tungsten wire was used as tip except for the measurements of the annealed films in 7.2.2, for which a electro-chemically fabricated platinum-iridium (Pt80/Ir20, GoodFellow) tip was prepared as described in Ref. [83].

The images were treated with the free software WSxM[1] [137] and, where possible, corrected for the thermal drift according to Ref. [231] with the open-source software GWYDDION[2] [207].

Low temperature measurements at OU

The LT STM system used at OU was built based on the design of Meyer [197] and includes a Besocke-Beetle type STM scanner [21], which, when scanning, is hanging from springs off the base part of a liquid helium bath cryostat, as shown in Fig. 4.4. The STM scanner is housed inside two thermal radiation shields, which also act as cryogenic pumps and thereby significantly decrease sample contamination due to residual gas particles. Electrochemically etched polycrystalline tungsten tips were used. See Refs. [132, 225] for further details.

[1] http://www.nanotec.es/products/wsxm/
[2] http://gwyddion.net/

Chapter 5

Optimizing the energy-level alignment at organic/metal interfaces

To achieve push-back compensation without having to invoke an interlayer in the device architecture, the applicability of the *functionalization approach*, which was introduced in Chapt. 1, was tested for TSeT. TSeT can be seen as derived from tetracene by substitution of four hydrogen atoms by selenium atoms, which is predicted to be a better electronic coupling group than sulfur [322, 223]. Sect. 5.1.1 presents XPS results that evidence chemisorption of TSeT on the Ag(111) and Au(111) surfaces via its selenium atoms. This results in pinned energy levels of TSeT, as derived from the UPS results for the same films. The effect is best seen for TSeT/Ag(111). For this interface, the push-back effect is largely compensated by the chemisorption. Very small HIBs are observed for both interfaces.

While small HIBs at O/M interfaces are an energetic prerequisite for many devices, layer-by-layer growth of the organic material is often desired in addition (e.g., in organic light-emitting diodes, OLEDs), which is also essential for a clear assessment of the energy-level alignment at the immediate TSeT/metal interface. However, the photoemission experiments show that TSeT exhibits pronounced 3D island growth when deposited onto substrates kept at room temperature (RT). To kinetically hinder the island formation, additional UPS experiments were performed for which the metals were cooled to 77 K (LT) during TSeT deposition. In these experiments, which are presented in Sect. 5.1.2, layering of lying-down molecules is observed. This growth mode enables the disentangling of the ELA at the interface and energy-level shifts observed for multilayer films, which are both reviewed in Sect. 5.1.3. For a controlled assessment of how the interplay of substrate-molecule and intermolecular forces affects the film morphology, [200, 150, 319, 173, 172] annealing procedures of LT-grown TSeT films were performed (Sect. 5.1.4). With the help of these data, finally the RT-grown multilayer films are discussed (Sect. 5.1.5).

The RT data was acquired at **BESSY**, while the LT results were obtained at **Chiba**.

In Sect. 5.2, the *interlayer approach* employing HATCN interlayers was re-

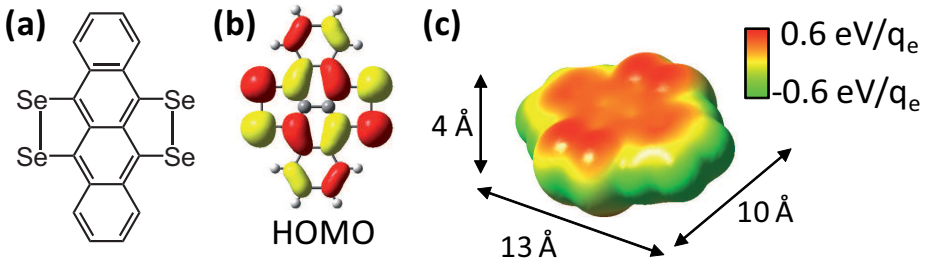

Figure 5.1: a), b), and c): Chemical structure, HOMO isodensity plot (iso value: 0.13 e/Å^3), and electrostatic potential map and geometric dimensions of tetraseleno-tetracene (TSeT), respectively.

sumed, which, as mentioned in Chapt. 1, had been started by B. Bröker, H. Glowatzki and others in my group before the start of my own project [106, 40, 41, 105]. They had found that HATCN on Ag(111) first forms a flat lying monolayer (ML), where the metal-to-molecule electron transfer [142, 152, 40] balances the metal surface electron "push-back" effect [142, 320]. Consequently, ϕ of flat lying monolayer HATCN/Ag is the same as that of the pristine Ag surface (ca. 4.6 eV). Deposition of further HATCN molecules induces a transition to a denser monolayer of almost upright-standing edge-on oriented HATCN molecules. This is accompanied by a different metal-to-molecule electron transfer and electron density distribution, which. This suggests that structural changes of such interlayers may have a significant impact on the actually achievable charge injection barriers at O/M semiconductor contacts.

Before discussing the photoemission data (obtained at **BESSY**), Sect. 5.2.1 discusses morphological details of the HATCN/Ag(111) system on the basis of RT-STM data that was acquired within the present work. Thereafter, Sect. 5.2, presents results that evidence the effect of the HATCN molecular orientation in interlayers on the hole injection barriers towards α-NPD (Sects. 5.2.2 - 5.2.4) and Alq_3 (Sect. 5.2.5), which are prototypical hole and electron transport materials in organic light emitting diodes, respectively. A significant effect is concluded on for both, α-NPD and Alq_3. In addition, a comparison of the ELA for interlayer-modified metal electrodes (flat-lying HATCN/Ag and edge-on HATCN/Ag) and pristine metal electrodes of the same work function (Ag and Au, respectively) is presented. This illustrates the importance of the push-back effect compensation by the HATCN interlayer on the energy level alignment when contacting organic materials with metal electrodes.

A large part of the results presented in Sect. 5.2 and Sect. 5.1 were published in Ref. [210] and [212], respectively.

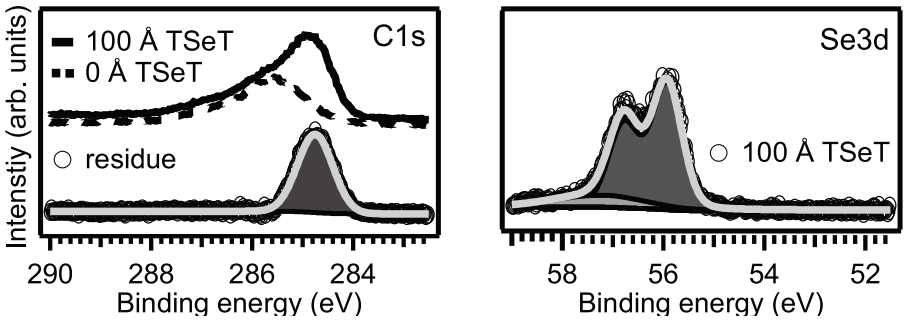

Figure 5.2: Se3d and C1s core level spectra for 100 Å TSeT/SiO_x. For the C1s spectrum, the contribution due to the carbon contamination of the SiO_x substrate (= 0 Å TSeT) was subtracted as shown.

5.1 Seleno groups control the energy-level alignment between conjugated organic molecules and metals

5.1.1 Room temperature film growth (interface region)

Whether TSeT indeed interacts with the metals Au and Ag via its seleno side groups was tested with XPS experiments that should yield characteristic core level binding energy shifts upon specific strong interactions. A film of nominal 100 Å TSeT deposited on SiO_x, for which no significant interaction is expected at the interface, served as reference system for bulk-like spectral features. The C1s and Se3d spectra are shown in Fig. 5.2. For the C1s spectrum, the contribution of the residual carbon contamination of the SiO_x substrate has to be subtracted. The remaining spectrum (residual) can be fitted with one Voigt peak at 284.75 eV. The Se3d region contains two doublets of very different intensity. The binding energy of the main feature ($Se3d_{5/2}$ at 55.9 eV) compares well to that found for bulk TSeT before [236]. The very weak and also broader feature at ca. 57 eV BE is most likely due to a shake-up process, as was observed for the closely related molecule tetrathio-tetracene (TTT) [236].

Figure 5.3 *(facing page)*: a): Se3d and C1s core level spectra for TSeT films of indicated coverage on Au(111) (left) and Ag(111) (right). For the Se3d spectra, the background due to the $Au5p_{3/2}$- and the Ag4p-contribution was subtracted, respectively (not shown). For both core levels, the spectral intensity which corresponds to the species found also for TSeT/SiO_x (shown by the black and gray filling) is termed "bulk-like". For the Se3d signal, two additional contributions at lower binding energy, identified as interface species (IF 1 and IF 2, IF 1 has the larger binding energy of the two), can be resolved. For the C1s signal, only one additional peak at lower binding energy (containing both IF species) can be resolved by a fitting procedure as detailed in the text. b): Fractions of bulk-like and IF species in the Se3d and C1s spectra [as found by the fits of the core levels in a)] as function of TSeT coverage.

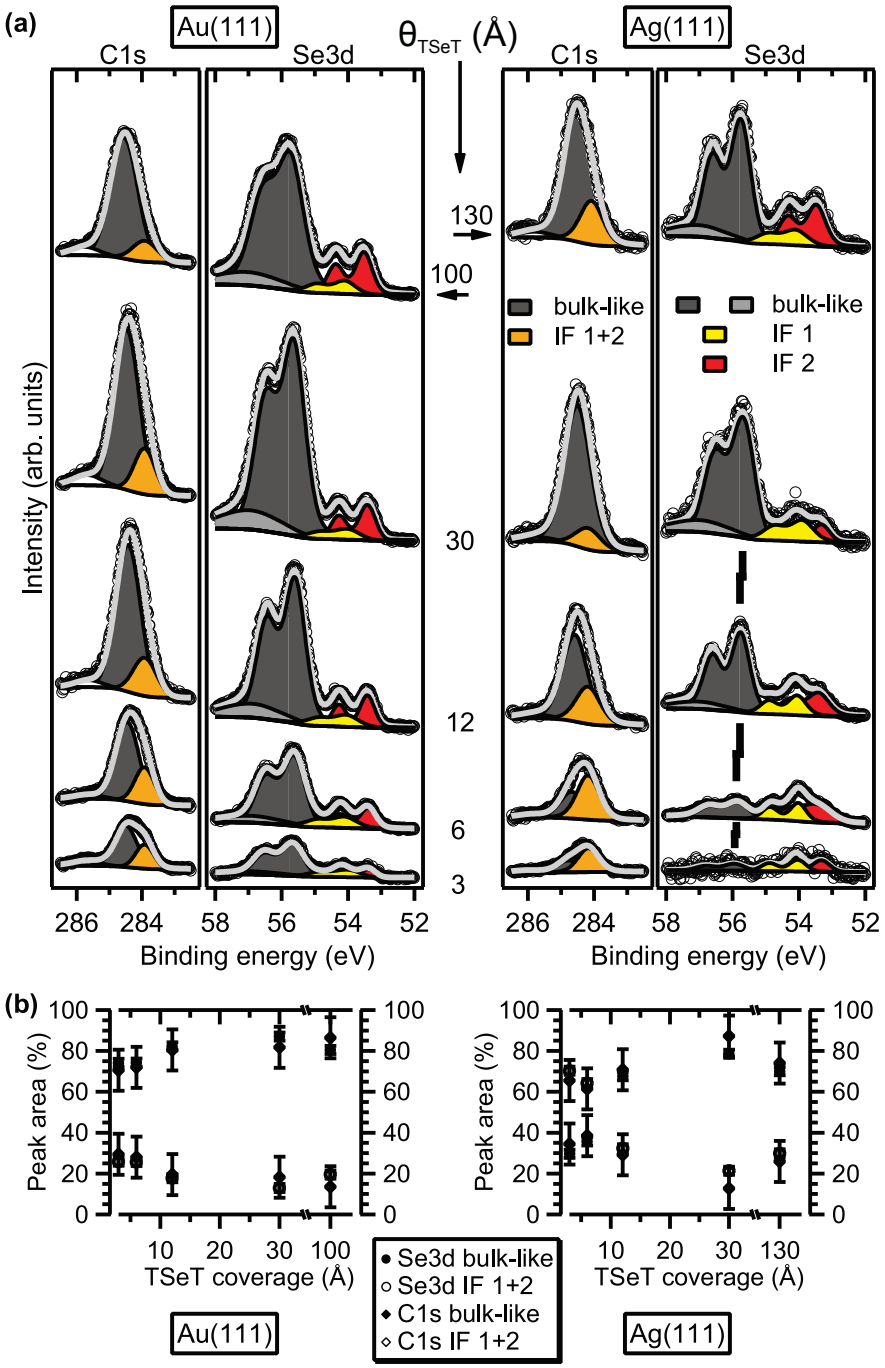
(a)
Au(111)
C1s
Se3d
θTSeT (Å)
Ag(111)
C1s
Se3d
130
100
30
12
6
3
bulk-like
IF 1+2
bulk-like
IF 1
IF 2
Intensity (arb. units)
286 284 58 56 54 52
Binding energy (eV)
286 284 58 56 54 52
Binding energy (eV)
(b)
Peak area (%)
0 20 40 60 80 100
10 20 30 100
TSeT coverage (Å)
Au(111)
Se3d bulk-like
Se3d IF 1+2
C1s bulk-like
C1s IF 1+2
10 20 30 130
TSeT coverage (Å)
Ag(111)

In Fig. 5.3 a), the Se3d and C1s spectra for several coverages of TSeT on Au(111) (left) and Ag(111) (right) are shown. The Se3d region overlaps with the energy positions of the $Au5p_{3/2}$ and Ag4p levels, and the presented spectra were corrected for photoelectron intensity stemming from these substrate features by a simple subtraction procedure (not shown). Starting from nominal sub-monolayer TSeT coverage (ca. 3 Å), four Se3d doublets are observed on each of these two metals. The two features at higher BE agree with the two bulk-like peaks observed for TSeT/SiO_x (vide supra). The two features at lower BE (Se $3d_{5/2}$ at 54.0 eV and 53.5 eV) are not present in the reference spectra for films on SiO_x, thus they must be attributed to TSeT interacting with the metal surfaces and are therefore referred to as interface species (IF 1 and IF 2, respectively).

Like the Se3d spectra, also the C1s spectra of TSeT / Au(111) and TSeT / Ag(111) differ from those of the TSeT film on SiO_x, as can be clearly seen by the peak asymmetry, particularly for low coverages. In a simple fit model, one contribution in the C1s spectra is attributed to the bulk-like species. By fixing the energy difference between $Se3d_{5/2}$ and C1s to the value that was found for "bulk" TSeT on SiO_x (228.8 eV), the second C1s contribution is found at 0.5 eV lower BE (i.e., too large to be only due to a difference in photo-hole screening efficiency), which is thus assigned to the interface species. This assumption is supported by the good agreement of the relative spectral weights of bulk-like and interface (IF 1 + IF 2) contributions for both elements' core levels, as illustrated as a function of coverage in Fig. 5.3 b). Note that the C1s to Se3d peak area ratio is consistent with the chemical formula of TSeT for all coverages. Some spectral intensity is also observed at ca 285.5 eV, which was not seen for TSeT/SiO_x (Fig. 5.2). This feature, which is too small to notably contribute to the quantitative analysis, probably stems from those carbon atoms of TSeT that are bound to selenium atoms, and, thus, undergo a different chemical shift upon chemisorption compared to the other carbon atoms [120]. Notably, the BE values of the interface species for Se3d and C1s are very similar to those found for selenolate SAMs on Au(111) and Ag(111), where the selenium atoms are covalently bound to the metal [63, 310, 263]. This strongly hints towards a similar interaction in terms of strength and bond mediation (i.e., via the selenium atoms) also between TSeT and Au and Ag.

In the chalcogenolate SAM-related literature, different explanations can be found for the occurrence of two Se3d-peaks with BEs similar to IF 1 and IF 2 found for TSeT/Au(111) and TSeT/Ag(111) [Fig. 5.3 a)]: For selenolate and thiolate SAMs on Ag(111) and Au(111), BE differences of the chalcogen core levels between films of different SAM types [262, 127] and also within one film [310] comparable to the 0.5 eV difference between IF 1 and IF 2 have been observed and were explained with differently bound chalcogenolate species. In particular, a systematic variation with the number of methylene groups was found for oligophenyl-substituted alkanethiolate SAMs (so-called odd-even effects) [262, 127] and explained with differently strained sulfur-metal bonds [122]. On the other hand, for benzeneselenol/Au(111) [63] and biphenyl methylenethiol / Ag(111) [127], two core level peaks have been attributed to two chemically different chalcogen species on the surface: chalcogen atoms in chalcogenolate molecules [at higher BE, which would correspond to IF 1 in Fig. 5.3 a)] and chalcogen atoms abstracted from the molecules [at lower BE, which would correspond to IF 2 in Fig. 5.3 a)]. In the present case, given the chemical structure of TSeT [Fig. 5.1 a)], containing four selenium atoms that are not spaced in

registry with the Ag(111) or Au(111) lattice, it is conceivable that the selenium atoms of TSeT form differently strained bonds with the Au and Ag surface. In addition, while TSeT is found to lie mostly flat on Au(111) and Ag(111) from the LT experiments (vide infra), it is possible that some TSeT molecules adopt an inclined (and thus differently bound) adsorption geometry, which was indeed observed for TTT/Au(111) from scanning tunneling microscopy (STM) [91].[1] These considerations allow rationalizing the observation of two interface species without invoking a breakage of Se-C bonds. However, with the insufficient atomistic-geometrical information for this particular system, no further speculation is attempted [2].

Having established that TSeT molecules bind to the metal surfaces strongly via their seleno groups, let us now examine how this affects the energy level alignment. Fig. 5.4 shows UPS spectra for some of the same samples already discussed with XPS from Fig. 5.3 a) (those that are representative for the TSeT monolayer range). Thicker TSeT films will be discussed after LT and annealing sections (Sects. 5.1.2 and 5.1.4, respectively), in order to allow a comprehensive discussion once both RT and LT data have been introduced. In the left part of Fig. 5.4 the SECO region is presented, which is used to determine the sample work function ϕ. Results for Au(111) and Ag(111) are reported in a) and b), respectively. The bottommost trace in each graph shows the spectra for the respective pristine metal surfaces. Up to 30 Å TSeT coverage, the work function of Au(111) is reduced by 1.05 eV (from an initial value of 5.50 eV) and by 0.15 eV on Ag(111) (from 4.60 eV). Thus, ϕ of 30 Å TSeT on both metals is 4.45 eV and the initial ϕ difference between Ag(111) and Au(111) of 0.9 eV is eliminated by deposition of the TSeT monolayer and the concomitant formation of an interface dipole $\Delta\phi$. From the very different $\Delta\phi$'s, a markedly different charge density rearrangements upon TSeT/metal interface formation in the two cases can be concluded on. Interestingly, a fully analogous behavior was observed for thiolate SAMs on the same metals [333]. For these interfaces, theoretical modeling indicated that the adsorption-induced work function change is dominated by the charge transfer between the sulfur atom and the metal, which is driven by the initial metal ϕ, thus resulting in very similar ϕ values after SAM formation [243, 123, 121, 124] (see also the discussion of Fermi-level pinning in the case of chemisorption in Sect. 2.5.2). The calculations found the same behavior for selenol and thiol docking groups. Therefore, the behavior of TSeT, i.e., yielding the same ϕ for TSeT/Au(111) and TSeT/Ag(111), together with the core level BEs that match those of selenolate SAMs, suggests that the selenium-metal bonds in these systems behave very similar to what was found for the SAMs. This gives strong evidence that the same energy-level alignment mechanism as found for the SAM/metal interface [123], also governs the energy level alignment at the TSeT/metal interface.

Note that $\Delta\phi$ for TSeT deposited on Au(111) is comparable to that induced by many physisorbed molecules, such as the prototypical organic semiconductor pentacene [162, 323], which also compares well to TSeT in terms of IE and molec-

[1] However, for selenolate and thiolate SAMs on Au(111) and Ag(111), marked differences were found for the preferred geometry depending on docking group [151, 18] and metal [257, 189, 310, 262, 127].

[2] It should be noted though, that in view of a varying ratio of IF 1 and IF 2, it is unlikely that only one bonding pattern for all TSeT molecules can explain both selenium interface species.

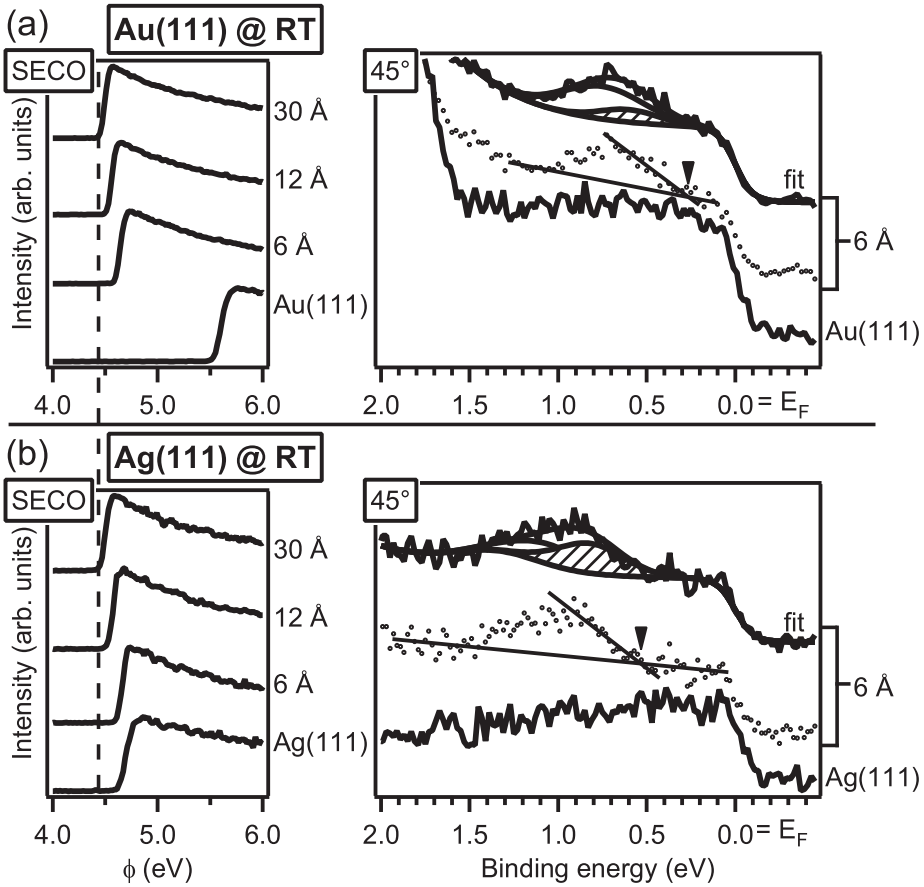

Figure 5.4: Room temperature UPS results of a) Au(111) and b) Ag(111) for the pristine metals and after deposition of the indicated nominal TSeT coverages. On the left, the SECO region is shown for TSeT coverages up to the approximate saturation of the vacuum level shift (30 Å). A dashed line illustrates the common $\phi = 4.45\,\mathrm{eV}$ at 30 Å in both cases. In the right figure part, the valence band region close to E_F is shown (measured with an angle of 45° between sample normal and detector). For both a) and b), only the spectrum for a TSeT film close to the nominal monolayer coverage (6 Å) is presented, which is used to determine the HOMO energetic position by a simple onset procedure, as illustrated for the dotted spectra. In addition, a fit in agreement with the findings from the LT data (vide infra) is presented for the identical spectra shown as continuous lines. The peak filled with dashed lines corresponds to the two interface species, and the one without filling accounts for the multilayer species. The relative intensities for the two fit contributions are approximated by the respective relative intensities determined from the core level fits presented in Fig. 5.3.

ular structure [3], or e.g. benzene[320]. However, the $\Delta\phi$ induced by pentacene is due to the push-back effect, whereas XPS clearly showed chemisorption of TSeT on Au(111). The impact of the selenium substitution on the ELA is more pronounced for TSeT/Ag(111), where $\Delta\phi$ is significantly smaller than reported for physisorbed molecules like pentacene [210, 160, 148] and other common COMs [76, 79]. Accordingly for TSeT, the push-back effect is to a significant extent counterbalanced by the charge density rearrangement induced by the seleno-Ag bond.

The low BE valence band region at an emission angle (θ) of $\theta = 45°$ is presented in the right part of Fig. 5.4. For a nominal TSeT coverage of 6 Å on both, Au(111) and Ag(111), a peak is found in the low BE valence region close to the E_F, which was not observed for the pristine metals, and can be readily ascribed to emission from the orbital of chemisorbed TSeT which is derived from the highest occupied molecular orbital (HOMO) of free TSeT. The low BE onsets of emission determined with the simple procedure illustrated in Fig. 5.4 are at 0.25 eV and 0.5 eV for Au(111) and Ag(111), respectively.

From the evolution of ϕ as function of nominal coverage it can be concluded that the monolayer is closed only beyond 12 Å or 30 Å on both substrates, which is well beyond the nominal monolayer-equivalent coverage (4 Å). Therefore, 3D-island formation is preferred over metal surface wetting for TSeT films deposited at RT. Accordingly, already films of very low nominal coverage not only contain TSeT molecules that are in contact with the metal surface, but also some that are located in multilayers, as is also supported by the XPS data in Fig. 5.3. In general, the ionization energies measured by UPS of molecules in the bulk and in contact with a metal surface are not the same, e.g. because the photo-hole screening efficiency of a metal is significantly larger than that of an all-molecular surrounding (Sect. 2.6). Indeed, as will be shown below for TSeT films grown at LT, the energy levels of multilayer TSeT molecules are at higher BE than the ones in contact with the metals. To account for this finding, which will be discussed in detail in the following section 5.1.2, Fig. 5.4 also presents fits that account for both species, with the *relative* spectral intensities as found for IF and bulk-like species in XPS. Note that the interface contribution of the HOMO-derived peak for TSeT/Au(111) has a lower *absolute* intensity as compared to TSeT/Ag(111) [Fig. 5.4 a) and b), respectively], which is consistent with the fact that multilayer molecules, which attenuate the interface signal, are much more abundant in the case of Au(111) [cf. Fig. 5.3 a)]. However, given the complex film morphologies, a detailed analysis of the HOMO-derived peaks is beyond the scope of the simple model employed.

5.1.2 Low temperature film growth

To clearly disentangle the energy levels right at the interface and in multilayers, which is to some extent impeded by the island growth mode at RT, TSeT films were also grown on Au(111), Ag(111), and Cu(111) single crystals cooled to 77 K (LT), whereby the tendency of TSeT to form islands was kinetically suppressed. Cu was added in this part of the study to extend the metal substrates towards typically higher reactivity with conjugated molecules. UPS spectra of

[3] The (lying) pentacene molecules in these cases have IE_{ML}'s of 4.9-5.19 eV, [162, 323, 160] and therefore compare slightly better to TSeT than tetracene, whose IE is larger than the one of pentacene by some 100 meV. [336, 249, 238]

the pristine metals at RT and LT, and for TSeT deposited on them at LT are reported in Figs. 5.5 a), b), and c), for Au(111), Ag(111), and Cu(111), respectively. When cooling Au(111) from RT to LT, ϕ decreases slightly from 5.43 eV to 5.27 eV and the surface state, visible at an emission angle $\theta = 0°$, shifts to higher BE due to lattice contraction [222], but does not decrease in intensity; thus Au(111) surface contamination due to adsorbates [59] is not impeding the results presented in the following[4]. Analogous observations were made for Ag(111), where the ϕ decrease upon cooling to 77 K is only 0.02 eV, the surface state shifts to higher BE, and it increases in intensity as was reported before [222]. For Cu(111), the ϕ decrease upon cooling to 77 K is 0.3 eV. Furthermore, the surface state is almost completely quenched when reaching 77 K. This indicates that, despite the best efforts, the Cu(111) surface did suffer from notable residual gas molecule adsorption during the cooling process; consequently, the Cu results will be considered as preliminary.

Au(111)

Depositing ca. 2 Å TSeT gives rise to a peak in the valence electron region with its maximum at 0.6 eV BE, shown in the very right part of Fig. 5.5 a), which is assigned to emission from the HOMO of TSeT. This peak is clearly visible at a take-off angle of $\theta = 45°$, while it is much less intense for $\theta =$

[4] In a control experiment the initial ϕ was recovered when increasing the temperature back to RT. The ϕ decrease upon cooling is therefore probably related to the adsorption of residual gas molecules, which only stick to the surface at low temperatures, and the concomitant push-back effect. The observed decrease of 0.16 eV is well below what was found for monolayer coverage of xenon (0.5 eV).[59]

Figure 5.5 *(facing page)*: a), b), and c): UPS results for TSeT films grown on Au(111), Ag(111), and Cu(111), respectively, with the samples held at 77 K and during subsequent annealing to 400 K. Shown are, from left to right, the SECO region, the valence band region at electron emission angle $\theta = 0°$, and zooms into the region close to E_F at $\theta = 0°$ and $\theta = 45°$. For a) – c), in each case the following samples are presented: Bottom: The pristine metals before (dashed lines) and after decreasing the sample temperature to 77 K (solid gray). Middle (labeled "growth"): TSeT films of the indicated nominal coverage deposited at 77 K. For a) and b), the first layer (filled with slanted lines with positive slope) and second layer contribution (without filling) for the lowest two TSeT coverages are also shown. The dashed spectra in a) show indications of sample charging as detailed in the main text. Top (labeled "annealing"): TSeT films of the respective maximum thickness during subsequent heating to the indicated sample temperature, or in the indicated sample temperature range. For b) and the annealing temperature between 77 K and 300 K, two SECO spectra measured at slightly different sample spots are shown, which both show signs of multilayer dewetting. The determination of a clear SECO spectrum as in a) and b) was not possible for this system and the SECO onset at lowest kinetic energy will be used for further analysis, since it gives the best guess for the situation which is still governed by ϕ of multilayer molecules. For a) [b)] and 325 K [300 K], the contributions used for the subtraction procedure described in the main text are shown with a filling of slanted lines with negative slope.

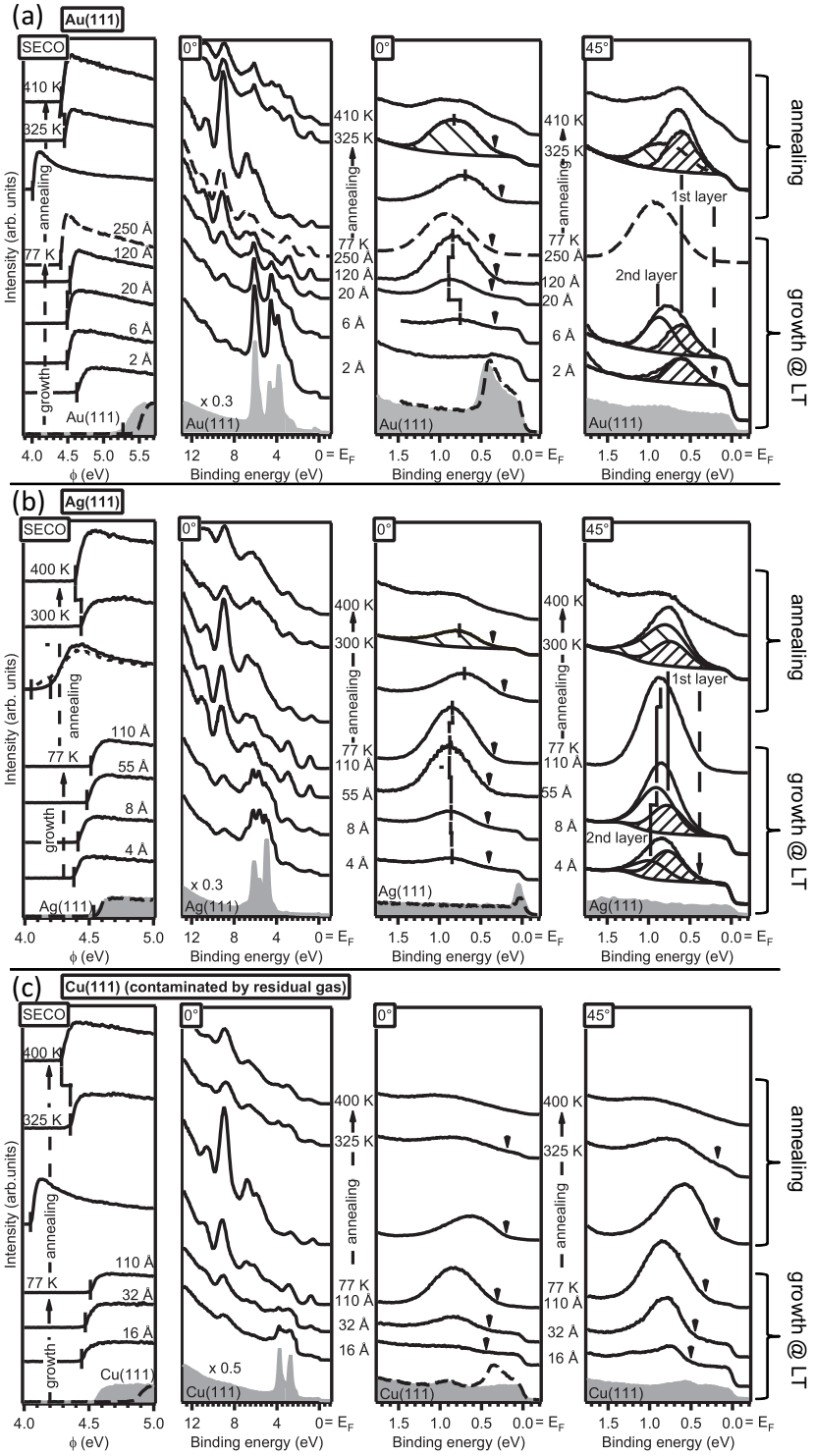
(a)
Au(111)
SECO
410 K
325 K
annealing
77 K
250 Å
120 Å
20 Å
6 Å
2 Å
growth
Au(111)
Intensity (arb. units)
0°
x 0.3
45°
1st layer
2nd layer
annealing
growth @ LT
4.0 4.5 5.0 5.5
ϕ (eV)
12 8 4 0 = E_F
1.5 1.0 0.5 0.0 = E_F
Binding energy (eV)
(b)
Ag(111)
400 K
300 K
110 Å
55 Å
8 Å
4 Å
Ag(111)
4.0 4.5 5.0
(c)
Cu(111) (contaminated by residual gas)
Intensity (arb.units)
32 Å
16 Å
Cu(111)
x 0.5

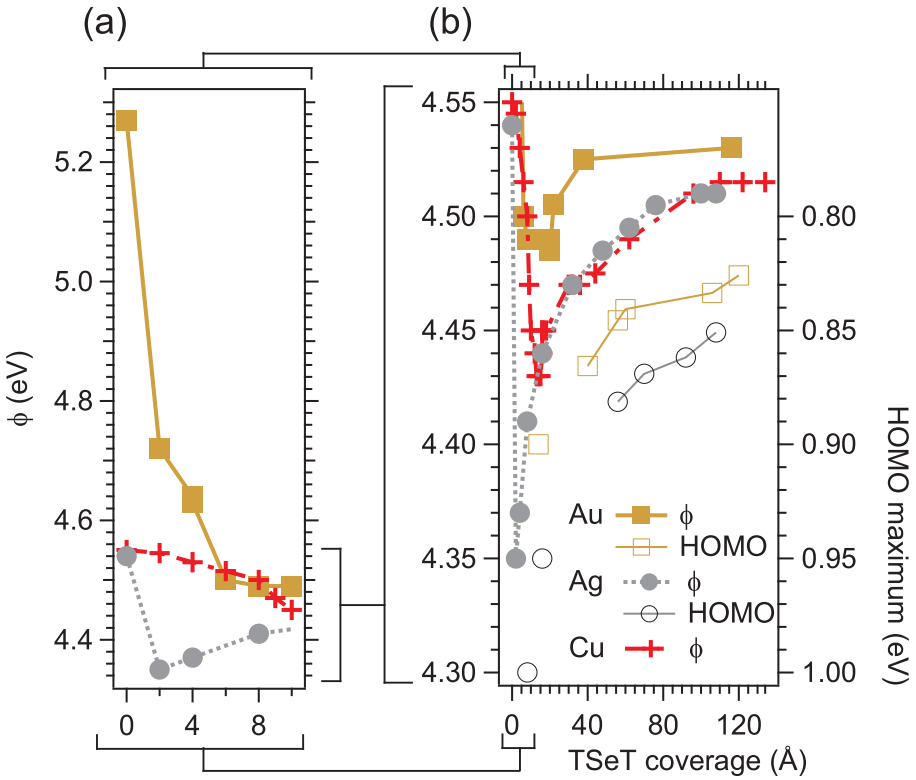

Figure 5.6: a): Evolution of ϕ as function of TSeT coverage (up to ca. 2 – 3 nominal monolayers) and with different substrates [Au(111), Ag(111), and Cu(111)] (samples were cooled to 77 K). b): The same as a) but including also thicker films. Note that the energy axis was decreased to emphasize the small ϕ increase with increasing coverage. The maximum of the HOMO-derived peak (HOMO maximum) is shown for Au(111) and Ag(111) to illustrate the parallel energetic shift of HOMO maximum and ϕ. For multilayer films, the values are plotted as symbols with connecting lines. For lower film thicknesses, interface effects predominate and the HOMO maxima were derived indirectly, as shown in Fig. 5.5. These values are plotted without the connecting lines. The ϕ values for Cu(111) are reported to illustrate their consistency with the other systems, despite the initial slight contamination of the Cu(111) surface by residual gas molecules and the qualitative differences of this system discussed in the main text.

0°. Such a θ-dependence of the HOMO-related spectral intensity is due to the selection rules of the photoelectric process and can be attributed to flat-lying molecules for the HOMO symmetry of TSeT [a_u in the D_{2h} symmetry group for an isolated molecule as shown in Fig. 5.1 b)] [274], consistent with the prevailing geometry also observed for TTT/Au(111) by STM [91]. The maximum of the HOMO-derived peak for the 6 Å coverage is located at higher BE than for 2 Å, due to a second contribution with its maximum at 0.9 eV, as shown by the best fit in the $\theta = 45°$ spectrum. The emergence of this feature in the valence spectrum is a good indication that at least a second molecular layer is present at this coverage. In view of the molecular dimensions shown in Fig. 5.1 c), this corroborates the reasoning that the first TSeT layer adsorbs flat-lying. The higher BE of the second layer can be explained by the less efficient photo-hole screening in multilayers compared to the monolayer in direct contact with the metal substrate[164, 331, 292]. In addition, the TSeT molecules chemisorb on Au(111). Thus, the monolayer molecules are chemically different from the multilayer TSeT molecules, which will result in different orbital energies [120].

At this coverage of 6 Å, ϕ has reached its minimum of $\phi_{ML} = 4.49$ eV. Together with the HOMO low BE onset at 0.2 eV, this gives the IE of the TSeT monolayer on Au of $IE_{ML} = 4.7$ eV. No ϕ change occurs between 6 Å and 20 Å coverage, as expected for multilayer formation once the chemisorbed monolayer is completed. However, going from 20 Å to 120 Å coverage gives rise to a small ϕ increase of 40 meV to 4.53 eV and a shift of the maximum of the HOMO-derived peak by the same amount towards E_F, i.e., a rigid shift. In Fig. 5.6, the HOMO maximum positions and ϕ values are summarized for all investigated coverages.

Such gradual energy level shifts when going from chemisorbed monolayer to multilayer have been reported frequently (e.g. Refs. [141, 75, 41, 253]), also for chalcogenolate SAM interlayers [22]. In the present case, the observed rigid parallel shift of HOMO and ϕ points to an electrostatic effect. At this point, the small shift is tentatively explained as stemming from polarization at the organic homo-junction, consisting of bulk-like TSeT on top of chemisorbed TSeT, similar to what was found in a recent theoretical study [82]. A second possible explanation is a complex growth scheme of TSeT, which causes a gradual reorientation of the chemisorbed first monolayer as function of multilayer coverage, similar to what was observed for HATCN/Au(111) [41, 94]. However, the annealing experiments reported below evidence a flat-lying first monolayer after dewetting of the multilayer molecules. Accordingly, to be consistent, an assumed reorientation of the chemisorbed first monolayer upon overlayer formation would have to be a reversible process. A third explanation will be discussed in the following section, after the results for the Ag(111) and Cu(111) surfaces have been presented.

The peak full-width-at-half-maximum (FWHM) of the HOMO-derived peak of the 120 Å thick film is 0.5 eV, i.e., slightly larger than the 0.4 eV for the first and second layer, which indicates that the arrangement of molecules in the multilayer probably deviates from the flat-lying arrangement found for low coverages.

The continued TSeT deposition up to a total coverage of ca. 250 Å, which corresponds to several ten monolayers, led to a rigid shift of the valence spectrum of ca. 0.1 eV to higher BE and a ϕ shift of 0.13 eV (leaving $IE_{thick} = 4.9$ eV essentially constant), together with a broadening of all peaks in the valence band. These observations are probably related to positive charging of the

molecular film during photoemission [159, 126].

Ag(111)

The SECOs for selected TSeT coverages on Ag(111) are shown in the left part of Fig. 5.5 b). The ϕ evolution derived from these and further coverages, plotted in Fig. 5.6, are now discussed first, which allows for a discussion of subtle changes in the energetic position of the HOMO-derived peak later on. ϕ first sharply decreased to a minimum of $\phi_{\mathrm{ML}} = 4.35\,\mathrm{eV}$ at 2 Å, which corresponds to a change of - 0.19 eV when compared to pristine Ag(111). No further ϕ decrease was observed when going beyond this coverage. Instead, already at 4 Å ϕ increased slightly by 20 meV, which marks the start of a gradual increase of in total 0.16 eV for the final coverage of 110 Å. Note that this behavior is qualitatively the same as was found for Au(111), and the ϕ value at ca. 110 Å, $\phi_{\mathrm{thick}} = 4.51\,\mathrm{eV}$, for TSeT/Ag(111) differs by only 20 meV from ϕ_{thick} for TSeT/Au(111).

With the coverage-dependent ϕ evolution at hand, let us now turn towards the valence region. For 4 Å TSeT/Ag(111), the HOMO-derived peak varies in intensity when comparing $\theta = 0°$ and 45° in a very similar way as was found for 6 Å TSeT/Au(111). This suggests a similar adsorption geometry of the monolayer in both cases, i.e., flat-lying; this is further supported by the fact that the minimum of ϕ is found between 2 Å and 4 Å coverage, which agrees well with the value that marked the onset of the formation of the second layer on Au(111). Since for a coverage of 6 Å TSeT on Au(111) the HOMO-derived feature contained a second contribution at higher BE, it can be conjectured that the same is also true for 4 Å TSeT/Ag(111). However, the assignment of two contributions at different BE is less obvious in the latter case, as is apparent from almost identical peak maxima found for the HOMO-derived peak throughout the coverage range from 4 Å to 55 Å. Still, as indicated in Fig. 5.5 b) for $\theta = 0°$, a small shift of about ten meV when going from 4 Å to 8 Å and another of ca. 20 meV when going to 55 Å coverage indicate a change of BE between first layer and subsequent layers. A preliminary fitting (which is justified by the findings from annealing experiments) of the HOMO-derived peak for 4 Å and 8 Å coverage yields a second contribution to be located at 1 eV for 4 Å and 0.95 eV for 8 Å, which is exactly what is expected for the HOMO of multilayer molecules if one extrapolates the rigid shift of ϕ and HOMO, found for higher coverages in Fig. 5.6, to the low coverage regime. This allows to conclude that the HOMO-derived peak of one ML of TSeT on Ag(111) peaks at 0.8 eV and its onset is at 0.4 eV [shown in Fig. 5.5 b) for $\theta = 45°$], which gives an only slightly higher $\mathrm{IE}_{\mathrm{ML}} = 4.75\,\mathrm{eV}$ than was found for TSeT/Au(111) (cf. Fig. 5.7).

Cu(111)

The monolayer region of TSeT on Cu(111) is discussed in less detail than for the other two metals for the following reasons: Firstly, the specific experiments that were indicative for the monolayer region on Au(111) and Ag(111), namely very thin coverages and a multilayer film annealed to ca. RT, gave much broader features in the case of Cu(111) as can be seen in Fig. 5.5. This indicates that TSeT reacts qualitatively different with Cu(111) compared to the other two metals. A qualitative difference in bond formation has also been found for (solution-processed) benzeneselenol/Cu(111) when compared to Au(111) and

Ag(111) [328, 329]. In addition, as mentioned before, the Cu(111) surface was not completely clean due to adsorbed rest gas molecules at LT.

When going beyond the coverage regime for which the spectra contain significant intensity from the direct TSeT/Cu(111) interface, energy position and overall behavior of the HOMO-derived peak and ϕ agree with what was found for multilayer films on the two other metal substrates. The ϕ evolution is included in Fig. 5.6 and is identical with the one for Ag(111). The continuous HOMO shift to lower BE with increasing coverage can be seen from the onsets indicated in the right part of Fig. 5.5 c).

Thus, even if the information on the monolayer contains the mentioned uncertainties, the overall energy level alignment of TSeT/Cu(111) follows the same trend as observed for TSeT/Au(111) and TSeT/Ag(111). The ϕ minimum in this case is in between the ϕ_{ML} values for the two other metals (Fig. 5.6). The present UPS results therefore indicate that the TSeT energy levels are similarly pinned on all three metal surfaces, consistent with what was observed for several thiol SAMs [333].

5.1.3 Discussion of the energy-level alignment

Fermi-level pinning at the interface

After having obtained precise $\Delta\phi$ values for the three coinage metals, the screening parameter $S = \mathrm{d}\phi_{\mathrm{final}}/\mathrm{d}\phi_{\mathrm{sub}}$ can now be easily derived, as shown in Fig. 5.8 a). The fit gives $S = 0.15 \pm 0.04$.

It is worthwhile to apply the CNL method [301, 300, 299] to the TSeT/metal interface, to see whether this system follows the CNL model. To do so, one must first obtain the density of induced interfaces states (IDIS), which is typically estimated by applying the Lorentzian function

$$\frac{1}{\pi}\frac{\Gamma_i/2}{(E-E_i)^2+(\Gamma_i/2)^2}$$

to the molecular energy levels E_i [301, 300, 299]. A Γ_i of 0.5 eV[5] is assumed for all E_i [300]. The CNL is obtained by integrating the IDIS up to the total number of electrons of the isolated TSeT molecule, which for TSeT gives a 0.70 eV energy distance between CNL and HOMO maximum. The spectrum shown in Fig. 5.8 b) has been shifted to align the experimental and theoretical HOMO maxima. The screening parameter can be calculated from equation (2.2), which relates S to $D(E_{\mathrm{F}})$, the IDIS at E_{F}, as was introduced in Sect. 2.7.3. For flat-lying molecules, the parameter α in (2.2) can be described as

$$\alpha = 4\pi e^2 d/A$$

which gives

$$S = \frac{1}{1+4\pi e^2 D(E_{\mathrm{F}})\frac{d}{A}} \tag{5.1}$$

where d and A are the TSeT-metal distance and the area occupied by one TSeT molecule, respectively. In lieu of A for TSeT, $A = 106\,\text{Å}^2$, as found from STM and low energy electron diffraction for TTT/Au(111) [91] will be used.

[5] The CNL is only very weakly-dependent on Γ_i, while S depends heavily on it.

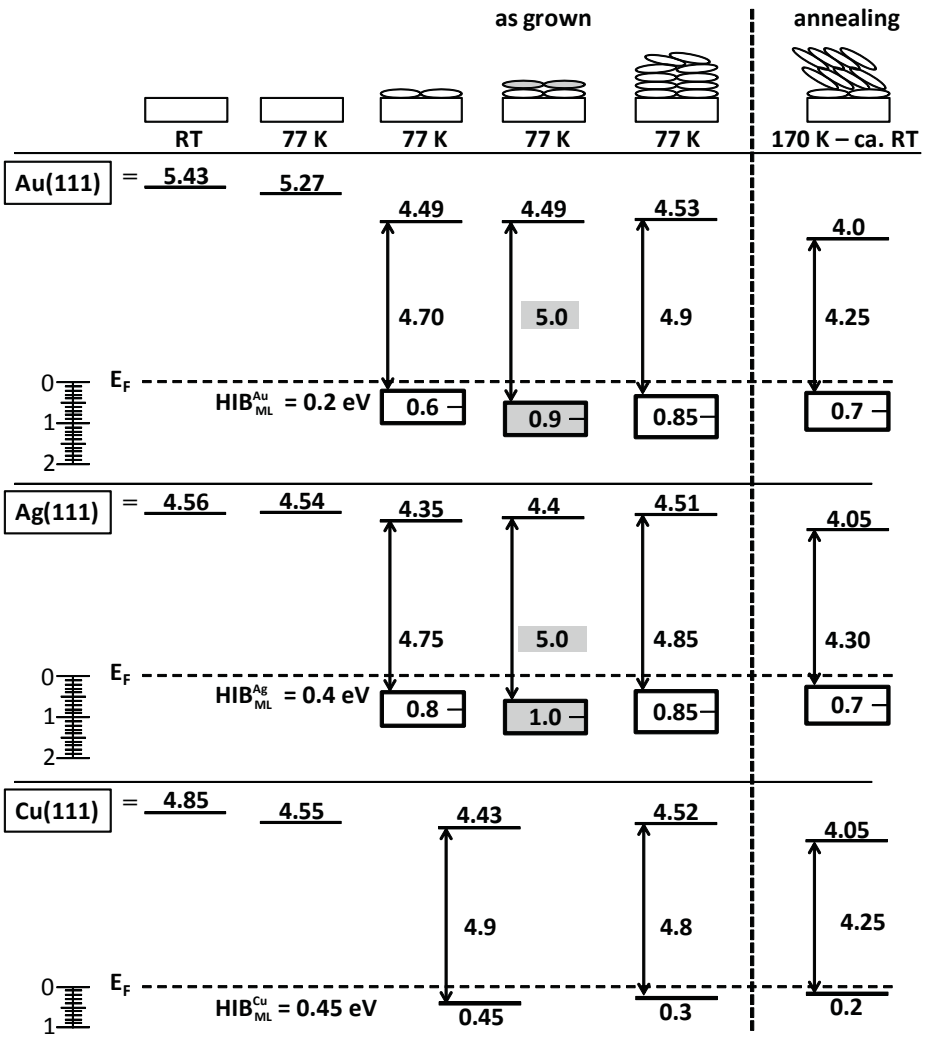

Figure 5.7: Energy level diagrams (bottom) and morphology models (top) for the following systems: From left to the vertical dashed line: the pristine metals at room temperature (RT) and 77 K, the first TSeT layer, the second TSeT layer, and a multilayer TSeT film for a sample temperature of 77 K. Very right: The multilayer TSeT film during a subsequent annealing, beyond 170 K and just before room temperature (RT) is reached. The respective substrates and a scale bar for positive binding energies in eV are shown on the left. For Au(111) and Ag(111), the HOMO maxima are given and the peak widths are indicated by the rectangles ranging to the peak onsets. Only the onsets are shown for Cu(111) and first and second layer are not differentiated because of the qualitative differences of this system discussed in the main text. In all cases, the onsets are used for determining the presented ionization energies and $\mathrm{HIB_{ML}}$'s.

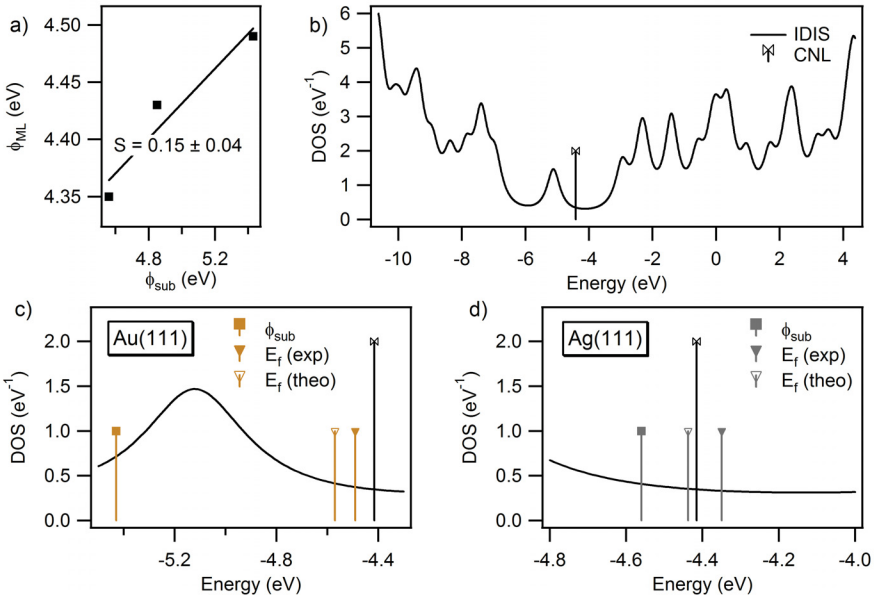

Figure 5.8: a): ϕ_{ML} as function of ϕ_{sub}, which allows deriving S. b): IDIS obtained from the TSeT Eigenvalues, shifted to correct for the experimental IE, and broadened with $\Gamma_i = 0.5\,\mathrm{eV}$ (see text). c) and d): Comparison of experimental and theoretical values for Au(111) and Ag(111), respectively.

Unfortunately, no data for d is available and $d = 3\,\text{Å}$ is assumed [120, 73]. $D(E_{\mathrm{F}})$ can be taken from Fig. 5.8 when multiplying the IDIS by 2. Eq. (5.1) gives $S \approx 0.15$ in very good agreement with the experimental value, which permits calculating the theoretical E_{F} according to [301, 300, 299]

$$E_{\mathrm{F}} - \mathrm{CNL} = S(\phi_{\mathrm{sub}} - \mathrm{CNL}) \tag{5.2}$$

With the values reported in Fig. 5.7, this gives an energy difference between HOMO maximum and E_{F} of 0.55 eV and 0.68 eV in the case of Au(111) and Ag(111), respectively. Fig. 5.8 c) and d) compares this with the respective experimental energy differences of 0.6 eV and 0.8 eV, which are also reported in Fig. 5.7.

In a more comprehensive approach [299], the CNL model takes the push-back effect into account. Therein, the procedure presented above is applied on the effective work function ϕ_{eff}, i.e., ϕ of the metal after overlayer formation as it would be without charge transfer [1, 339]. ϕ_{eff} can be obtained theoretically if the adsorption geometry of the COM is known [196], which is not the case for TSeT. However, the small S in the present case implies that the push-back is largely screened [299], which explains the overall good agreement reported above. Remarkably, though, if, for the case of Ag(111), one accounted for a ϕ decrease before applying equation (5.2), one would end up with a value for E_{F} which is on the same side of the CNL as the experimental one (i.e., towards the VL).

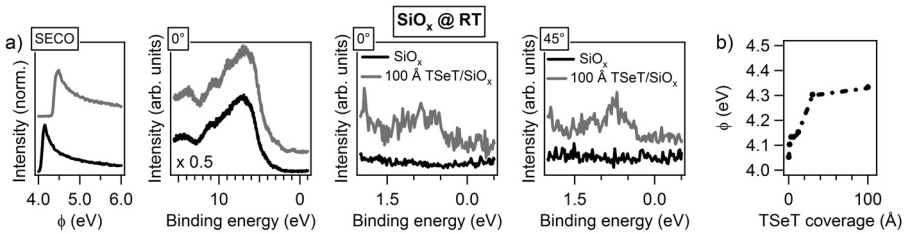

Figure 5.9: a): Room temperature UPS results of SiO_x for the as received substrate and after deposition of 100 Å nominal TSeT coverage. From left to right, the SECO region, a large valence band region (measured with an emission angle of 0°) and the region close to E_F (measured with emission angles of 0° and 45°) are presented. b): Coverage-dependent evolution of ϕ.

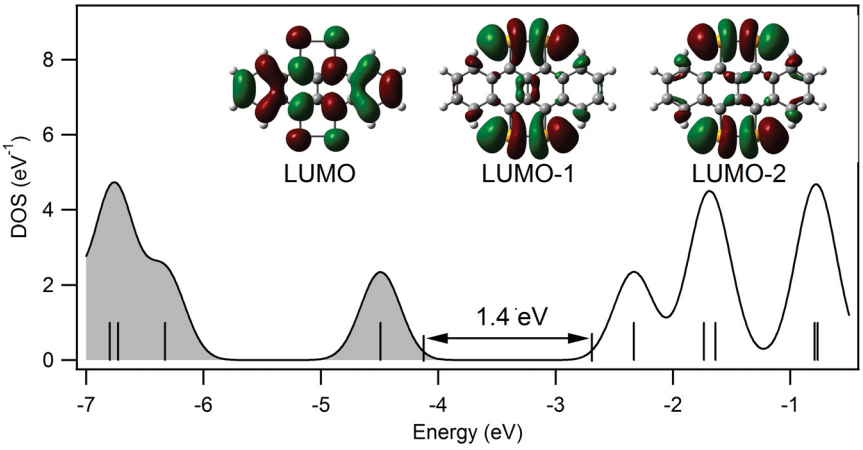

Figure 5.10: DFT results for TSeT. The Eigenvalues are given as vertical lines and as spectrum by applying a Gaussian broadening with a FWHM of 0.4 eV. The onsets of HOMO and LUMO are indicated by ticks and their energy difference is given. The insets present isodensity plots for LUMO – LUMO-2.

Energy-level shifts for multilayer films

As can be seen in Figs. 5.6 and 5.7, different values for the ϕ shift at the [bulk-like TSeT]/[chemisorbed TSeT] homo-junction were found in the cases of Au(111), Ag(111), and Cu(111) which results in identical energy level alignments for the multilayer films with respect to the metal Fermi level. It is noted in that context that for TSeT deposited on SiO_x at *room temperature*, ϕ slightly increases with increasing coverage and seems to trend towards 4.5 eV, as shown in Fig. 5.9 that presents UPS results for the same sample that was also used for the XPS reference spectra shown in Fig. 5.2. Note that TSeT hardly covers the SiO_x surface when the sample is at room temperature, as seen by the very weak HOMO-derived peak and pronounced substrate features at a nominal coverage of 100 Å. For this interface, no chemisorption was found from the XPS results, which in the case of SiO_x excludes the chemisorption-related explanation for multilayer-related energy shifts that was provided above in case of

the metal substrates. Another explanation, which also rationalizes the observation of a common ϕ_{thick} for all these substrates, is electrode-to-overlayer charge transfer induced by Fermi-level pinning of *unoccupied* TSeT states, as discussed for metal electrodes in Chapt. 6. It was shown that such pinning-induced long-range charge transfer can result in gradual energy level shifts as presently discussed for TSeT [195, 306, 215]. Notably, in view of the proximity of the HOMO-onset to E_{F}, this implies an energy distance between HOMO-onset and unoccupied states that is lower than TSeT's optical gap of ca. 1.3 eV [267] and the HOMO-LUMO-gap estimated from the DFT results (cf. Fig. 5.10). This could be caused by disorder [49]. The 0.1 eV increase of the HOMO-derived peak FWHM when going from thin to multilayer films gives an estimate for this effect, however, it does not comprise the very-low density of tailing gap states [48, 49]. Impurities are another source of intra-gap states [160, 153, 175, 227, 141]. For TSeT it was found that the conductivity increases significantly when a vacuum deposited film is heated to 375 K under UHV conditions, which was ascribed to the contact with residual oxygen and the formation of acceptor impurity levels [267]. However, the annealing of TSeT/metal to only slightly above 375 K leads to a drastic change in the valence band spectra for all employed metals, as will be discussed in Sect. 5.1.4. Therefore, the decrease in conductivity observed in Ref. [267] could also be a temperature induced effect at the metal contacts. Still, the influence of impurities cannot be ruled out for the presented experiments. Additional experiments are needed to unambiguously resolve the origin of the multilayer-related shifts. These are, however, beyond the scope of the current study, which is focused on the ELA at the immediate O/M interface only, and discusses multilayer films in relation to morphological aspects.

5.1.4 Annealing of films grown at low temperature

To be in a better position to discuss the film growth of TSeT at RT, the multilayer films deposited at LT were annealed by slowly increasing the sample temperature up to ca. 400 K over a time of ca. 15 hours. The corresponding spectra are included in Fig. 5.5. The observations obtained are almost identical for all metals and will be discussed in detail for Au(111); only (small) differences observed for the other two metals will be discussed thereafter.

Au(111)

Starting when the sample temperature reached ca. 170 K, ϕ gradually decreased from 4.53 eV to 4.0 eV, while the HOMO onset shifted from 0.35 eV to 0.25 eV BE, i.e., the IE decreased by more than 0.6 eV. This temperature-induced process can be explained by gradual dewetting of TSeT from Au(111), as also observed e.g. for pentacene/Au [150]. This allows the molecules to rearrange (most likely a transformation from an amorphous to a polycrystalline film), which can impact IE for the following two reasons: Firstly, a better/closer molecular packing can increase the intermolecular screening (Sect. 2.6), which was found to decrease the IE by up to 0.3 eV when going from disordered to crystalline films [248, 96], and can explain part of the observed IE difference. Secondly, the orientation of the molecules with respect to the substrate can change [200, 319, 47], which was shown to significantly influence the IE [76, 47, 57]. In the present case, a reorientation is indeed indicated by a change of the relative

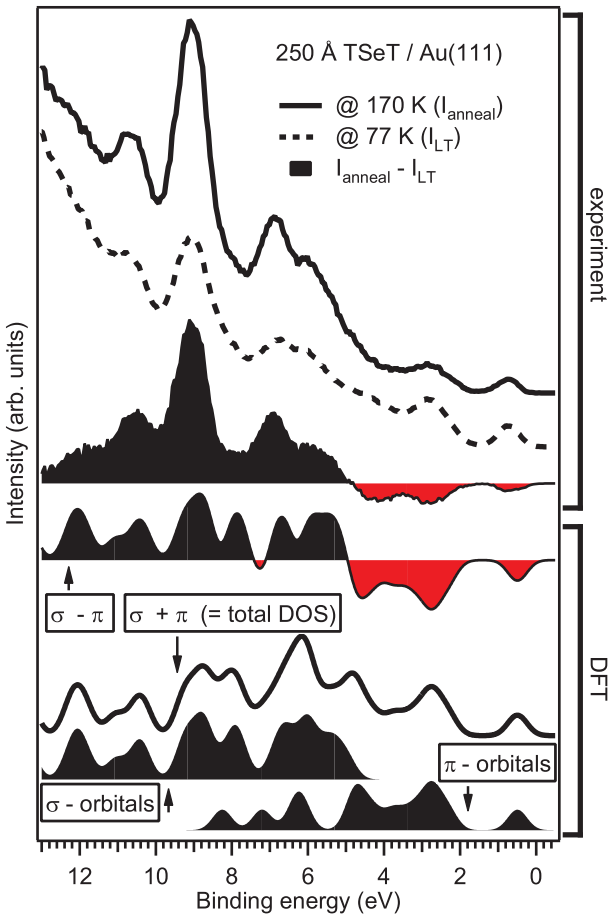

Figure 5.11: Top part (labeled "experiment"): UPS spectra obtained before and during the annealing of a multilayer TSeT-film on Au(111) [the same as shown in Fig. 5.5 a)] and the difference spectrum illustrating where the annealing induces an intensity increase (black solid) and decrease (red solid). Bottom part (labeled "DFT"): Calculated density of states (DOS, broadened with a Gaussian having FWHM = 0.6 eV) belonging to π- and σ-orbitals (black solid, at bottom as labeled). Also shown are the total DOS (black line) and a difference spectrum indicating where σ-orbitals are more (black solid) and less important (red solid) for the DOS than the π-orbitals. Spectra have been shifted to align the HOMO maxima.

peak intensities in the valence region. The features higher in BE than ca. 5 eV are much more intense than before annealing started, while the peaks at lower BE decrease in intensity. The latter ones are derived from π-orbitals, while the former ones are mainly from σ-orbitals, as illustrated in more detail in Fig. 5.11. In accordance with similar systems [319, 47], the observed intensity variation can therefore be interpreted as an increasing inclination of the backbone of the TSeT molecules ("lying-to-standing" transition). Such a transition is consistent with the observed IE decrease, since both, the Se and H atoms have a positive partial charge [236], while the π-electrons create a negative partial charge above and below the TSeT backbone. This results in a significantly anisotropic potential of an isolated TSeT molecule, as shown in Fig. 5.1 c), which translates to an IE decrease between a film of flat-lying and inclined molecules, as was introduced in Sect. 2.3 and is further detailed in Refs. [57, 125, 244]. Reorientation-induced IE decreases of comparable magnitude were reported before [76, 47, 57]. Note that for lying-to-standing transitions of related molecules often a constant ϕ is observed and the change in IE is reflected only by a shift of the molecular levels [76, 79]. This is not the case for TSeT on Au. The HOMO level is very close to E_F already at LT, and the orientation-induced movement of the HOMO would bring it even above E_F, i.e., into extreme electronic non-equilibrium. In return, electrons are transferred from the TSeT HOMO to the metal, i.e., pinning sets in. Consequently, a significant dipole is built up as evidenced by the ϕ decrease. This ensures that also the reoriented molecules with lower film IE have their HOMO below E_F. The apparent finite energy difference between HOMO-onset and E_F can be rationalized by the tailing HOMO gap states, which are not accessible with the experimental sensitivity of the employed setup [195, 48, 275, 276, 191].

When reaching ca. 325 K, ϕ increases again (gradually over ca. 1 h) to $\phi = 4.45$ eV, which is similar to ϕ_ML and ϕ_thick. Substrate features can now be seen again in the valence region, in particular the Au d-band, between 2 eV and 7 eV BE, and also the Fermi edge. Obviously, annealing leads to a dramatic change of the aspect ratio of the multilayer film, from quasi-2D to pronounced 3D. Therefore, the signal contribution from multilayer areas is reduced, i.e., the valence signal from the monolayer appears prominently and ϕ is increased due to the area-averaging of the SECO measurement. When comparing the HOMO-derived peak at $\theta = 0°$ and $\theta = 45°$ emission angle, additional intensity at lower BE can be seen for the latter case. The difference spectrum gives a peak that agrees very well in energy position and shape with the spectrum of the 2 Å film during the initial deposition sequence. This indicates that the monolayer does not dewet and reorient up to this temperature.

Increasing the sample temperature up to 380 K causes only a slight broadening of the valence features (not shown). However, at 400 K – 410 K the intensity of the molecular features reduces drastically and irreversibly; when going back to RT the spectrum remains unchanged. This final annealing step also induces a ϕ decrease of 0.05 eV. The origin of these observations is likely desorption of intact molecules, probably accompanied by (substrate-mediated) chemical reactions and desorption of reaction products, similar to what was reported for benzeneselenolate/Au(111) [63, 151] and TTT/Au(111) [91].

Ag(111)

On Ag(111) the dewetting (indicated by the beginning of the SECO shift to higher kinetic energies) sets in already at ca. 285 K [was ca. 325 K for Au(111)]. This difference between the two substrates agrees with the observation of more pronounced dewetting on Ag(111) observed during the RT measurements (see below). However, another reason for the observation of dewetting already at lower temperatures might be the lower film thickness employed [less than half of that for Au(111)].

In addition, on Ag(111) the HOMO-derived peak of the film after dewetting (between 300 K and 380 K) has a different shape and its intensity varies differently as a function of θ than was observed for Au(111). Still, like for Au(111), a feature that is significantly higher in intensity at $\theta = 45°$ than at $\theta = 0°$ can clearly be seen. Therefore, the same subtraction procedure was performed as in the case of Au(111). This yields a feature with its maximum at 0.8 eV, which is attributed to the TSeT monolayer, consistent with the discussion for the LT-film growth above.

Cu(111)

On Cu(111), the shift of the SECO to higher kinetic energies sets in at around 300 K. As mentioned before, the HOMO-derived feature for the annealed film is very broad already at 325 K. However, another change in spectral shape and ϕ decrease is seen when the sample temperature reaches 400 K, showing that also in this case the TSeT film undergoes a significant structural change at this temperature.

5.1.5 Multilayer films grown at room temperature

With the conclusions drawn from the LT film growth and annealing experiments, let us now turn back to RT-grown TSeT films and discuss the multilayer regime. Figs. 5.12 a) and b) presents the UPS data for TSeT films of the indicated nominal coverages grown on Au(111) and Ag(111), respectively. The respective XPS data were already presented in Fig. 5.3. The first observation is that even for the highest TSeT coverage on Au(111) (100 Å) as well as on Ag(111) (130 Å) [topmost spectra in Figs. 5.12 a) and b), respectively], significant spectral intensity from the substrates – apparent from still visible Fermi edges and valence region shapes that are different for Au and Ag – can be observed. Since UPS is a very surface sensitive technique, with a sampling depth of only a few Å, this supports the notion of pronounced 3D island growth on both metal substrates at RT, as was discussed above based on XPS data and the SECO evolution only.

As discussed in the LT section (Sect. 5.1.2), the contribution of the HOMO-derived peak that can be attributed to the multilayer is at higher BE than that of the monolayer, as can be seen in the fits shown for a coverage of 6 Å and an emission angle of $\theta = 45°$ in the very right part of Fig. 5.12. With increasing coverage, this feature gradually shifts by ca. 0.25 eV to lower BE for Ag(111) and a (smaller) shift is observed also for Au(111); analogous shifts are seen in the bulk-like core levels. These shifts are in part of the same nature as those observed in the LT measurements, i.e., of electrostatic origin, with a

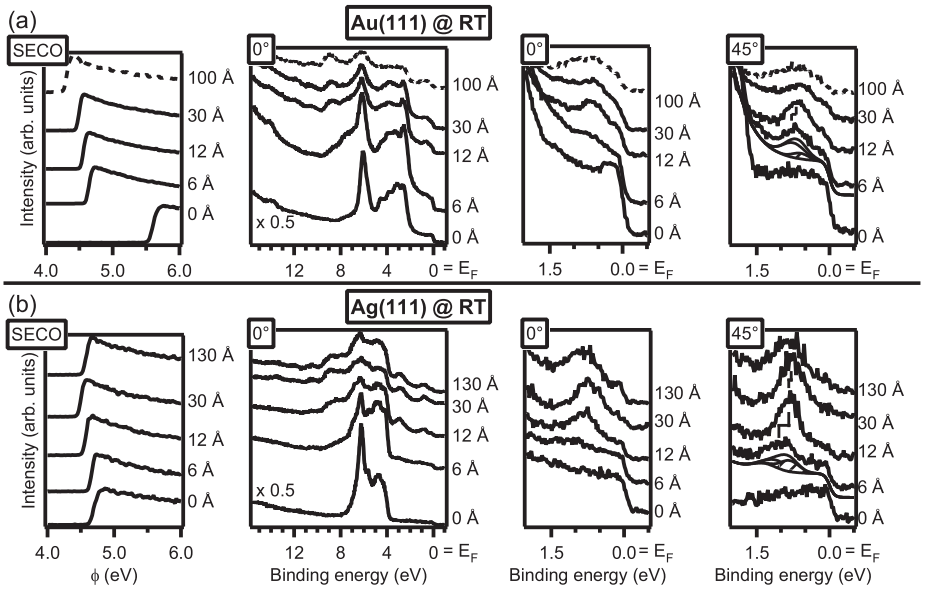

Figure 5.12: Room temperature UPS results of a) Au(111) and b) Ag(111) for the pristine metals and after deposition of the indicated nominal TSeT coverages. Shown are, from left to right, the SECO region, the valence band region at $\theta = 0°$, and zooms into the region around E_F for $\theta = 0°$ and $\theta = 45°$. The dashed spectra in a) show indications of sample charging.

corresponding shift of the SECO to higher kinetic energy not being observable due to 3D-island growth. However, the HOMO maxima observed for RT-grown multilayer films [0.6 eV and 0.75 eV for 30 Å TSeT on Au(111) and Ag(111), respectively] are at lower BE than observed for multilayer films grown at LT (0.85 eV in both cases). Recalling the observations during the annealing of the LT-grown films, this probably results from an increased inclination of TSeT molecules, with a further contribution from better screening in the RT-grown films (i.e., improved intermolecular order).

As can be seen in Fig. 5.3 a) (most clearly for the Se3d spectra and coverages less than 30 Å), the spectral intensity of the bulk-like (= multilayer) contribution in the case of Ag(111) is lower than for Au(111) for identical nominal coverages. This can be due to a lower sticking coefficient and/or more pronounced dewetting of multilayer TSeT molecules in the former case, which (both) means that TSeT molecules have less affinity to TSeT-monolayer-covered Ag(111) than to TSeT-monolayer-covered Au(111). This difference, which is consistent with the observed dewetting behavior of multilayer TSeT during the annealing of LT-grown films, is reflected in the following different observations for higher nominal TSeT coverages on Ag(111) and Au(111): For Ag(111), the substrate features become more prominent when going from 30 Å to 130 Å TSeT coverage due to significant dewetting [75]. Consistently, for this coverage step also the interface species in XPS become more intense [Fig. 5.3 b)] and an increase in intensity is also observed for the Ag3d core level (not shown).

For Au(111), on the other hand, the substrate contribution in the valence region decreases when increasing the coverage to 100 Å, evidencing that dewet-

ting is less pronounced in this case. At the same time, the SECO shifts to lower kinetic energy and all peaks significantly broaden. A pronounced broadening is also observed for the core level peaks in XPS, and the bulk-like feature shifts to higher BE, i.e., rigidly with the SECO. These observations (which, as mentioned before, likely stem from photoemission-induced sample charging) match those for the LT measurements, where, however, they were made only for a TSeT coverage of ca. 250 Å. This indicates columns of at least the same height for the RT-grown 100 Å TSeT film on Au(111), which further supports the notion of pronounced 3D island growth also in this case. It is worth noting that SECO and valence band evolution as function of coverage for RT-grown TTT/Au(111) was reported before [282] and parallels the one reported here for TSeT/Au(111).

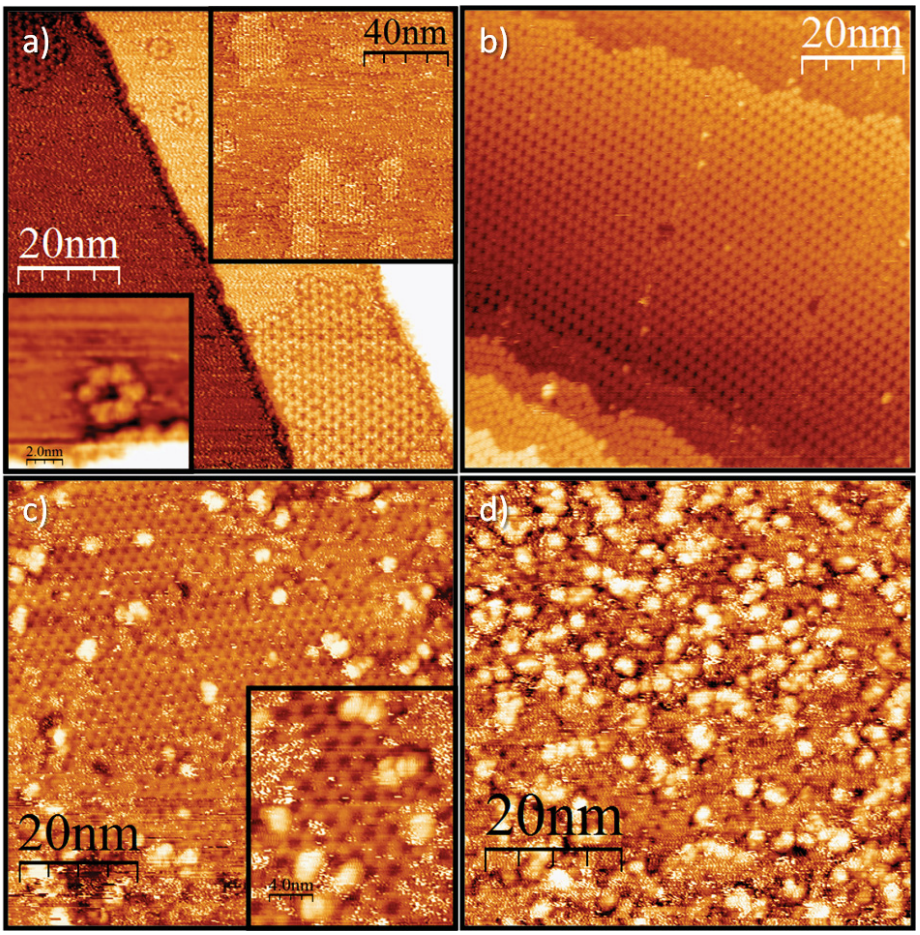

Figure 5.13: a), b), c), and d): STM images of HATCN / Ag(111) for HATCN coverages of 1 Å, 2 Å, 3 Å, and 4 Å, respectively. [Imaging parameters: a): -1.4 V, 0.2 nA, Insets: -1.4 V, 0.1 nA, b): -1.4 V, 0.4 nA, c) and d): -1.9 V, 0.2 nA]

5.2 Tuning hole-injection barriers at organic/metal interfaces exploiting the orientation of a molecular acceptor interlayer

5.2.1 STM of HATCN/Ag(111)

STM data for a flat-lying HATCN layer had been presented before [106, 105]. The structure of the flat-lying interlayer had been found to be characterized by flat-lying HATCN molecules in a honeycomb arrangement, where uncovered Ag patches are exposed via nanocavities [106]. Identical findings have also been reported for HATCN/Au(111) [321]. In Fig. 5.13, STM images of several coverages of HATCN/Ag(111) are shown. These images present details for the flat-lying layer that were not contained in previous studies. In Fig. 5.13 a), isolated honeycombs can be seen for a nominal HATCN coverage of 1 Å. Fig.

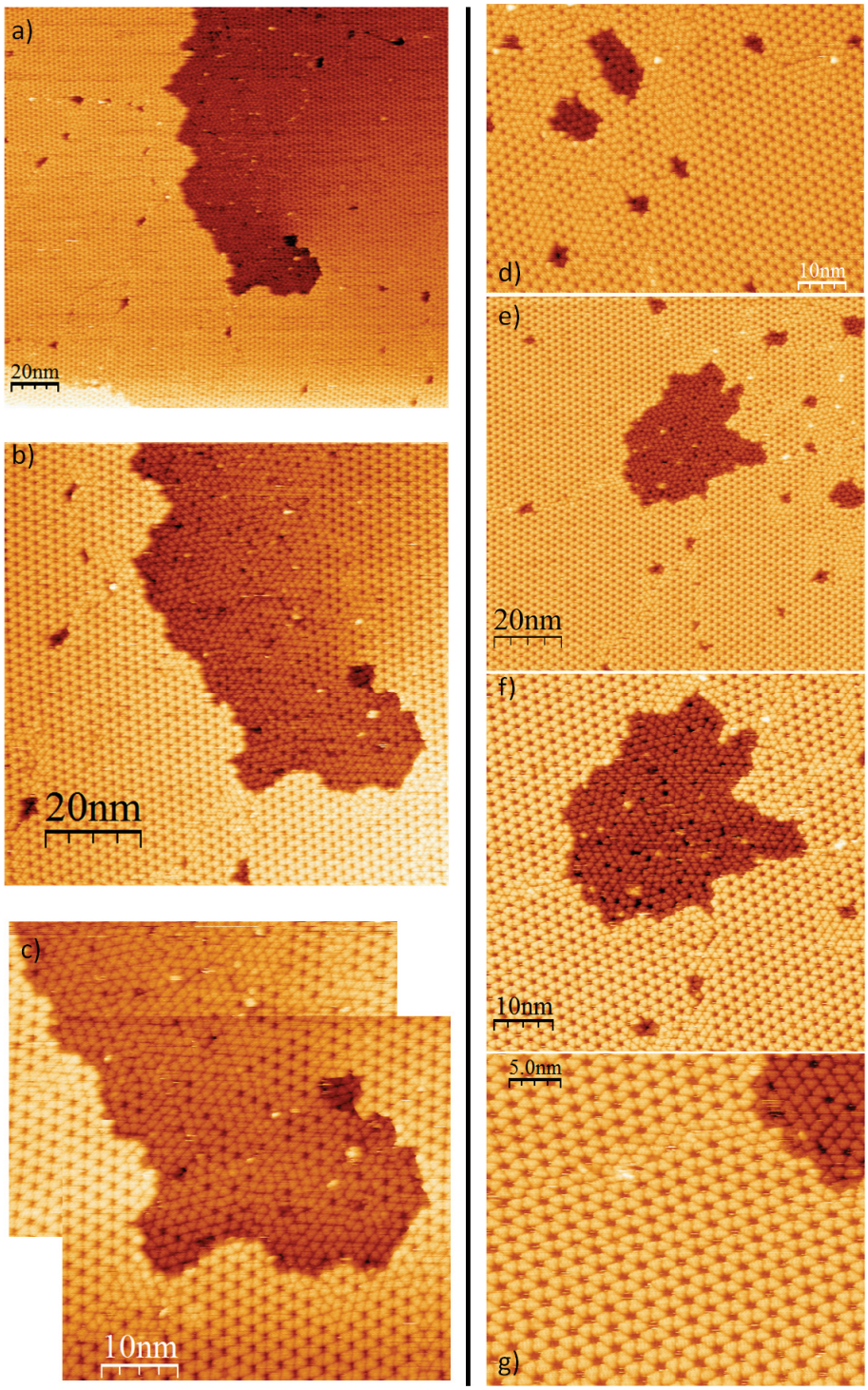

Figure 5.14: STM images of HATCN / Ag(111) for a HATCN coverage of 2 Å [the same sample as in Fig. 5.13 b)]. [Imaging parameters: a) - c): -1.2 V, 0.7 nA, d): -1.0 V, 0.7 nA, e) - g): -1.2 V, 0.8 nA]

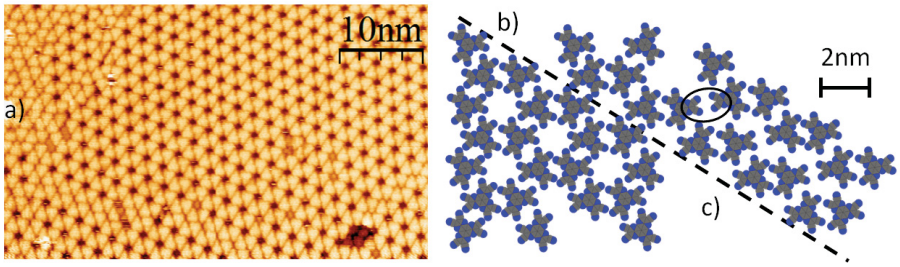

Figure 5.15: a): Zoom for the same sample as in Fig. 5.14. b) and c): Molecular models for the honeycomb arrangement and a denser arrangement, respectively [Imaging parameters: -1.0 V, 0.7 nA]

5.13 b) presents a HATCN film with a complete flat-lying monolayer. At certain locations, a HATCN packing that deviates from the (prevailing) honeycomb pattern is observed. More STM images of this film can be found in Fig. 5.14. The denser arrangement of flat-lying HATCN molecules seems to be related to grain boundaries or special cites of the Ag(111) surface like narrow terraces [cf. Fig. 5.13 b)] and holes. The honeycomb pattern and the denser arrangement are illustrated in Fig. 5.15 b) and c), respectively. They look very similar along the row direction that is indicated by the dashed line. The two arrangements thus mainly differ by the offset that two such rows have with respect to each other. This results in a denser packing for the structure presented in Fig. 5.15 c), which resembles the P1 arrangement observed for the related molecule hexahydroxy triphenylene on Ag(111) [224]. The existence of a dense flat-lying HATCN film was concluded on in a UPS study of HATCN deposited on top of a monolayer α-NPD / Ag(111), for which it was found that the HATCN molecules diffuse underneath the α-NPD molecules. The HATCN molecules were proposed do not reorient to form an edge-on orientation under these conditions [5]. The present STM results substantiate the reasoning in Ref. [5]. While the reorientation of HATCN molecules was evidenced by a multitude of experimental techniques [40], STM images of edge-on molecules have not been reported yet. In this context it is noted first, that the encircled nitrile groups in 5.15 c) have an electrostatic very unfavorable mutual arrangement [321], which, in addition to what is laid out in Ref. [40], might make a reorientation to an edge-on geometry preferred over the formation of this denser packing. Fig. 5.14 c) and d) show STM images of HATCN coverages of 3 Å and 4 Å, respectively, (i.e. more than a full flat-lying monolayer arranged in honeycombs), which evidence large protrusions (apparent height ca. 3 Å larger than for flat-lying HATCN) that increase in number with coverage and might very well result from edge-on HATCN molecules. Unfortunately, a clear identification of edge-on HATCN molecules was not possible.

5.2.2 α-NPD on pristine Ag and Au

The top part of Fig. 5.16 a) shows the valence spectra and SECOs for α-NPD deposited with incremental coverage on Ag(111). The values for the HIB and ϕ determined from these spectra are summarized in Fig. 5.18 – as are the ones for the other systems discussed in this text. ϕ of pristine Ag(111) was 4.60 eV. In the

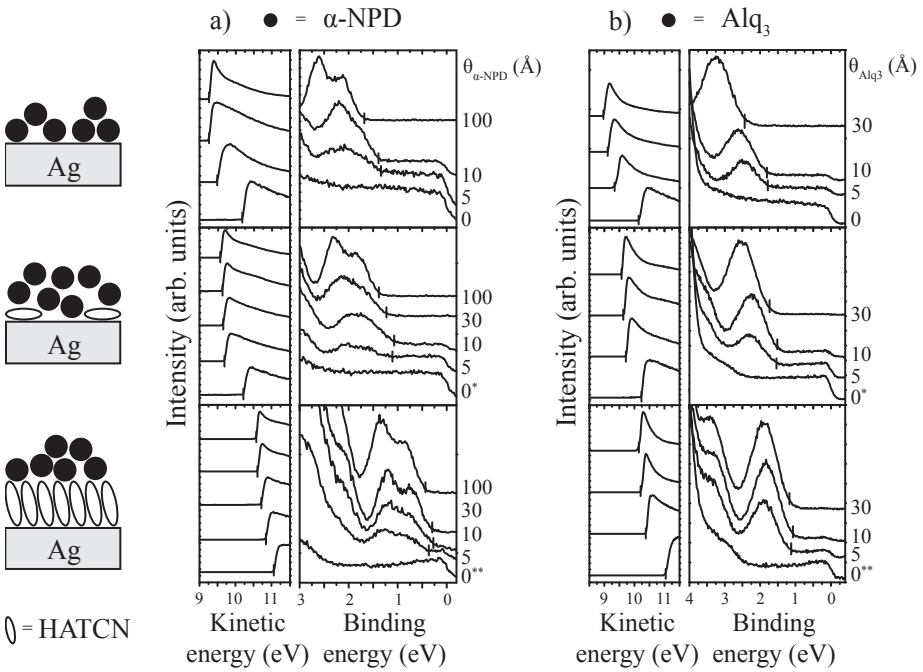

Figure 5.16: a) and b): UPS valence and SECO spectra for α-NPD and Alq_3, respectively (the thickness is denoted by $\theta_{\alpha-\mathrm{NPD}}$ and $\theta_{\mathrm{Alq_3}}$, respectively) deposited on (from top to bottom) pristine Ag(111), flat-lying HATCN interlayer on Ag(111), and edge-on HATCN interlayer on Ag(111). The flat-lying and edge-on HATCN interlayer spectra are labeled 0* and 0** respectively.

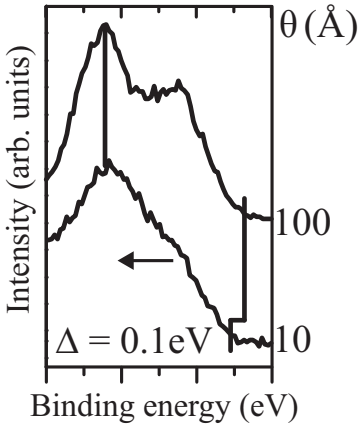

Figure 5.17: The spectrum of 10 Å α-NPD / Ag(111) (shifted to higher BE to align the HOMO-1 peaks as indicated by the arrow) and 100 Å α-NPD / Ag(111) taken from Fig. 5.16. The HOMO shift from mono- to multilayer is illustrated by the shift of the HOMO-onset.

coverage range from 2 Å to 10 Å (spectra not shown) ϕ decreased linearly with coverage to 3.65 eV and remained constant for yet higher coverages, indicating the completion of the molecular monolayer at ca. 10 Å. The lowering of ϕ is due to a modification of the Ag surface dipole by the push back effect, which corresponds to a compression of the electron tail spilling out of the clean metal surface (Sect. 2.5.1).

The valence spectra show a distinct photoemission feature spanning from 1.4 eV to 2.7 eV binding energy (BE) for low α-NPD coverages. It consists of emission from the highest and second highest occupied molecular orbital (HOMO and HOMO-1) [130]. The HOMO low-energy onset is at 1.40 eV BE in the monolayer regime and undergoes a shift of 0.35 eV to higher BE for multilayers (see, e.g., 100 Å spectrum), i.e., the HIB into multilayer α-NPD from Ag is 1.75 eV. The constant ϕ when going from 10 Å to 100 Å coverage indicates to the absence of charging. Consequently, the observed shift predominantly results from a difference in the metal-substrate mediated photo-hole screening for α-NPD monolayer versus multilayer (Sect. 2.6). However, the energy splitting between HOMO peak maximum and all other valence band features is apparently 0.1 eV larger in the α-NPD multilayer compared to the monolayer (shown for the HOMO-1 in Fig. 5.17).

As no interface states close to E_F are observed, it can be concluded that the interaction between α-NPD and Ag(111) is rather weak, i.e., physisorptive rather than involving significant charge transfer or covalent bond formation. Consequently, the difference in the HOMO-HOMO-1 energy splitting does not reflect a chemical interaction, but is most likely due to different molecular properties in the monolayer versus multilayer. Similar observations were reported for p-sexiphenyl adsorbed on Ag(111) [166] and explained by a change in the twist angle of the phenyl units [37]. In the case of α-NPD, the HOMO is localized on the central biphenyl core [130]. Accordingly, the observed differential shift would correlate to an increased twist of the biphenyl unit in the monolayer because the HOMO is at higher BE. This suggests that the interaction of α-NPD with the Ag surface is predominately mediated by the phenyl or naphthyl endgroups, which would be enabled by an increased biphenyl inter-ring twist angle. However, another mechanism may cause apparent changes of peak maxima in photoemission from molecular materials [324]. The strength of hole-vibration coupling, which governs the intensity distribution of vibronic replica on the high

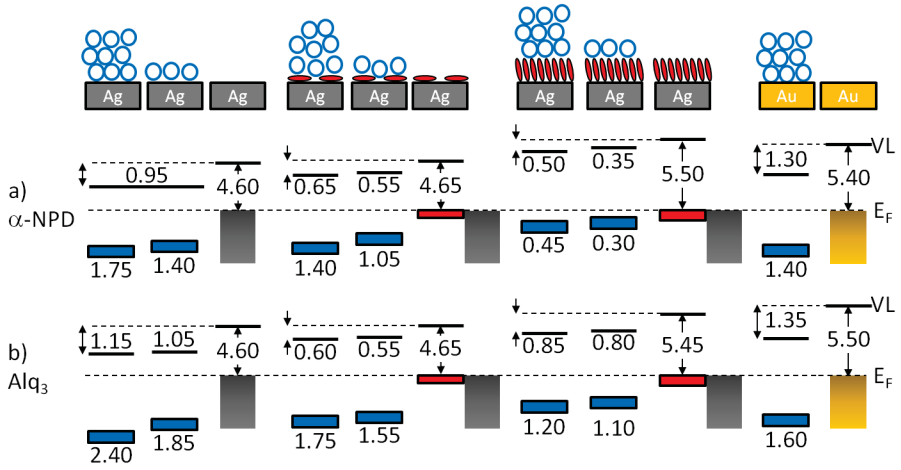

Figure 5.18: a) and b): Schematic energy level diagrams of α-NPD and Alq_3, respectively, on (columns from left to right) pristine Ag(111), flat-lying HATCN interlayer on Ag(111), edge-on HATCN interlayer on Ag(111) and Au [polycrystalline Au for α-NPD (data taken from Ref. [305]) and Au(111) for Alq_3 (data taken from Ref. [39])]. Note that to minimize effects of the permanent molecular dipole moment of Alq_3, a nominal coverage of 30 Å was chosen as multilayer for the respective systems. This is in contrast to the α-NPD results for which the multilayers have a nominal coverage of 100 Å.

BE side of the vibronic ground-state transition (Sect. 3.1.2), may be different for mono- and multilayer. Consequently, the apparent shift in the maximum of emission from the α-NPD HOMO may be due to a larger Huang-Rhys factor [111] for the monolayer that interacts directly with the metal substrate.

The electronic structure of α-NPD on Au investigated by UPS was reported in detail by Wan *et al.* [305]. Their most important findings will be shortly reviewed in the following. For multilayers, the HIB was 1.4 eV and ϕ of the molecule-covered Au was 4.1 eV, i.e., 1.3 eV lower than ϕ of the pristine Au. The differences found for the ϕ-change and HIB for α-NPD on the two metals mainly reflects the difference in the specifics of the push-back of Ag versus Au (cf. Sect. 2.5.1). Noteworthy, while ϕ values of the pristine metal surfaces differ by 0.8 eV, HIB values (for multilayers) differ only by 0.35 eV. Let us now turn towards α-NPD deposited on HATCN pre-covered Ag(111). Two different pre-coverages were chosen: (i) 2 Å HATCN corresponding to a flat-lying monolayer with a ϕ value of 4.65 eV [essentially the same as pristine Ag(111)], and (ii) 12 Å HATCN corresponding to an edge-on monolayer with a ϕ value of 5.50 eV [essentially the same as pristine Au(111)].

5.2.3 α-NPD on the flat-lying HATCN interlayer

The coverage dependent valence and SECO spectra for α-NPD deposited on Ag(111) with a flat-lying HATCN interlayer are displayed in the middle part of Fig. 5.16 a). The valence region of this layer exhibits a weak and broad feature spreading from ca. 1.3 eV BE up to E_F. These states have been assigned to

LUMO-derived hybrid state also involving a contribution from the Ag bands, which is partially filled due to metal-to-molecule electron charge transfer. Upon adsorption of 2 Å HATCN, ϕ remains unchanged because the push back effect is counterbalanced by the charge transfer [106].

For ca. half-monolayer to monolayer (5 Å and 10 Å) of α-NPD deposited on the flat-lying HATCN interlayer, ϕ decreased by 0.55 eV and the HOMO low-BE onset was at 1.05 eV. The overall ϕ reduction upon multilayer α-NPD deposition was 0.65 eV, and the HOMO onset shifted to 1.40 eV BE. The observed ϕ decrease upon α-NPD deposition is 0.3 eV smaller than for pristine Ag(111), but not zero as might be expected for non-interacting molecule-molecule interfaces (Sect. 2.3). This behavior may be explained by considering that α-NPD partially adsorbs on the free Ag patches (the nanocavities of the HATCN honeycomb structure), which leads to a push-back, however, reduced in magnitude as most of the surface is covered by HATCN. Such considerations have recently been substantiated by a more comprehensive study, for which the same COMs, but an indium tin oxide substrate was employed [318].

Upon adsorption of multilayer α-NPD, the HOMO onset shifted towards higher BE by 0.35 eV, as expected for decreased photo-hole screening. Compared to α-NPD/Ag(111), where the VB shifted by 0.45 eV to higher BE, a reduction of the substrate-induced screening by 0.10 eV is now found, probably due to the lower screening efficiency of the HATCN interlayer compared to the metal.

5.2.4 α-NPD on the edge-on HATCN interlayer

The second interlayer that was investigated comprised nominal 12 Å HATCN coverage on Ag(111), which equals an edge-on HATCN monolayer. Due to the different bonding pattern, this interlayer increases ϕ to 5.50 eV compared to 4.60 eV for pristine Ag(111) [40]. This will enable a good comparison to the results obtained on pristine Au with a very similar ϕ (5.40 eV, see above).

Photoemission spectra of α-NPD films of increasing coverage on edge-on HATCN / Ag(111) are displayed in the bottom part of Fig 1 a). The total ϕ decrease up to 100 Å α-NPD coverage was only 0.50 eV. The HOMO-onset was at 0.3 eV for the α-NPD monolayer and it shifted to 0.45 eV BE for the multilayer. The ϕ and HIB values that were found for α-NPD on edge-on HATCN/Ag(111) directly indicate that the energy level alignment at this interface is governed by Fermi-level pinning [35, 304, 161]. This substrate's ϕ (5.50 eV) is larger than the ionization energy of α-NPD (5.20-5.45 eV). If vacuum level alignment occurred, the HOMO of α-NPD would be placed above E_F, i.e., a situation out of thermodynamic equilibrium (HOMO-pinning). In the integer charge transfer model for pinning, electron transfer from α-NPD into the substrate occurs, which leads to an interface dipole that pulls the occupied levels of the organic overlayer below E_F to establish equilibrium (Sect. 2.7). The interfacial charge transfer results in a mixture of positive polarons and neutral molecules in the first α-NPD monolayer. From the discussion of LUMO-pinning in Sect. 6, one can conjecture that in the present case of HOMO-pinning, the energy levels of the neutral α-NPD are at higher BE than those of neutral α-NPD. The resulting spectrum gives a HIB of 0.3 eV for half a α-NPD monolayer. For a full α-NPD monolayer, the fraction of charged molecules is decreased (cf. the discussion in Sects. 6.2.1 and 6.2.2), which gives rise to a small shift of the HOMO-onset to lower BE. The following HOMO-onset shift to 0.45 eV when increasing the

coverage beyond the first monolayer is probably due to the filling of tailing intragap states [195, 275]. This value corresponds to the BE for neutral molecules in the multilayer. Similar observations were reported, e.g., for the E_F-pinning behavior of diindenoperylene on high ϕ conductive polymer electrodes [304]. In addition, part of this shift to higher BE may be due to the reduced screening by the underlying HATCN/Ag as the film thickness increases. Consistently, the final sample ϕ of 5.0 eV found here corresponds to the ϕ_{pin+}, which defines the border between E_F-pinning and the Schottky-Mott limit (Sect. 2.7) for α-NPD [35, 161].

Another mechanism that could explain pinning in this case was recently put forward by Rissner *et al.* [237]. Here, no long-range charge transfer between the pinned molecular overlayer and substrate is involved, but rather charge density rearrangement within the α-NPD layer due to polarization may cause the interface dipole that brings the system to equilibrium. However, the experimental evidence that will be presented in Sect. 6.2, clearly supports integer charge transfer rather than polarization as cause for pinning at O/O interfaces. As outlined above, this model can also explain the small shifts of the α-NPD HOMO onset within and beyond ML coverage of the overlayer.

Two more comments for the α-NPD/HATCN heterojunction are worth noting: First, the same HIB of 0.3 eV as in the present case of 1 ML edge-on HATCN/Ag(111) was reported for 20 nm HATCN/Au by UPS [157], even though this latter template had a significant larger ϕ of 6.1 eV. Second, an only slightly larger HIB of 0.4 eV has been found for a nominal coverage of 5 Å HATCN on Ag(111) (ϕ = 5.3 eV) [41], i.e., in between an all-flat-lying and an all-edge-on HATCN monolayer.

5.2.5 Alq_3 on the HATCN interlayers and comparison to α-NPD

Alq_3, which has a similar IE as α-NPD (5.8 eV as compared to 5.4 eV), was used as another molecular overlayer in order to validate the generality of the observed effect of the HATCN interlayer. The corresponding spectra are shown in Fig. 5.16 b) and the characteristic energy level values are summarized in Fig. 5.18 b). The values for Alq_3/Au(111) are from literature [39]. ϕ for multilayer Alq_3 was 3.45 eV (4.15 eV) in case of the bare Ag (Au) substrate. These values are similar to those found for α-NPD, which suggests a push back effect of comparable magnitude for both molecules. Due to the higher IE of Alq_3 the HIB is generally larger than for α-NPD. On Ag it is 1.85 eV for the ML and amounts to 2.40 eV for the multilayer. This yields a difference of 0.55 eV, of which 0.45 eV are induced by screening and 0.1 eV stem from the permanent intramolecular dipole of Alq_3, as seen from the concomitant ϕ-change. On Au, the HIB for a 30 Å Alq_3 film is 1.60 eV.

For Alq_3 deposited on silver pre-covered with flat-lying HATCN (initial ϕ of 4.65 eV), ϕ is 4.05 eV. This ϕ change of 0.6 eV is almost the same as for α-NPD. This is expected, as the adsorption in the remaining HATCN-uncovered Ag surface area should induce a similar push back effect for the two molecules. The HIB of Alq_3 on flat-lying HATCN/Ag(111) is 1.55 eV for the monolayer, i.e., 0.30 eV lower compared to the bare Ag electrode. For the edge-on HATCN interlayer (initial ϕ of 5.45 eV), ϕ reduces upon adsorption of Alq_3 by 0.85 eV, giving a final ϕ of 4.6 eV. The HIB of Alq_3 is 1.10 eV for the ML and 1.20 eV for the

multilayer. The significant ϕ decrease observed for Alq_3 deposited on edge-on HATCN/Ag(111) points towards E_F-pinning on this high ϕ substrate. However, the HIB of 1.10-1.20 eV seems rather high compared to α-NPD. Nonetheless, HIB values of this magnitude in the pinning regime can yet be rationalized when deep intra-gap states in the organic semiconductor are present [195, 279, 153]. The present experiments find the pinning level for Alq_3 to be 1.10 eV for the ML. A similar HIB value (1.2 eV) was found for a ML of Alq_3 on the conductive polymer poly(ethylenedioxythiophene):poly(styrenesulfonate) (PEDT:PSS with a ϕ: 5.1 eV) and attributed to pinning at gap states with a density too low to be directly observed in UPS [305]. Recently, pinning for Alq_3 was indeed clearly evidenced by Lindell *et al.* in an extensive study that covered a wide ϕ_{sub}-range [185]. The ϕ_{pin+} in this latter study was even slightly smaller than $\phi_{pin+} = 4.6$ eV found presently and in [305], which can be attributed to a higher degree of alignment of the Alq_3 dipole moments in the case of inorganic substrates used by Lindell *et al.* than on organic films [185, 317].

In essence, the qualitative behavior of Alq_3 on Ag, Au and the two flat-lying and edge-on HATCN interlayers on Ag parallels that of α-NPD, providing solid support for the general validity of the concepts for the application of interlayers that are discussed in the following.

The flat-lying HATCN interlayer features essentially the same ϕ value as pristine Ag(111) (ca. 4.6 eV), and ϕ of the upright standing HATCN layer resembles that of Au (ca. 5.5 eV). However, the HIB values determined for α-NPD and Alq_3 on electrodes with comparable ϕ with and without the acceptor interlayer differ notably. In both cases the HIB is significantly lower when HATCN interlayers are present, which is also reflected by smaller ϕ-changes resulting from deposition of the organic semiconductor (see Fig. 5.18). For instance, ϕ decreases by 1.3 eV for α-NPD on Au, whereas the decrease is only 0.5 eV when an edge-on HATCN interlayer on Ag(111) is used as electrode. Note that part of this 0.5 eV ϕ decrease is due to E_F-pinning, and might be even smaller if pinning did not occur. As noted above, the ϕ decrease for weakly adsorbed organic molecules on clean metal surfaces is due to the push-back effect, i.e., the electron density spilling out into vacuum at the free metal surface is partially moved back into the metal due to Pauli repulsion [12]. A similar effect may be operative for the HACTN-covered Ag surfaces as well, however, greatly reduced in magnitude as the α-NPD and Alq_3 induced ϕ decrease is much smaller. Consequently, it appears that the mechanically "soft matter" molecular interlayer is electronically more rigid than the "hard matter" Ag and Au.

5.3 Conclusions

As an approach to functionalize the active material directly, tetracene with four peripheral selenium atoms (TSeT) was employed and studied at the interface with Au(111) and Ag(111) with XPS, which evidences chemisorption via the selenium atoms in both cases. UPS results obtained for TSeT deposited on these metals and Cu(111) reveal different molecule-induced work function changes, which give rise to an almost identical work function for TSeT monolayers on the three metals (within 0.15 eV), while the initial metal work function values vary by almost 1 eV. This situation can be explained by charge density rearrangements at the seleno-metal-bonds resulting from Fermi-level pinning predominantly at the selenium-related levels. A seleno- (or chalcogeno-) functionalization therefore offers a good strategy to counterbalance the push-back effect at the organic/metal interface, which reduces the work function in the case of physisorption. This is particularly relevant for TSeT/Ag(111), since Ag(111) has the lowest ϕ of the three metals. In this case, almost vacuum level alignment is found, and the low IE of TSeT allows a very low hole injection barrier (only 0.4 eV).

When the samples are cooled to 77 K during deposition, TSeT grows in a kinetically limited layer-by-layer fashion on Au(111), Ag(111), and Cu(111). Molecules in multilayers change orientation from lying to vertically inclined upon annealing and pronounced dewetting occurs. Consistently, TSeT exhibits 3D-island growth when the metal substrates are at RT. Therefore, despite the favorable energy level alignment for hole injection from a metal, TSeT itself is not suitable for device applications. However, similar seleno-functionalization should be applicable also to organic semiconductors that have more favorable morphology and film growth, and, therefore, offers a promising route to fabrication of air-stable organic material with yet minimized hole injection barriers at noble metal contacts.

For the interlayer approach, HATCN interlayers of two different orientations on Ag(111) were employed to tune the energy level alignment at organic semiconductor / metal electrode interfaces. Ultraviolet photoelectron spectroscopy experiments revealed that employing such acceptor interlayers significantly reduced the hole injection barriers for organic semiconductors, up to 1.3 eV for α-NPD, and up to 1.2 eV for Alq_3, compared to pristine Ag. Most notably, even when the acceptor-modified electrodes exhibited the same ϕ as pristine metal surface [flat-lying HATCN/Ag(111) and Ag(111), and edge-on HATCN/Ag(111) and Au] substantial HIB reductions were accomplished through the mere presence of the acceptor interlayer. This is attributed to a more rigid character of the surface electron density of the metal-adsorbed HATCN layers compared to the electronically "soft" surface of metals, where considerable electron density spills out into vacuum. Consequently, the electron push-back effect due to the deposition of an organic semiconductor is less pronounced for molecularly modified metal electrodes, which is beneficial for their use as charge injection contacts in organic electronic devices.

Chapter 6

Role of charge transfer, dipole-dipole interactions, and electrostatics in Fermi-level pinning at molecular heterojunctions on metal surfaces

From an energetic point of view it is straightforward to demand that in an electronically contacted system in equilibrium all occupied energy levels be located below E_F, while all unoccupied states have to be located above it. If this is not fulfilled in the case of vacuum-level alignment, charges will flow and create electric fields to realign the energy levels accordingly. Clearly, this should also hold for the second organic layer in a multi-layer stack.

It was therefore occasionally predicted [36, 33] that the charges in such a setup originate from the conductive contacts. This is a very reasonable assumption, as the molecular level alignment is actually determined by the electrochemical potential of the substrate - as already clearly phrased by the term "Fermi-level pinning".

To test this prediction, UPS, XPS, and STM experiments for two material combinations were carried out. The architecture of both systems consisted of a Ag(111) surface that was pre-covered with a physisorbed molecular layer, on top of which a strong acceptor was deposited. Section 6.1 discusses the first heterostructure, which employed materials that were already encountered in Sect. 5, namely HATCN and Alq_3.[1].

EA_{HATCN} is higher than ϕ of Alq_3/Ag(111). Consequently, the LUMO of

[1] It was attempted to study also the second possible bilayer for the materials used in Part 1, namely HATCN on top of α-NPD-precovered Ag(111) surface. However, a careful UPS-study [5] revealed that in this case HATCN molecules diffuse underneath the α-NPD layer and form a dense flat-lying monolayer.

HATCN would be positioned below the occupied states of the substrate if vacuum level alignment was assumed. Details concerning the first Alq_3 monolayer on Ag(111) are given in Sect. 6.1.1, which were not presented in Sect. 5.2.5. From the UPS results discussed in Sect. 6.1.2, equilibrium is found to be established via electron transfer to HATCN. The location of HATCN at the very surface of the bilayer structure is evident form XPS results presented in Sect. 6.1.3. UPS data for a blend film of the two materials and a comparison with the data from Sect. 5.2.5 are discussed in Sect. 6.1.4, which allows excluding an interface dipole that is localized at the O/O interface. Instead, additional core level and valence region data evidence an electrostatic potential drop within the Alq_3 interlayer, which strongly suggest that the charges that fill the HATCN LUMO originate from the metal substrate. Sect. 6.1.5 completes the discussion of this heterostructure by arguing that the ϕ change of 0.75 eV observed upon HATCN adsorption is attributed to the combination of the two following counteractive effects. The dipoles formed by the MOCT increase ϕ. They also produce an electric field which induces a reorientation of the polar Alq_3 molecules. This, in turn, counterbalances the ϕ increase.

Section 6.2 is concerned with the second heterostructure, which comprised C_{60} and sexithiophene (6T). This material combination constitutes a better-controllable and tunable system, as detailed below, and therefore allows deriving a more generally valid and comprehensive picture of the ELA of O/O heterostructures on metal substrates in the case of pinning. C_{60} was deposited on one monolayer 6T (ML 6T) and a bilayer 6T (BL 6T) pre-covered Ag(111). Previously, well-defined morphologies for these systems had been reported by Zhang *et al.* [335] and Chen *et al.* [54], respectively. Complications due to polar molecules in the interlayer, as was observed for Alq_3, are avoided for 6T. Both systems exhibit a MOCT. With a Å-by-Å deposition of C_{60} on the ML 6T interlayer, it is demonstrated that only a fraction of the C_{60} molecules within the first overlayer undergoes a MOCT (Sect. 6.2.1) and the coverage dependent evolution of the ratio between these molecules and neutral C_{60} is carefully analyzed (Sect. 6.2.2). Sect. 6.2.3 compares the ratio of charged to neutral C_{60} molecules in the ML and BL case. The ratios are found to differ markedly for the two systems, demonstrating a dependence on the overlayer-to-metal distance. In Sect. 6.2.4, the potential drop observed in the 6T layer as well as the energy position of the neutral C_{60} frontier levels are proposed to result from electric fields induced by the interface dipoles. This statement is further supported by classical electrostatics calculations. These findings establish a coherent picture for the energy alignment at Fermi-level pinned O/O interfaces of thin films in contact with metals. As is laid out in Sect. 6.2.5, the same reasoning might also apply to cases of pinned molecular and organic heterojunctions comprising thicker layers. This was tested by applying the model to one such system that had been measured and analyzed before. Finally, Sect. 6.2.6 tentatively analyzes RT-STM results for C_{60} / 6T / Ag(111) and discusses the interdependence of the molecular assembly in the first C_{60} overlayer and the MOCT-induced dipole-dipole repulsion.

The presented XPS (UPS) data were obtained at **BESSY** (**HU**) unless otherwise stated. Most of the results presented in Sect. 6.1 were published in Ref. [6]. Section 6.2 contains results from [211] and [4].

6.1 Metal-to-acceptor charge transfer through a molecular spacer layer (MOCT)

6.1.1 Formation of the Alq_3 monolayer (ML)

RT-STM results of Alq_3 / Ag(111) are presented in Fig. 6.1 and show that Alq_3 molecules arrange into rows, which for their part form ordered grains of up to ca. 100 nm length. The intermolecular spacing between two adjacent rows found from Fig. 6.1 a) matches the value of 1.7 nm reported before [334]. The encircled area of two consecutively taken images [6.1 b)] evidences that molecules outside of ordered domains can readily move, as expected for physisorbed molecules. The overall Alq_3 network, however, is not affected by the STM measurements, which gives confidence that it can indeed prevent the HATCN molecules from touching the Ag(111) surface.

Figs. 6.2 a) – c) depict the SECO and valence region spectra, recorded in normal emission, of Ag(111), 1 ML (corresponding to 12 Å mass-thickness) Alq_3 / Ag(111), and 2 Å HATCN / ML Alq_3 / Ag(111) (sequentially deposited). The deposition of 1 ML Alq_3 / Ag(111) was calibrated by incremental deposition of molecules until the Ag surface state completely vanished. The sample ϕ, which was 4.5 eV for the pristine Ag(111), decreased by 0.9 eV upon deposition of 1 ML Alq_3 and amounted to 3.6 eV, very similar to the experiments discussed in Sect. 5.2.5. The overall VB spectrum of one ML Alq_3 shows that the Ag4d contribution, between 4 and 7 eV binding energy is largely attenuated. The low BE region was already presented in Fig. 5.16. Importantly, the frontier peak of emission from Alq_3, which is centered at 2.4 eV and has a full width of ca. 1 eV, is in fact constituted of the HOMO, HOMO-1 and HOMO-2 that are localized on each ligand of the molecule [130, 66]. For simplicity, this emission feature will be referred to as the HOMO-peak of Alq_3. No molecule-derived gap states are observed, which evidences that Alq_3 interacts weakly with the silver surface.

6.1.2 Valence electronic structure of HATCN deposited on ML Alq_3/Ag(111)

Upon deposition of 2 Å HATCN (which corresponds to ca. one layer of flat-lying molecules [40]) on top of 1 ML Alq_3 / Ag(111), the ϕ increases by 0.75 eV. In the valence region near E_F, a ca. 1 eV broad occupied density of states (DOS), with a peak maximum at ca. 0.6 eV BE, clearly emerges upon HATCN deposition. Because of the high IE of HATCN (ca. 9.1 eV) [40], this DOS cannot be attributed to the HATCN HOMO but indicates a (partial) filling of the LUMO of neutral HATCN whose EA is ca. 4 – 4.5 eV.[2]

Close inspection of this peak yields no evidence that this state is intersected by E_F, i.e., HATCN adsorbed on 1 ML Alq_3 / Ag(111) is not metallic. In contrast, the corresponding gap states of HATCN deposited directly on a bare Ag(111) surface do intersect E_F, indicating a metallic molecular adsorbate (see Fig. 6.3). This was also discussed in Sects. 5.2.3 and 5.2.4 for both HATCN / Ag(111) monolayer phases (flat-lying and vertically inclined), and explained

[2] Calculations based on Density Functional Theory (DFT, B3LYP/6-31+G* level) give an EA of 4 eV.

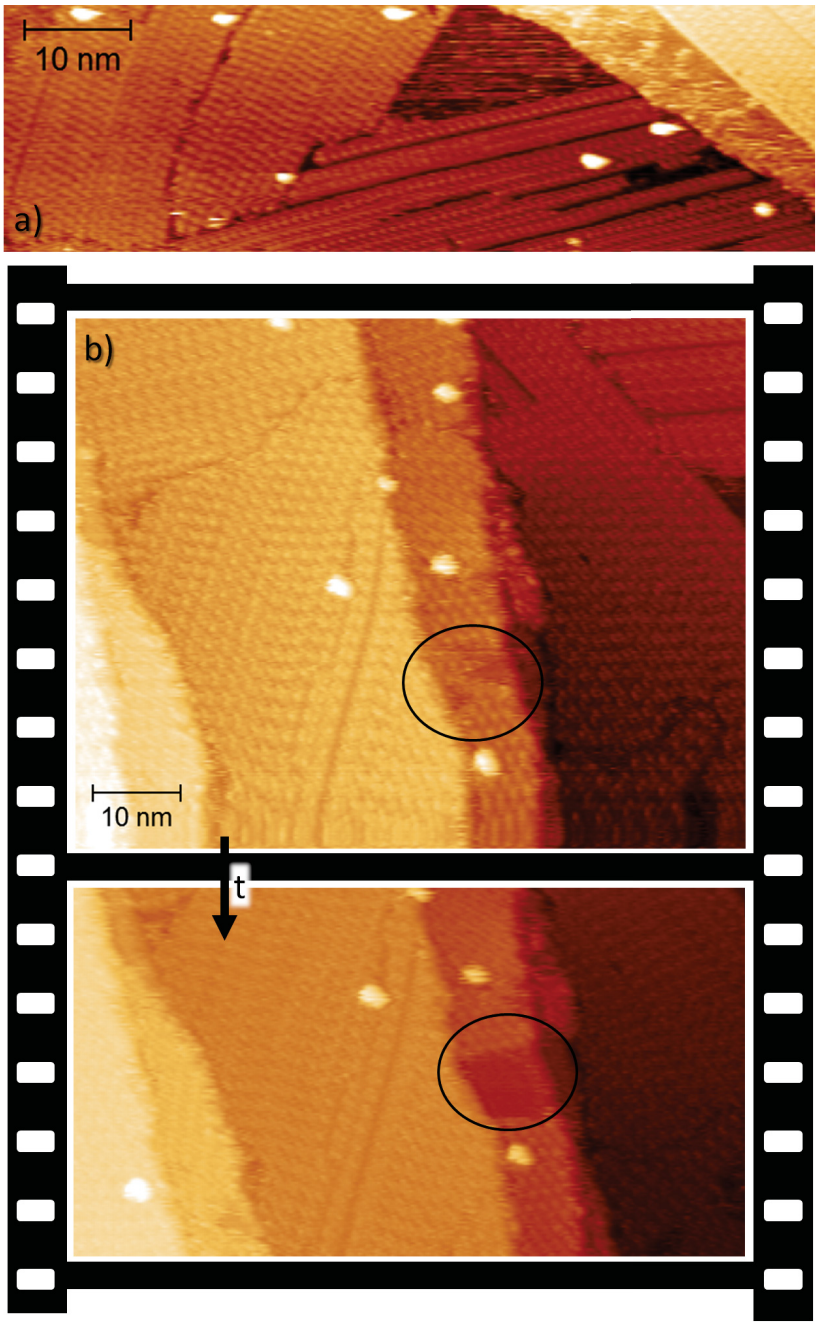

Figure 6.1: a): An STM image of Alq_3 / Ag(111) that exhibits rows of Alq_3 molecules. b): Two consecutively taken images of another region. Some molecules in the encircled area are found to be mobile and are not observed in the second scan. [Imaging parameters: 1.1 V, 0.6 nA]

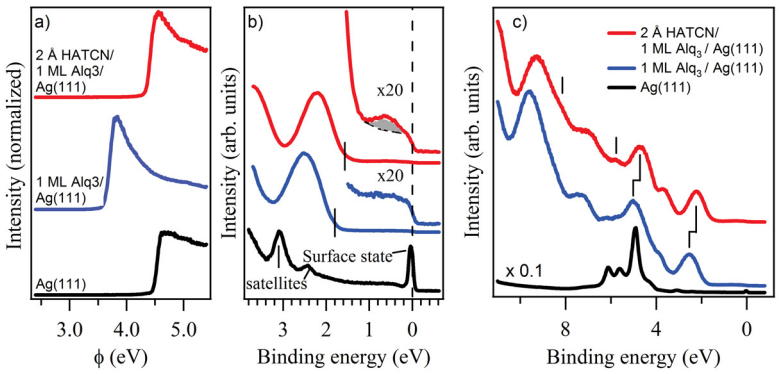

Figure 6.2: a) – c): SECO, top valence, and large range valence spectra, respectively, of (from bottom to top) Ag(111), 12 Å (ca. 1 ML) Alq_3 / Ag(111), and 2 Å HATCN / 1 ML Alq_3 /Ag(111). The thin vertical lines in b) show the Alq_3 HOMO-onset and in c) denote shifts and changes of the spectrum induced upon HATCN deposition (see text).

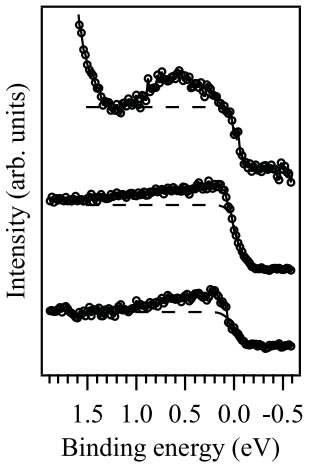

Figure 6.3: From top to bottom, top valence band spectra of 3 Å HATCN / 1 ML Alq_3 / Ag(111), ca. 2 Å HATCN / Ag(111) and 12 Å HATCN / Ag(111) (lying and standing HATCN on Ag(111), respectively, see text). All spectra were taken with a photon energy of 35 eV at BESSY.

by a strong hybridization of the HATCN LUMO and the continuum of metal states[40].

Consequently, HATCN molecules interact differently with the Alq_3 / Ag(111) surface compared to a pristine Ag(111) surface. Since interdiffusion of two sequentially deposited organic materials on metal substrates was observed for HATCN deposited on α-NPD pre-covered Ag(111) [5], and the order of a metal-adsorbed molecular layer influences the electronic properties, as demonstrated for the case of PTCDA sub-monolayers formed on Ag(111) [156], one explanation for the particular line-shape and energy position of the LUMO-derived peak observed here is a consequence of HATCN diffusing through Alq_3 and chemisorbing in a disordered manner on the silver substrate.

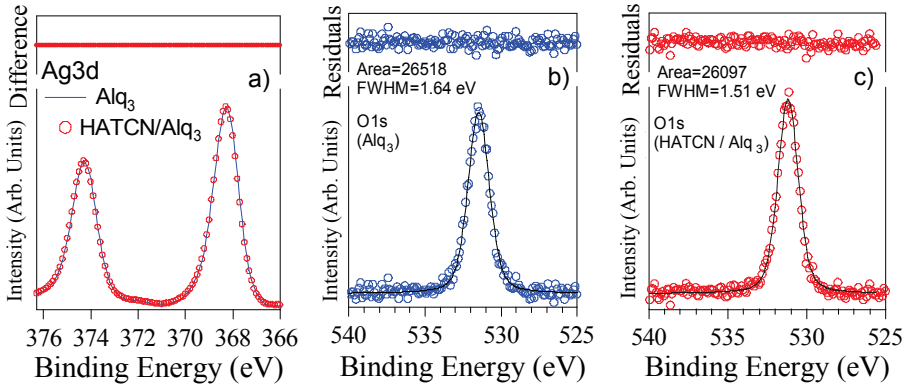

Figure 6.4: a): Normalized Ag3d core levels measured on 1 ML Alq_3 / Ag(111) (full blue line) and 2 Å HATCN / 1 ML Alq_3 / Ag(111) (red circles). b): Fit (full black line) of the O1s spectrum measured on 1 ML Alq_3 / Ag(111) (blue circles). c): Fit (full black line) of the O1s spectrum measured on 2 Å HATCN / 1 ML Alq_3 / Ag(111) (red circles). The measurements were performed at HU on the same sample that is presented in Fig. 6.2.

6.1.3 Location of the HATCN molecules

It is therefore crucial to determine the morphology of the current system, in particular the position of the HATCN molecules, which is possible by employing the short photoelectron mean free path (ca. 20 Å) and elementary selectivity of XPS. If the HATCN molecules are indeed located at the very surface, they should attenuate the intensity of Alq_3 core levels the same as the intensity of the substrate core levels. Because HATCN contains C and N, only the intensity variations of the O1s and Ag3d levels, which are exclusively related to the substrate and Alq_3, respectively, are presented in 6.4. As a first step, the Ag3d peak spectra with and without HATCN adsorbate, whose absolute intensity exhibited a decrease of about 13 % after HATCN deposition, were normalized to the same intensity [Fig. 6.4 a)]. The same normalization factors were then applied to the O1s spectra, and the area under the peaks was determined using a fitting routine. The best fits were realized using a Voigt profile (65 % Gaussian and 35 % Lorentzian) as shown in Fig. 6.4 b) and c). This showed that the areas of the peaks before and after HATCN deposition differ by only 1.5 % (with an estimated error of 3 %). As the spectral intensity of O1s (Alq_3 specific) thus varies like that of Ag3d (metal substrate specific) it is established that HATCN indeed adsorbs on the surface of Alq_3. The fit also gave that the O1s peak full width at half maximum (FWHM) is decreased by about 8% (0.13 eV) upon HATCN adsorption.

6.1.4 Origin of the charge transfer

Having established that the HATCN layer is located at the very surface, possible origins of the electron transfer to the LUMO of HATCN will now be discussed. The first possible mechanism is a charge transfer between the two organic materials, as illustrated in Fig. 6.7 b). This explanation seems unlikely when

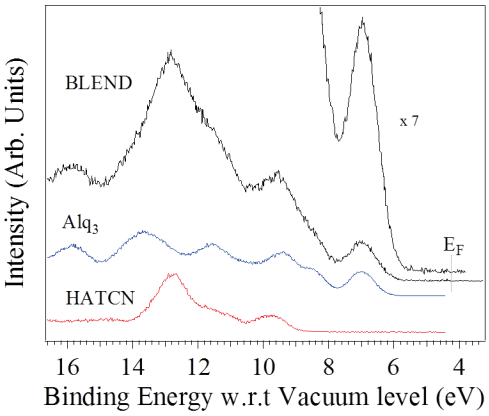

Figure 6.5: Valence band spectra of (from bottom to top) 48 Å HATCN / Ag(111), 50 Å Alq_3 / Ag(111), and 100 Å HATCN : Alq_3 blend film (ratio 1:2). The spectra of the pristine materials are shifted to match with the features observed in the blend film. All spectra were taken with a photon energy of 35 eV at BESSY.

observing that the valence band spectrum of an Alq_3 : HATCN blend film, which is shown in Fig. 6.5 (molar ratio 2 Alq_3 : 1 HATCN), can be described as a simple sum of spectra recorded for individual pristine HATCN and Alq_3 films (shifted to higher and lower binding energy, respectively, to take account of the different sample ϕ values). Most importantly, no gap state close to E_F is observed for the blend, revealing the absence of organic-organic charge transfer. This is actually to be expected due to the mismatch of the electron affinity $\approx$ 4 - 4.5 eV of HATCN and the Alq_3 ionization energy of 5.7 eV.

Consequently, charge transfer between the metal and the HATCN through the Alq_3 spacer layer is left as second possible explanation. Let us test this assumption of a metal to overlayer charge transfer (MOCT) by considering the Alq_3 energy levels after HATCN overlayer formation. A MOCT should have a significantly different effect than an interface dipole localized directly at the O/O interface.

In the large energy range VB spectra presented in Fig. 6.2 c), a comparison of the spectra before and after HATCN deposition shows a rigid shift of the Alq_3 spectrum to lower BE. Due to the small amount of deposited HATCN, the HATCN contributions are relatively weak and only lead to minor modifications of the shape of the spectrum (as indicated by vertical lines). As can be seen more precisely in Fig. 6.2 b), the Alq_3 HOMO-peak onset shifts from 1.80 eV BE to 1.50 eV BE. In addition, a narrowing of the HOMO-peak FWHM by 0.1 eV is found. An according 0.3 eV shift towards lower BE is also observed for the core levels specific to Alq_3 [C1s, O1s and Al2p, see Fig. 6.6 a)[3]]. A FHWM decrease similar to that of the Alq_3 HOMO-peak was also observed for the O1s core level, as discussed above. This narrowing will be commented on at the very end of section 6.1.5.

First, let us compare the energy level alignment for the currently discussed heterostructure HATCN/Alq_3 on Ag(111) with the same heterostructure de-

[3]N1s core levels of Alq_3 and HATCN cannot be resolved unequivocally

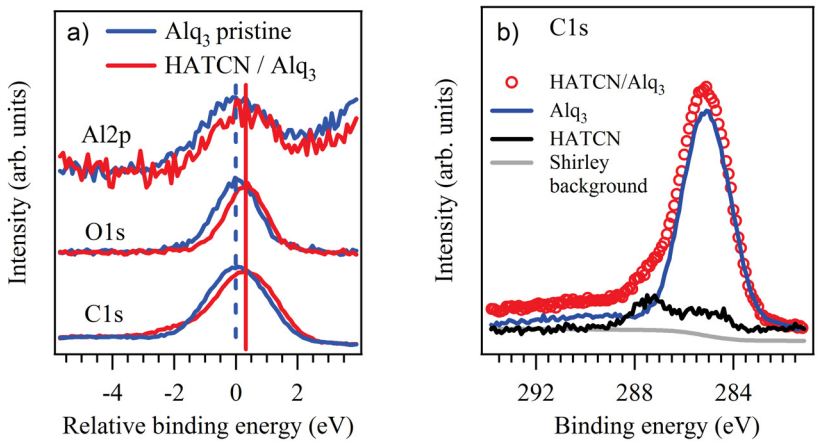

Figure 6.6: a): Comparison between Alq_3 core levels before (blue lines) and after (red lines) HATCN adsorption showing a rigid shift of Alq_3 core levels. Note that the increase in intensity of the C1s peak at -2 eV relative BE after HATCN deposition corresponds to the C1s component of the HATCN molecules as shown in b). b): C1s peak measured for 2 Å HATCN / 1 ML Alq_3 /Ag(111) (red circle). The C1s component of Alq_3 (blue line) was subtracted to obtain the C1s contribution due to HATCN (black line).

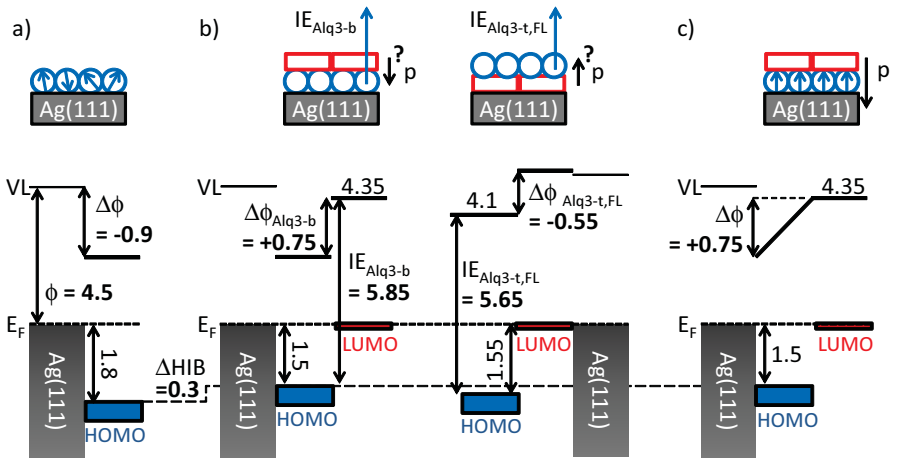

Figure 6.7: a): Energetic (bottom) and morphological (top) situation of ML Alq_3/Ag(111). b): Bottom: Comparison of the energy level diagrams for the HATCN/Alq_3 heterolayer deposited in the two possible sequences. Top: The corresponding morphology and the dipoles for the hypothetical case that the $\Delta\phi$'s are caused by an interface dipole p due to an interaction at the O/O interface. c): Schematic energy level diagram of the occupied DOS of HATCN on ML Alq_3/Ag(111). The upper part depicts the Alq_3 reorientation induced by the electric field formed between HATCN and Ag(111).

posited in reverse order, i.e. Alq_3/HATCN on Ag(111), which was discussed in section 5.2.5. The present case, where Alq_3 is below the HATCN layer will be referred to as Alq_3-b, while Alq_3-t denotes the case where Alq_3 was located on top of the HATCN layer.

The HATCN orientation in the overlayer of the Alq_3-b system is not known. Flat-lying molecules seem more likely in view of the adsorption-induced interaction and also because the HATCN coverage is the same as in the Alq_3-t,FL system with flat-lying (FL) HATCN molecules in the interlayer. In this case, the interface dipole upon formation of the O/O interface was $\Delta\phi_{\mathrm{Alq_3\text{-}t,FL}} = 0.55\,\mathrm{eV}$. This is smaller than $\Delta\phi_{\mathrm{Alq_3\text{-}b}} = 0.75\,\mathrm{eV}$. However, one can argue that this is because the HATCN molecules in the Alq_3-t,FL system are in contact with the metal, which decreases the interface dipole at the O/O interface. Then it is not valid to simply compare the magnitude of the interface dipoles in the two cases. The reader is reminded that the ELA for the Alq_3-t,FL system was actually explained consistently completely without invoking a charge transfer at the O/O interface by instead considering a push-back effect in the open nano-cavities of the HATCN honeycomb network.

The following discussion has therefore to limit itself to the ionization energies of Alq_3. If the interface dipole was located at the O/O interface the difference between the IE's of Alq_3 on either side of the interface ($\Delta\mathrm{IE}_{\mathrm{Alq_3 t/b}}$) should equal the interface dipole that was found in the current case of Alq_3-b ($\Delta\phi_{\mathrm{Alq_3\text{-}b}} = 0.75\,\mathrm{eV}$), as illustrated in Fig. 6.7 b). In contrast, if we assume a MOCT, the Alq_3 molecules are located in the center of the potential drop induced by the charge transfer, as shown in Fig. 6.7 c). Therefore, the MOCT model predicts $\Delta\mathrm{IE}_{\mathrm{Alq_3 t/b}}$ to be ca. $1/2\,\Delta\phi_{\mathrm{Alq_3\text{-}b}} \approx 0.38\,\mathrm{eV}$.

$\mathrm{IE}_{\mathrm{Alq_3\text{-}b}}$ and $\mathrm{IE}_{\mathrm{Alq_3\text{-}t,FL}}$ can be taken from Fig. 6.7 b), but need to be corrected for the photo-hole screening of the respective surrounding. The difference in screening efficiency for Alq_3 in contact with Ag(111) and on top of the flat-lying HATCN interlayer can be derived from Fig. 5.18 by comparing the IE's for the respective monolayer and multilayer films. This monolayer-specific screening, p^{ML}, is $p^{\mathrm{ML}}_{\mathrm{Alq_3\text{-}b}} = 0.45\,\mathrm{eV}$ and $p^{\mathrm{ML}}_{\mathrm{Alq_3\text{-}t,FL}} = 0.15\,\mathrm{eV}$ for Alq_3 on pristine Ag(111) and flat-lying HATCN pre-covered Ag(111), respectively. Thus we have $\Delta\mathrm{IE}_{\mathrm{Alq_3 t/b}} = (\mathrm{IE}_{\mathrm{Alq_3\text{-}b}} + p^{\mathrm{ML}}_{\mathrm{Alq_3\text{-}b}}) - (\mathrm{IE}_{\mathrm{Alq_3\text{-}t,FL}} + p^{\mathrm{ML}}_{\mathrm{Alq_3\text{-}t,FL}}) = 0.5\,\mathrm{eV}$.

Notably, the IE of the Alq_3 overlayer in the Alq_3-t,FL system simply equals that of bulk Alq_3 if, as done above, the difference in photo-hole screening is accounted for. The discussion is therefore exactly the same when simply taking Alq_3 on pristine Ag(111). Then, Alq_3 in the Alq_3-b system before HATCN deposition can used as Alq_3-t. Obviously, in this case $p^{\mathrm{ML}}_{\mathrm{Alq_3\text{-}b}} = p^{\mathrm{ML}}_{\mathrm{Alq_3\text{-}t}}$. Accordingly, $\Delta\mathrm{IE}_{\mathrm{Alq_3 t/b}}$ is just the difference between the IE's of Alq_3 in the Alq_3-b system before and after HATCN deposition, which equals the difference between $\Delta\phi_{\mathrm{Alq_3\text{-}b}}$ and the shift of the HOMO-onset (ΔHIB). $\Delta\phi_{\mathrm{Alq_3\text{-}b}} - \Delta\mathrm{HIB} = 0.45\,\mathrm{eV}$, which is consistent with the above result of 0.5 eV within the experimental accuracy.

To conclude the above discussion, not all of $\Delta\phi_{\mathrm{Alq_3\text{-}b}}$ is felt by the Alq_3 molecules in the interlayer, but 0.3 eV (i.e. ΔHIB; almost half of the total potential) drops in between Alq_3 and the substrate. This clearly favors the MOCT model over a charge transfer at the O/O interface.

6.1.5 MOCT-induced work function increase and concomitant polarization of the Alq_3 interlayer

In the following, the amount of charge transferred per HATCN molecule, the behavior of ϕ, and the shift of the Alq_3 HOMO-onset and core levels will be discussed. Within the limit of the unknown respective photoemission cross-sections and orientation-dependent photoelectron angular distributions [216, 154], the number of extra charges per HATCN can be estimated by determining the intensity ratio of the Alq_3 HOMO emission and that of the partially filled HATCN LUMO, when also taking into account the number of molecules probed in the experiment. The latter was done via the C1s spectrum of the Alq_3 / HATCN system. By subtracting the component of the pristine Alq_3 monolayer (whose intensity is assumed to decrease like the Ag3d intensity, see above) from the overall C1s spectrum, the HATCN contribution can be determined as shown in Fig. 6.6 b). By comparing the area of these two components, a ratio of Alq_3 : HATCN of 5 $\pm$ 1 is obtained. This is consistent with the nominal coverages estimated with the QCM during sample fabrication (12 Å and 2 Å, respectively). In the valence region, the ratio of the Alq_3 HOMO and the HATCN LUMO is 35 $\pm$ 5.0. As noted in the beginning, the Alq_3 HOMO-peak contains contributions of three molecular orbitals, and thus accommodates 6 electrons. Taking into account that there is 1 HATCN for 5 Alq_3 molecules, we find that the HATCN LUMO is filled with 1.2 $\pm$ 0.3 electrons. Even though this is not a scrupulously justified estimation, the number is remarkably close to filling with an integer electron, and strongly suggests the occurrence of a static charge transfer from the silver to the HATCN LUMO. With the following discussion of C_{60}/6T/Ag(111) in Sect. 6.2 in mind, it has to be noted that, a priory, not all HATCN molecules can be assumed to take part in the MOCT. However, given the low coverage of HATCN and its EA possibly higher than that of C_{60}, this assumption might still be valid.

As test of the hitherto considerations, the Helmholtz equation [247] can be used to compare the observed ϕ increase of 0.75 eV upon HATCN deposition with what is expected for the MOCT model:

$$\Delta\phi = \frac{qNp}{\epsilon_0\epsilon_r} \tag{6.1}$$

with q the elementary charge, N the dipole density on the surface, p the dipole moment perpendicular to the surface, ϵ_0 the vacuum permittivity, and ϵ_r the relative dielectric constant. The footprint area of a flat-lying HATCN molecule is ca. 0.9 nm^2. With a Alq_3 : HATCN ratio of 5 : 1 and assuming flat-lying HATCN, the surface density of HATCN (and thus the dipole density) is about 0.2 molecules/nm^2. Further assuming a charge of one electron per HATCN and a relative dielectric constant ϵ_r of 2.5, [203] a $\Delta\phi$ of 0.75 eV is found when the distance HATCN-silver is about 5.5 Å. This distance is smaller than the expected HATCN adsorption distance from Ag, which can be deduced from the Alq_3 approximate size of 1 nm. For a molecule-substrate distance of 1 nm, the Helmholtz equation shows that $\Delta\phi$ should be 0.65 eV larger than the experimental observations. This discrepancy might be due to three different facts: First, a HATCN-Ag(111) distance of 1 nm is a rather rough estimation since, for instance, HATCN could partially penetrate the space between two ligands of Alq_3, which would notably decrease the adsorption height. Second, as already

mentioned above, it is possible that not all HATCN molecules undergo a charge transfer, which was indeed found for the C_{60}-comprising systems discussed later on. Third, Alq_3 is a polar molecule with a permanent dipole moment μ of ca. 4 D [203]. However, when the pristine Alq_3 monolayer on Ag(111) is completed, the ϕ decrease is similar to what is observed for other non-polar organic molecular layers adsorbed on Ag(111) and can be ascribed to the push-back effect only. This suggests that for ML Alq_3 / Ag(111) the vertical components of the intrinsic dipole moments of Alq_3 contribute negligibly to the ϕ change. Consequently, the molecules likely adopt no preferential orientation or, alternatively, are arranged with their dipole moment aligned in an anti-parallel fashion . However, the situation can be different for HATCN / Alq_3 / Ag(111). Indeed, this system is similar to a dielectric slab placed inside in a charged parallel plate capacitor (with the positive and negative charges located in the metal electrode and the HATCN layer, respectively). In this scenario, the Alq_3 molecules possibly undergo a reorientation upon HATCN adsorption in order to align their intrinsic dipole to the electric field created inside the plate capacitor, as depicted in the top part of Fig. 6.7 c). When going from a randomly toward a vertically oriented Alq_3 dipole layer (with the positive pole pointing upward), the ϕ increase due to electron transfer to HATCN will be counterbalanced. Such an effect can decrease ϕ by up to ca. 1 eV [185, 325, 326]. Therefore, the current experimental findings can be conciliated with electrostatic considerations involving such a molecular reorientation. In addition, the proposed molecular reorientation can account for the observed narrowing of the Alq_3 energy levels upon HATCN adsorption.

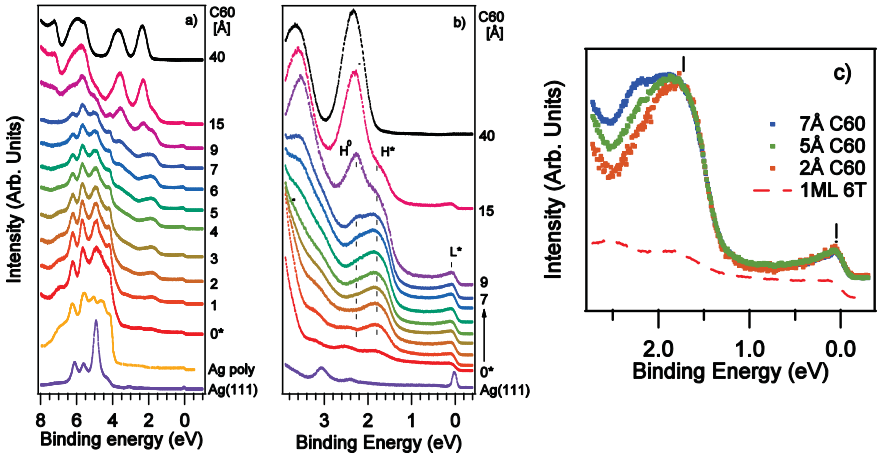

Figure 6.8: a) From bottom to top: Valence band spectra of Ag(111), of a polycrystalline Ag sample, of ML 6T/Ag(111) and evolution of the valence band upon increasing C_{60} thickness on ML 6T/Ag(111). On the right part of the graph, 0* denotes ML 6T/Ag(111) and the values above the respective C_{60} film thickness. b) Zoom into the low binding energy region of the corresponding spectra (except for polycrystalline Ag). c) C_{60} HOMO and Fermi-level region of 2 Å, 5 Å and 7 Å C_{60} on ML 6T/Ag(111) after background removal due to ML 6T/Ag(111) represented by the bottom dashed line spectrum. HOMO, HOMO* and LUMO* (see text) are marked with a dash.

6.2 Doping of C_{60} (sub)monolayers by Fermi-level pinning induced electron transfer

6.2.1 Valence band and Core level spectra: Charged and neutral C_{60} within the first C_{60} monolayer

A monolayer of 6T on Ag(111) was obtained by desorption the multilayers of a thick film upon annealing at ca. 250 °C, leaving only the (intact) first layer on the substrate

Figure 6.8 shows the valence electron region for C_{60} grown on ML 6T / Ag(111). Fig. 6.8 a) and b) show different energy ranges of a collection of valence band spectra corresponding - from bottom to top - to Ag(111), polycrystalline Ag [Fig. 6.8 a) only], ML 6T/Ag(111) (denoted 0*), and the subsequent C_{60} thickness dependent series up to nominally 40 Å of C_{60} deposited on ML 6T/Ag(111). The most intense features in the bare Ag spectra between 4.0 eV and 7.5 eV binding energy correspond to the silver d-band, and the flat background going from 4 eV BE up to E_F is due to the silver sp band. Upon formation of ML 6T on Ag(111), the Ag(111) d-band changes dramatically and becomes very similar to the d-band of polycrystalline Ag. This can be explained by Umklapp scattering (diffraction) of the substrate photoelectrons by the molecular overlayer [7, 187, 102, 28, 103]. Additional intensity due to ML 6T is mostly visible between 1 and 4 eV BE.

In the zoom of the silver sp band region shown in Fig. 6.8 b), the intense and sharp peak located at E_F in the clean Ag(111) spectrum is due to the Ag(111) Shockley surface state. This state completely vanishes upon formation of ML 6T. Three features in the density of states are detected for ML 6T/Ag(111), which are assigned to the highest occupied molecular orbital levels of 6T with their peak maximum at 1.8 eV BE, 2.5 eV BE and 3.2 eV BE (for the HOMO, HOMO-1, and HOMO-2, respectively), and with the 6T HOMO onset at 1.3 eV BE [cf. Fig. 6.16 c)]. As no intra-gap states are observed, the 6T layer can be considered as weakly interacting with the silver surface.

Upon C_{60} deposition, C_{60}-related DOS clearly emerges, in particular in the sp-band region. In the energy region of the silver d-band, Ag-related DOS spectral weight remains important up to 9 Å C_{60}, which corresponds to ca. 1 ML C_{60} (also c.f. Fig. 6.9). The 40 Å C_{60} spectrum is representative of a thick neutral C_{60} film with its HOMO peak maximum located at 2.35 eV BE and its onset at 1.85 eV BE. The intermediate 15 Å C_{60} spectrum is a weighted sum of the first and the second layer C_{60} contributions, showing that the DOS corresponding to the second C_{60} layer and thick C_{60} are very similar.

In the sp-band region, from the first C_{60} deposition on, an increase in intensity in the immediate Fermi-level vicinity is observed. This DOS is intersected by the Fermi-level and the system can thus be considered metallic. The spectral weight of this feature keeps increasing up to 9 Å C_{60} coverage and decreases again for thicker films, demonstrating its interfacial character. Its line shape and intensity closely resembles the partially filled LUMO-derived states observed at the C_{60}/Ag interfaces. This feature is therefore referred to as LUMO* and attributed to a charge transfer toward the C_{60} molecules [20, 192, 136, 252]. For low C_{60} coverage, the C_{60} HOMO emission is observed with a peak maximum at 1.8 eV BE and an onset at 1.3 eV BE, i.e., at about 0.55 eV BE less than for the 40 Å C_{60} film. Notably, when going from 1 Å to 7 Å C_{60}, the C_{60} HOMO feature becomes increasingly broadened on its high binding energy side [see Fig. 6.8 b)] until a clear peak emerges in the 9Å spectrum at the energy position of the thick C_{60} film. The C_{60} HOMO broadening is therefore attributed to the development of the intrinsic (neutral) C_{60} HOMO, denoted $HOMO^0$ in the following. For 15 Å C_{60}, the C_{60} $HOMO^0$ peak becomes then dominant over the initially observed HOMO-related emission, whose intensity vanishes completely for the thick-film 40Å C_{60} spectrum. Therefore, the low BE C_{60} HOMO is attributed to the C_{60} interface-HOMO (i.e., the monolayer) that is denoted HOMO*. Fig. 6.8 c) shows the top VB spectra of 2 Å, 5 Å, and 7 Å C_{60} from which the background due to ML 6T/Ag(111) has been removed, revealing the contributions due to C_{60} only. The background removal procedure was performed consistently such that no negative intensity occurred. This procedure remains approximate because, for instance, no energy shift of the (however relatively weak) 6T features was considered and a more detailed analysis of these spectra will be provided later on. After background removal, the spectra were normalized to the HOMO* peak maximum. This procedure highlights that the LUMO* and HOMO* intensities vary similarly for the three shown coverage and that the increase in intensity between 2 eV and 2.7 eV BE is related to the development of the intrinsic C_{60} HOMO. The ratio of HOMO* and LUMO* spectral weight (assuming a symmetric HOMO* lineshape) is ca. 9. Considering the 5-fold degeneracy of the neutral C_{60} HOMO and assuming the same photoemission cross-section for both levels, the charge in the LUMO* would

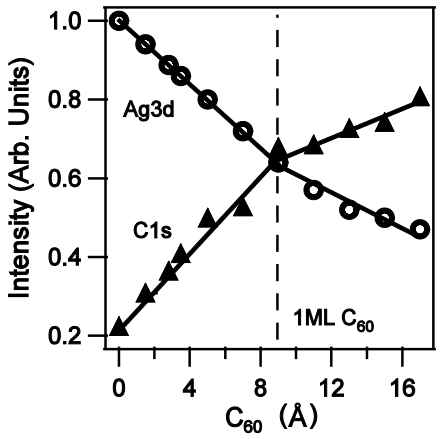

Figure 6.9: Evolution of the Ag3d (open circles) and C1s (filled triangles) relative signal intensities as a function of C_{60} thickness. The transition in the change of slopes at 9 Å C_{60} is due to the completion of the first C_{60} monolayer. Measurements were performed at HU.

correspond to ca. 1.1 electron, which, in view of the imperfect subtraction procedure, also allows for the physically reasonable value of exactly one electron in the LUMO*. Therefore, the C_{60} HOMO* and LUMO* derived features are attributed to C_{60} molecules charged with one electron, which will be referred as C_{60}^{-1} in the following. Note that the smaller HOMO*-LUMO* gap for C_{60}^{-1} as compared to the HOMO-LUMO gap for C_{60}^{-1} results from additional screening mechanisms due to the electron in the partially filled LUMO* [250, 192, 190].

The question of the C_{60} growth mode is particularly important since neutral C_{60} could be located either in the first C_{60} layer or in subsequent layers. In a previous STM study on the same system, no island growth mode was reported [335]. STM measurements that were performed within the present work are presented in Fig. 6.10 and confirm this finding. Furthermore, some ordered C_{60} structures shown in this figure were not reported in [335]. STM and UPS probe film properties on dramatically different length scales. Therefore XPS was employed to study the growth behavior of C_{60} on ML 6T / Ag(111) on a length scale that is more comparably to that of UPS. The obtained normalized intensities of the C1s and Ag3d core levels signals as a function of C_{60} nominal thickness[4] are reported in Fig. 6.9, which clearly shows a linear variation of both signals up to at least 9 Å thickness, beyond which the second C_{60} layer starts to grow as inferred from the change of slopes. This evidences that no 3D islands form before 9 Å nominal thickness, which is thus assumed to represent the complete C_{60} monolayer. Therefore, these results allow concluding that indeed the *first* C_{60} ML is composed of a mixture of neutral (C_{60}^{0}) and anionic (C_{60}^{-1}) molecules.

In the following, XPS is used to probe the different chemical states of the molecules present at the surface and will additionally serve as tool to investigate the electrostatic potentials induced by the interfacial charge transfer.

In Fig. 6.11 a), the S2p CL of 6T for ML 6T/Ag(111), 3 Å (0.33 ML) C_{60} and 7 Å (0.77 ML) C_{60} are presented. Upon 3 Å C_{60} deposition the S2p shifts toward lower BE by 0.17 eV, then by an additional 0.2 eV for 7 Å C_{60}. As the S2p shift is gradual and without significant broadening of the peaks, it does

[4]The 6T C1s spectral weight was subtracted from the total C1s intensity in order to obtain only the intensity from the C_{60} C1s core level. The 6T C1s signal was approximated to decrease like the Ag3d signal.

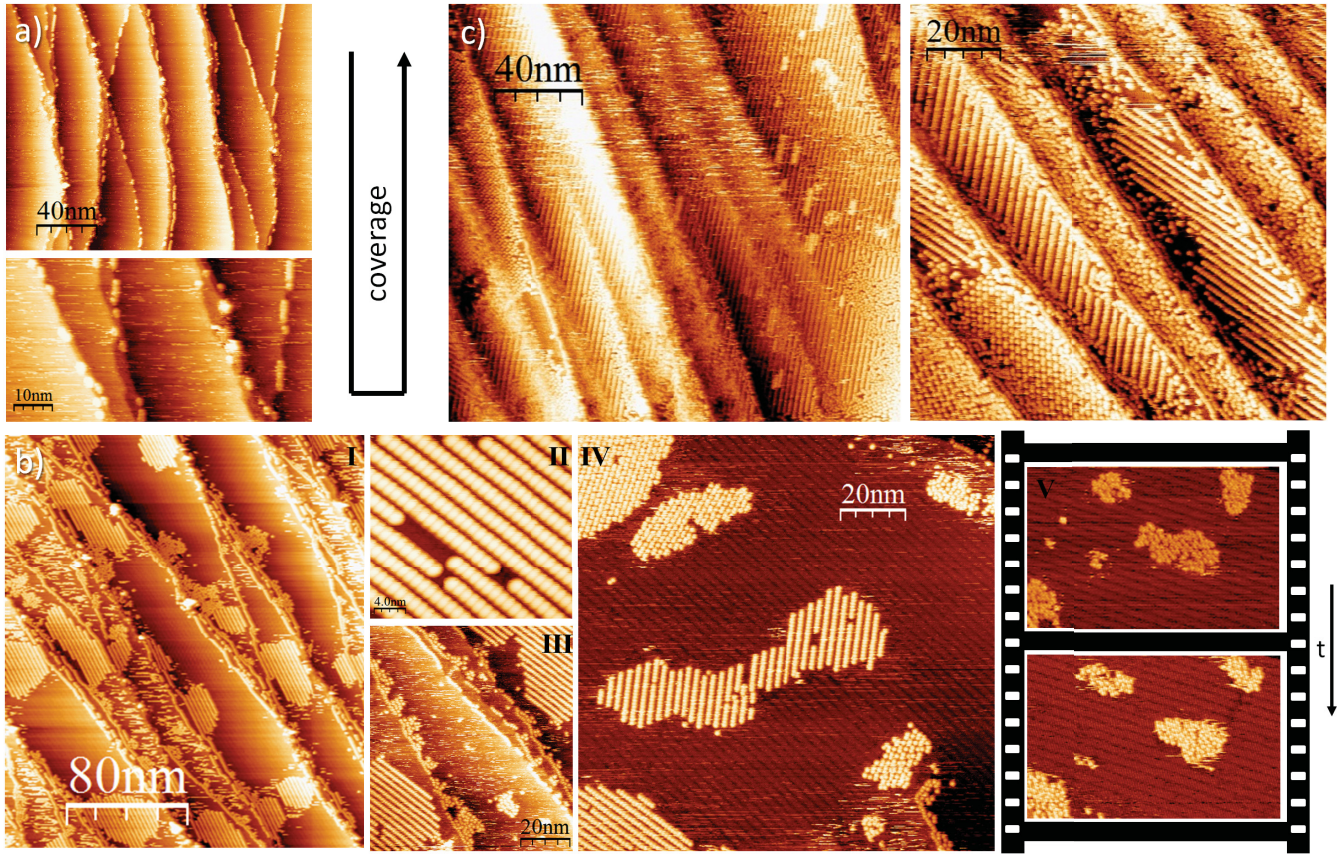

Figure 6.10: a), b), and c): STM images of C_{60}/ML 6T/Ag(111) for very low coverage, ca. half-monolayer coverage, and close to monolayer coverage. The two images in the lower right corner where taken consecutively as illustrated by the time-arrow. [Imaging parameters: a): -1.5 V, 0.7 nA, b) I: -1.4 V, 0.4 nA, II: -1.2 V 0.8 nA, III: 1.5 V, 0.4 nA, IV: 1.6 V, 0.5 nA, V: 1.6 V, 0.4 nA c) -1.2 V, 1.4 nA]

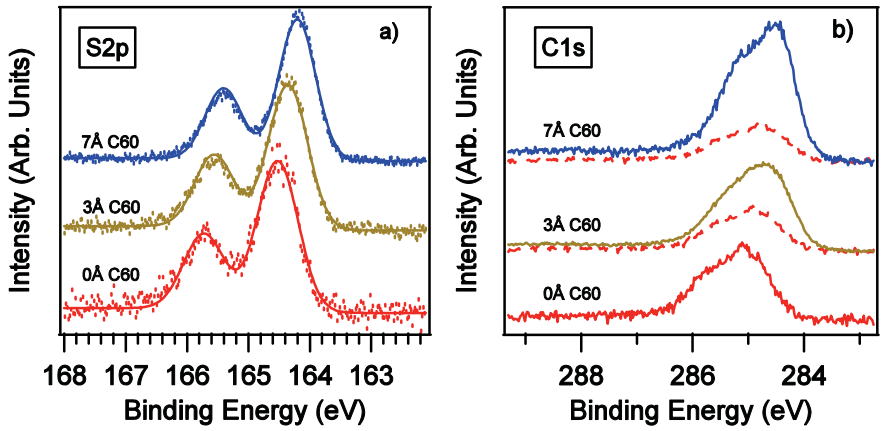

Figure 6.11: a) Normalized S2p CL spectra of pristine ML 6T on Ag(111) (bottom) and after deposition of 3 Å and 7 Å C_{60}. b) C1s CL spectra of the same systems. The spectra symbolized by dashed lines below the C1s spectra represent the 6T contribution (see text).

not result from a change in the chemical state of the 6T molecules. Therefore, it is of electrostatic origin. As the shift magnitude depends on the amount of deposited C_{60}, it has to be related to the total amount of charges transferred from the silver to the C_{60} overlayer. Fig. 6.11 b) shows the corresponding C1s CL spectra. To determine the C_{60} C1s contribution of these spectra, the as-measured spectrum is displayed together with the 6T C1s spectrum. The C1s signal of 6T consists of two features, stemming from the two differently bonded carbon atoms in the thiophene rings [110]. It is displayed, for each coverage, shifted in energy like the S2p CL and with its intensity renormalized consistently with the Ag MNN Auger peak intensity attenuation. This procedure is shown in Fig. 6.12. Note that without a shift of the 6T C1s spectrum, a shoulder due to the 6T features should be observed on the high BE tail of the C1s spectra in Fig. 6.11 b). This is consistent with the electrostatic considerations discussed above for HATCN/Alq_3/Ag(111) and in more detail for the present system below, according to which a potential drop within the spacer layer rigidly shifts all its energy levels.

By subtracting, the 6T C1s part of the 3 Å and 7 Å C_{60} spectra are obtained, which are presented together with the result of a fitting procedure in Fig. 6.13 a) and Fig. 6.13 b), respectively. These spectra clearly demonstrate two C_{60} C1s contributions separated by ca. 0.74 eV, which, from the relative spectral weight evolution, can be attributed to C_{60}^{0} and C_{60}^{-1}, at high and low BE respectively. This interpretation compares well with what was reported by Macovez *et al.* for the surface of the fcc phase of RbC60 films where these two charge states have also been observed [192]. The fit results give a C_{60}^{0} : C_{60}^{-1} ratio of 1 : 2 and 1 : 1.2 for 3 Å and 7 Å C_{60}, respectively.

Noteworthy, these findings also imply that, if electron fluctuations occur between different C_{60} molecules, the fluctuation time-scale is much longer than the typical time-scale of the photoemission process (ca. 1 fs), as the CL spectra

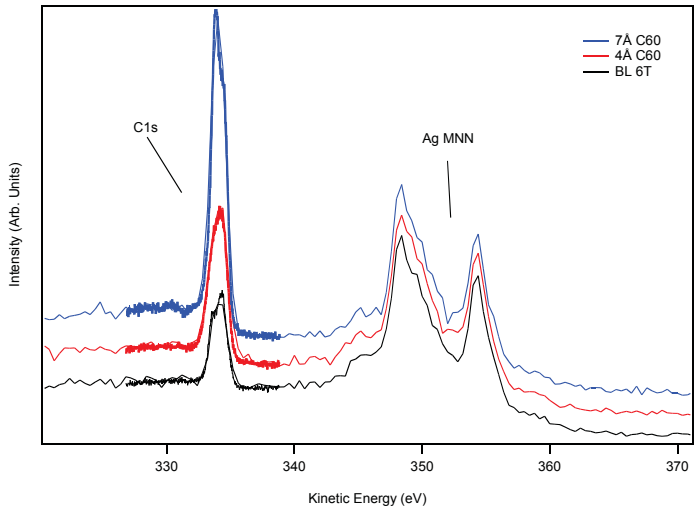

Figure 6.12: XPS region used for normalizing the C1s intensity for the subtraction procedure. The AgMNN region was used to determine the attenuation of photoelectrons originating from the C1s orbital of 6T upon C_{60} deposition. For an excitation energy of ca. 620 eV, the kinetic energies of photoelectrons originating from AgMNN and C1s are 350 eV and 335 eV respectively. The presented data are for the BL system. The ML case is completely equivalent.

of the ML are not notably broadened compared to those of thick films. Also, this suggests that charge transport does not occur via band transport (delocalization) but rather via a hopping process, as expected in narrow band materials such as fullerides [192].

It is now possible to evaluate details of the VB spectra line-shapes by simulating them via a summation including i) two C_{60} contributions (C_{60}^{0} and C_{60}^{-1}) whose proportions were determined from the fit results in Fig. 6.13; ii) a shifted 6T contribution, with the same shift as observed for the S2p CL, and iii) a valence band spectrum of a polycrystalline Ag (most appropriate because of the surface Umklapp experienced by the silver photoelectrons upon crossing the molecular layers). In Fig. 6.13 c) and d), the VB spectra simulations are shown for the 3 Å and 7 Å C_{60} coverages and compared to the as-measured spectra. The experimental spectra are remarkably well reproduced using the C_{60}^{0} : C_{60}^{-1} ratio determined from the C1s spectra. The two C_{60} VB spectra employed in the simulations are the ones of the thick film (i.e. neutral molecules) located at the energy position as observed in the 40 Å C_{60} film to represent the neutral species, and the same but shifted by 0.55 eV to lower BE without additional broadening to account for the anion contribution. The 6T DOS is simulated by the appropriately shifted spectrum of a thick, pristine film 6T/Ag(111).

6.2.2 Work function evolution

SECO spectra, from which the work function ϕ is determined, are shown in Fig. 6.14 a). Upon formation of 1 ML 6T /Ag(111), ϕ decreases from 4.55 eV [clean Ag(111)] to 3.8 eV. As 6T weakly interacts with Ag(111), this ϕ decrease can be

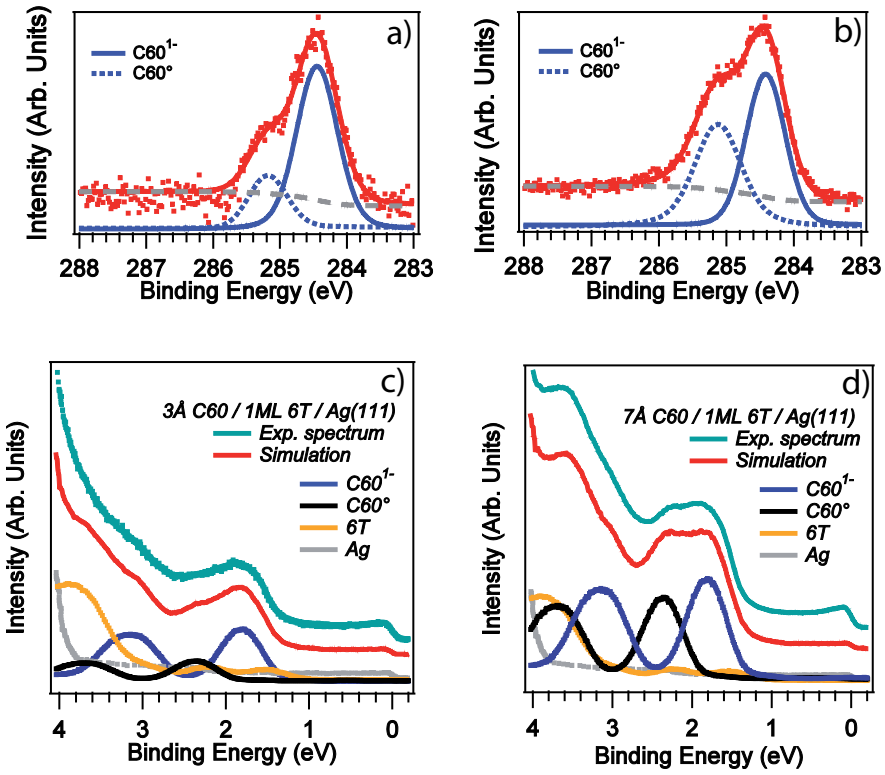

Figure 6.13: a) and b): Deconvolution of the C1s C_{60} CL spectra of 3 Å and 7 Å C_{60} on ML 6T, respectively, obtained after subtraction of the 6T contribution from the as-measured C1s spectra presented in Fig. 6.11 b). The blue dots and blue lines correspond to the Gaussian components used to fit the experimental C1s spectra (red dots). The gray dotted lines represent the employed Shirley background. The red lines show the result of the fits. (shifts and the relative C_{60} spectral weights are provided in the text). c) and d): As-measured VB spectra (top, green) of 3 Å and 7 Å C_{60}/ML 6T/Ag(111), respectively, compared with simulated VB spectra (middle, red) resulting from the summation of (bottom spectra) one C_{60} bulk-like spectra (C_{60}^{0}, black), a shifted C_{60} bulk-like spectra (C_{60}^{-1}, blue), a shifted 6T bulk-like spectrum (orange) and the spectrum of a polycrystalline Ag sample (gray). The data were obtained at BESSY.

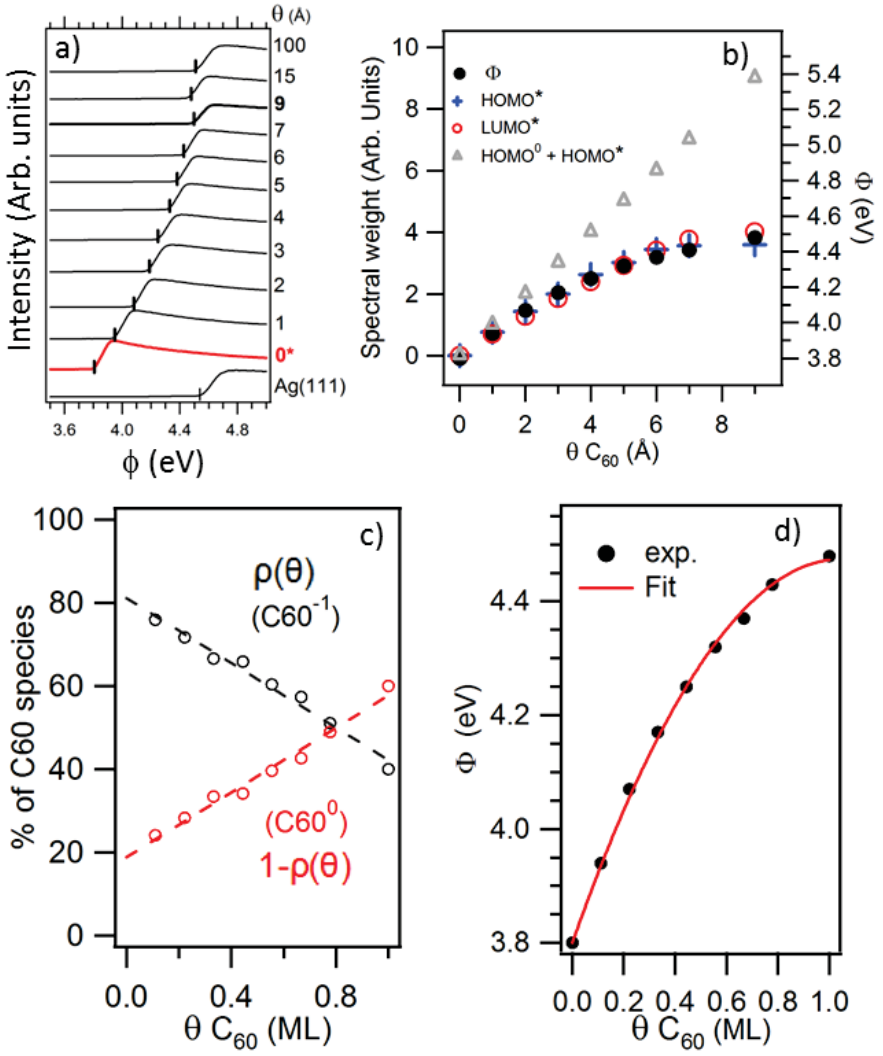

Figure 6.14: a) Secondary electron cutoff spectra for Ag(111), ML 6T /Ag(111) (red line, denoted 0*) and for increasing C_{60} thickness. 9 Å C_{60} represent the 1 ML C_{60} /ML 6T/Ag(111) system. b) ϕ profile (black dots) compared to the spectral weight evolution of $HOMO^0$ + HOMO* (gray triangle), HOMO* (blue cross) and LUMO* (red circles). c) Evolution of the proportion of C_{60}^{-1} ($\rho(\theta)$) (black open circles) and C_{60}^{0} ($1-\rho(\theta)$) (red open circles) as a function of C_{60} coverage within the sub-monolayer regime as deduced from graph a) (see text). d) Fit of the work function profile using (6.4) and parameter values given in the text.

attributed to the push-back effect, as discussed in Sect. 2.5.1. Upon deposition of 15 Å C_{60}, ϕ increases back to 4.5 eV and remains constant for higher C_{60} coverages, demonstrating the formation of an abrupt interface dipole upon C_{60} adsorption, which, in view of the previous conclusions, has to be related to the electron transfer toward a part of the C_{60} ML. The increase of ϕ is not linear with coverage despite the fact that no C_{60} 3D islands form before completion of the C_{60} monolayer. This non-linearity in the ϕ vs. coverage dependence could either be related with the variation in the fraction of charged and neutral species within the C_{60} monolayer, in line with the phenomenological model developed by Topham and coworkers [288]. On the other hand, depolarization within the C_{60} layer could explain the observed behavior according to the model by Langmuir [178] and recently suggested for tetrathiafulvalene/Au(111) [95].

It is possible to decide between both explanations by comparing the coverage-dependence of ϕ with those for the HOMO*, HOMO*+HOMO^0, and LUMO* spectral weights as depicted in Fig. 6.14 b). It can be seen that the spectral weight in the region including the HOMO^0 and HOMO* increases linearly with C_{60} coverage, while the spectral weight of the HOMO* and LUMO* both increase asymptotically, very similar to the ϕ profile. This shows unambiguously that the ϕ change is determined by the absolute amount of charges transferred to the C_{60} layer and that depolarization plays no considerable additional role. The curves in Fig. 6.14 b) can be used to extract the fractions of C_{60}^{-1} $[\rho(\theta)]$ and C_{60}^{0} $[1-\rho(\theta)]$ as a function of C_{60} coverage (θ) within the monolayer range. As depicted in Fig. 6.14 c), $\rho(\theta)$ varies linearly with θ. It can therefore be written in the form

$$\rho(\theta) = b - \alpha\theta \tag{6.2}$$

where b and α are constants whose values are deduced from the graph in Fig. 6.14 d) and amount to ca. 0.81 and 0.42 ML^{-1}, respectively. The net ϕ increase as a function of θ is given by the relation:

$$\Delta\phi(\theta) = \theta\rho(\theta)\phi_0 \tag{6.3}$$

where ϕ_0 corresponds to the work function increase for an assumed complete C_{60} charged layer, i.e. when considering a molecular layer composed of only C_{60}^{-1}. Inserting (6.2) into (6.3) gives:

$$\Delta\phi(\theta) = b\theta\phi_0 - \alpha\theta^2\phi_0 \tag{6.4}$$

Fitting the work function profile [Fig. 6.14 d)] using b and α gives a value of 1.6 eV for ϕ_0. Finally, for the complete monolayer the fraction of neutral and charged C_{60} amounts to 58 % and 42 %, respectively.

6.2.3 Comparison of C_{60} adsorbed on ML and BL α-sexithiophene on Ag(111)

This part explores how the thus-far discussed characteristics of the C_{60} / 6T / Ag(111) system changes when the 6T spacer layer is changed to a bilayer (BL).

The 6T bilayer film was prepared by monitoring the decrease in intensity of the Ag(111) core levels upon adsorption of 1 ML 6T, assuming that they decrease similarly from 0 to 1 ML and from 1 to 2 ML [Fig. 6.15 a)]. The reference for the Ag CL signal attenuation upon adsorption of 1 ML 6T / Ag(111) was determined from a routinely prepared monolayer film (see above).

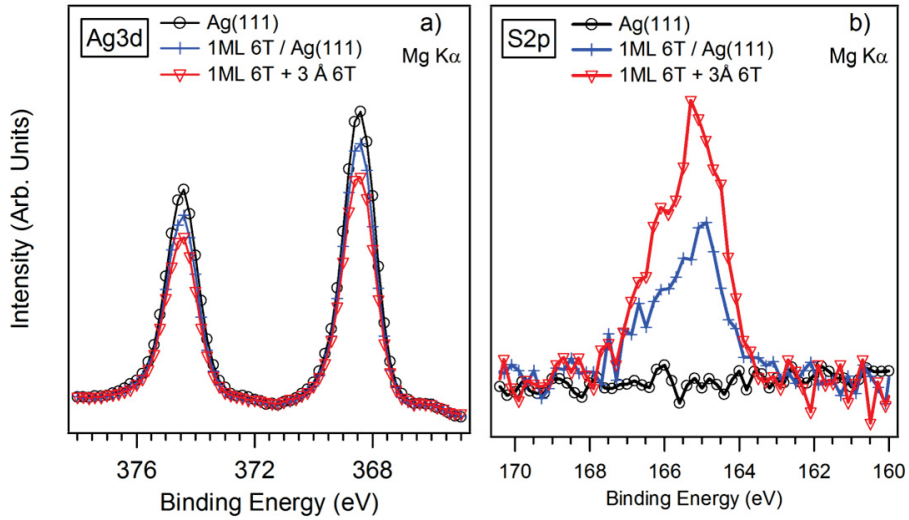

Figure 6.15: Realization of the bilayer 6T film on Ag(111) by monitoring XPS intensities. a): Ag3d spectra of clean Ag(111), 1 ML 6T / Ag(111) obtained by annealing a thicker film at ca. 250 °C, and 3 Å 6T deposited on top of 1 ML 6T / Ag(111). b): S2p spectra for the corresponding coverages. The Ag3d intensity decrease measured when going from clean Ag(111) to 1 ML 6T / Ag(111) was used as reference for the signal attenuation upon adsorption of 1 ML 6T. A mean free path of 9 ML is found, consistent with the values reported for PTCDA (7ML) at kinetic energies around 885 eV [108]. Further 6T was then deposited by steps of 1 and 0.5 Å until the Ag3d CL had decreased again by the same relative amount as observed when going from the clean to the 1 ML 6T covered Ag(111). This was achieved for an additional 3 Å 6T. At the same time, the S2p intensity increases by about a factor of 1.8. 1 ML 6T + 3 Å 6T can be therefore safely attributed to a bilayer of 6T (BL 6T) on Ag(111). The data were obtained at HU.

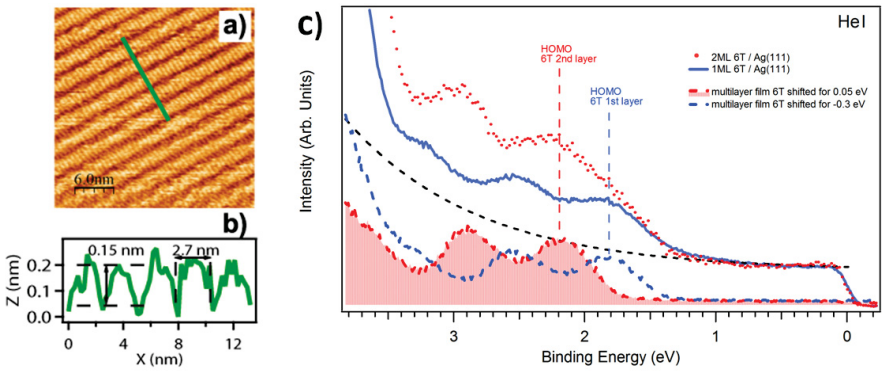

Figure 6.16: a): STM image of BL 6T / Ag(111) (30x30 nm^2). b): Height profile between the molecular rows in image a). (Scanning parameters: I = 1 nA ; $U_{\mathrm{Sample}} = -1$ V). c): Details of the valence band spectrum of the bilayer 6T film on Ag(111). The spectra of ML 6T and BL 6T on Ag(111) are shown as blue thick line and red dots, respectively. At the bottom of the graph, the DOS of a pristine thick 6T film is used to entangle the spectral features of the 1 BL 6T / Ag(111) spectrum as a superimposition of the first and second 6T layer. The black dashed line represents the background due to the silver sp-band. The shifted 6T spectra correspond to the DOS of the first (bottom, dashed blue line) and second (bottom, dashed and filled red line) 6T layer. The inelastic mean free path of the photoelectrons deduced from the attenuation of the 1st layer HOMO is 2.8 (6T) ML, in agreement with Ref [108].

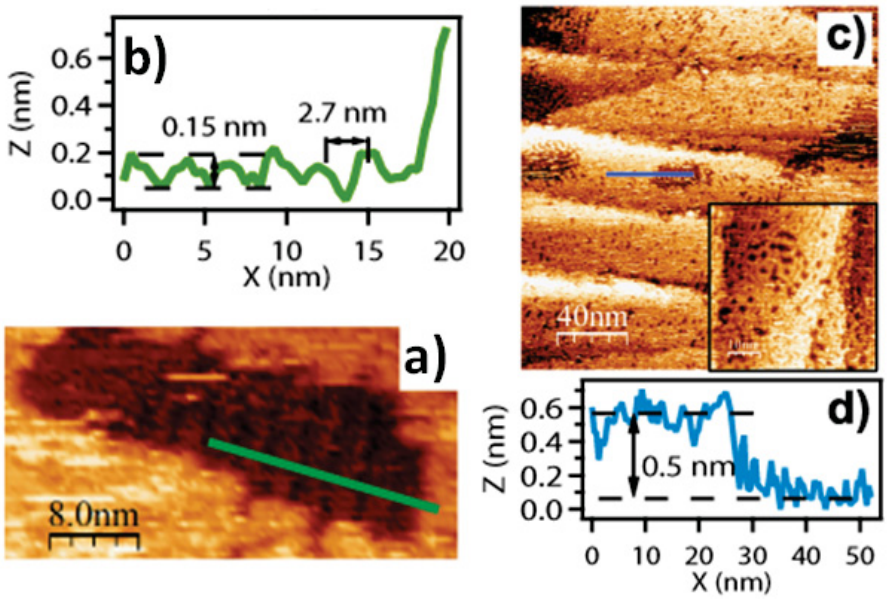

Figure 6.17: STM images of 6 Å C_{60} / BL 6T / Ag(111), measured on the same sample as presented in Fig. 6.19. a) and b): STM image (40x20 nm^2) of 6T not covered with C_{60} and corresponding height profile, respectively. c): STM image (200x200 nm^2) showing C_{60} on 6T and uncovered 6T areas. A magnification of a region with "worm-like" structures is displayed in the inset (50x50 nm^2). d): The height profile along the blue line in c). [Scanning parameters: -1 V, 1 nA]

A representative scanning tunneling microscopy (STM) image of the 6T bilayer is shown in Fig. 6.16 a). The 6T molecules form rows with the long axes oriented perpendicular to the row direction, and an inter-row spacing of about 2.7 nm [Fig. 6.16 b)], consistent with the study by Chen *et al.* [54].

The 6T-derived valence region photoemission features, shown in Fig. 6.16 b), consist of at least four contributions. These can be explained by the first two highest occupied molecular orbitals (HOMO and HOMO-1) of the first and second 6T layers, with the HOMO peak maxima at 1.80 eV and 2.15 eV BE for the first and second layers, respectively. The different BE can be rationalized by the more efficient photo-hole screening of the first 6T layer by the metallic substrate.

Figs. 6.17 a) and c) show representative STM images of the 6 Å C_{60} film. About 65 % of the surface is covered with a loosely packed and disordered C_{60} layer of uniform apparent height, i.e. without 3D islands. The vast majority of the structures resemble the worm-like structures as also found by Zhang *et al.* for C_{60} / ML 6T / Ag(111) [335]. The periodicity and height [Fig. 6.17 b)] measured inside the hole in the C_{60} layer shown in Fig. 6.17 a) coincide with those of the 6T bilayer rows in Figs. 6.16 a) and b). Sub-monolayer C_{60} coverage is therefore evidenced by STM, consistent with the 6 Å nominal coverage, which is ca. 60 % of the height of a densely-packed C_{60} monolayer [167]. The reader is reminded that for C_{60} / ML 6T / Ag(111) 9 Å were identified as a complete ML. When assuming the same growth for C_{60} / BL 6T / Ag(111), the 6 Å coverage

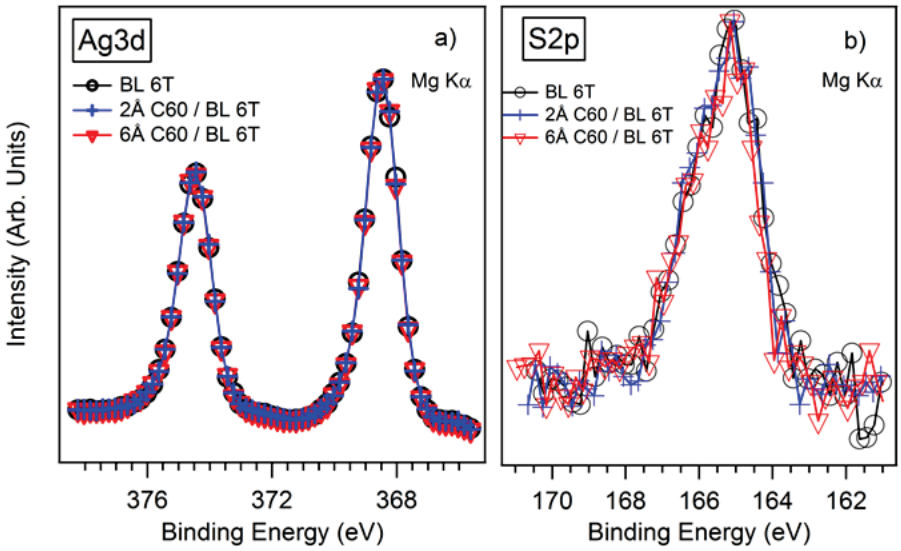

Figure 6.18: a): Normalized Ag3d core levels for the pristine BL 6T, 2 Å C_{60} and 6 Å C_{60} adsorbed on the BL 6T. b): S2p signal from 6T normalized with the same factors as used for normalizing the Ag3d CL. The S2p core levels have been shifted in energy in order to be superimposed. Note that if diffusion of C_{60} to the silver surface would occur and would be responsible for the presence of charged C_{60} molecules (40 % of the total amount of deposited C_{60}), the S2p signal would be much less attenuated than the Ag3d signal. The fact that the Ag3d and S2p signals vary very similarly demonstrates that no C_{60} diffusion occurs to the substrate (C_{60} molecules adsorb on top of the 6T film). The data were obtained at HU.

corresponds to 66 % of a full ML. No signs for diffusion of C_{60} molecules to the Ag(111) surface is evidenced by the STM data presented in Fig. 6.17, which is also strongly supported by the more extensive STM study of the same system by Chen *et al.* [54], who found that even after annealing at 380 K, the C_{60} does not diffuse to the silver surface. In addition, also for this system, the relative attenuation of the Ag substrate and the 6T core levels signal upon C_{60} adsorption was carefully monitored. Figure 6.18 shows an identical decrease of the S2p and Ag3d signals, which shows that C_{60} in-diffusion does not occur and all the C_{60} molecules, including those corresponding to the significant HOMO* and LUMO* spectral intensities, are located on top of the BL 6T.

The SECO and VB regions of C_{60} on top of BL 6T are shown in Fig. 6.19 a) - c). Upon C_{60} adsorption, the formation of an interface dipole is observed and ϕ increases from 3.8 eV to 4.55 eV for a thick C_{60} film. Furthermore, the ϕ profile displayed in Fig. 6.19 e), which shows that ϕ does not increase linearly with coverage but varies in a similar fashion as was observed when the 6T spacer layer film was 1 ML. The VB spectra exhibit qualitatively the same features as encountered previously, namely i) a partially filled C_{60} LUMO (LUMO*) and ii) the HOMO region is composed of two contributions corresponding to $HOMO^0$ and HOMO* due to C_{60}^0 and C_{60}^{-1}. Furthermore, it can be also seen that the

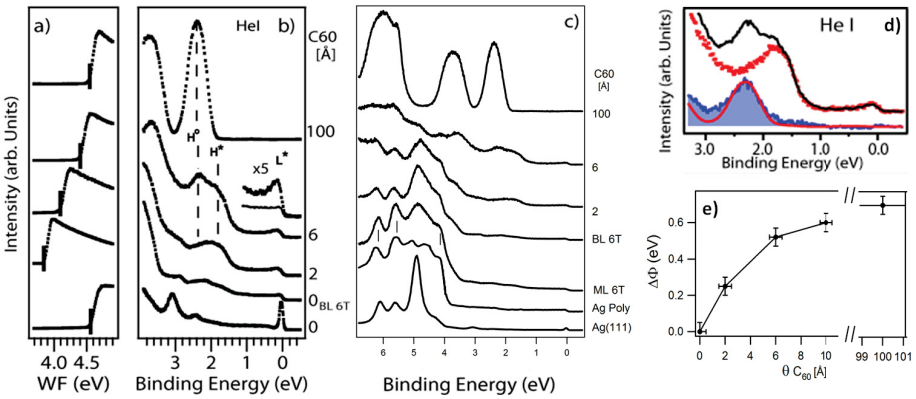

Figure 6.19: a) – c): SECO and valence spectra of C_{60} / BL 6T / Ag(111). The spectra correspond, from bottom to top, to Ag(111), BL 6T on Ag(111) (denoted $0_{\mathrm{BL\,6T}}$), 2 Å, 6 Å, and 100 Å C_{60} on BL 6T / Ag(111). A magnification of the 6 Å C_{60} spectrum is also presented together with the BL 6T / Ag(111) background. H^0, H* and L* refer to $HOMO^0$, HOMO*, and LUMO*, respectively (see main text). For the broad valence band regions shown in c) also the spectrum of a polycrystalline silver sample is shown to illustrate the surface-Umklapp scattering and angle averaging of the silver d-band [7, 187, 102, 28, 103]. The spectrum of pristine silver was multiplied by 0.15. d): Superimposition of the 2 Å (red dots) and 6 Å (black solid line) C_{60} after background removal due to BL 6T / Ag(111). The difference of these two spectra yields the (blue shaded) spectrum at the bottom, which is compared to a thick film C_{60} spectrum (red line). e): Evolution of the work function as a function of C_{60} coverage.

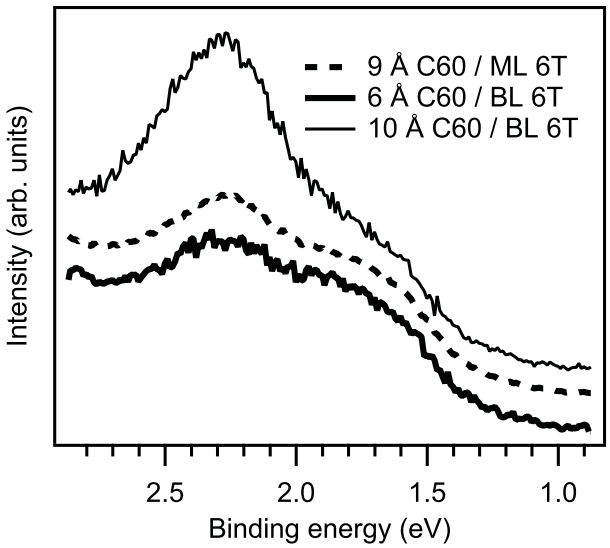

Figure 6.20: Comparison of the HOMO region for 9 Å C_{60}/ML 6T, 6Å C_{60}/BL 6T and 10 Å C_{60}/BL 6T. The spectra are normalized to the HOMO* intensity in order to reflect the relative $HOMO^0$ and HOMO* intensities.

relative intensity of $HOMO^0$ increases with respect to that of HOMO* as a function of coverage.

The following shows how the C_{60}^0 / C_{60}^{-1} ratio for a complete C_{60} layer is influenced as a function of the 6T spacer layer thickness. Fig. 6.20 shows a superimposition of the VB spectra of 6 Å (0.66 ML) and 10 Å (1.1 ML) C_{60} on BL 6T/Ag(111) and 9 Å (1 ML) C_{60} on ML 6T/Ag(111). The spectra are normalized to the HOMO* intensity in order to reflect the variation of neutral and charged species of these systems. It can be seen that the C_{60}^0 and C_{60}^{-1} fractions for 1 ML C_{60}/ML 6T and 0.66 ML C_{60}/BL 6T are very similar.

The 1.1 ML C_{60}/BL 6T shows a pronounced increase in C_{60}^0 intensity as compared to 0.66 ML C_{60}/BL 6T. The estimated spectral weight due to the second C_{60} layer (which is assumed to consist only of C_{60}^0 molecules) amounts to slightly less than 10 % of the total spectral weight. Accordingly, the spectral weight of C_{60}^0 within the first C_{60} layer is much larger than what was observed for 1 ML C_{60}/ML 6T. The C_{60}^{-1} and C_{60}^0 fractions for 1 ML C_{60} on BL 6T are estimated to be ca. 0.3 and 0.7 respectively.

The XPS spectra for the BL system, shown in Fig. 6.21, present similar features as observed when ML 6T is used as spacer layer: The C1s spectra after C_{60} deposition, shown with separate corresponding 6T contributions for 4 and 7 Å C_{60} coverage, evidence the presence of two additional features, which have to be attributed to C_{60} species with a ratio varying with coverage. For a quantitative analysis of the C_{60} C1s signal, the 6T contribution is removed. To account for the electrostatic potential drop in the 6T interlayer and the signal attenuation, the C1s 6T background in Fig. 6.21 b) was shifted by the same amount as observed for S2p and decreased in relative intensity as measured for the AgMNN (Fig. 6.12). Like discussed already for the ML 6T, without the

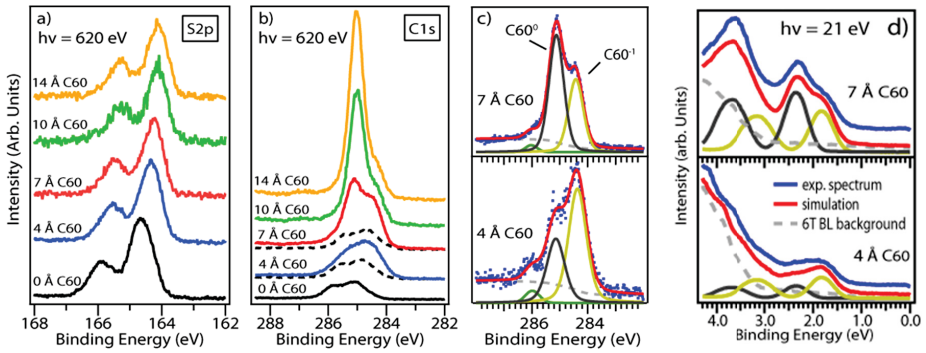

Figure 6.21: a): S2p CL spectra of BL 6T / Ag(111) before and after deposition of 4 Å, 7 Å, 10 Å and 14 Å C_{60}. b): C1s spectra of the same systems as in a). Dashed lines show the estimated C1s 6T contributions in the spectra of 4 Å and 7 Å C_{60} / BL 6T (see text). c): Fit of the C_{60} C1s contributions after subtracting the 6T contributions in b), for 4 Å and 7 Å C_{60}. The high and low BE components correspond to C_{60}^{0} and C_{60}^{-1}, respectively. d): Simulation (red line) of the valence spectra for another sample with 4 Å and 7 Å C_{60} coverage using shifted thick film C_{60} valence spectra and a background due to the BL 6T / Ag(111). The relative intensity of both employed C_{60} spectra is determined from the fit of the C1s spectra in c). The data were obtained at BESSY.

shift, a shoulder should be visible on the high BE tail of the C1s measured after C_{60} deposition. The so-obtained difference spectra are presented in Fig. 6.21 c) and fitted with two main components with Voigt lineshape. The components at 285.1 eV and 284.4 eV are identified as neutral C_{60} (C_{60}^{0}) and anionic C_{60} (C_{60}^{-1}) respectively. To account for the high BE shoulder, a Gaussian peak was added at 1.6 eV higher BE from the C_{60}^{-1} C1s main peak. However, it is unclear whether this small peak of $< 4\,\%$ spectral weight has to be attributed to a shake-up of the main C_{60}^{-1} C1s peak or if it results from a discrepancy in the subtraction procedure (possibly due to not-accounting for a different shift of the C1s peaks stemming from the first and second 6T layer, as shown in Fig. 6.22 for the S2p spectra).

S2p spectra, displayed in Fig. 6.21 a), exhibit a gradual shift to lower BE upon C_{60} deposition. However, the shift of the S2p spectrum is ca. 0.15 eV larger than for the ML 6T case. The fitting procedure shown in Fig. 6.22 a) helps discriminating between the first and second 6T layer contributions, which are separated by 0.4 eV in BE before C_{60} deposition. This energy difference is attributed mainly to differences in screening of the photo-holes [142] and compares well with the energy difference of 0.35 eV that was identified for the HOMO and HOMO-1 of the first and second 6T layer [Fig. 6.16 c)]. In addition, upon increasing C_{60} thickness up to 1 ML C_{60}, the full-width-at-half-maximum (FWHM) of the $S2p_{3/2}$ component decreases by 0.15 eV from 0.95 eV to 0.8 eV. The fitting reveals that this is due to a differential shift of the CL corresponding to the first (0.3 eV shift) and second (0.5 eV shift) 6T layer, which leave the two contributions separated by 0.2 eV after completion of the C_{60} monolayer. Importantly, this evidences an electrostatic potential drop in the direction normal to the sample. This can be explained quantitatively by the potential drop induced

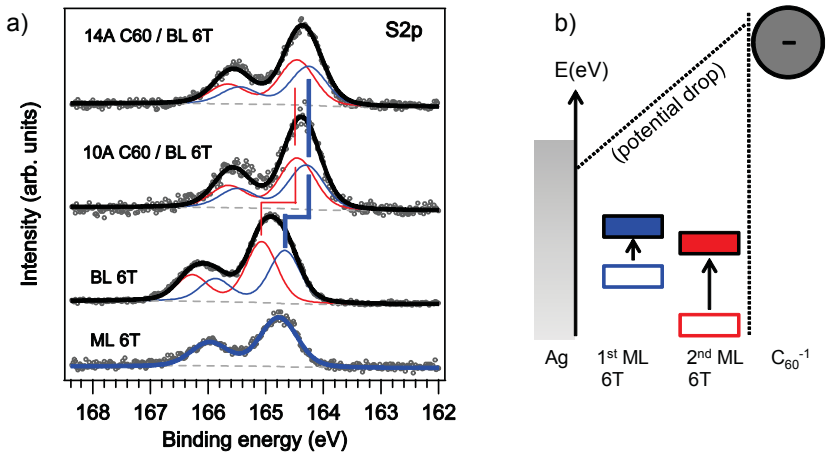

Figure 6.22: a): S2p spectra obtained for (from bottom to top) ML 6T/Ag(111), BL 6T/Ag(111), and 10 Å and 14 Å C_{60} deposited on BL6T/Ag(111). Dots correspond to the experimental spectra. Blue and red lines correspond to the fit of the first and second 6T layer contributions, respectively. The black lines depict the result of the fit for each spectrum. Further details on the results of the fits are given in the text. b): Scheme of the effect of the potential drop on the relative position of the first and second layer 6T CL before (empty rectangles) and after (filled rectangles) C_{60} deposition.

by the charge transfer from the Ag(111) to a fraction of the C_{60} molecules, as detailed in section 6.2.4 below.

Like for HATCN and Alq_3, EA and IE of C_{60} and 6T, respectively, have a large energy mismatch (ca. 1 eV) such that, based on general grounds, no inter-molecular charge transfer is expected. For the C_{60}/6T interface, a charge transfer between the molecules can be further ruled out as it is not observed when the substrate employed has a higher work function and the 6T layer has a similar thickness [307]. In fact, none of the features shown above (including the interface dipole formation, the 6T core levels shifts, and the two distinct C_{60} C1s components) were reported in Ref. [307]. Also, for the present systems, considering an inter-molecular charge transfer would not explain the fact that different charge states are observed within the C_{60} layer and not within the 6T layer. Furthermore, invoking inter-molecular charge transfer does not provide a satisfactory explanation for the fact that the fraction of the two C_{60} species depends on the 6T spacer layer thickness. This allows concluding that the effect of intermolecular interactions (involving charge transfer or hybridization) is very small and plays a negligible role in explaining the observations.

The following section discusses the consequences when assuming that charges in the overlayer (responsible for interface dipoles) originate from the substrate, as proposed in the MOCT model. A coherent picture is drawn on this basis, which allows explaining the experimental observations quantitatively. Electrostatic considerations are employed to address the questions why i) the C_{60} layer is not homogeneously charged, ii) the fractions of charged and neutral molecules vary with the 6T spacer layer thickness, and iii) C_{60} molecules, which do not

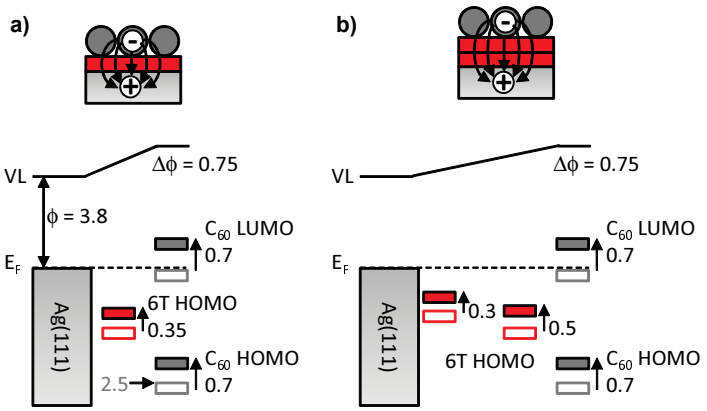

Figure 6.23: a) and b): Energy level diagram for 1ML C_{60}/ML 6T/Ag(111) and 1ML C_{60}/BL 6T/Ag(111), respectively. Empty rectangles depict the energy position of 6T HOMO, neutral C_{60} HOMO and neutral C_{60} LUMO assuming VL alignment (before contact). Filled rectangles show the actual energy level alignment as determined experimentally. The difference between both, depicted by the arrows and the associated numbers, results from the potential drop due to the dipoles formed with charged C_{60} molecules. At the top, the electric field lines and the potential drop ΔV are illustrated for each system.

undergo charge transfer in the monolayer, can still be at electronic equilibrium within that layer.

6.2.4 Energy-level alignment and electrostatic considerations

For a comprehensive understanding of ELA, the following part considers the potential drop in between two charged molecules. This allows the neutral C_{60} molecules in the overlayer to be at electronic equilibrium without undergoing a charge transfer, as is explained in the following.

The negative pinning work function, $\phi_{\mathrm{pin}-}$, of C_{60} was reported to be 4.5 eV [36, 29], which means that for a substrate with $\phi < 4.5$ eV, charge transfer must occur to establish electronic equilibrium (i.e., to prevent that the empty C_{60} LUMO is located below E_{F}). With the help of Fig. 6.23, let us first look at the situation as it is expected for simple vacuum level alignment between the neutral C_{60} molecules and the 6T interlayer. As the work function of 6T/Ag(111) is 3.8 eV, the neutral C_{60} HOMO peak maximum should be found at 3 eV BE (and its onset at 2.5 eV BE). Given a charge transport gap (determined from HOMO and LUMO onset energy difference) of about 2.4 eV as determined by combined direct and inverse photoemission [309, 314], electronic equilibrium would not be encountered for these molecules. In contrast, the present results show that the HOMO peak maximum of the neutral C_{60} is positioned at 2.3 eV BE (and onset at ca. 1.8 eV), i.e., where the neutral C_{60} molecules are electronically stable. The following will demonstrate that the discrepancy between the expected neutral C_{60} HOMO BE, assuming VL alignment, and the actual one is due to the potential drop, which was also found to affect the 6T CL.

Table 6.1: Experimental (ex) and theoretical (th) values of $\Delta\phi$ and ΔV for a full C_{60} monolayer ($\theta = 1$) on top of a monolayer 6T (ML) and a bilayer 6T (BL). The fractions of C_{60}^{-1} for this coverage, i.e. $\rho(1)$, were derived from experiment, as explained in section 6.2.2. $\Delta\phi_{\mathrm{th}}$ was calculated with (6.1). Details on the ΔV_{th} profiles and the determination of ΔV_{ex} are provided in Figs. 6.24 and 6.23, respectively. $6T_1$ and $6T_2$ are the first and second 6T layer, respectively.

	$\rho(1)$	z_{th} (Å)	$\Delta\phi_{\mathrm{ex}}$ (eV)	$\Delta\phi_{\mathrm{th}}$ (eV)	ΔV_{ex} (eV)			ΔV_{th} (eV)		
					$6T_1$	$6T_2$	C_{60}^0	$6T_1$	$6T_2$	C_{60}^0
ML	0.42	4.5	0.75	0.85	0.35		0.7	0.3		0.65
BL	0.3	7	0.7	0.87	0.3	0.5	0.7	0.25	0.45	0.65

The energy position of the neutral C_{60} HOMO is now reconsidered by accounting for electrostatic fields arising from MOCT. It is possible to calculate the change in the electrostatic potential induced upon C_{60}^{-1} adsorption within a simple image charge model in order to test the previous assumptions. For this, let us consider an ordered network of dipoles (corresponding to anion C_{60} molecules) and their mirror charge in the metal substrate, which are described as negative and positive point charges, respectively.

Within the scope of this work only classical calculations were performed.[5] The 1 ML C_{60}/ML 6T/Ag(111) and 1 ML C_{60}/BL 6T/Ag(111) systems are simulated as a square network of C_{60}^{-} whose dimensions give an C_{60}^{-} areal density N in agreement with the experimentally observed C_{60} fractions. The electron-image plane distance z is chosen such that the electron in the charged C_{60} is located at the bottom part of the molecule (see Tab. 6.1). This can be intuitively justified by considering the attraction between the charge and its image. Describing the electrons as point charges remains an approximation to the actual spatial extent of the frontier π orbitals, which are delocalized and also tail out of the C_{60} cage. Test calculations including charges homogeneously spread over small disks (with diameter of 0.8 nm corresponding to the diameter of a C_{60} molecule) were also performed and gave comparable results.

As a first test, the expected work function increase can be calculated by the Helmholtz equation (Eq. (6.1)). With $\epsilon_{\mathrm{r}} = 4$[6] [340, 118, 330, 226] and a charge transfer of one electron, we find $\Delta\phi = 0.85\,\mathrm{eV}$ for 1 ML C_{60}/ML 6T and $\Delta\phi = 0.87\,\mathrm{eV}$ for 1ML C_{60}/BL 6T (with $z = 5\,\text{Å}$ and $z = 7.5\,\text{Å}$, respectively), which is in reasonable agreement with the experimental values.

This permits to simulate the electrostatic potential caused by the MOCT in more detail. The potential drop ΔV within the molecular layers at a point M can be calculated as the sum of the potentials created by the positive and

[5] When looking in the corresponding literature it seems to be still under debate how well such a classical treatment induces errors for adsorbates in close vicinity to metal surfaces. While according to one study "long-range electrostatic interaction between molecules and metals can be approximated by means of a simple image-charge model" [90], the results of another paper "make it evident that interaction of dipoles on the surface will [..] be substantially modified, if the non-locality of the substrate screening properties is taken into account." [99]. For the present systems, on the other hand, the adsorbate should be at a large-enough distance from the image plane (i.e., the metal surface) for the classical treatment to be appropriate.

[6] To simplify the calculations, a common relative permittivity for both materials was assumed.

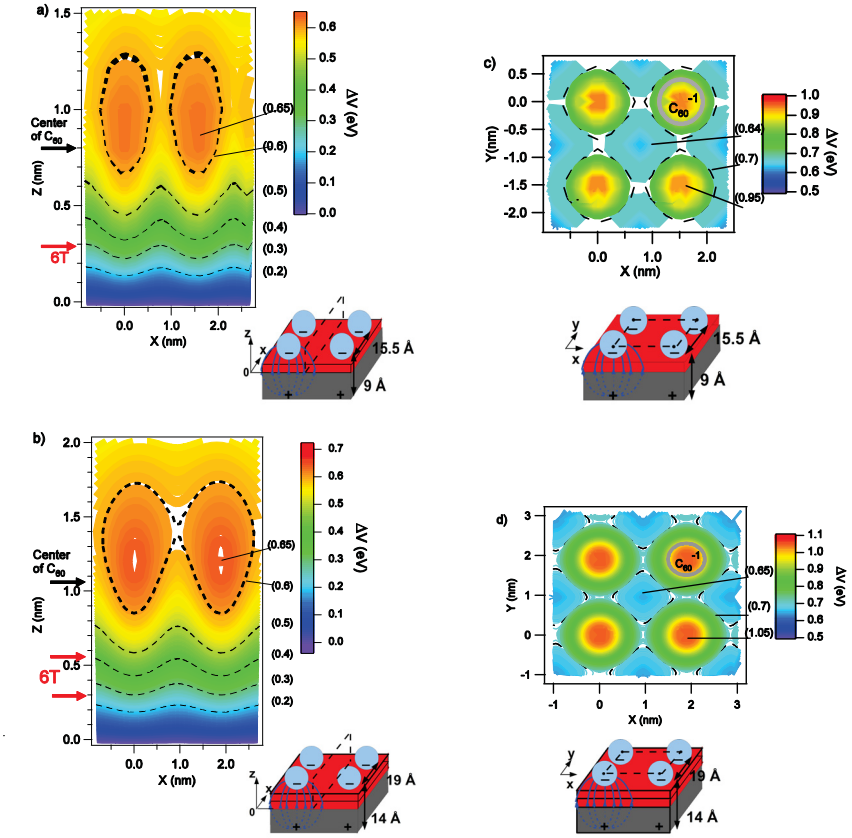

Figure 6.24: a) and b): Map of the potential increase ΔV for C_{60}/ML 6T/Ag(111) and C_{60}/BL 6T/Ag(111), respectively, within the plane normal to the surface as schematically depicted in the insets. The arrows on the left represent the approximate position of the 6T layers. c) and d): The same as a) and b), but for the plane parallel to the surface 2 Å above the location of the point charges (i.e. going through the center of the C_{60} molecules). Note that the point charges are located below the higher ΔV values in the graph. The dotted lines on the potential map present the isocontours corresponding to the values in between parentheses.

negative monopoles on each side of the image plane and, in the simple point charge model, is given by:

$$\Delta V(M) = \frac{1}{4\pi\epsilon_{\mathrm{r}}\epsilon_0} \sum_i \frac{q_i}{r_i(M)} \,, \tag{6.5}$$

where q_i corresponds to the charge of the ith monopole and $r_i(M)$ represents the distance between the ith monopole and any point M in space. A map of the resulting increase in potential ΔV in a plane normal to the sample is shown in Fig. 6.24 a) and b) for C_{60} on ML 6T and BL 6T, respectively.

From these calculations, the potential at the adsorption sites of neutral C_{60} is seen to increase by ca. 0.6 - 0.65 eV for 1 ML C_{60}/ML 6T and ca. 0.6 – 0.7,eV for 1 ML C_{60}/BL 6T, consistent with the energy difference of 0.7 eV between assumed vacuum level alignment and measured values mentioned earlier. Furthermore, the potential increase within the 6T layer is in very good agreement with the experimental data and reproduces the differential shift of the 6T features observed in the XPS spectra of BL 6T (see Fig. 6.22). Representative averages of the numerical results are resumed in Tab. 6.1. The experimental values in this table were derived from the energy level diagram as measured compared to what would be expected for vacuum level alignment, as resumed in Fig. 6.23.

Maps of the induced electrostatic potential in a plane parallel to the surface and cutting through the center of the C_{60} molecules are displayed in Fig. 6.24 c) and d). The potential is rather homogeneous in the xy plane and therefore not expected to lead to a significant broadening of the neutral C_{60} HOMO, again consistent with the experimental observations.

6.2.5 Application to device-relevant architectures

This part is dedicated to the consequences of the present findings on the ELA at molecular (organic) heterojunctions in contact with a metal, or, more generally, conductive electrodes. For these systems, in most cases photoemission measurements do not reveal DOS at E_{F} that could be directly attributed to charge transfer to the organic overlayer. The analysis provided in this study might help understanding this discrepancy. Indeed, the fact that not all molecules are charged may allow attributing the lack of DOS at the E_{F} for those cases as being due to too small amount of charges at the interface to be detected. In first approximation, the density of dipoles resulting from electrode-to-overlayer charge transfer necessary to create the observed work function changes is expected to vary inversely proportional with the overlayer–electrode distance. As a result, the density of dipoles will be dramatically reduced when increasing the organic spacer layer thickness to values typically employed for organic electronic devices.

As proof of principle, the electrostatic calculations presented above will be applied to the recently reported system diindenoperylene (DIP) grown on 10 nm C_{60} adsorbed on a conductive polymer electrode made of poly(ethylenedioxythiophene:poly(styrenesulfonate) (PEDT:PSS) [313], which was discussed in more detail in [315]. The C_{60}/PEDT:PSS system had $\phi = 5.55$ eV. E_{F}-pinning was found for the DIP HOMO and ϕ decreased by 0.45 eV as a result of the creation of an interface dipole by adsorption of the first DIP layer. The

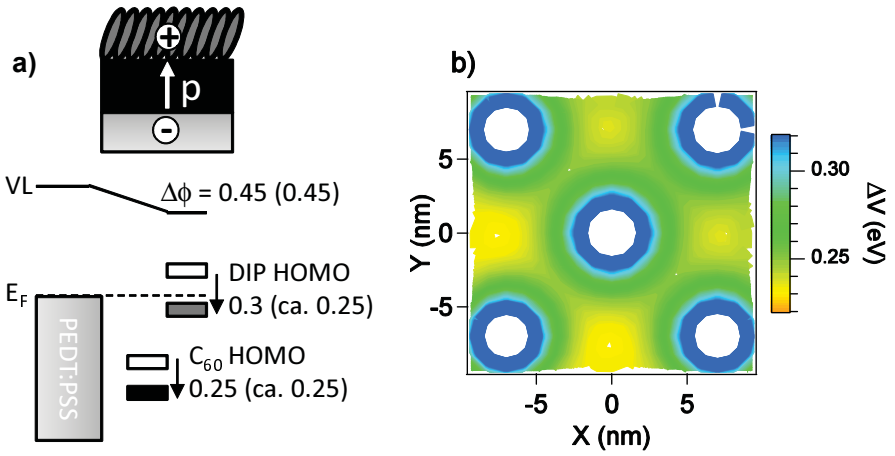

Figure 6.25: a): Energy level diagram of DIP/ 10 nm C_{60}/PEDT:PSS from [313]. Filled rectangles show the actual energy level alignment and empty rectangle the energy level alignment when assuming VL alignment. Values in parentheses are the average energy shift determined theoretically. b): The potential map in the last C_{60} layer as calculated with Eq. (6.5) (see text). The isocontours are plotted for a potential drop between 0.22 eV and 0.32 eV.

DIP HOMO onset was measured at 0.3 eV BE and no DOS was observed at E_F. Because DIP has an IE of 5.4 eV, VL alignment would have placed its HOMO onset 0.15 eV above E_F. Furthermore, upon DIP deposition, the HOMO of the C_{60} spacer layer continuously shifted to higher BE by 0.25 eV. Fig. 6.25 a) shows the actual energy level diagram of this system and the expected one in the hypothetical case of VL alignment. Applying the Helmholtz equation to this system (placing the negative end of the interface dipole at the substrate surface and the positive one in the first DIP layer), it is found that a dipole density of $N = 0.01\,\mathrm{nm}^2$ (i.e., one charged DIP molecule for ca. $100\,\mathrm{nm}^2$) is sufficient to induce the observed work function decrease. The potential drop, as determined with Eq. (6.5), shows a homogeneous potential decrease of ca. 0.27 ($\pm$0.03) eV in the topmost C_{60} spacer layer and in the DIP overlayer as shown in Fig. 6.25 b). These values are consistent with the experimental observations. The low N explains why charged DIP molecules are not readily observed. This first "reality check" of the MOCT model suggests that it can be used (within its limitations) to adequately explain the electronic properties of many application-relevant organic-organic interfaces.

6.2.6 Effect of dipole-dipole interactions

For a MOCT through a spacer layer, as proposed in the present work, one should encounter large dipole moments, oriented normal to the sample surface and formed by charges in the overlayer and their counterparts inside the metal. Thus, the impact of dipole-dipole interactions cannot be neglected [287, 95, 330]. This is clearly seen by the observation that the dipole-dipole repulsion makes the MOCT less likely to occur with increasing coverage, as evident from the decreasing fraction of charged molecules in the organic overlayer with coverage

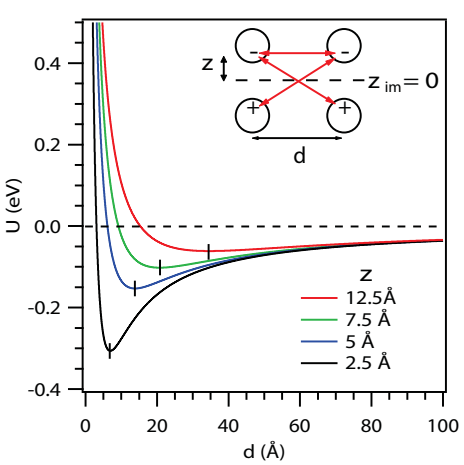

Figure 6.26: Interaction potentials between two dipoles formed by electrons and their image charge in the metal as a function of d, the distance between two adjacent dipoles, and for different electron - image charge distances $2z$, ranging from 5 to 25 Å (from bottom to top). The vertical lines show the position of minimum energy for each profiles. Inset: geometry of the considered system; the red arrows show the interactions taken into account in the model. z_{im} is the position of the image plane.

[Fig. 6.14 c)]. The models commonly used for organic/metal interfaces treat the dipole-dipole repulsion as collective response of the electron density that is delocalized over the hybridized metal/adsorbate system [288, 95]. Obviously this is not appropriate for the localized integer charges in the MOCT model. It is therefore particularly tempting to speculate how the charged and neutral molecules are distributed in the C_{60} overlayer and how the Coulomb force affects the self-assembly. In Ref. [287] it was suggested that "STM images can unambiguously reveal the emergence of peculiar 1D patterns at the submolecular level, which [...] could be regarded as a strong indication of charge transfer at the adsorbate/substrate interface". Thus, it does not come as a surprise that the structures observed in the STM images do not resemble densely packed C_{60} assemblies found on 6T when no charge transfer was present [307], but indicate that charge-transfer-induced dipoles play a role on the molecular self-assembly via a repulsive interaction.

The "1D patterns" mentioned in the above quote from Ref. [287] refer to structures that neither evidence molecules that repel each other, nor exhibit a dense packing. The reason for this is the coexistence of short-range attractive and long-range repulsive intermolecular forces. The short-range component was identified as hydrogen bonds in the case of tetrathiafulvalene/Au(111) [95]. However, in Ref. [287], no hydrogen bonds are expected to form between the rubrene molecules, and, as is argued by the authors, dispersion forces are sufficiently large at small distances to overcome the repulsive long-range coulomb interaction between the positively charged molecules. It is important to note that for the discussion of intermolecular forces induced by MOCT, the term dipole-dipole repulsion is slightly misleading, since, when computing the interaction between two charged molecules, the image charges in the metal do not interact with each other. This is illustrated in Fig. 6.26 and, for the simple image charge model introduced above, yields the following interaction potential

$$U(d) = \frac{q^2}{4\pi\epsilon_{\mathrm{r}}\epsilon_0}\left(\frac{1}{d} - \frac{2}{\sqrt{2z^2+d^2}}\right) = \frac{q^2}{4\pi\epsilon_{\mathrm{r}}\epsilon_0 d}\left(1 - \frac{2}{\sqrt{1+\frac{2z^2}{d^2}}}\right) \qquad (6.6)$$

where d is the horizontal distance between the two charged molecules. Note

that the attractive interaction between each electron and its image, which would add an offset to $U(d)$, is neglected. In Fig. 6.26, interaction potential profiles obtained from Eq. (6.6) with $\epsilon_r = 4$ are shown as a function of d for several z. The profiles depicted with $z = 5\,\text{Å}$ and $z = 7.5\,\text{Å}$ are representative of the C_{60}/ML 6T/Ag(111) and C_{60}/BL 6T/Ag(111) cases, respectively.

For low d, the interaction is dominated by the Coulomb repulsion, which is more pronounced for larger z, since the screening by the image charges is less efficient. Notably, $U(d)$ exhibits a minimum for $d = 2.6\,z$ (i.e., beyond the next-neighbor distance in a dense C_{60} packing for both relevant z's), and the interaction starts being attractive when d increases further. This is due to the counter charges in the metal surface and therefore somewhat resembles the like-likes-like interaction discussed for ionic colloids [140, 337]. However, at these distances the interaction with other molecules make a two-particle treatment increasingly inappropriate.

As mentioned above, in Ref. [287] it was assumed that dispersion forces are responsible for a short-range attractive force and therefore found to stabilize the formation of 1D structures. However, the corresponding free parameters in the theoretical model were introduced *ad hoc* to achieve just that. In the present system another situation is more conceivable: two charged C_{60} could be linked via one neutral C_{60}, since, due to induction, the short-range interaction between neutral and charged molecules is certainly attractive. Such an arrangement could result in the formation of 1D structures, e.g. the lines observed in the STM images in Fig. 6.10. The patterns with isolated molecules found in the same images are then readily explained by the lack of a short range attractive force between charged molecules, and thus should indeed be formed in areas where this species predominates.

Notably, the STM images in Fig. 6.10 suggest that the formation of particular C_{60} patterns might also be related with their orientation with respect to the 6T template. Furthermore it needs to be pointed out that the above discussion does not elaborate on the possibility that not only the position of the molecules, but also their charge state can change. However, it is very well possible that charges flow from one C_{60} molecule to another, e.g., via the metal surface. Indeed it should be very interesting to probe the charge state of individual molecules (e.g. by Kelvin probe atomic force microscopy) and to see whether charge ordering phenomena can be observed.

6.3 Conclusions

A strong electron acceptor molecule, HATCN, was deposited on-top of a physisorbed Alq_3 monolayer adsorbed on Ag(111). The location of HATCN at the very surface was deduced from core level photoemission measurements. The valence band spectra reveal the emergence of an interface DOS in the vicinity of the Fermi level. This DOS is attributed to a charge transfer from the metal to the top HATCN molecular layer through the Alq_3 layer, possibly involving the transfer of one electron per molecule. The (relatively low) ϕ increase suggests a reorientation of Alq_3 and its dipole moment upon HATCN adsorption.

In a more comprehensive follow-up study, C_{60} was deposited on substrates consisting of ML 6T and BL 6T on Ag(111) and the evolution of ϕ and VB during interface formation was monitored. For 6T-covered Ag(111), ϕ is well below $\phi_{\mathrm{pin}-}$ of C_{60}, and therefore upon C_{60} adsorption an interface dipole arises. Remarkably, the work function is found to increase asymptotically. The ϕ increase, which is correlated with the emergence of the partially filled C_{60} LUMO in the VB spectra, results from an integer charge transfer from the metal to the C_{60} overlayer through the neutral 6T spacer layer. A careful analysis of the core levels and valence band spectral weights of the different contributions leads us to further conclude that two C_{60} species, namely neutral (C_{60}^{0}) and charged (C_{60}^{-1}), are observed simultaneously and in different proportions at different C_{60} coverages within the sub-monolayer regime. This varying fraction is identified as the cause for the non-linearity of the ϕ profile. When C_{60} is deposited on BL 6T on Ag(111), similar features are found with the difference that the fraction of charged C_{60} molecules is systematically lower. Dipole-dipole interaction is proposed as the driving force leading to the occurrence of a layer composed of mixed neutral and charged C_{60} species. Electrostatic considerations allow for a quantitative analysis of the energy shift of the 6T spectral features as being due to the potential drop over this neutral spacer layer. The energy level alignment at these interfaces could thus be explained in a coherent picture of integer charge transfer and associated charge dilution in the C_{60} overlayer.

The model was applied successfully to apprehend the energy level alignment recently reported for another organic/organic interface grown on a conductive polymer substrate. It is therefore suggested that substrate-to-organic overlayer charge transfer and the resulting electric field are key prerequisites for understanding the energy level alignment at molecular and organic heterojunctions in contact with metals or conductive electrodes.

Chapter 7

Polar molecules at organic/metal interfaces: Molecular self-assembly and energy-level alignment

STM can most easily access molecules in direct contact with a conductive surface. In this setup, however, the molecules' dipoles are partially screened by the substrate and, in addition, their mutual interaction might be further masked by site-specific molecule-substrate [251] and adsorption-induced intermolecular [303, 89, 214] interactions. Therefore, it is crucial to choose a simple system for which the expected effect of the built-in dipole moment μ is clearly identifiable. In addition, the influence of interactions that can potentially have the same effect as μ should be tested with related systems that (to the largest degree possible) differ only in μ. Under these conditions it should be possible to identify also subtle changes induced by the dipole-dipole interaction.

Accordingly, first the reference system for the following discussion, 6P deposited on cooled Ag(111) is presented in Sect. 7.1.1. This system had been studied before [133, 166, 32] and no significant interaction at the O/M interface was expected.

The following sections 7.1.2 and 7.1.3 report the results of LT-STM studies of the partly fluorinated 6P derivatives meta-2F-6P/Ag(111) and ortho-2F-6P/Ag(111), respectively. The molecules are found to form supra-molecular chains via hydrogen bond formation involving the fluorine atoms. Remarkably, the two derivatives exhibit a range of different vertical offsets between neighboring molecules along the chains, which is partly explained by a preferred epitaxial registry, but can only be fully understood when accounting for an influence of the different built-in dipoles of the derivatives.

In two-dimensional structures, the dipole contribution is expected to manifest itself more subtly, since a variety of structures is predicted already for ideal[1] dipole networks [296]. Indeed, four different phases, including one with

[1]The short range interaction of real dipoles additionally differs from that of ideal ones due to the non-point-like charge distribution [254, 158, 296].

a ferroelectric unit cell, have been observed by low temperature STM [72, 270] for the polar molecule 4-methoxy-3,3',5,5'-tetra-tertbutylazobenzene (M-TBA) on Au(111), while for the corresponding non-polar derivatives, diM-TBA and TBA, only one phase has been observed. In a more recent study [188], titanyl phthalocyanine (TiOPc) was found to undergo a phase transition of its in-plane dipole moment from ferroelectric to anti-ferroelectric as function of the rhomboid angle α of its unit cell. The experimental critical α agrees well with theoretical predictions [241, 86, 31, 88]. Unfortunately, due to the appearance of the inclined TiOPc molecules, some ambiguity concerning the identification of the molecular orientations remained.

From the STM images of the 6P derivatives, an unambiguous determination of their orientation was not possible due to the virtually symmetric appearance. Therefore, ID28, which has a highly asymmetric chemical structure, on Au(111) was employed for the RT experiments presented in Sect. 7.2. The part of ID28 that consists of a dicarboxylic-anhydride functionalized perylene core is identical to the corresponding part of PTCDA, which allows estimating the strength of the molecule-substrate interaction and a part of the intermolecular forces for ID28/Au(111). For PTCDA/Au(111), a predominantly physisorptive bonding [284] and a flat surface potential energy surface (or corrugation potential) was found experimentally [255] and theoretically [202], which should hold even more for ID28, since its bulky side groups prevent the central benzene ring in the perylene core, which for PTCDA was found to be the main reaction center [84], and the nitrogen atom from interacting strongly with the surface. For weakly-bound cases like on Au(111), PTCDA exclusively forms herringbone and square arrangements, which are explained as being due to hydrogen bonds between the oxygen and hydrogen atoms [311, 202] together with the possibility to compensate PTCDA's large quadrupole moment by a pairwise near-orthogonal arrangement [273, 104]. The hydrogen bonds were identified as responsible for the formation of an in-plane herringbone arrangement of PTCDA at several organic hetero-interfaces [56]. On the other hand, they were found to be comparable weak by scanning tunneling *hydrogen* microscopy of PTCDA/Au(111) [311].

Sect. 7.2.1 reports the four different ordered phases that were observed for pristine films of ID28/Au(111). The effects of ripening and application of an electric field with the STM tip on the molecular self-assembly are shown. Sect. 7.2.2 discusses, by means of XPS and UPS data (both BESSY), as well as STM results, how annealing at 300 °C leads to geometric and electronic changes of the molecules. The annealing also makes the molecules arrange in two new phases which are both more densely packed than the pre-annealing phases. Thereafter, hints for the influence of the permanent dipole moments on the molecular arrangement in the STM data are carefully discussed in Sect. 7.2.3. The final section 7.2.4 presents UPS results (obtained at HU) that evidence a preferred orientation of ID28 molecules in multilayer films, leading to a surface potential of 1.2 eV. Further data shows the reversible partial removal of this potential by visible light irradiation.

7.1 Para-Sexiphenyl (6P) and partly fluorinated 6P derivatives on Ag(111)

7.1.1 Unsubstituted 6P

First, the reference system, namely 6P deposited on Ag(111) at ca. 70 K, will be discussed. At low coverage, isolated molecules are observed, which are mostly oriented (with their long molecular axis) along the [1-10] (= azimuthal) direction of the Ag(111) substrate as was reported before [133, 32]. About 10 % of 6P molecules were found oriented along the Ag [11-2] (= interazimuthal) direction [134]. From earlier work [133, 166] a face-on configuration with a torsional angle of 11.4° between adjacent phenyl-groups can be concluded on. At higher coverage, the 6P molecules arrange in clusters with their long molecular axis oriented ca. 8° offset with respect to the interazimuthal direction and stack perpendicular to their long molecular axis. An intermolecular distance along the stacking direction of 6.2 ± 0.2 Å was found [134].

A different molecular arrangement has been found in another work by Chen *et al.*, who deposited 6P onto Ag(111) at room temperature (RT) and annealed the system to 380 K [58] before their measurements.[2] Under these conditions, 6P molecules arranged in rows with an intermolecular distance of 7.0 ± 0.2 Å along the stacking direction. A face-on geometry and an exact interazimuthal alignment was observed for these molecules. Deposition of further 6P molecules on top of such a 6P template at RT led to insertion of differently oriented (edge-on) molecules in between the face-on molecules.

7.1.2 Meta-2F-6P

Let us move on to the dipole-functionalized 6P derivatives. The electrostatic potentials for meta-2F-6P (with the fluorine in meta position) and ortho-2F-6P (with the fluorine in ortho position) are presented in Fig. 7.1 c) and d), respectively. Even though we want to investigate the role of the dipole-dipole interaction for the self-assembly, the substitution of two hydrogen atoms will potentially influence the intermolecular interaction also via the formation of hydrogen bonds and a changed molecule-substrate interaction. Therefore an assessment of how these two factors affect the self-assembly before discussing the role of the non-vanishing permanent dipole moment is crucial.

In Fig. 7.1 a), the expected mutual orientations of two face-on meta-2F-6P molecules are sketched when permitting both fluorine atoms to form a hydrogen bond each. Both proposed arrangements can indeed be found in Fig. 7.2 a), which presents STM data for the low coverage regime of meta-2F-6P/Ag(111). For the 180° configuration, several parallel offsets are observed and a line scan

[2] For comparison, for 6P on Au(111) deposited at RT, a number of different molecular arrangements has been observed by RT-STM [93], including some with the molecules' orientation offset with respect to the azimuthal or interazimuthal directions. In addition, subtle substrate temperature-dependent differences on the molecular orientation were found for this system from XRD [113]. Au(111) has a lattice constant very similar to the one of Ag(111) and for another physisorbed molecule (diindenoperylene), comparable arrangement were found for the two substrates [138, 68]. Accordingly, it is not surprising that our data indicates that, just like for 6P on Au(111), the molecular arrangement of 6P on Ag(111) shows a large variation and sample temperature-dependence (however, due to a different molecule-substrate interaction maybe with shifted critical temperatures).

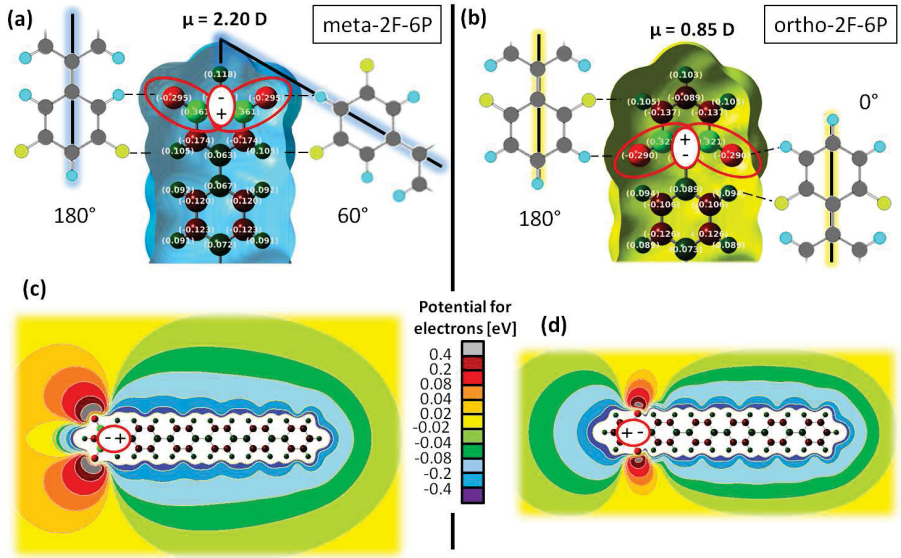

Figure 7.1: a) and b): Ball-and-stick model of meta-2F-6P and ortho-2F-6P, respectively. Only the part of the molecules where two hydrogen atoms of 6P were substituted by fluorine is shown. The central part presents the Mulliken charges on top of the atoms. The intramolecular polar bonds and the resulting dipole are illustrated by red ellipses without and with filling, respectively. The gray, yellow, and blue atoms for the adjacent molecules correspond to carbon, hydrogen, and fluorine, respectively. These molecules, which are of the same species as the central one, show the expected arrangements for two molecules that link via two H$\cdots$F bonds. c) and d): The electrostatic potential for meta-2F-6P and ortho-2F-6P, respectively.

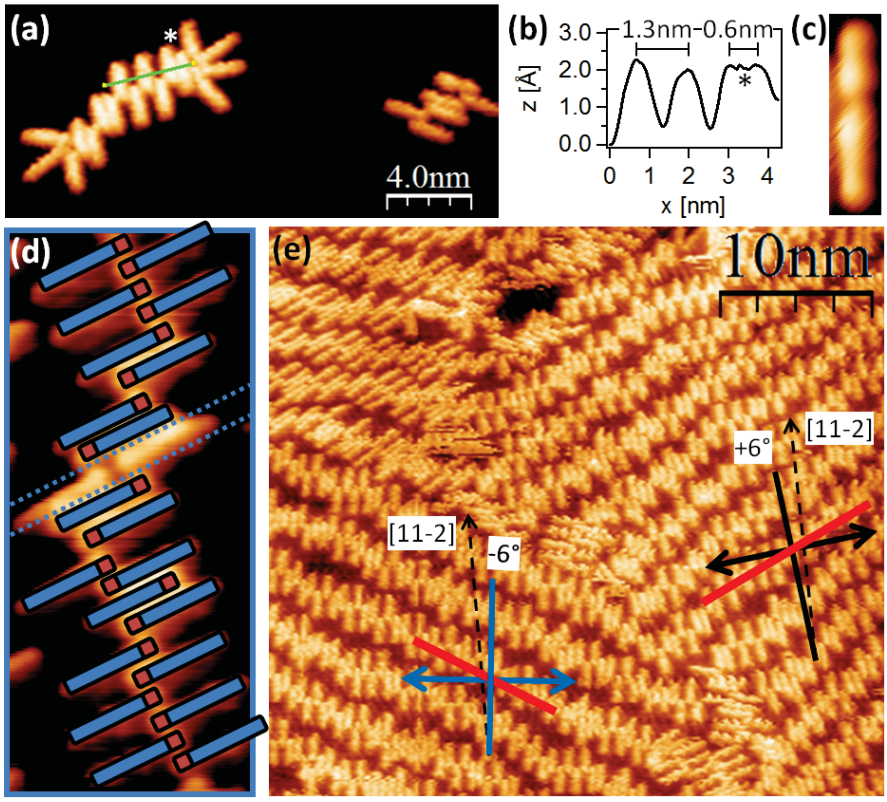

Figure 7.2: a): Typical clusters found at low meta-2F-6P coverage. The line profile measured along the red line is presented in b). c): An impurity that was occasionally observed. d): A grain boundary between two ladder-like structures. e): Molecular rows observed for medium coverage. The dashed arrows show the Ag[11-2] direction. The thin blue and black lines give the orientation of the long molecular axes, and arrows point in the perpendicular direction, while the thick red lines indicate the average stacking direction of the molecular rows. [Imaging parameters: a): -1.0 V, 10 pA; c): -1.0 V, 5.8 pA; d): -1.0 V, 10 pA; e): -1.0 V, 30 pA]

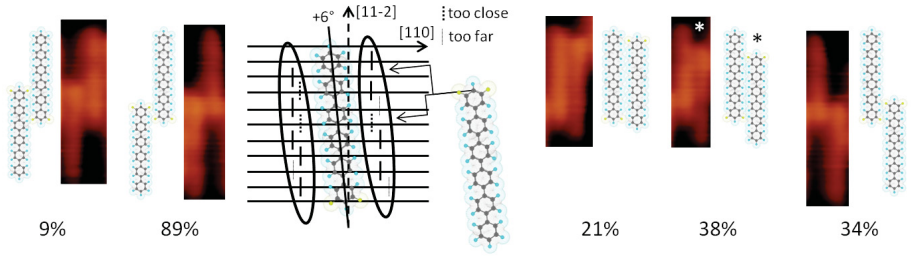

Figure 7.3: Ball-and-stick model of two meta-2F-6P molecules. The van der Waals radius is illustrated by the shaded area. Horizontal lines correspond to the location of Ag(111) hollow sites along [110]. Molecules with the same epitaxial registry as the central one would be located such that the indicated carbon atom in the right molecule sits where horizontal lines meet with vertical lines. The configurations with solid lines are found experimentally, while those with dashed and thin dotted lines are not observed. f): STM images of the most-frequently observed configurations, together with their abundance and the corresponding configuration derived from the model. [Imaging parameters: -1.0 V, 5 pA]

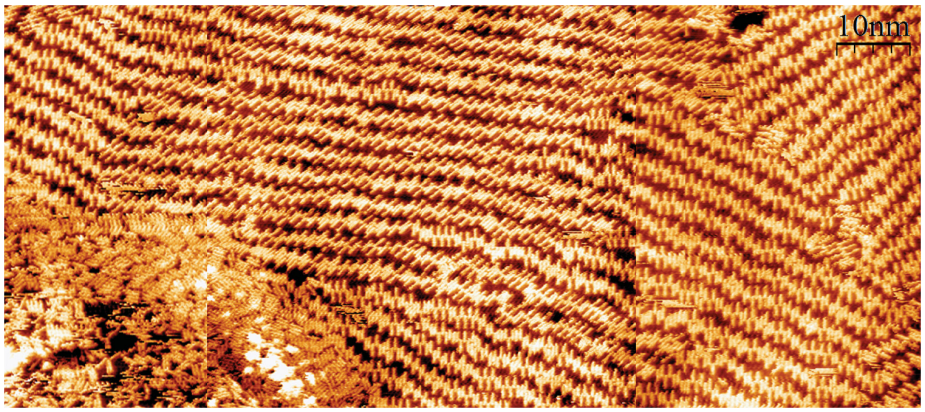

Figure 7.4: Several overlaid large scale images of meta-2F-6P. The structures in the lower left corner resemble the low-coverage arrangements presented in 7.2 a). [Imaging parameters: -1.0 V, 30 pA]

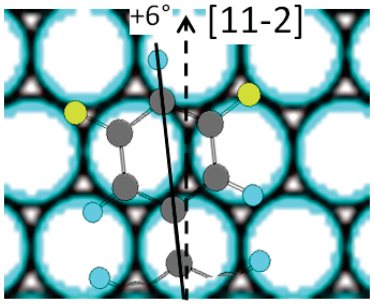

Figure 7.5: Ball-and-stick model of a meta-2F-6P molecule 6° rotated with respect to the Ag[11-2] direction illustrating the reasoning that the location of fluorine on top of Ag(111) hollow sites is what determines the molecules' orientation.

in Fig. 7.2 b) indicates that these are not equally spaced. When increasing the areal density by depositing more molecules, only the 180° configuration prevails and supramolecular chains are formed, as presented in Figs. 7.2 d) and e). Some molecules appeared with what seems like a neck, as shown in 7.2 c). These molecules are probably impurities and were omitted from the analysis to the best effort. Chain length $> 100\,\mathrm{nm}$ are presented in Fig. 7.4. Occasionally, the 60° configuration was observed when the local areal density was lower than that presented in Fig. 7.2 e). On the other hand, when the local areal density was higher, a more densely-packed log-raft-like arrangement was found. Both structures can be seen in the lower left bottom of Fig. 7.4. By and large, the chains in Fig. 7.2 e) consist of a head-to-head arrangement of adjacent molecules. Only when two sides of the chain are joined by a more complex arrangement (which might result from the convergence of two separate chains) a head to tail configuration *has* to occur, as illustrated in Fig. 7.2 d). Black and blue lines in Fig. 7.2 e) indicate two different enantiomers that can be identified by their respective misaligned by 6° with respect to the interazimuthal direction. As can be seen in Fig. 7.6, the same misalignment is found also for ortho-2F-6P. The difference with respect to the orientations observed for unsubstituted 6P might arise to allow the Fluorine atoms to be located on top of hollow sites, as illustrated in Fig. 7.5 for meta-2F-6P (without loss of generality). The same reasoning was applied to the nitrogen atoms of cyano-substituted 6P in Ref. [155]. Like was done in this other case, an epitaxial registry will be assumed in the following. With this assumption, one can predict the possible arrangements of adjacent meta-2F-6P molecules in the 180° configuration, as shown in Fig. 7.3. Due to the 6° tilt with respect to the interazimuthal direction, the arrangements with different vertical offset also vary in the intermolecular distance along the stacking direction. In addition, due to the mismatch of the interatomic spacing along the interazimuthal direction of Ag(111) and the interring spacing of 6P, a different vertical offset of two adjacent meta-2F-6P molecules results in different mutual configuration of their peripheral atoms. Accordingly, even though all arrangements indicated in Fig. 7.3 allow for two hydrogen bonds to be formed, they will not be equally favorable (i.e., also when *not* taking the van der Waals interaction into consideration). The most frequently found arrangements are presented in Fig. 7.3[3]. Notably, all configurations with the head-up (= partially fluorinated phenyl ring pointing upwards) molecule on the left side have a large parallel offset ("zipper arrangement"), while the configuration with the head-up molecule on the right side also include small parallel offsets. The arrangement for which the smallest intermolecular distance is expected is marked with an asterisk in Fig. 7.3. As mentioned above, a reduced spacing for this arrangement is indeed found from the line profile in Fig. 7.2 b). Such side-by-side arrangements for the head-up molecule on the left side do not fit with an epitaxial adsorption and were only sparsely found experimentally. This difference in preferred stacking on either side of a given molecule explains the observed (20° – 30°) misalignment of the stacking direction when compared to an assumed side by side arrangement, as indicated in Fig. 7.2 e) by bold (red) lines and two sided-arrows respectively. A similar misalignment was also found for 6P-clusters on Au(111) [93]. The important difference between 6P and meta-2F-6P is that the 6P molecules always

[3] At times, also the other arrangements indicated by a black line in Fig. 7.3 are found.

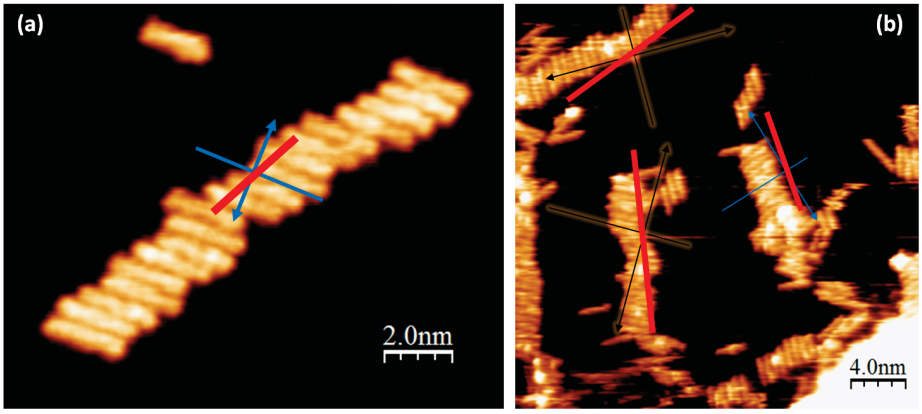

Figure 7.6: a) and b): STM images of ortho-2F-6P at low and medium coverage, respectively. Like in 7.2 e), the thin blue and black lines give the orientation of the long molecular axes, and arrows point in the perpendicular direction, while the thick red lines indicate the average stacking direction of the molecular rows. [Imaging parameters: a): -1.5 V, 10 pA, b): -1.0 V, 10 pA]

try to minimize the parallel offset to maximize the van der Waals (vdW) interaction[4]. Therefore, the observed patterns clearly show that another interaction, which is similarly important to the vdW interaction, favors a large lateral offset. Strikingly, the intramolecular dipoles of meta-2F-6P molecules [illustrated in Fig. 7.1 c)] in the most frequently observed configuration (i.e., with large vertical offset; see Fig. 7.3) arrange very similar to the side-by-side anti-parallel alignment that one would expect for two ideal dipoles.

7.1.3 Ortho-2F-6P

As can be seen from the Mulliken charges given in Fig. 7.1 a), the hydrogen atoms in the partially fluorinated phenyl ring are slightly more positive than the ones in unsubstituted phenyl rings. Therefore, also from a hydrogen-bond perspective the zipper arrangement is more favorable. In a study of tetrathiafulvalene on Au(111), a finite vertical offset in molecular rows was indeed found to stem from hydrogen bonds only [95]. Therefore, ortho-2F-6P was employed to test whether the hydrogen bonds or the intramolecular dipole drives the zipper assembly. As can be seen from the very similar Mulliken charges for both derivatives reported in Figs. 7.1 a) and b), this should not affect the strength of the hydrogen bonds in the 180° configuration. The dipole moment of ortho-2F-6P, on the other hand, is less than half of that of meta-2F-6P and points in the opposite direction, as shown in Fig. 7.1 b). No zipper arrangement is observed for ortho-2F-6P/Ag(111), as can be seen in Figs. 7.6 a) and b). This clearly proves the role of the macroscopic dipole moment for the molecular assembly of meta-2F-6P. The variation in vertical offsets for adjacent ortho-2F-6P molecules suggests a delicate balance of different forces (and, in turn, an influence of the dipole moment) also in this case. However, it will not be attempted to study the

[4] if they do not repel each other altogether because of substrate-mediated interactions; see e.g. [214]

role of the (significantly smaller) dipole moment for two reasons. Firstly, the electric potential deviates significantly from that of an ideal dipole, as shown in Fig. 7.1 d). This makes the influence of the dipole-dipole interaction more complicated and probably significantly more compatible with a vdW-dominated assembly. Both makes a clear identification much more difficult. Secondly, and different from meta-2F-6P, the ortho position of the fluorine atoms allows a 0° configuration that accommodates two hydrogen bonds, as illustrated in Fig. 7.1 b). This, together with the fact that the position of the fluorine atoms cannot be identified in the STM images, makes an identification of the exact configurations from experiment too speculative.

Table 7.1: Unit cell dimensions for all observed phases. α is the rhomboid angle of the unit cell. γ is the angle between a and the Au[11-2] direction. # mols. is the number of molecules per unit cell and A the unit cell's area.

	a (nm)	b (nm)	α (°)	γ (°)	# mols.	$\frac{A}{\#mols.}$ (nm^2)
HB	1.75	5.30	83	37	4	2.30
S	3.50	5.30	83	37	8	2.30
P	4.33	5.34	36	-10	6	2.27
sP	5.57	4.03	58	-14	8	2.38
HB$_A$	2.11	3.61	93	2	4	1.90
S$_A$	7.16	2.42	118	16	8	1.91

7.2 ID28/Au(111)

7.2.1 As deposited-films

Adsorption geometry of pair-wise arranged ID28

Fig. 7.7 a) shows a large-scale image of the Au(111) surface covered by almost a full monolayer ID28. The five Au(111) terraces have been leveled to allow for a better intra-terrace contrast. Ordered phases can be observed on three of the terraces and are labeled HB and P, for herringbone and parallelogram, respectively. Unresolved areas are due to mobile molecules and bright spots likely stem from molecules that are located on top of the first ML. Fig. 7.7 b) shows a highly-resolved zoom into an area with a HB and a P grain on the left and right side, respectively, which reveals that both arrangements consist of the identical two building blocks (encircled). Both building blocks consist of a group of four small features in the center and two large elongated features at the ends, which can be readily attributed to the phenyl groups with the attached tert-butyl groups [198, 261, 264, 251] and the perylene-derived core of ID28, respectively. Therefore, both building blocks can be identified as consisting of a pair of ID28 molecules that have their long molecular axis ca. parallel to the Au surface and face each other with their side groups.

For the further discussion it is important to note that ID28/Au(111) shows strikingly different appearances as function of the tip conditions. Spontaneous changes of the intramolecular contrast were routinely observed while scanning with fixed bias and set-point current, which is most likely induced by the STM tip becoming decorated with residual gas [311, 16, 114, 60] or ID28 molecules [177, 234, 70, 62, 213]. Three identifiable appearances of ID28 were encountered throughout the work: The data discussed thus far give perylene-derived core and side groups with similar apparent height, which will be referred to as "full-appearance" and is intermediate to the extreme cases where either the perylene-derived core or the side groups appear as located at much smaller height or do not show up in the images at all, which will be termed "side-groups only" and "core only" appearance, respectively. A similar change seems to be also induced by changing the tunneling bias, which, however, could be investigated only for annealed films, and will therefore be discussed in the corresponding section 7.2.2. In Fig. 7.8, side-groups-only and core-only appearances are shown for all arrangements encountered in this study. The dimensions of the corresponding

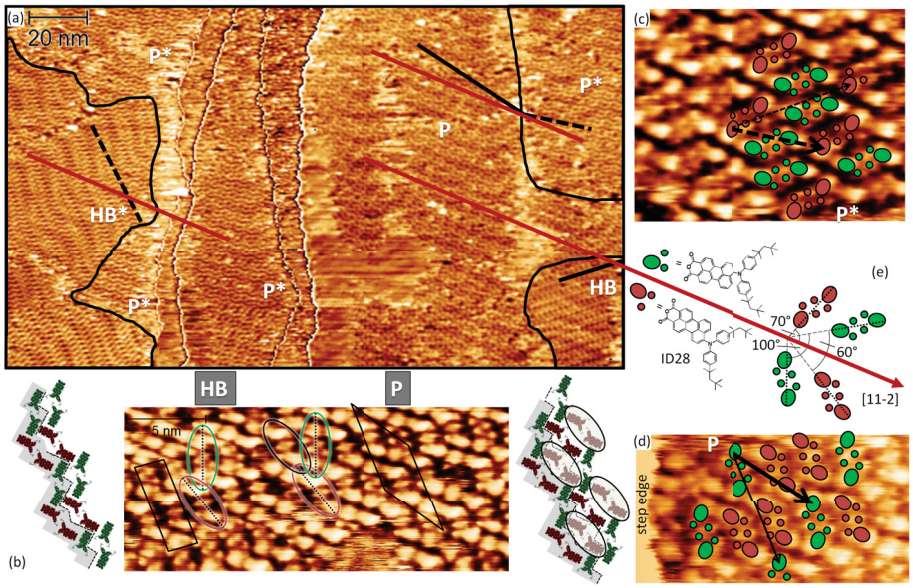

Figure 7.7: a): Large scale image showing five terraces with several grains of the two phases HB and P for ca. 0.85 ML ID28/Au(111). The Au(111) herringbone reconstruction is also visible and can be used to identify the orientation of the Au(111) lattice as illustrated by the long arrow. b): Molecularly resolved image of the area around a phase boundary with HB on the left and P on the right side. Since the exact conformation of the molecules on the surface is not known, a simplified representation is used to determine the arrangements and pair-wise orientation from the STM images. In the models for the HB and P structures, the representations of the molecules are simplified as flat-lying space-filling models of the ID28 molecules without tert-octyl groups (as calculated by DFT) overlaid with the chemical structure of ID28. The encircled molecules, together with the shaded rows, illustrate how one could hypothetically arrive from the racemic HB to the non-racemic P phase. c) and d): Molecularly resolved images of the mirror symmetric P* and P arrangements, respectively. In d), some molecules at a step edge can be observed whose orientations differ from the ones found for the other molecules. f): Chemical structure of the two surface-enantiomers of ID28 and the various orientations of the enantiopure pairs with respect to the [11-2] direction of Au(111). [Imaging parameters: a): -1.5 V, 0.4 nA, b) – d): 1.5 V, 0.3 nA]

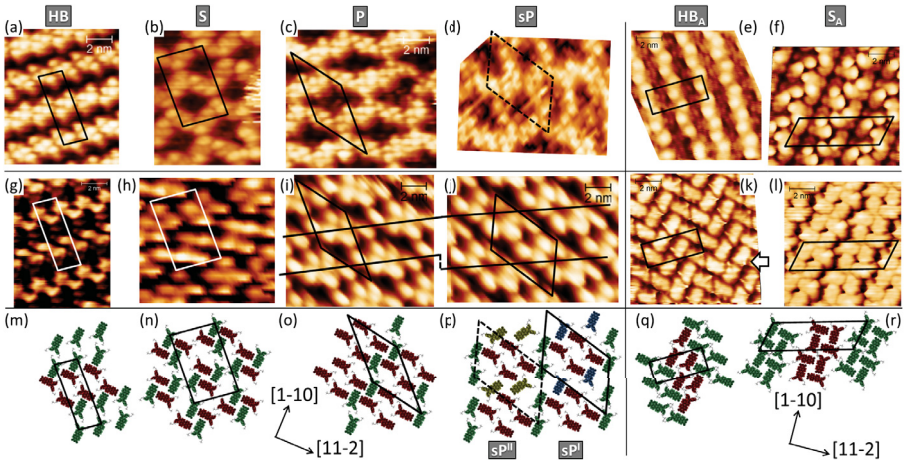

Figure 7.8: a) – f): Molecularly resolved images of HB, S, P, sP, HB_A, and S_A respectively, measured with tip conditions under which the perylene-derived cores appear lower than the side groups. g) – l): The same as a) – f), but with tip conditions under which the perylene-derived cores appear higher than the side groups. The lines in i) and j) indicate the split-lines in the P arrangement where extra molecules are inserted to arrive at sP. The arrow in k) points to a defect consisting of an enantiopure pair of the opposite type. m) – r): Models of the respective molecular arrangements. The vertical line divides pre- and post-annealing phases, for which the substrate orientation was slightly different as shown by the coordinate systems. [Imaging parameters: a) – c) and h): -1.5 V, 0.4 nA, d): -1.4 V, 0.4 nA, e): -1.8 V, 0.7 nA, f): -1.7 V, 0.8 nA, g): 1.5 V, 0.3 nA, i) and j): -1.5 V, 0.3 nA, k): 1.8 V, 0,7 nA, l): -0.85 V, 0.8 nA]

unit cells are listed in Tab. 7.1.

None of the appearances allows directly determining a possible tilt of the perylene-derived core. Such a tilt for as deposited-ID28 is however suggested by the following two facts. Firstly, gas phase-ID28 has a significantly three-dimensional conformation, with one phenyl group above and the other one below the perylene plane [181], which will not be significantly altered by the physisorption on Au(111). Secondly, the two side groups appear with approximately the same height in all images. These two conditions can only be fulfilled simultaneously if the perylene-derived core is tilted with respect to the gold surface. This implies that the horizontal projection of the perylene-derived core of as deposited-ID28/Au(111) is narrower in reality than in our models for the molecular arrangements for which flat-lying molecules are employed.

Due to its asymmetric chemical structure, ID28 exhibits two enantiomers when adsorbed on Au(111). Throughout this work, the green and red color each signifies one of them as defined in 1 e). The herringbone reconstruction of the Au(111) surface is not lifted by the adsorption of ID28 molecules, as clearly seen in Fig. 7.8 a), which readily allows simultaneously determining substrate and adsorbate orientations. This is done by employing simplified representations of the ID28 molecule, which are placed on full-appearance images. The results are illustrated in Fig. 7.8 e). The two ID28 pairs are not mirror symmetric with respect to any Au(111) high symmetry direction [11-2], which means that they do not have the same epitaxial registry. This can explain why they appear slightly differently in the STM images [176, 112, 156, 171]. Other possible reasons are differences in the adsorption geometry, or the mutual arrangement. Unfortunately, while the angle between the two different pairs can be determined with high precision, the appearance of the perylene-derived core does not allow precisely identifying the in-plane orientation of the individual molecules. Still, the pairs can be indirectly determined as enantiopure for the following reasons. Firstly, in a hypothetical racemic case, the two pairs would have two very different arrangements to match the observed patterns, while for enantiopure pairs each pair is simply one of the two mirror-symmetric arrangements of either enantiomer type. It is more likely that only one, namely the energetically most favorable arrangement prevails. Secondly, enantiopure pairs with identical mutual arrangements of the two molecules in each pair are indeed found unambiguously for the herringbone arrangement HB_A that emerges after annealing [cf. Fig. 7.8 q) and discussion below]. Thirdly, enantiopure pairs are conserved under a rotation by 180°, while racemic ones are not. Within one given STM image, equivalent pairs always look identical, showing no indications for pairs which differ by a rotation by 180°.[5]

All arrangements have an equivalent mirror-symmetric arrangement with respect to Au[11-2]. An asterisk is used to differentiate the two if both are present within one image, as can be seen in Fig. 7.8 a) and in detail for the example of P and P* in Figs. 7.7 c) and d), respectively. While HB is racemic, P is enantioenriched with a 1:2 ratio for the two enantiomers, notably in such a way that for P (P*) the red (green) pairs, rotated – (+) 30° with respect to the Au[11-2] orientation, are in the majority, meaning that this epitaxial registry

[5]STM images show small shifts for all pairs when comparing rotated and original image. However, since by and large the shifts have the same direction for both pairs, while the pairs themselves do not, these rather point to an asymmetric tip shape than to pairs rotated by 180° with respect to each other.

(for the enantiopure pair only or the complete unit cell) is more favorable than for the corresponding case with a higher fraction of pairs with + (-) 10° offset, which is only observed very rarely and without long-range order.

Rearrangements induced by the STM measurement

Fig. 7.9 a) shows a large scale area as it was first observed. The tunneling conditions give a side-groups-only appearance. HB and P structures, as well as areas without long-range order can be seen. Fig. 7.9 b) shows another scan of approximately the same area after seven intermediate scans. Note the change to a core-only appearance. Significant changes of the molecular structures can be seen, and are presented for selected areas also for some intermediate scans in Figs. 7.9 b) and c).

Notably, by scanning, a square phase (S; S-like for structures whose ordered grains do not extend for more than one unit cell) was created in some of the areas that were exhibiting an HB structure before.[6]. Importantly, the grains with the highest degree of long range order are S* rather than S, while they were initially also HB, and not HB*. Two formation paths are discussed in the following, that lead from an HB to an S or an S* arrangement, respectively. The successive scans presented in Fig. 7.9 c) (with increasing scan number from left to right) show some examples for an HB-to-S rearrangement, while the phase boundary shown in Fig. 7.9 d) allows directly comparing HB and S arrangement. Half of the enantiopure pairs are at the same position in both arrangements, indicating a rearrangement by a dislocation of the other half, as illustrated in the molecular models in the left and right part of Fig. 7.9 d): If, at every second position of the enantiomer-pure rows (dotted lines) in the HB arrangement, the shaded enantiopure pairs [which correspond to the shaded column in Fig. 7.8 b)] move along the dashed lines until the pairs of different enantiomer type roughly changed positions, one ends up with S. In contrast, to arrive from HB to S*, all molecules have to be rotated. This might be best achieved by the splitting of existing enantiopure pairs and the subsequent formation of new ones, as indicated by the lines in the top and bottom part of Fig. 7.9 e), which connect identical molecules before and after rotation, respectively.

Fig. 7.9 f) shows a similar rearrangement process (for another sample and with ca. opposite bias). Here, a well-ordered HB-domain is separated from an unresolved area by S-like structures. Interestingly, the domain boundary changes in both directions, meaning that S-like arrangements also transform back to HB-structures.

Ripening of monolayer phases

For the sub-monolayer film presented in Fig. 7.9 f), which was grown in a single deposition of a few minutes, exclusively phase HB is observed as long-range ordered. The extended S-like and P-like structures for the same film [Figs. 7.10 a) and b)], could be pristine structures, or due to the tip-induced rearrangement discussed above. In contrast, the film presented in Fig. 7.7,

[6] A tip-induced transformation of a herringbone to a square structure was also observed for PTCDA on Au(111) [ChizhovJChrystGrowth2000]. For this molecule, this is accomplished by providing more space through the removal of molecules, which, however seems not to be what happens in the present case and the unit cell size per molecule for HB and S are identical within the experimental resolution.

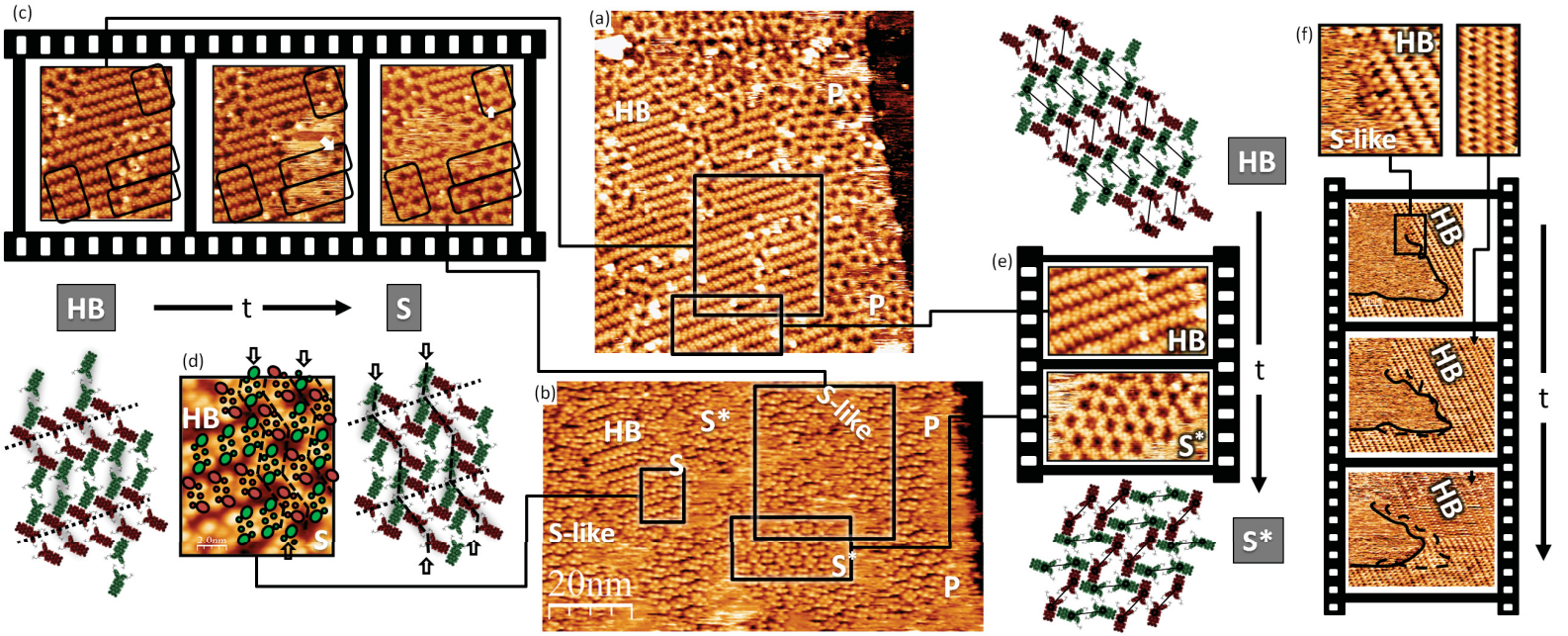

Figure 7.9: a): Large scale image (side-groups-only appearance). Different phases are indicated by the letters. b): Similar area as a) after 6 intermediate scans (core-only appearance). c) (from top to bottom): Cutout from a) and the fourth and fifth consecutive scan of the same area. Arrows point to selected locations where the enantiopure pair type changed compared to the preceding scan. d): Grain boundary between structures HB and S (side-groups-only appearance) overlaid with simple representations of ID28 molecules. The difference between HB and S is a displacement of the molecules at every second position along the herringbone, as emphasized by the arrows pointing at such positions. A model for the arrangement HB (S) with corresponding lines and arrows is shown on the left (right). e) (from top to bottom): Cutout from a) and the sixth consecutive scan of the same area. A model for the arrangement HB (S*) is shown on top (below). f): Three consecutive scans of a different film (core-only appearance). The dashed lines show the phase boundary of the respective previous scan. S-like structures are seen at the phase boundary between unresolved and resolved molecules. The insets shows close-ups of the phase boundary (left) and a defect line in the HB structure that allows identifying identical positions in the images (right). [Imaging parameters: a) – e): -1.5 V, 0.4 nA, f): 1.6 V, 0.8 nA; scans lasted 6-9 minutes]

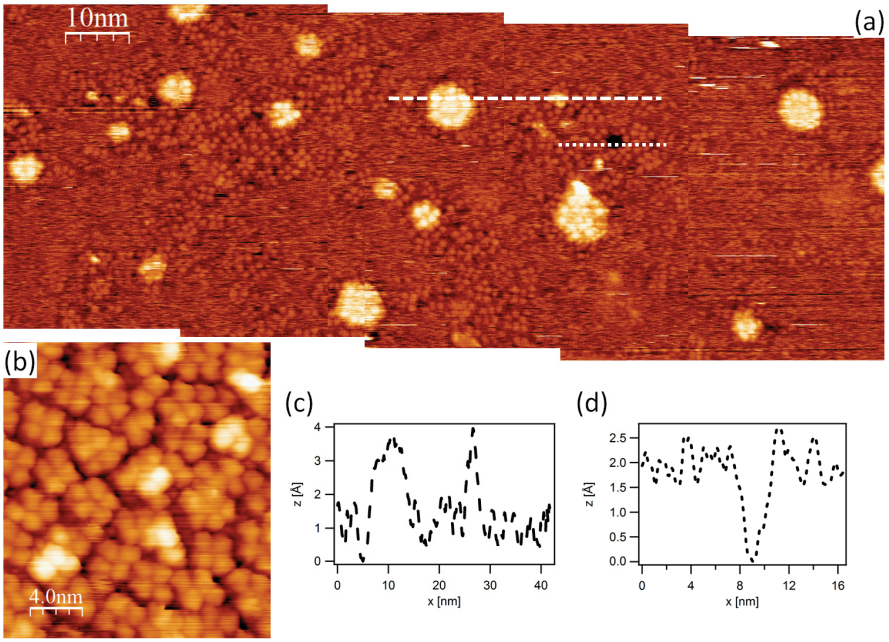

Figure 7.10: a): Molecularly resolved large scale image of an area without large-range order (= S-like). Protruding objects of the same size as the other molecules can be resolved and identified as molecules in the second layer. Several sizes of second-layer clusters can be seen. b): Zoom into a similar area as shown in a). c) and d): Line scan for the upper and lower line shown in a), respectively. [Imaging parameters: a): 1.8 V 0.8 nA, b): 1.9 V 0.8 nA]

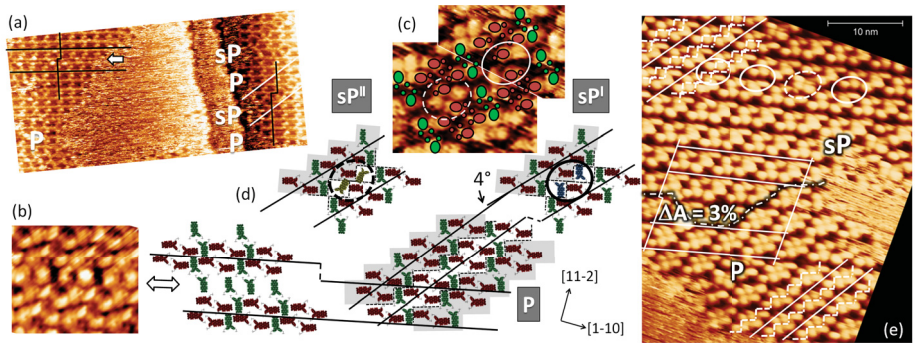

Figure 7.11: a): Large-scale image (with side-groups-only appearance) showing the two defect lines occasionally encountered for P structures. b) Detailed image (with core-only appearance) of a defect line as the one marked by the arrow in a). c): Two molecularly resolved images (with core-only appearance; merged at the white line) of a sP defect line, which illustrate that two of the molecules in each circled area are not paired. The circles correspond to the circles in d) and e). d): Models for all arrangements. e): Large scale image (with core-only appearance) showing a long-range ordered P and sP structure in the lower and upper part, respectively. The footprint of sP is deduced to be ca. 3 % larger than that of P. [Imaging parameters:, a): -1.8 V, 0.3 nA, b): -1.5 V, 0.4 nA, c): -0.85 V, 0.01 nA, e): -1.5 V, 0.3 nA].

which was deposited in a step-wise fashion over several hours, shows significant ripening of the P phase, while the HB phase is much less abundant. In the P structures, occasionally ordered defect lines were observed. One encountered case is marked with an arrow in Fig. 7.11 a) and the close up in Fig. 7.11 b). The other one, which is the focus of the following discussion, is labeled sP (for split P). It comes in two different arrangements (sP^{I} and sP^{II}), which are shown in detail in Fig. 7.11 c). This sP arrangement was also observed as long-range ordered phase, however only for a film for which the stepwise deposited molecules were residing longer on the surface before the final coverage was reached. Unfortunately, no image of sP with full-appearance tunneling conditions was obtained. Still it is possible to identify all enantiopure pairs by comparing with the data in Fig. 7.8, which in turn allows identifying two unpaired molecules per sP unit cell as shown in Fig. 7.11 c). Unpaired molecules are also evident by groups of two instead of four small features in the side-groups-only appearance shown in Fig. 7.8 d). The enantiomer-type of the unpaired molecules remains unclear[7], and the enantiomer ratio for sP has to be stated as in between 1:1 and 1:3. As shown in Fig. 7.11 e), sP has a ca. 3 % larger unit cell size per molecule than P. This film was the one with the longest ripening time in this study and did not show any traces of the HB phase. Instead, mostly phase P was observed. In addition, a long-ranger ordered S structure could be evidenced. Accordingly, ID28 very quickly forms the HB phase, while it takes about one day at low coverage and room temperature to allow most molecules

[7]Slightly differently oriented HB-arrangements in Fig. 7.12 a) and the reoriented pairs at the step edge in Fig. 7.7 d) evidence some adaptability of the ID28's epitaxial registry, which prevents identifying the enantiomer type by the orientation only.

to arrange in the P phase, which is when they only start forming phases sP and S. This sequence is sensible, given that the number of molecules per unit cell is 4, 6, and 8 for HB, P, and sP and S, respectively.

7.2.2 Annealing

Effect of mild annealing

Fig. 7.12 a) shows a large area scan of a sample for which slightly more than ML coverage was deposited in a single deposition. Just like for the single-deposition sub-monolayer film, HB is the only long-range ordered phase. A large number of grain boundaries and slightly different grain orientations are apparent. After mild annealing at ca. 200 °C, the sample exhibits a significantly increased long-range order with domains routinely extending over several 100 nm, as shown in Fig. 7.12 b). Defects are seen at certain locations that seem to be related with specific sites of the Au(111) herringbone reconstruction. In addition, extensive areas without long-range order are resolved. This annealing step goes along with the removal of multilayer molecules, as evident in the UPS spectra shown in Fig. 7.13 b): When comparing the bottommost (red) spectra and the middle (brown) ones, which correspond to the as deposited-film and the same film annealed at 200 °C, respectively, the HOMO-derived peak decreases in intensity and width, while the Au(111)-related features increase in intensity and the work function increases by 0.1 eV. This is exactly the reverse of what is observed when going beyond monolayer coverage for the deposition series discussed later on.

Molecular assembly and adsorption geometry after moderate annealing

After annealing at ca. 300 °C, none of the hitherto discussed structures prevail. Instead, the two new structures HB_A and S_A are found, as presented in Figs. 7.12 c) – f). Further details of these structures are presented in Figs. 7.8 and 7.14. Important differences exist between the pre- and post-annealing phases HB and S, and HB_A and S_A, respectively. HB and HB_A are both herringbone-like,

---

Figure 7.12 *(facing page)*: a): Large scale image (with core-only appearance) of a sample with more than monolayer coverage. b): Large scale image (with side-groups-only appearance) of the same sample after annealing at ca. 200 °C. The ordered domains now stretch over several hundred nm. Also disordered domains can be seen. c) – f): Large scale images (with core-only appearance) of the same sample after annealing at ca. 300 °C. In c), two different phases can be seen on either side of the step edge. The number of molecules in a fixed area is given for both phases. In d) and f), the Au(111) herringbone reconstruction can be clearly identified. In d) and e), the S_A-like structure is found to form in low-density regions within a HB_A domain, or in between two inequivalent HB_A domains (indicated by the staggered line), respectively. In f), a stacking defect (adjacent enantiopure rows consisting of the same enantiomer) is observed for the lower 3/4 of the image (marked with an arrow). [Imaging parameters: a): -1.5 V, 1.4 nA, b): -1.5 V, 0.9 nA, c) and f): -1.0 V, 0.8 nA, d): 1.8 V, 0.7 nA, e): 1.9 V, 0.7 nA]

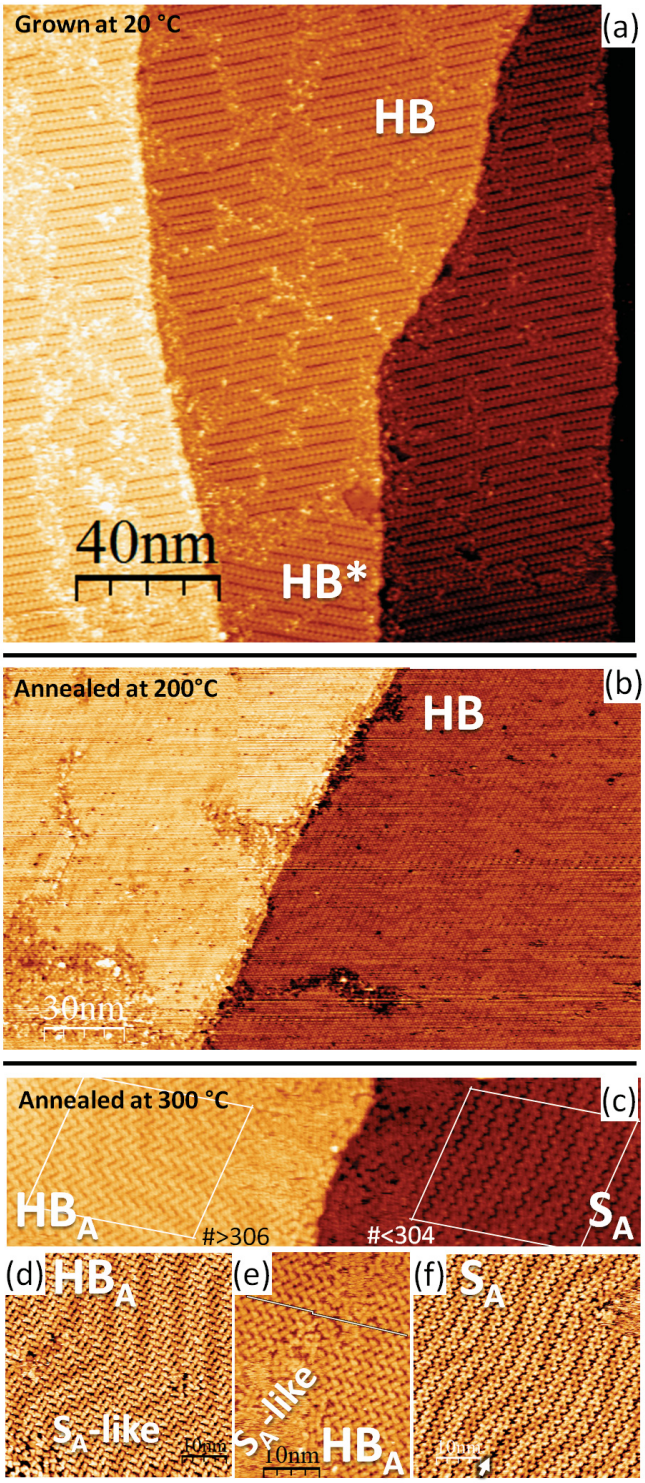
Grown at 20 °C
(a)
HB
40nm
HB*
Annealed at 200°C
(b)
HB
30nm
Annealed at 300 °C
(c)
HB$_A$
#>306
#<304
S$_A$
(d) HB$_A$
S$_A$-like
10nm
(e)
S$_A$-like
HB$_A$
10nm
(f) S$_A$
10nm

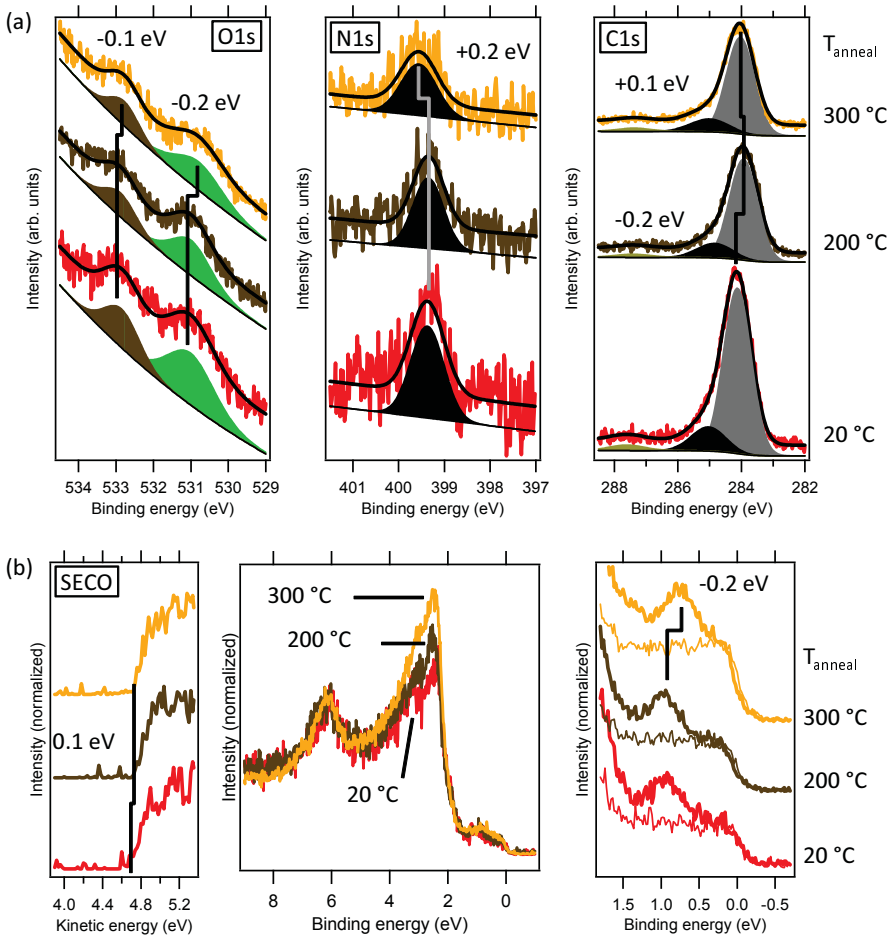

Figure 7.13: a): XPS results of an ID28/Au(111) film slightly beyond ML-coverage after annealing at the indicated temperatures (20 °C = as deposited). b): UPS results for the same films. From left to right the SECO, the valence band region, and zooms into the region close to E_F are shown. The presented valence band spectra were acquired with a take-off angle of 45°. For the zooms also normal-emission spectra are shown as thin lines.

but the distance between the two molecules in the enantiopure pairs is smaller for HB_A. Notably, as can be seen when comparing Figs. 7.8 a) and e), the tert-octylphenyl groups now accommodate a much smaller footprint, and instead of four corresponding features for a molecular pair, as in HB, only two are observed for one given tip condition for HB_A. A corresponding decrease from two bright features per molecule to only one is also found when comparing S_A [Fig. 7.8 f)] and S [Fig. 7.8 b)]. These observations evidence an annealing-induced change of the tert-octylphenyl groups. Another significant difference between S_A and S, is that the squares of four hydrogen-bonded perylene-derived cores are racemic in the case of S, while they are enantiopure for S_A. Notably, while one enantiopure S_A quartet is stabilized by hydrogen bonds, such a quartet is not linked to another quartet of either enantiomer-type by either the hydrogen bonds or enantiopure pairs which are the dominating patterns in all other arrangements. The distance between adjacent quartets of the same enantiomer-type is very low, which supports a changed conformation of annealed ID28. The distance between rows of different kinds of enantiomers, on the other hand, is comparably large. The unit cell per molecule of S_A is slightly larger than that of HB_A as illustrated in Fig. 7.12 c). Fig. 7.12 f) presents a S_A-like structure that formed in an area of lower areal density, thereby linking the two incompatible, because laterally offset, HB_A grains. HB_A and S_A resemble the herringbone and square phases that were observed for PTCDA on Au(111) [61, 194, 176, 209, 202]. There, too, the square phase (rather than the herringbone one) is found if space permits [61] and in between two herringbone structures to link shifted grains [61, 194, 202].

The XPS data shown in Fig. 7.13 shows that the oxygen and nitrogen atoms react differently to the annealing. While the oxygen O1s core level shifts to lower binding energy and therefore follows the trend of the HOMO shown in Fig. 7.13 b) and discussed below, the N1s peak shifts to higher binding energy. This corroborates the above reasoning that the amino-bound part of the molecules changes during the annealing process. Consistently, the shift of the C1s, which originates from all parts of the molecules, is in between those for O1s and N1s. No change of the atomic ratios could be observed within the experimental resolution, which is evidence for no detachment of, say, all tert-octyl groups. However, the measurements are not sensitive to more subtle changes in the atomic ratio.

Electronic structure of annealed-ID28

Fig. 7.13 b) presents the UPS results for the annealing series. Notably, the annealing at 300 °C does not change the width of the peak that correspond to electrons originating from the HOMO of ID28. It does however cause a shift of this HOMO-derived peak by 0.2 eV to lower binding energy, while the work function ϕ stays constant, as evident by the unchanged SECO, resulting in an ionization energy decrease from 5.3 eV to 5.1 eV. This can be explained by the conformation change, which was estimated by DFT to result in a binding energy decrease of ID28's HOMO[8], and might also influence the ionization energy of

[8] To simulate the altered conformation, the structure of ID28 was recalculated after placing two gold atoms underneath the nitrogen atom. The thus-found conformation was fixed, the gold atoms removed, and all energy levels recalculated. The calculated increase in total energy for such a change is low enough to be compensated by increased intermolecular and/or

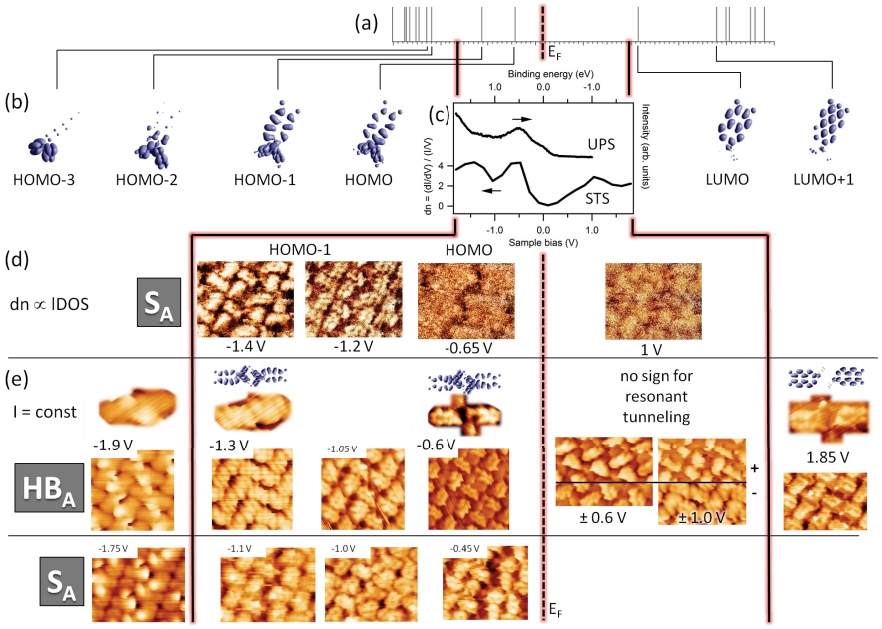

Figure 7.14: a): Energy eigenvalues for ID28 without tert-octyl groups as calculated by DFT, shifted by 0.3 eV to higher binding energies to better match the UPS data. b): The most relevant corresponding molecular orbitals. c): HeI-UPS spectrum (upper curve) and dn spectrum from STS (lower curve) for the same sample. d): dn-images at selected bias values (derived from the spacially resolved I-V data). The pattern at 1 V did not show sudden changes of contrast or intensity for different V. e): Constant current images of HB_A and S_A at indicated sample biases. The insets show close-ups of the molecular arrangement and (if appropriate) the corresponding calculated molecular orbitals. For the constant current images shown in between 0 and +1.8 V, the polarity was switched during the scans at the indicated positions. The orientation of the HB_A grain in the image for ± 0.6 V differs by that in the other ones by 60°. [Imaging parameters 0.7-0.8 nA].

the molecular layer via an altered molecular orientation [244, 125], or a better photo-hole screening facilitated by a closer contact between perylene core and metal surface [289]. A better screening is additionally expected due to the denser molecular packing [248, 96].

As mentioned above, frequent interactions between the tip and the molecular film of as deposited-ID28/Au(111), resulting in drastic changes of the tunneling conditions, prevented a systematic bias-dependent analysis of pre-annealing system. Still, the data allow deriving a trend as function of bias voltage: the core-only appearance is predominantly observed at low bias, while the side-groups-only images are observed for high bias, with a transition region around $1.4\,\mathrm{V} < |V| < 1.8\,\mathrm{V}$, for which, depending on the tip conditions, all appearances are observed. The tunneling junction was significantly more stable for annealed-ID28. This allowed studying the effect of varying the tunneling bias on the constant current images, as presented in Fig. 7.14 e). In addition, meaningful I-V-data could be obtained, which helps identifying electronic effects in the STM images. dn maps at different V, presented in Fig. 7.14 d) (for S_A only), were determined numerically from the acquired I-V data according to $\mathrm{d}n = (\mathrm{d}I/\mathrm{d}V)/(I/V)$, which gives the approximate local density of states (lDOS) (Sect. 3.2 [332]. Since no significant shape variations for dn spectra obtained at different locations were observed, a dn spectrum integrated over the whole area is shown in 8 c). Two clear maxima are seen at negative sample bias (= probing of occupied states), which go along with sudden changes of the dn maps and agree well with corresponding peaks in UPS and also the energies theoretically expected for HOMO and HOMO-1, respectively. In contrast, the minor peak at positive bias is not accompanied by a change in contrast or intensity in the dn maps. Let us now look at the constant current images for HB_A, which allow identifying the individual molecules better than those for S_A. For low bias, the perylene-derived core can clearly be identified. Additional features show up in the images, one in close proximity of the core, which stems from one of the phenyl rings, and one well separated from the core, which cannot be clearly identified and could stem from a side group of either of the two molecules in the enantiopure pair. While at positive bias the molecules do not appear with significant intensity variations, for negative polarity significant intramolecular contrast is found. This is clearly seen for the constant current images shown in between 0 and +1.8 V in Fig. 7.14 e), for which the polarity was switched during the scans at the indicated positions. The contrast for low negative bias closely resembles the HOMO lDOS expected from DFT. When approaching the bias corresponding to HOMO-1, the appearance changes markedly. Notably, the offset between the two molecules now seems to have increased, which agrees with the theoretical data that finds HOMO and HOMO-1 with higher lDOS at different sides of the perylene-core. For positive bias, sub-molecular features observed at 1.85 V can be attributed to the LUMO.

For negative bias exceeding -1.75 V, a feature becomes most prominent at a location in the STM images where there was no signal at low and medium bias. The most probable explanation for this observation is that this feature stems from the second tert-octylphenyl group, which, after the annealing, is now located at significantly larger height than the rest of the molecule. A position in the tunnel gap closer to the tip corresponds to a lower potential difference

molecule-surface interactions.

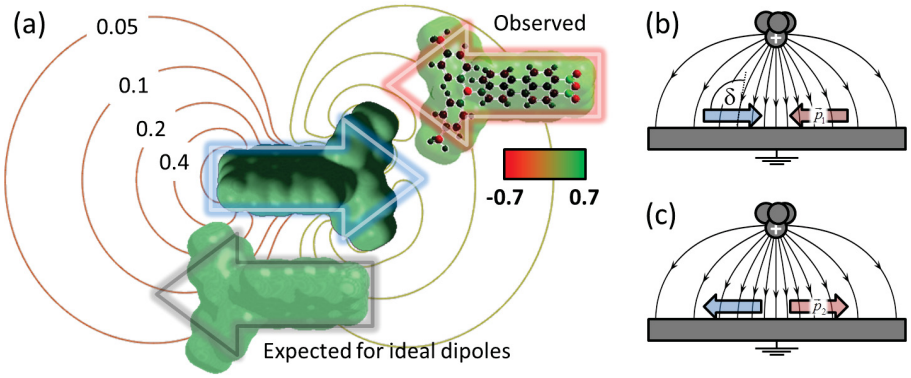

Figure 7.15: a): Central and upper part: Enantiopure pair as observed for as deposited-ID28/Au(111). Shown are the electrostatic potential for electrons (in eV) created by the left molecule, the Mulliken charges (in e) of the right molecule, and both built-in dipoles. Note that the tert-octyl groups are neglected. In the bottom part, the side-by-side antiparallel arrangement expected when taking into account only the dipole moment of ID28 is shown for comparison. b): The dipoles of an enantiopure pair seen from the side with the electric field created by a monoatomic STM tip for positive bias between tip and sample (= negatively biased sample). Horizontal dipoles are used in view of the unknown inclination of the molecules. c): The same as b), but with the orientation of the molecules rotated by 180°.

with respect to it, causing the resonant tunneling to contribute significantly only at higher bias [199, 260]. The observed change in contrast might be enhanced by the fact that at higher bias the tunneling process includes also HOMO-2 and HOMO-3, which are almost exclusively located on the phenyl-groups, and, in addition, states of the tert-octyl-groups. Notably, the emergence of a new feature at the same position was also observed for positive sample bias when approaching ca. +1.9 V. The molecular energy levels, on the other hand, are significantly asymmetric with respect to the Fermi level (E_F), as shown in Fig. 7.14 a). The observed symmetric behavior is expected in cases of absent interaction between adsorbate and substrate [62, 85], which is indeed to be expected for an assumed elevated position of this molecular feature.

7.2.3 Discussion of a possible influence of the intramolecular dipole on the molecular arrangement and rearrangement

Let us start with an energetic consideration. The ripening process leads to the formation of more complex phases, and thus decreases the system's entropy. This has to be driven by an energy gain for the observed arrangements. A small contribution might come from an increase in the strength of the hydrogen bonds when going from HB to the other phases [176, 311, 202]. Another reason could be a better match of the larger unit cells (and, in case of an enantioenriched phases, also the enriched enantiopure pair) on the one side, and the Au(111) surface and its herringbone reconstruction on the other side. Furthermore, the formation

of the racemic S phase is favored by the molecules' interaction with the STM tip, which is discussed in more detail below. That said, the complexity of the structures gives a first strong hint that the long-range dipole-dipole interaction has a significant influence in the formation process.

All observed arrangements result in in-plane anti-ferroelectric phases. While for simple systems (e.g. polar spheres) it is relatively straightforward to predict whether the ground state for a particular 2D lattice is ferroelectric or anti-ferroelectric [241, 86, 31, 88], for the current system this is prevented by the influence of higher-order multipole moments [158, 296], hydrogen bonds [182], the complex shape of the molecules, and large unit cells. What remains is to employ our experimental observations as reference for a theoretical assessment to come.

Next, outstanding characteristics of the arrangements will be discussed in detail. All ordered as deposited-phases consist exclusively of the enantiopure pairs presented in detail in Fig. 7.15 a), with the exception of the unpaired molecules in sP, which will be discussed in the next paragraph. The importance of a pair-wise arrangement with opposing side-groups is nicely illustrated by the side-groups-only appearance: The abundance of the pattern consisting of four bright spots arranged in a diamond-like shape [e.g. in Fig. 7.9 a)] evidences that the vast majority of molecules indeed arrange in this particular pair-wise fashion. Further support for its dominance in the molecular arrangements can be seen when comparing S and sP phases. The two additional molecules in sP leave all of the enantiopure pairs untouched and instead split the hydrogen bond-stabilized parallelogram [see Figs. 7.8 i) and j) and Fig. 7.11 d)]. This particular arrangement might be favored by (at least) three possible contributions: Firstly, intermolecular attraction mediated by tert-butyl-groups, as was recently shown for di(tert-butyl)terphenyl/Au(111) [264], secondly, a dense packing facilitated by the interdigitation of the tert-butyl-groups, similar to what was observed for hexa-tert-butylhexabenzocoronene/Cu(110) [251], and thirdly, the formation of an anti-ferroelectric phase, resulting from the anti-parallel arrangement. Notably, an enantiopure pair deviates significantly from the side-by-side antiparallel arrangement that would be expected when simply assuming two ideal dipoles with the electrostatic potential of ID28, which is also shown in Fig. 7.15 a) for comparison. The dipole-dipole interaction of the observed tail-to-tail arrangement will rather destabilize isolated dimers arranged in this fashion. Therefore, an additional stabilizing effect of an assumed anti-ferroelectric ground state on the particular pair-wise arrangement will arise only for an extended 2D structure.

The unpaired molecules in the sP phase are the only ones in all observed ordered as deposited-phases whose orientation is not fixed by the enantiopure pair-wise arrangement, and they do indeed adopt different orientations in sP^{I} and sP^{II}. Thus, they could, in principle, have an antiparallel mutual orientation in a hypothetical sP^{III} unit cell. However, all observed unit cells [some encircled in Fig. 7.11 e)] have exclusively antiparallel oriented molecules, notably with an arrangement that, compared to the enantiopure pairs, more matches the expected side-by-side arrangement of two dipoles. This gives a strong hint that their mutual orientation is indeed driven by a long-range dipole-dipole interaction.

Let us move on to the structures that emerged after annealing the ID28 film at 300 °C. As can be seen in Fig. 7.8, HB_A is essentially a more densely

packed HB-arrangement, with the long molecular axes of the two antiparallel molecules almost without lateral offset. Qualitatively, this structure equals the herringbone structure found for PTCDA if one treats one enantiopure pair of annealed-ID28 as one quasi-PTCDA molecule[9]. In contrast, the S_A structure does not contain any enantiopure pairs. Instead single molecules orient in a square-like fashion similar to what was observed for PTCDA. Notable, such a PTCDA-like square structure of unpaired annealed-ID28 molecules is anti-ferroelectric, in contrast to a hypothetical PTCDA-like herringbone structure of unpaired annealed-ID28 molecules, which would have all molecules of one particular orientation pointing in the same direction, and thus would be ferro-electric.

Lastly, it will be discussed how the large dipole moments of the ID28 molecules might influence their response to the STM measurement. Figs. 7.15 b) and c) show the electric field of a positively charged mono-atomic STM tip (= negative sample bias) together with two different dipole arrangements. The electric field has a finite anti-parallel (parallel) component in the direction of the molecular dipole $\vec{p_1}$ ($\vec{p_2}$). Therefore, when the tip is placed in between an enantiopure-pair [corresponding to Fig. 7.15 b)] it would be favorable for the pair to split, e.g., by rotating away from each other. The energy difference per molecule between the two situations shown in Figs. 7.17 c) and d) can be estimated[10] as

$$E = -\left(\vec{p_2}\cdot\vec{E} - \vec{p_1}\cdot\vec{E}\right) = 2\,\vec{p_1}\cdot\vec{E} = -2\mu|\vec{E}|\cos\delta \tag{7.1}$$

With a sample bias of $V = -1.5\,\mathrm{V}$, a tip-sample spacing of $d = 7\,\text{Å}$ [135], $\alpha = 99°$ [see definition in Fig. 7.15 b)], a dipole moment of $|\vec{p_1}| = \mu = 12$ debye, and if we assume $|\vec{E}| = V/d$ and thus neglect a small geometry-induced effect [112], we find $\Delta E = -167\,\mathrm{meV}$. This energy is sufficient to trigger structural transitions for weakly interacting systems [112]. Therefore, the HB-to-S* rearrangement shown in Fig. 7.9 e) could indeed be induced by a splitting of enantiopure pairs, which, together with a field induced torque, would allow the molecules to link to new partners. Analogously, a coalescence of the perylene cores under the tip apex with the side-groups facing outwards will be favorable for the same bias polarity, which could explain why the S and S-like phases, which realize this situation nicely, are created during the scan. As discussed above and shown in Fig. 7.9 f), a transfer from HB to S-like was also observed for positive sample bias. However, in this case no stable and long-range-ordered structures were observed. Instead, the HB phase was found to reassemble. At this point it is not clear if this latter process is a thermodynamic effect or induced by the tip.

7.2.4 Multilayer films (on top of as deposited-ID28)

Preferential out-of-plane alignment of multilayer molecules

Fig. 7.10 shows the STM images with the best resolution within this study that evidence the formation of a second molecular layer on top of as deposited-ID28.

[9] Consequently, the same reasoning as for PTCDA concerning the (net) quadrupole moment and hydrogen bonds apply to the super-structure.

[10] In view of the unknown adsorption geometry, a simple formula based on classical electrostatics and geometric considerations is used. This "back of the envelope" calculation should suffice to appraise the relevance of the energy contribution due to the intramolecular dipole.

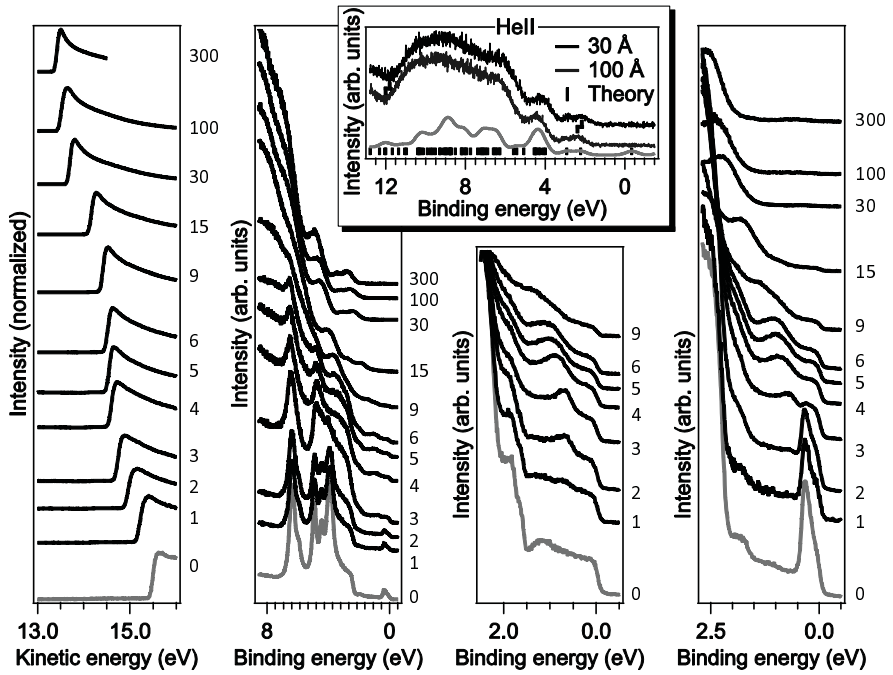

Figure 7.16: From left to right: SECO, valence band region for normal emission, and zooms into the region close to E_F for 45° take-off angle and normal emission for ID28 films of increasing thicknesses (in Å), all measured with HeI. Inset: Valence band of thick films measured with HeII. The Eigenvalues for the free molecule (without tert-octyl groups) are shown for comparison as lines and as broadened spectrum (Gaussian broadening with FWHM = 0.7 eV).

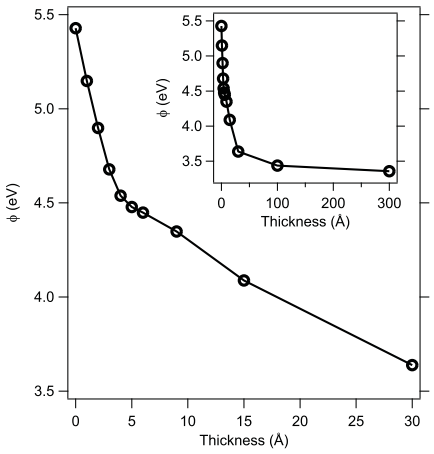

Figure 7.17: Film thickness-dependent evolution of the sample work function (ϕ).

The core-only appearance of the molecules in this layer is very similar to what is observed for the molecules in the first layer, and the apparent height of the second layer of 2.5 Å [found from the line scan in Fig. 7.10 c)] points to ca. lying molecules.

Fig. 7.16 presents the UPS results for a deposition series of ID28/Au(111). A sudden change of the ϕ vs. thickness slope in Fig. 7.17 clearly shows the completion of the first monolayer at 3 – 4 Å. Until this coverage ϕ decreases by 0.9 eV, which mostly stems from the push-back effect [320]. Fig. 7.16 shows that for a nominal coverage of 3 Å, the Au surface state is almost, and for 4 Å it is completely quenched (while it was still observed for 1.5 monolayers of PTCDA/Au(111) [209]). Much less HOMO-derived intensity is observed at normal emission than for an emission angle of 45°, while comparable intensity was observed for these two measurement geometries for standing ID28 molecules [316]. Such a difference stems from the selection rules in the photoelectronic process and, in turn, confirms the lying orientation of the molecules for monolayer films found from STM.

When increasing the coverage, ϕ continues to decrease linearly by roughly 0.1 eV per 3 Å (ca. 1 flat-lying ML) for the first 30 Å (and by another 0.2 eV until 300 Å). This effect can be attributed to a preferential vertical alignment of the multilayer molecules, as was observed before for vacuum-deposited Alq_3 and other polar molecules [144, 143, 293, 204, 315] (and for even more when deposited at low sample temperatures [13, 228, 229, 53]). To quantify the average inclination angle θ of the molecular dipoles, the areal density N of the multilayers are assumed to equal that of the first ML, i.e. $N = (2.5\,\mathrm{nm}^2)^{-1}$. The Helmholtz equation (6.1) can be adjusted to give the work function change $\Delta\phi$ as function of θ as

$$\Delta\phi(\theta) = \frac{qN\mu\cos\theta}{\epsilon_0\epsilon_\mathrm{r}}, \tag{7.2}$$

with the elementary charge q and the vacuum permittivity ϵ_0. For a relative permittivity of $\epsilon_r = 3$, we find θ to be ca. -10° (i.e. with the molecules having their dicarboxy anhydride side on average closer to the sample than the amino side). The increasingly similar shape of the HOMO-derived peaks in UPS for 45° take-off angle and normal emission for coverages beyond 3 Å (Fig. 7.16) indicates that the orientation of multilayer molecules deviates from that of the first layer. The continuous ϕ shift levels off beyond 30 Å and ϕ saturates at ca. 3.3 eV.

Reversible partly removal of surface potential by visible light irradiation

Beyond 30 Å, a shift of the energy levels measured by UPS could be induced by external visible light irradiation. As shown in Fig. 7.18 b) for a film thickness of 100 Å, the SECO shifts towards higher kinetic energies when the film is irradiated with visible light, with a magnitude that is a function of the light intensity. Figs. 7.18 a) and c) present the maximal obtained shifts of 0.3 and 0.4 eV for 100 and 300 Å, respectively. As can be seen in Fig. 7.18 d), corresponding shifts to lower binding energy are observed for the valence region. By placing different filters in the UV light beam, the SECO could be measured for the dark and illuminated situation with very different photon fluxes (ca. 100x), which did not result in notable changes of the SECO positions [shown by overlaid spectra

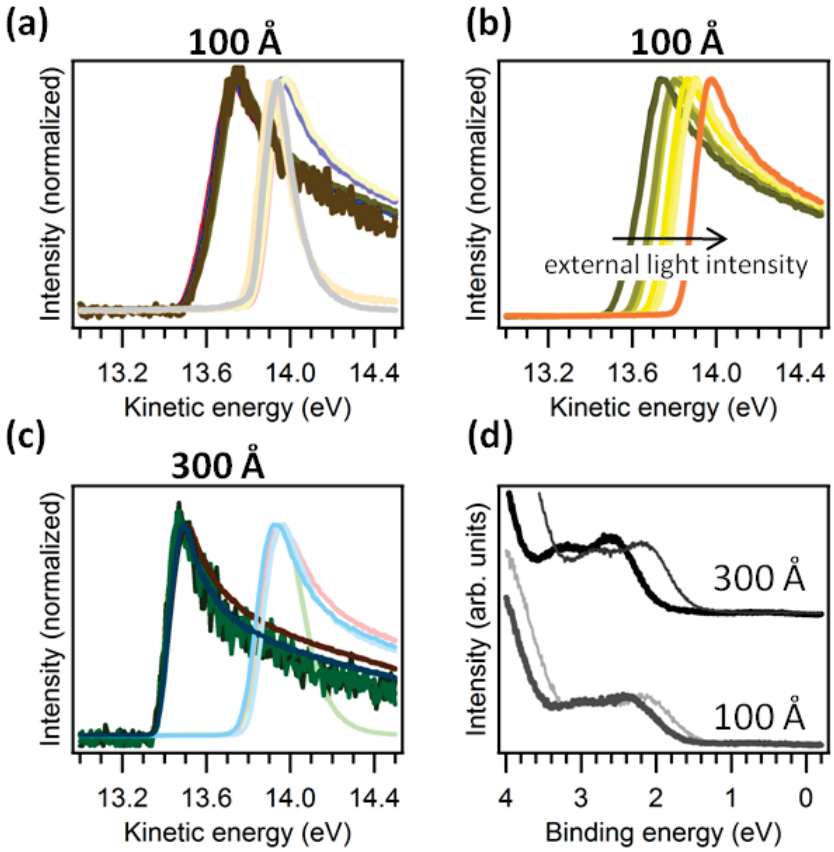

Figure 7.18: a): SECOs with and without external visible light for a film of 100 Å ID28/Au(111). Spectra for different UV-light filter thicknesses are overlaid to show that the SECO positions do not change as function of UV-light intensity. b): SECOs at various external light intensities for the same film. c): The same as a) but for a coverage of 300 Å. d): Valence region for two different nominal coverages with (thin line) and without (thick line) external light.

in Figs. 7.18 a) and c)]. This and the absence of peak broadening in the valence band spectra indicate that sample charging [159, 126] is not the reason for the observed phenomenon. An alternative explanation is that free electrons are generated by the visible light irradiation, which are then transported towards the sample surface by the potential gradient, where they partly compensate the field created by the permanent dipoles, similar to what is discussed for Alq_3 [221, 220, 219] and 5,7-dihydro-5,7-dioxo-6H-cyclopenta[b]pyridin-6-ylide (4N-PI) [294]. Different from these (Kelvin probe-based) results, the present measurements did not find a permanent removal of the giant surface potential. This might result from the (PES-inherent) photoelectric process that provides holes for the electrons to recombine with, or alternative might be due to the fact that the electrons are not immobilized in traps as discussed for those other cases. To decide between these two options, the present results should be compared with a technique that does not itself rely on charge flow such as the Kelvin probe method.

7.3 Conclusions

The two fluorine atoms in the partly fluorinated 6P derivatives form hydrogen bonds with adjacent molecules. This results in ribbon formation for both derivatives, consisting of side-by-side stacked molecules. Notably, the derivative with the larger dipole moment (meta-2F-6P) evidences a pronounced vertical offset for adjacent molecules along the ribbons, which is not observed for the other type (ortho-2F-6P). This clearly shows the influence of the built-in dipole μ on the molecular assembly and therefore reveals that μ is not fully screened by the metal for typical intermolecular distances of small molecules.

No asymmetry in the appearance of the 2F-6P molecules could be resolved by STM. This prevented the determination of the molecular orientation, and thus the dipole orientation in 2D dipolar networks that formed at higher local coverage. To prevent ambiguities, another polar molecule, namely the perylene-derivative ID28 was employed for studying the influence of the build-in dipole moment on the molecular assembly at higher coverage. By room temperature STM, as deposited-ID28 is found to adopt a flat-lying, probably slightly tilted orientation in the monolayer regime. Four ordered phases were identified, HB, P, sP, and S. The phases P, sP, and S are too much under kinetic control to emerge for a single deposition of several minutes, which can be rationalized by the larger number of molecules in their unit cells (6 for P and 8 for sP and S, compared to only 4 for HB). The molecules are found to form identical enantiopure pairs with opposing side-groups, with the exception of 25 % of the molecules in the low-density phase sP, which, nevertheless, also form anti-parallel pairs with each other. The STM tip can induce the rearrangement of the HB phase into the S and its mirror-symmetric S* phase, which, for the latter case, invokes a rotation of the molecules, and therefore also changes the preferred orientation of the whole ensemble. The re-formation of the HB phase is also demonstrated. Thus, this process, in principle, allows reversibly changing the anisotropy of a molecular film by the application of an electric field, and therefore has great technologic potential, e.g., in displays and data storage.

Upon annealing, a change of the ID28 adsorption geometry occurs, which allows the molecules to obtain a denser packing, and is accompanied by electronic changes. The thereby-formed HB_A and S_A phases exhibit apparent similarities to PTCDA's herringbone and square phase, respectively, the striking difference being the formation of a super-arrangement for HB_A, in which two annealed-ID28 molecules correspond to one PTCDA molecule. Notably, the S_A phase facilitates a microscopic separation of the two annealed-ID28 enantiomers into densely packed enantiopure rows with a comparably large inter-row spacing.

Strikingly, all observed monolayer phases give in-plane anti-ferroelectric arrangements of the molecules' permanent dipole moments. This is realized by enantiopure pairs for HB_A and the pre-annealing structures (except for the unpaired molecules in sP which form long-distance antiparallel pairs), while it is facilitated by enantiopure quartets in S_A. In contrast, a preferred out-of-plane orientation of the dipoles is clearly observed by ultraviolet photoelectron spectroscopy for multilayer films. A continuous work function decrease by more than 1 eV beyond the full monolayer is observed, which resembles the GSP observed for other dipolar molecules. The potential is partly removed only while the sample is illuminated with visible light. This reversible process demands further attention.

Our results form a solid foundation for further studies on the presented systems, for instance by DFT calculations, molecular dynamics simulations, and vacuum-Kelvin probe measurements.

Chapter 8

Conclusions and Outlook

The first part of this work was devoted to the mitigation of push-back related interface dipoles at organic/metal interfaces. This effect notoriously increases hole injection barriers for physisorbed molecules with respect to the expected energy-level alignment in the case of simple vacuum alignment. My project started off with a double-tracked approach that made use of two strategies that were already known from literature.

First, the fact that COMs with peripheral selenium groups chemisorb on coinage metals via selenium-metal bonds could be shown to counterbalance the push-back effect for the small molecule TSeT. Notably, TSeT is a *donor* molecule with IE $< 5\,\mathrm{eV}$, for which typically electron transfer from the COM to the metal is found [186, 39, 42], resulting in significant ϕ decreases [39, 42] and large HIBs [42]. The absence of this effect in the case of TSeT yields extremely small HIBs. Comparing the results for TSeT with those of chalcogenate SAMs on the same surfaces allows concluding that the presented observations are related to the fact that the TSeT-metal bonds via selenium are largely independent from TSeT's conjugated core. This is an important finding that can be exploited for the design of COMs acting as hole transport materials in organic electronics. TSeT itself, however, is found to exhibit pronounced 3D island growth at room temperature, which is unfavorable for the fabrication of devices with well-defined layer morphologies, as is often demanded in organic electronics.

Second, the strong acceptor molecule HATCN was employed to modify the Ag(111) surface acting as electrode to contact the prototypical charge transport materials α-NPD and Alq_3. Flat-lying HATCN molecules (found at very low HATCN coverages) counterbalance the push-back effect at the HATCN/Ag(111) interface. The remaining push-back effect observed upon overlayer formation is ascribed to Ag patches that are left uncovered by the porous molecular network of flat-lying HATCN molecules. For higher HATCN coverage, the HATCN molecules reorient into an edge-on orientation, which results in a ϕ increase by ca. $1\,\mathrm{eV}$ as compared to the unmodified silver. For the thus-created high ϕ electrode edge-on HATCN/Ag(111), both organic overlayers were found to exhibit HOMO-pinning, demonstrating that the respective ultimate lowest HIBs can be achieved by HATCN modification of Ag electrodes.

The above results identify Fermi-level pinning at organic/organic interfaces as crucial process in controlling the ELA in related devices. This raises the question of the underlying mechanisms. PES is not sensitive to unoccupied

molecular orbitals. Thus, in the above data, pinning-induced emptying of the HOMO could be inferred only by the ϕ decrease upon overlayer formation and small shifts of the α-NPD and Alq_3 HOMO-related features as function of overlayer coverage, while their unoccupied former-HOMO level remained invisible. Therefore, organic heterostructures exhibiting *LUMO-pinning* were selected for the fundamental study presented in the second part of my work.

For the first experiments to elucidate LUMO-pinning, simply the architecture of the aforementioned organic heterostructures were reversed. α-NPD proved unsuitable as interlayer due to inter-diffusion upon HATCN deposition [5]. In contrast, the system HATCN/Alq_3/Ag(111) was found to have the expected structure. For this system, equilibrium is found to be established via electron transfer to the HATCN LUMO. Notably, the metal substrate, and not the interlayer, is pinpointed as origin of the transferred electrons. Thus, metal to overlayer charge transfer (MOCT) is identified as the microscopic process that controls Fermi-level pinning in the case of organic/organic heterostructures on metal substrates. Furthermore, the ϕ change of 0.75 eV observed upon HATCN adsorption is attributed to the combination of two effects, the MOCT-dipoles and a reorientation of the polar Alq_3 molecules by the concomitant electric field.

To investigate further details of the MOCT-model, the C_{60}/6T/Ag(111) model system was selected. The rod-shaped and non-polar 6T grows layer-by-layer up to bilayer coverage on Ag(111) and, thus, provided an ultra-thin and tunable interlayer. C_{60}'s asymmetric shape allowed excluding orientation-induced changes of the energy levels. In addition, C_{60} exhibits pronounced HOMO-related features in the valence band region already for sub-monolayer coverages. From these it was possible to identify a one-to-one correlation between the ϕ increase and the C_{60} molecules that undergo a MOCT and become negatively charged. Notably, a significant fraction of the molecules in the first C_{60} overlayer remain neutral. With increasing coverage, this fraction increases, leading to a sub-linear increase of ϕ as a function of coverage. In addition, also an increase of the 6T interlayer thickness from monolayer to bilayer gives rise to an increased fraction of neutral C_{60} molecules. These results are in good agreement with theoretical predictions by other groups. Further tests of the MOCT-model, for both interlayer thicknesses, were possible by comparing the experimental MOCT-induced energy level shifts (derived from XPS for the 6T interlayer and UPS for the C_{60} overlayer) with the predictions of a simple electrostatic model that was developed by P. Amsalem in my group. Since C_{60} can be readily identified by STM measurements, it was also possible to investigate the effect of the MOCT-induced dipole-dipole repulsion on the molecular assembly in the first C_{60} overlayer. Lastly, the MOCT model was applied successfully to apprehend the energy level alignment recently reported for another organic heterostructure grown on a conductive polymer substrate. The comprehensive results presented in the current work strongly suggest that the microscopic details of charge transfer and concomitant electric field proposed by the MOCT-model are key prerequisites for understanding the energy level alignment at molecular and organic heterojunctions in contact with metals or conductive electrodes.

The MOCT-induced reorientation of Alq_3 mentioned above illustrates the importance of polar COMs for the ELA at related interfaces. The third part of this work was part of a multi-technique research effort on the effect of such polar COMs at COM/metal [174] and COM/oxide [317] interfaces undertaken

by my group. Details of the theoretical treatment of dipole-dipole interactions at such interfaces are still discussed controversial [90, 99], while predicting the influence of intramolecular dipoles on bulk phases is hampered by the complexity of intermolecular interactions. With LT-STM of low and medium coverage submonolayer films and RT-STM of films with thicknesses slightly below and above full monolayer coverage, contributions for both problem areas were obtained.

By employing two different 6P derivatives, which both have two hydrogen atoms of one terminal ring substituted by fluorine, the effect of hydrogen bonding and substrate-adsorbate interactions could be investigated independent of the dipole-dipole interaction. Both derivatives form hydrogen bond-mediated ribbons when adsorbed on Ag(111), which is an important finding in itself, since organic fluorine's potential to form hydrogen bonds had been challenged [81]. A preferred epitaxial registry can be found from the stacking along the ribbons. While the preceding characteristics are found for both derivatives, a significant vertical offset between adjacent molecules along the ribbons is found preferably for one derivative, and can consistently be ascribed to its larger dipole moment. More precisely, the vertical offset constitutes an observable that allows accessing the delicate balance of the various forces in this system, which should make the presented data suitable for testing theoretical models.

ID28, a perylene-derivative with highly asymmetric chemical structure, was employed for studying the influence of the intramolecular dipole moment on the molecular assembly at higher coverage. Four ordered phases, consisting of flat-lying molecules, were identified for ID28/Au(111). A clear trend towards an increase of unit cell complexity with ripening time was observed. The most-complex unit cells can be achieved by manipulation with the STM tip, as can a change of the averaged molecular orientation. Upon annealing at 300 °C, significant changes of the ID28 adsorption geometry and the molecular arrangements occur, which also affects the ELA at the ID28/Au(111) interface. All observed monolayer phases exhibit in-plane anti-ferroelectric arrangements of the intramolecular dipoles μ. For films up to 300 Å, however, the out-of plane component of μ does not follow this seemingly preferred anti-ferroelectric arrangements. Instead, the molecules are (on average) oriented with their amino side pointing upward. The potential induced by this preferential alignment is partly removed when the sample is illuminated with visible light and completely recovers afterward. The implications of these observations have yet to be explored in forthcoming studies.

Abbreviations

Abbreviation	Description
6P	Para-Sexiphenyl
6T	α-SexiThiophene
Alq_3	Aluminium-tris(8-hydroxychinolin)
α-NPD	N,N'-diphenyl-N,N'-bis(1-naphthyl)- -1,1'-biphenyl-4,4'-diamine
BE	Binding Energy
BESSY	Endstation SurICat at the synchrotron BESSY II
C_{60}	buckminsterfullerene
CL	Core Level
Chiba	Chiba University
CNL	Charge Neutrality Level
COM	Conjugated Organic Molecule
DFT	Density Functional Theory
DOS	Density Of States
EA	Electron Affinity
E_F	Fermi Energy
EIB	Electron Injection Barrier
ϕ	Work function
FWHM	Full Width at Half Maximum
HATCN	1,4,5,8,9,12-HexaAzaTriphenylenehexaCarboNitrile
HIB	Hole Injection Barrier
HOMO	Highest Occupied Molecular Orbital
HU	Humboldt University
ID28	9-(bis-p-tert-octylphenyl)-amino-perylene- -3,4-dicarboxy anhydride
ICT	Integer Charge Transfer
IE	Ionization Energy
lDOS	local Density Of States
LUMO	Lowest Unoccupied Molecular Orbital
ML	MonoLayer
MOCT	Metal-to-Overlayer Charge Transfer
MBE	Molecular Beam Epitaxy
OLED	Organic Light Emitting Diode
OU	Ohio University
PES	PhotoElectron Spectroscopy
PTCDA	3,4,9,10-Perylene-TetraCarboxylic-DiAnhydride
QCM	Quartz Crystal Microbalance

RT	Room Temperature
LT	Low Temperature
S	Screening parameter in the CNL model
SECO	Secondary Electron Cut-Off
STM	Scanning Tunneling Microscopy/Microscope
STS	Scanning Tunneling Spectroscopy
TSeT	TetraSeleno-Tetracene
TTT	tetrathio-tetracene
UHV	Ultra High Vacuum
UPS	Ultraviolet Photoelectron Spectroscopy
VB	Valence Band
VL	Vacuum Level
XPS	X-ray Photoelectron Spectroscopy

Bibliography

[1] Enrique Abad, José Ortega, and Fernando Flores. Metal/organic barrier formation for a C_{60}/Au interface: From the molecular to the monolayer limit. *Phys. Status Solidi A*, 209(4):636–646, 2012.

[2] Carlo Adamo and Vincenzo Barone. Toward reliable density functional methods without adjustable parameters: The PBE0 model. *J. Chem. Phys.*, 110(13):6158–6170, 1999.

[3] Dana M. Alloway, Michael Hofmann, Darrin L. Smith, Nadine E. Gruhn, Amy L. Graham, Ramon Colorado, Vicki H. Wysocki, T. Randall Lee, Paul A. Lee, and Neal R. Armstrong. Interface dipoles arising from self-assembled monolayers on gold: Photoemission studies of alkanethiols and partially fluorinated alkanethiols. *J. Phys. Chem. B*, 107(42):11690–11699, 2003.

[4] P. Amsalem, J. Niederhausen, A. Wilke, G. Heimel, R. Schlesinger, S. Winkler, A. Vollmer, J. P. Rabe, and N. Koch. Role of charge transfer, dipole-dipole interactions, and electrostatics in Fermi-level pinning at a molecular heterojunction on a metal surface. *Phys. Rev. B*, 87:035440, 2013.

[5] P. Amsalem, A. Wilke, J. Frisch, J. Niederhausen, A. Vollmer, R. Rieger, K. Müllen, J. P. Rabe, and N. Koch. Interlayer molecular diffusion and thermodynamic equilibrium in organic heterostructures on a metal electrode. *J. Appl. Phys.*, 110(11):113709, 2011.

[6] Patrick Amsalem, Jens Niederhausen, Johannes Frisch, Andreas Wilke, Benjamin Bröker, Antje Vollmer, Ralph Rieger, Klaus Müllen, Jürgen P. Rabe, and Norbert Koch. Metal-to-acceptor charge transfer through a molecular spacer layer. *J. Phys. Chem. C*, 115(35):17503–17507, 2011.

[7] J. Anderson and G.J. Lapeyre. Chemisorption-induced surface umklapp processes in angle-resolved synchrotron photoemission from W(001). *Phys. Rev. Lett.*, 36(7):376–379, 1976.

[8] R.L. Anderson. Experiments on Ge-GaAs heterojunctions. *Solid-State Electron.*, 5(5):341–351, 1962.

[9] Neal R. Armstrong, Weining Wang, Dana M. Alloway, Diogenes Placencia, Erin Ratcliff, and Michael Brumbach. Organic/organic' heterojunctions: Organic light emitting diodes and organic photovoltaic devices. *Macromol. Rapid Commun.*, 30(9–10):717–731, 2009.

[10] Emmanuel Arras, Ari Paavo Seitsonen, Florian Klappenberger, and Johannes V. Barth. Nature of the attractive interaction between proton acceptors and organic ring systems. *Phys. Chem. Chem. Phys.*, 14:15995–16001, 2012.

[11] Yuri Avlasevich, Chen Li, and Klaus Mullen. Synthesis and applications of core-enlarged perylene dyes. *J. Mater. Chem.*, 20:3814–3826, 2010.

[12] Paul S. Bagus, Klaus Hermann, and Christof Wöll. The interaction of C_6H_6 and C_6H_{12} with noble metal surfaces: Electronic level alignment and the origin of the interface dipole. *J. Chem. Phys.*, 123(18):184109, 2005.

[13] Richard Balog, P. Cicman, N. C. Jones, and D. Field. Spontaneous dipole alignment in films of N_2O. *Phys. Rev. Lett.*, 102:073003, 2009.

[14] J. Bardeen. Tunnelling from a many-particle point of view. *Phys. Rev. Lett.*, 6:57–59, 1961.

[15] John Bardeen. Surface states and rectification at a metal semi-conductor contact. *Phys. Rev.*, 71:717–727, 1947.

[16] L. Bartels, G. Meyer, and K.-H. Rieder. Controlled vertical manipulation of single CO molecules with the scanning tunneling microscope: A route to chemical contrast. *Appl. Phys. Lett.*, 71(2):213–215, 1997.

[17] J. V. Barth, H. Brune, G. Ertl, and R. J. Behm. Scanning tunneling microscopy observations on the reconstructed Au(111) surface: Atomic structure, long-range superstructure, rotational domains, and surface defects. *Phys. Rev. B*, 42:9307–9318, 1990.

[18] Asif Bashir, Daniel Käfer, Jan Müller, Christof Wöll, Andreas Terfort, and Gregor Witte. Selenium as a key element for highly ordered aromatic self-assembled monolayers. *Angew. Chem. Int. Ed.*, 47(28):5250–5252, 2008.

[19] Axel D. Becke. Perspective: Fifty years of density-functional theory in chemical physics. *The Journal of Chemical Physics*, 140(18):18A301, 2014.

[20] P.J. Benning, F. Stepniak, D.M. Poirier, J.L. Martins, J.H. Weaver, L.P.F. Chibante, and R.E. Smalley. Electronic properties of K-doped C_{60}(111): Photoemission and electron correlation. *Phys. Rev. B*, 47(20):13843–13847, 1993.

[21] K. Besocke. An easily operable scanning tunneling microscope. *Surf. Sci.*, 181(1–2):145–153, 1987.

[22] M. G. Betti, A. Kanjilal, C. Mariani, H. Vázquez, Y. J. Dappe, J. Ortega, and F. Flores. Barrier formation at organic interfaces in a Cu(100)-benzenethiolate-pentacene heterostructure. *Phys. Rev. Lett.*, 100:027601, 2008.

[23] G. Binnig and H. Rohrer. Scanning tunneling microscopy. *Surf. Sci.*, 126(1–3):236–244, 1983.

[24] G. Binnig, H. Rohrer, Ch. Gerber, and E. Weibel. Surface studies by scanning tunneling microscopy. *Phys. Rev. Lett.*, 49:57–61, 1982.

[25] G. Binnig, H. Rohrer, Ch. Gerber, and E. Weibel. Tunneling through a controllable vacuum gap. *Appl. Phys. Lett.*, 40(2):178–180, 1982.

[26] G. Binnig, H. Rohrer, Ch. Gerber, and E. Weibel. (111) facets as the origin of reconstructed Au(110) surfaces. *Surf. Sci. Lett.*, 131(1):L379–L384, 1983.

[27] G. Binnig, H. Rohrer, Ch. Gerber, and E. Weibel. 7×7 reconstruction on Si(111) resolved in real space. *Phys. Rev. Lett.*, 50:120–123, 1983.

[28] F.C. Bocquet, L. Giovanelli, P. Amsalem, L. Petaccia, D. Topwal, S. Gorovikov, M. Abel, N. Koch, L. Porte, A. Goldoni, and J.-M. Themlin. Final-state diffraction effects in angle-resolved photoemission at an organic-metal interface. *Phys. Rev. B*, 84(24), 2011.

[29] Menno Bokdam, Deniz Çakir, and Geert Brocks. Fermi level pinning by integer charge transfer at electrode-organic semiconductor interfaces. *Appl. Phys. Lett.*, 98(11):113303, 2011.

[30] G. Borstel. Theoretical aspects of photoemission. *Appl. Phys. A*, 38(3):193–204, 1985.

[31] J.G. Brankov and D.M. Danchev. Ground state of an infinite two-dimensional system of dipoles on a lattice with arbitrary rhombicity angle. *Physica A*, 144(1):128–139, 1987.

[32] Kai-Felix Braun and Saw-Wai Hla. Probing the conformation of physisorbed molecules at the atomic scale using STM manipulation. *Nano Lett.*, 5(1):73–76, 2005.

[33] S. Braun, X. Liu, W.R. Salaneck, and M. Fahlman. Fermi level equilibrium at donor-acceptor interfaces in multi-layered thin film stack of TTF and TCNQ. *Org. Electron.*, 11(2):212–217, 2010.

[34] Slawomir Braun, Michel P. de Jong, Wojciech Osikowicz, and William R. Salaneck. Influence of the electrode work function on the energy level alignment at organic-organic interfaces. *Appl. Phys. Lett.*, 91(20):202108, 2007.

[35] Slawomir Braun, Wojciech Osikowicz, Ying Wang, and William R. Salaneck. Energy level alignment regimes at hybrid organic-organic and inorganic-organic interfaces. *Org. Electron.*, 8(1):14–20, 2007.

[36] Slawomir Braun, William R. Salaneck, and Mats Fahlman. Energy-level alignment at organic/metal and organic/organic interfaces. *Adv. Mater.*, 21(14–15):1450–1472, 2009.

[37] J. L. Brédas, G. B. Street, B. Themans, and J. M. Andre. Organic polymers based on aromatic rings (polyparaphenylene, polypyrrole, polythiophene): Evolution of the electronic properties as a function of the torsion angle between adjacent rings. *J. Chem. Phys.*, 83(3):1323, 1985.

[38] Jean-Luc Brédas, David Beljonne, Veaceslav Coropceanu, and Jérôme Cornil. Charge-transfer and energy-transfer processes in π-conjugated oligomers and polymers: A molecular picture. *Chem. Rev.*, 104(11):4971–5004, 2004.

[39] B. Bröker, R. P Blum, J. Frisch, A. Vollmer, O. T. Hofmann, R. Rieger, K. Müllen, J. P. Rabe, E. Zojer, and N. Koch. Gold work function reduction by 2.2 eV with an air-stable molecular donor layer. *Appl. Phys. Lett.*, 93(24):243303, 2008.

[40] B. Bröker, O. T. Hofmann, G. M. Rangger, P. Frank, R. P. Blum, R. Rieger, L. Venema, A. Vollmer, K. Müllen, J. P. Rabe, A. Winkler, P. Rudolf, E. Zojer, and N. Koch. Density-dependent reorientation and rehybridization of chemisorbed conjugated molecules for controlling interface electronic structure. *Phys. Rev. Lett.*, 104(24):246805, 2010.

[41] Benjamin Bröker. *Electronic and structural properties of interfaces between electron donor/acceptor molecules and conductive electrodes*. PhD thesis, HU Berlin, 2010. http://edoc.hu-berlin.de/dissertationen/broeker-benjamin-2010-10-25/PDF/broeker.pdf.

[42] Benjamin Bröker, Ralf-Peter Blum, Luca Beverina, Oliver T. Hofmann, Mauro Sassi, Riccardo Ruffo, Giorgio A. Pagani, Georg Heimel, Antje Vollmer, Johannes Frisch, Jürgen P. Rabe, Egbert Zojer, and Norbert Koch. A high molecular weight donor for electron injection interlayers on metal electrodes. *ChemPhysChem*, 10(17):2947–2954, 2009.

[43] W. Brütting, editor. *Physics of Organic Semiconductors*. Wiley-VCH, Weinheim, 2005.

[44] H. Bulou and C. Goyhenex. Local strain analysis of the herringbone reconstruction of Au(111) through atomistic simulations. *Phys. Rev. B*, 65:045407, 2002.

[45] Kieron Burke. Perspective on density functional theory. *The Journal of Chemical Physics*, 136(15):150901, 2012.

[46] C. Bürker, N. Ferri, A. Tkatchenko, A. Gerlach, J. Niederhausen, T. Hosokai, S. Duhm, J. Zegenhagen, N. Koch, and F. Schreiber. Exploring the bonding of large hydrocarbons on noble metals: Diindoperylene on Cu(111), Ag(111), and Au(111). *Phys. Rev. B*, 87:165443, 2013.

[47] F. Bussolotti, S. W. Han, Y. Honda, and R. Friedlein. Phase-dependent electronic properties of monolayer and multilayer anthracene films on graphite [0001] surfaces. *Phys. Rev. B*, 79:245410, 2009.

[48] Fabio Bussolotti, Satoshi Kera, Kazuhiro Kudo, Antoine Kahn, and Nobuo Ueno. Gap states in pentacene thin film induced by inert gas exposure. *Phys. Rev. Lett.*, 110:267602, 2013.

[49] Fabio Bussolotti, Jinpeng Yang, Alexander Hinderhofer, Yuli Huang, Wei Chen, Satoshi Kera, Andrew T. S. Wee, and Nobuo Ueno. Origin of the energy level alignment at organic/organic interfaces: The role of structural defects. *Phys. Rev. B*, 89:115319, 2014.

[50] Lei Cai, Hongwei Qu, Chenxi Lu, S. Ducharme, P. A. Dowben, and Jiandi Zhang. Surface structure of ultrathin copolymer films of ferroelectric vinylidene fluoride (70%) with trifluoroethylene (30%) on graphite. *Phys. Rev. B*, 70:155411, 2004.

[51] Nadia Camaioni and Riccardo Po. Pushing the envelope of the intrinsic limitation of organic solar cells. *J. Phys. Chem. Lett.*, 4(11):1821–1828, 2013.

[52] Ute B. Cappel, Stefan Plogmaker, Erik M. J. Johansson, Anders Hagfeldt, Gerrit Boschloo, and Hakan Rensmo. Energy alignment and surface dipoles of rylene dyes adsorbed to TiO_2 nanoparticles. *Phys. Chem. Chem. Phys.*, 13:14767–14774, 2011.

[53] Andrew Cassidy, Oksana Plekan, Richard Balog, Nykola C. Jones, and David Field. Spontaneous electric fields in films of CF_3Cl, CF_2Cl_2 and $CFCl_3$. *Phys. Chem. Chem. Phys.*, 15:108–113, 2013.

[54] L. Chen, W. Chen, H. Huang, H. L. Zhang, J. Yuhara, and A. S. Wee. Tunable arrays of C_{60} molecular chains. *Adv. Mater.*, 20(3):484–488, 2008.

[55] Lan Chen, Hui Li, and Andrew Thye Shen Wee. One-dimensional molecular chains with dispersive electronic states. *Nano Lett.*, 9(12):4292–4296, 2009.

[56] Wei Chen, Han Huang, Shi Chen, Lan Chen, Hong Liang Zhang, Xing Yu Gao, and Andrew Thye Shen Wee. Molecular orientation of 3,4,9,10-perylene-tetracarboxylic-dianhydride thin films at organic heterojunction interfaces. *Appl. Phys. Lett.*, 91(11):114102, 2007.

[57] Wei Chen, Han Huang, Shi Chen, Yu Li Huang, Xing Yu Gao, and Andrew Thye Shen Wee. Molecular orientation-dependent ionization potential of organic thin films. *Chem. Mater.*, 20(22):7017–7021, 2008.

[58] Wei Chen, Hong Liang Zhang, Han Huang, Lan Chen, and Andrew Thye Shen Wee. Self-assembled organic donor/acceptor nanojunction arrays. *Appl. Phys. Lett.*, 92(19):193301, 2008.

[59] Yen C. Chen, J. E. Cunningham, and C. P. Flynn. Dependence of rare-gas-adsorbate dipole moment on substrate work function. *Phys. Rev. B*, 30:7317–7319, 1984.

[60] Zhihai Cheng, Shixuan Du, Wei Guo, Li Gao, Zhitao Deng, Nan Jiang, Haiming Guo, Hao Tang, and H.-J. Gao. Direct imaging of molecular orbitals of metal phthalocyanines on metal surfaces with an O_2-functionalized tip of a scanning tunneling microscope. *Nano Res.*, 4(6):523–530, 2011.

[61] I Chizhov, A Kahn, and G Scoles. Initial growth of 3,4,9,10-perylenetetracarboxylic-dianhydride (PTCDA) on Au(111): a scanning tunneling microscopy study. *J. Cryst. Growth*, 208(1–4):449–458, 2000.

[62] Christopher L. Claypool, Francesco Faglioni, William A. Goddard, Harry B. Gray, Nathan S. Lewis, and R. A. Marcus. Source of image contrast in STM images of functionalized alkanes on graphite: A systematic functional group approach. *J. Phys. Chem. B*, 101(31):5978–5995, 1997.

[63] F. P. Cometto, E. M. Patrito, P. Paredes Olivera, G. Zampieri, and H. Ascolani. Electrochemical, high-resolution photoemission spectroscopy and vdW-DFT study of the thermal stability of benzenethiol and benzeneselenol monolayers on Au(111). *Langmuir*, 28(38):13624–13635, 2012.

[64] Xavier Crispin, Victor Geskin, Annica Crispin, Jérôme Cornil, Roberto Lazzaroni, William R. Salaneck, and Jean-Luc Brédas. Characterization of the interface dipole at organic/ metal interfaces. *JACS*, 124(27):8131–8141, 2002.

[65] Anna Cristadoro, Min Ai, Hans Joachim Räder, Jürgen P. Rabe, and Klaus Müllen. Electrical field-induced alignment of nonpolar hexabenzocoronene molecules into columnar structures on highly oriented pyrolitic graphite investigated by STM and SFM. *J. Phys. Chem. C*, 112(14):5563–5566, 2008.

[66] Alessandro Curioni, Mauro Boero, and Wanda Andreoni. Alq_3: ab initio calculations of its structural and electronic properties in neutral and charged states. *Chem. Phys. Lett.*, 294(4–5):263–271, 1998.

[67] Gabriele D'Avino, Sébastien Mothy, Luca Muccioli, Claudio Zannoni, Linjun Wang, Jérôme Cornil, David Beljonne, and Frédéric Castet. Energetics of electron-hole separation at P3HT/PCBM heterojunctions. *J. Phys. Chem. C*, 117(25):12981–12990, 2013.

[68] Dimas G. de Oteyza, Esther Barrena, Miguel Ruiz-Oses, Inaki Silanes, Bryan P. Doyle, J. Enrique Ortega, Andres Arnau, Helmut Dosch, and Yutaka Wakayama. Crystallographic and electronic structure of self-assembled DIP monolayers on Au(111) substrates. *J. Phys. Chem. C*, 112(18):7168–7172, 2008.

[69] P. Delhaes, C. Coulon, S. Flandrois, B. Hilti, C. W. Mayer, G. Rihs, and J. Rivory. Investigations on a new series of organic conductors – the tetraselenotetracene iodines (TSeT-IX). *J. Chem. Phys.*, 73(3):1452–1463, 1980.

[70] Z. T. Deng, H. Lin, W. Ji, L. Gao, X. Lin, Z. H. Cheng, X. B. He, J. L. Lu, D. X. Shi, W. A. Hofer, and H.-J. Gao. Selective analysis of molecular states by functionalized scanning tunneling microscopy tips. *Phys. Rev. Lett.*, 96:156102, 2006.

[71] Peter I. Djurovich, Elizabeth I. Mayo, Stephen R. Forrest, and Mark E. Thompson. Measurement of the lowest unoccupied molecular orbital energies of molecular organic semiconductors. *Org. Electron.*, 10(3):515–520, 2009.

[72] Carlo Dri, Maike V. Peters, Jutta Schwarz, Stefan Hecht, and Leonhard Grill. Spatial periodicity in molecular switching. *Nat. Nanotech.*, 3(11):649–653, 2008.

[73] S. Duhm, A. Gerlach, I. Salzmann, B. Bröker, R. L. Johnson, F. Schreiber, and N. Koch. PTCDA on Au(111), Ag(111) and Cu(111): Correlation of interface charge transfer to bonding distance. *Org. Electron.*, 9(1):111–118, 2008.

[74] Steffen Duhm, Christoph Bürker, Jens Niederhausen, Ingo Salzmann, Takuya Hosokai, Julien Duvernay, Satoshi Kera, Frank Schreiber, Norbert Koch, Nobuo Ueno, and Alexander Gerlach. Pentacene on Ag(111): Correlation of bonding distance with intermolecular interaction and order. *ACS Appl. Mater. Interfaces*, 5(19):9377–9381, 2013.

[75] Steffen Duhm, Hendrik Glowatzki, Valentin Cimpeanu, Jürgen Klankermayer, Jürgen P. Rabe, Robert L. Johnson, and Norbert Koch. Weak charge transfer between an acceptor molecule and metal surfaces enabling organic/metal energy level tuning. *J. Phys. Chem. B*, 110(42):21069–21072, 2006.

[76] Steffen Duhm, Georg Heimel, Ingo Salzmann, Hendrik Glowatzki, Robert L. Johnson, Antje Vollmer, Jürgen P. Rabe, and Norbert Koch. Orientation-dependent ionization energies and interface dipoles in ordered molecular assemblies. *Nat. Mater.*, 7(4):326–332, 2008.

[77] Steffen Duhm, Ingo Salzmann, Benjamin Bröker, Hendrik Glowatzki, Robert L. Johnson, and Norbert Koch. Interdiffusion of molecular acceptors through organic layers to metal substrates mimics doping-related energy level shifts. *Appl. Phys. Lett.*, 95(9):093305, 2009.

[78] Steffen Duhm, Qian Xin, Shunsuke Hosoumi, Hirohiko Fukagawa, Kazushi Sato, Nobuo Ueno, and Satoshi Kera. Charge reorganization energy and small polaron binding energy of rubrene thin films by ultraviolet photoelectron spectroscopy. *Adv. Mater.*, 24(7):901–905, 2012.

[79] Steffen Duhm, Qian Xin, Norbert Koch, Nobuo Ueno, and Satoshi Kera. Impact of alkyl side chains at self-assembly, electronic structure and charge arrangement in sexithiophene thin films. *Org. Electron.*, 12(6):903–910, 2011.

[80] Jack D. Dunitz and Angelo Gavezzotti. Attractions and repulsions in molecular crystals: What can be learned from the crystal structures of condensed ring aromatic hydrocarbons? *Acc. Chem. Res.*, 32(8):677–684, 1999.

[81] Jack D. Dunitz and Robin Taylor. Organic fluorine hardly ever accepts hydrogen bonds. *Chem. Eur. J.*, 3(1):89–98, 1997.

[82] David A. Egger, Victor G. Ruiz, Wissam A. Saidi, Tomas Bucko, Alexandre Tkatchenko, and Egbert Zojer. Understanding structure and bonding of multilayered metal-organic nanostructures. *J. Phys. Chem. C*, 117(6):3055–3061, 2013.

[83] Stefan Eilers. *Strukturelle und Elektronische Eigenschaften von Nanographen-Graphen-Systemen sowie Schnitt- und Faltverhalten von Graphen.* PhD thesis, HU Berlin, 2013. http://edoc.hu-berlin.de/dissertationen/eilers-stefan-2013-04-05/PDF/eilers.pdf.

[84] M. Eremtchenko, J. A. Schaefer, and F. S. Tautz. Understanding and tuning the epitaxy of large aromatic adsorbates by molecular design. *Nature*, 425(6958):602–605, 2003.

[85] Francesco Faglioni, Christopher L. Claypool, Nathan S. Lewis, and William A. Goddard. Theoretical description of the STM images of alkanes and substituted alkanes adsorbed on graphite. *J. Phys. Chem. B*, 101(31):5996–6020, 1997.

[86] S. Fazekas, J. Kertész, and D. E. Wolf. Two-dimensional array of magnetic particles: The role of an interaction cutoff. *Phys. Rev. E*, 68:041102, 2003.

[87] R.M. Feenstra, Joseph A. Stroscio, and A.P. Fein. Tunneling spectroscopy of the Si(111)2×1 surface. *Surf. Sci.*, 181(1–2):295–306, 1987.

[88] J. D. Feldmann, G. J. Kalman, P. Hartmann, and M. Rosenberg. Ground state of magnetic dipoles on a two-dimensional lattice: Structural phases in complex plasmas. *Phys. Rev. Lett.*, 100:085001, 2008.

[89] I. Fernandez-Torrente, S. Monturet, K. J. Franke, J. Fraxedas, N. Lorente, and J. I. Pascual. Long-range repulsive interaction between molecules on a metal surface induced by charge transfer. *Phys. Rev. Lett.*, 99:176103, 2007.

[90] Delia Fernández-Torre, Oona Kupiainen, Pekka Pyykkö, and Lauri Halonen. Long-range interactions between polar molecules and metallic surfaces: A comparison of classical and density functional theory based models. *Chem. Phys. Lett.*, 471(4–6):239–243, 2009.

[91] Benjamin Fiedler, Elena Rojo-Wiechel, Johann Klassen, Julia Simon, Johannes Beck, and Moritz Sokolowski. Ordered structures of two sulfur containing donor molecules on the Au(111) surface. *Surf. Sci.*, 606(23–24):1855–1863, 2012.

[92] F. Flores, J. Ortega, and H. Vázquez. Modelling energy level alignment at organic interfaces and density functional theory. *Phys. Chem. Chem. Phys.*, 11:8658–8675, 2009.

[93] C. B. France, F. Andrew Frame, and B. A. Parkinson. Multiple two-dimensional structures formed at monolayer and submonolayer coverages of p-sexiphenyl on the Au(111) surface. *Langmuir*, 22(18):7507–7511, 2006.

[94] Paul Frank, Norbert Koch, Markus Koini, Ralph Rieger, Klaus Müllen, Roland Resel, and Adolf Winkler. Layer growth and desorption kinetics of a discoid molecular acceptor on Au(111). *Chem. Phys. Lett.*, 473(4–6):321–325, 2009.

[95] J. Fraxedas, S. Garcia-Gil, S. Monturet, N. Lorente, I. Fernandez-Torrente, K. J. Franke, J. I. Pascual, A. Vollmer, R.-P. Blum, N. Koch, and P. Ordejon. Modulation of surface charge transfer through competing long-range repulsive versus short-range attractive interactions. *J. Phys. Chem. C*, 115(38):18640–18648, 2011.

[96] R. Friedlein, X. Crispin, M. Pickholz, M. Keil, S. Stafstroem, and W.R. Salaneck. High intercalation levels in lithium perylene stoichiometric compounds. *Chem. Phys. Lett.*, 354(5–6):389–394, 2002.

[97] M. J. Frisch, G. W. Trucks, H. B. Schlegel, G. E. Scuseria, M. A. Robb, J. R. Cheeseman, G. Scalmani, V. Barone, B. Mennucci, G. A. Petersson, H. Nakatsuji, M. Caricato, X. Li, H. P. Hratchian, A. F. Izmaylov, J. Bloino, G. Zheng, J. L. Sonnenberg, M. Hada, M. Ehara, K. Toyota, R. Fukuda, J. Hasegawa, M. Ishida, T. Nakajima, Y. Honda, O. Kitao, H. Nakai, T. Vreven, J. A. Montgomery, Jr., J. E. Peralta, F. Ogliaro, M. Bearpark, J. J. Heyd, E. Brothers, K. N. Kudin, V. N. Staroverov, R. Kobayashi, J. Normand, K. Raghavachari, A. Rendell, J. C. Burant, S. S. Iyengar, J. Tomasi, M. Cossi, N. Rega, J. M. Millam, M. Klene, J. E. Knox, J. B. Cross, V. Bakken, C. Adamo, J. Jaramillo, R. Gomperts, R. E. Stratmann, O. Yazyev, A. J. Austin, R. Cammi, C. Pomelli, J. W. Ochterski, R. L. Martin, K. Morokuma, V. G. Zakrzewski, G. A. Voth, P. Salvador, J. J. Dannenberg, S. Dapprich, A. D. Daniels, Ö. Farkas, J. B. Foresman, J. V. Ortiz, J. Cioslowski, and D. J. Fox. Gaussian 09 Revision A.02. Gaussian Inc. Wallingford CT 2009.

[98] H. Fukagawa, S. Hosoumi, H. Yamane, S. Kera, and N. Ueno. Dielectric properties of polar-phthalocyanine monolayer systems with repulsive dipole interaction. *Phys. Rev. B*, 83:085304, 2011.

[99] Alexander M. Gabovich, Mai Suan Li, Henryk Szymczak, and Alexander I. Voitenko. Image forces for a point-like dipole near a plane metal surface: An account of the spatial dispersion of dielectric permittivity. *Surf. Sci.*, 606(3–4):510–515, 2012.

[100] Weiying Gao and Antoine Kahn. Controlled p-doping of zinc phthalocyanine by coevaporation with tetrafluorotetracyanoquinodimethane: A direct and inverse photoemission study. *Appl. Phys. Lett.*, 79(24):4040, 2001.

[101] Alejandro Gil-Villegas, George Jackson, and Simon C. McGrother. Computer simulation of dipolar liquid crystals. *J. Mol. Liq.*, 76(3):171–181, 1998.

[102] L. Giovanelli, P. Amsalem, T. Angot, L. Petaccia, S. Gorovikov, L. Porte, A. Goldoni, and J.-M. Themlin. Valence band photoemission from the Zn-phthalocyanine/Ag(110) interface: Charge transfer and scattering of substrate photoelectrons. *Phys. Rev. B*, 82:125431, 2010.

[103] L. Giovanelli, F.C. Bocquet, P. Amsalem, H.-L. Lee, M. Abel, S. Clair, M. Koudia, T. Faury, L. Petaccia, D. Topwal, E. Salomon, T. Angot, A.A. Cafolla, N. Koch, L. Porte, A. Goldoni, and J.-M. Themlin. Interpretation

of valence band photoemission spectra at organic-metal interfaces. *Phys. Rev. B*, 87(3), 2013.

[104] K. Glöckler, C. Seidel, A. Soukopp, M. Sokolowski, E. Umbach, M. Böhringer, R. Berndt, and W.-D. Schneider. Highly ordered structures and submolecular scanning tunnelling microscopy contrast of PTCDA and DM-PBDCI monolayers on Ag(111) and Ag(110) . *Surf. Sci.*, 405(1):1–20, 1998.

[105] Hendrik Glowatzki. *Structural and electronic properties of self-assembled molecular layers at the organic/metal interface*. PhD thesis, HU Berlin, 2009. http://edoc.hu-berlin.de/dissertationen/glowatzki-hendrik-2009-06-15/PDF/glowatzki.pdf.

[106] Hendrik Glowatzki, Benjamin Bröker, Ralf-Peter Blum, Oliver T. Hofmann, Antje Vollmer, Ralph Rieger, Klaus Müllen, Egbert Zojer, Jürgen P. Rabe, and Norbert Koch. "Soft" metallic contact to isolated C_{60} molecules. *Nano Lett.*, 8(11):3825–3829, 2008.

[107] E. P. Goodings, D. A. Mitchard, and G. Owen. Synthesis, structure, and electrical properties of naphthacene, pentacene, and hexacene sulphides. *J. Chem. Soc., Perkin Trans.*, 1:1310–1314, 1972.

[108] Tina Graber, Frank Forster, Achim Schöll, and Friedrich Reinert. Experimental determination of the attenuation length of electrons in organic molecular solids: The example of PTCDA. *Surf. Sci.*, 605(9–10):878–882, 2011.

[109] Mark T. Greiner, Michael G. Helander, Wing-Man Tang, Zhi-Bin Wang, Jacky Qiu, and Zheng-Hong Lu. Universal energy-level alignment of molecules on metal oxides. *Nat. Mater.*, 11(1):76–81, 2012.

[110] Mandy Grobosch and Martin Knupfer. Energy level alignment and interface states at α-sexithiophene/Ag interfaces. *Org. Electron.*, 8(5):625–630, 2007.

[111] Nadine E. Gruhn, Demetrio A. da Silva Filho, Tonja G. Bill, Massimo Malagoli, Veaceslav Coropceanu, Antoine Kahn, and Jean-Luc Brédas. The vibrational reorganization energy in pentacene: Molecular influences on charge transport. *JACS*, 124(27):7918–7919, 2002.

[112] W. Guo, S.X. Du, Y.Y. Zhang, W.A. Hofer, C. Seidel, L.F. Chi, H. Fuchs, and H.-J. Gao. Electrostatic field effect on molecular structures at metal surfaces. *Surf. Sci.*, 603(17):2815–2819, 2009.

[113] T. Haber, S. Muellegger, A. Winkler, and R. Resel. Temperature-induced epitaxial growth modes of para-sexiphenyl on Au(111). *Phys. Rev. B*, 74:045419, 2006.

[114] J. R. Hahn and W. Ho. Single molecule imaging and vibrational spectroscopy with a chemically modified tip of a scanning tunneling microscope. *Phys. Rev. Lett.*, 87:196102, 2001.

[115] P.C. Hariharan and J.A. Pople. The influence of polarization functions on molecular orbital hydrogenation energies. *Theor. Chim. Acta*, 28(3):213–222, 1973.

[116] P. Jeffrey Hay and Willard R. Wadt. Ab initio effective core potentials for molecular calculations. potentials for K to Au including the outermost core orbitals. *J. Chem. Phys.*, 82(1):299–310, 1985.

[117] P. Jeffrey Hay and Willard R. Wadt. Ab initio effective core potentials for molecular calculations. potentials for the transition metal atoms Sc to Hg. *J. Chem. Phys.*, 82(1):270–283, 1985.

[118] A.F. Hebard, R.C. Haddon, R.M. Fleming, and A.R. Kortan. Deposition and characterization of fullerene films. *Appl. Phys. Lett.*, 59(17):2109–2111, 1991.

[119] W. J. Hehre, R. Ditchfield, and J. A. Pople. Self–consistent molecular orbital methods. XII. further extensions of Gaussian-type basis sets for use in molecular orbital studies of organic molecules. *J. Chem. Phys.*, 56(5):2257–2261, 1972.

[120] G. Heimel, S. Duhm, I. Salzmann, A. Gerlach, A. Strozecka, J. Niederhausen, C. Bürker, T. Hosokai, I. Fernandez-Torrente, G. Schulze, S. Winkler, A. Wilke, R. Schlesinger, J. Frisch, B. Broker, A. Vollmer, B. Detlefs, J. Pflaum, S. Kera, K. J. Franke, N. Ueno, J. I. Pascual, F. Schreiber, and N. Koch. Charged and metallic molecular monolayers through surface-induced aromatic stabilization. *Nat. Chem.*, 5(3):187–94, 2013.

[121] Georg Heimel, Ferdinand Rissner, and Egbert Zojer. Modeling the electronic properties of π-conjugated self-assembled monolayers. *Adv. Mater.*, 22(23):2494–2513, 2010.

[122] Georg Heimel, Lorenz Romaner, Jean-Luc Brédas, and Egbert Zojer. Odd-even effects in self-assembled monolayers of ω-(biphenyl-4-yl)alkanethiols: A first-principles study. *Langmuir*, 24(2):474–482, 2008.

[123] Georg Heimel, Lorenz Romaner, Egbert Zojer, and Jean-Luc Brédas. Toward control of the metal-organic interfacial electronic structure in molecular electronics: A first-principles study on self-assembled monolayers of π-conjugated molecules on noble metals. *Nano Lett.*, 7(4):932–940, 2007.

[124] Georg Heimel, Lorenz Romaner, Egbert Zojer, and Jean-Luc Brédas. The interface energetics of self-assembled monolayers on metals. *Acc. Chem. Res.*, 41(6):721–729, 2008.

[125] Georg Heimel, Ingo Salzmann, Steffen Duhm, and Norbert Koch. Design of organic semiconductors from molecular electrostatics. *Chem. Mater.*, 23(3):359–377, 2011.

[126] C. E. Heiner, J. Dreyer, I. V. Hertel, N. Koch, H.-H. Ritze, W. Widdra, and B. Winter. Anisotropy in ordered sexithiophene thin films studied by angle-resolved photoemission using combined laser and synchrotron radiation. *Appl. Phys. Lett.*, 87(9):093501, 2005.

[127] K. Heister, H.-T. Rong, M. Buck, M. Zharnikov, M. Grunze, and L. S. O. Johansson. Odd-even effects at the S-metal interface and in the aromatic matrix of biphenyl-substituted alkanethiol self-assembled monolayers. *J. Phys. Chem. B*, 105(29):6888–6894, 2001.

[128] M. Henzler. The origin of surface states. *Surf. Sci.*, 25(3):650–680, 1971.

[129] S Hüfner. *Photoelectron Spectroscopy. Principles and Applications.* Springer, Berlin, 3rd edition, 2003.

[130] I. G. Hill, A. Kahn, J. Cornil, D. A. dos Santos, and J. L. Brédas. Occupied and unoccupied electronic levels in organic π-conjugated molecules: comparison between experiment and theory. *Chem. Phys. Lett.*, 317(3–5):444–450, 2000.

[131] I. G. Hill, A. J. Makinen, and Z. H. Kafafi. Initial stages of metal/organic semiconductor interface formation. *J. Appl. Phys.*, 88(2):889–895, 2000.

[132] Saw-Wai Hla. Scanning tunneling microscopy single atom/molecule manipulation and its application to nanoscience and technology. *J. Vac. Sci. Technol., A*, 23(4):1351–1360, 2005.

[133] Saw-Wai Hla, Kai-Felix Braun, Bernhard Wassermann, and Karl-Heinz Rieder. Controlled low-temperature molecular manipulation of sexiphenyl molecules on Ag(111) using scanning tunneling microscopy. *Phys. Rev. Lett.*, 93:208302, 2004.

[134] Saw-Wai Hla and Yuan Zhang. private communication.

[135] W.A Hofer. Challenges and errors: interpreting high resolution images in scanning tunneling microscopy. *Prog. Surf. Sci.*, 71(5–8):147–183, 2003.

[136] B.W. Hoogenboom, R. Hesper, L.H. Tjeng, and G.A. Sawatzky. Charge transfer and doping-dependent hybridization of C_{60} on noble metals. *Phys. Rev. B*, 57(19):11939–11942, 1998.

[137] I. Horcas, R. Fernández, J. M. Gómez-Rodríguez, J. Colchero, J. Gómez-Herrero, and A. M. Baro. WSXM: A software for scanning probe microscopy and a tool for nanotechnology. *Rev. Sci. Instrum.*, 78(1):013705, 2007.

[138] Han Huang, Jia-Tao Sun, Yuan Ping Feng, Wei Chen, and Andrew Thye Shen Wee. Epitaxial growth of diindenoperylene ultrathin films on Ag(111) investigated by LT-STM and LEED. *Phys. Chem. Chem. Phys.*, 13:20933–20938, 2011.

[139] J. Hwang, A. Wan, and A. Kahn. Energetics of metal-organic interfaces: New experiments and assessment of the field. *Mater. Sci. Eng., R*, 64(1–2):1–31, 2009.

[140] Norio Ise. Like likes like: counterion-mediated attraction in macroionic and colloidal interaction. *Phys. Chem. Chem. Phys.*, 12:10279–10287, 2010.

[141] H. Ishii, N. Hayashi, E. Ito, Y. Washizu, K. Sugi, Y. Kimura, M. Niwano, Y. Ouchi, and K. Seki. Kelvin probe study of band bending at organic semiconductor/metal interfaces: examination of Fermi level alignment. *Phys. Status Solidi A*, 201(6):1075–1094, 2004.

[142] Hisao Ishii, Kiyoshi Sugiyama, Eisuke Ito, and Kazuhiko Seki. Energy level alignment and interfacial electronic structures at organic/metal and organic/organic interfaces. *Adv. Mater.*, 11(8):605–625, 1999.

[143] Takashi Isoshima, Youichi Okabayashi, Eisuke Ito, Masahiko Hara, Whee Won Chin, and Jin Wook Han. Negative giant surface potential of vacuum-evaporated tris(7-propyl-8-hydroxyquinolinolato) aluminum(iii) [Al(7-Prq)3] film. *Org. Electron.*, 14(8):1988–1991, 2013.

[144] Eisuke Ito, Yuuki Washizu, Naoki Hayashi, Hisao Ishii, Noritaka Matsuie, Kazuma Tsuboi, Yukio Ouchi, Yutaka Harima, Kazuo Yamashita, and Kazuhiko Seki. Spontaneous buildup of giant surface potential by vacuum deposition of Alq_3 and its removal by visible light irradiation. *J. Appl. Phys.*, 92(12):7306–7310, 2002.

[145] Shunji Ito, Mike Wehmeier, J. Diedrich Brand, Christian Kübel, Rebekka Epsch, Jürgen P. Rabe, and Klaus Müllen. Synthesis and self-assembly of functionalized hexa-peri-hexabenzocoronenes. *Chem. Eur. J.*, 6(23):4327–4342, 2000.

[146] G. E. Jabbour, B. Kippelen, N. R. Armstrong, and N. Peyghambarian. Aluminum based cathode structure for enhanced electron injection in electroluminescent organic devices. *Appl. Phys. Lett.*, 73(9):1185–1187, 1998.

[147] Aleksander Jablonski. Escape depth of photoelectrons. *Surf. Interface Anal.*, 21(11):758–763, 1994.

[148] B. Jaeckel, J. B. Sambur, and B. A. Parkinson. The influence of metal work function on the barrier heights of metal/pentacene junctions. *J. Appl. Phys.*, 103(6):063719, 2008.

[149] N. Jiang, Y. Y. Zhang, Q. Liu, Z. H. Cheng, Z. T. Deng, S. X. Du, H.-J. Gao, M. J. Beck, and S. T. Pantelides. Diffusivity control in molecule-on-metal systems using electric fields. *Nano Lett.*, 10(4):1184–1188, 2010.

[150] D. Kaefer, C. Wöll, and G. Witte. Thermally activated dewetting of organic thin films: the case of pentacene on SiO_2 and gold. *Appl. Phys. A*, 95(1):273–284, 2009.

[151] Daniel Kaefer, Asif Bashir, and Gregor Witte. Interplay of anchoring and ordering in aromatic self-assembled monolayers. *J. Phys. Chem. C*, 111(28):10546–10551, 2007.

[152] Antoine Kahn, Norbert Koch, and Weiying Gao. Electronic structure and electrical properties of interfaces between metals and π-conjugated molecular films. *J. Polym. Sci., Part B: Polym. Phys.*, 41(21):2529–2548, 2003.

[153] Wolfgang L. Kalb, Simon Haas, Cornelius Krellner, Thomas Mathis, and Bertram Batlogg. Trap density of states in small-molecule organic semiconductors: A quantitative comparison of thin-film transistors with single crystals. *Phys. Rev. B*, 81:155315, 2010.

[154] S. Kera, H. Yamane, H. Fukagawa, T. Hanatani, K.K. Okudaira, K. Seki, and N. Ueno. Angle resolved UV photoelectron spectra of titanyl phthalocynine monolayer film on graphite. *J. Electron. Spectrosc. Relat. Phenom.*, 156–158(0):135–138, 2007.

[155] Dirk Kühne, Florian Klappenberger, Régis Decker, Uta Schlickum, Harald Brune, Svetlana Klyatskaya, Mario Ruben, and Johannes V. Barth. Self-assembly of nanoporous chiral networks with varying symmetry from sexiphenyl-dicarbonitrile on Ag(111). *J. Phys. Chem. C*, 113(41):17851–17859, 2009.

[156] L. Kilian, A. Hauschild, R. Temirov, S. Soubatch, A. Schöll, A. Bendounan, F. Reinert, T.-L. Lee, F. S. Tautz, M. Sokolowski, and E. Umbach. Role of intermolecular interactions on the electronic and geometric structure of a large π-conjugated molecule adsorbed on a metal surface. *Phys. Rev. Lett.*, 100:136103, 2008.

[157] Yong-Ki Kim, Jeong Won Kim, and Yongsup Park. Energy level alignment at a charge generation interface between 4,4'-bis(N-phenyl-1-naphthylamino)biphenyl and 1,4,5,8,9,11-hexaazatriphenylene-hexacarbonitrile. *Appl. Phys. Lett.*, 94(6):063305, 2009.

[158] V. E. Klymenko, V. M. Rozenbaum, V. V. Kukhtin, and O. V. Shramko. Stabilization of the long-range order within a square dipole lattice by the quadrupole interaction. *Solid State Commun.*, 88(5):373–375, 1993.

[159] N. Koch, D. Pop, R. L. Weber, N. Böwering, B. Winter, M. Wick, G. Leising, I. V. Hertel, and W. Braun. Radiation induced degradation and surface charging of organic thin films in ultraviolet photoemission spectroscopy. *Thin Solid Films*, 391(1):81–87, 2001.

[160] N. Koch, I. Salzmann, R.L. Johnson, J. Pflaum, R. Friedlein, and J.P. Rabe. Molecular orientation dependent energy levels at interfaces with pentacene and pentacenequinone. *Org. Electron.*, 7(6):537–545, 2006.

[161] N. Koch and A. Vollmer. Electrode-molecular semiconductor contacts: Work-function-dependent hole injection barriers versus Fermi-level pinning. *Appl. Phys. Lett.*, 89(16):162107, 2006.

[162] N. Koch, A. Vollmer, S. Duhm, Y. Sakamoto, and T. Suzuki. The effect of fluorination on pentacene/gold interface energetics and charge reorganization energy. *Adv. Mater.*, 19(1):112–116, 2007.

[163] Norbert Koch. Organic electronic devices and their functional interfaces. *ChemPhysChem.*, 8(10):1438–1455, 2007.

[164] Norbert Koch. Energy levels at interfaces between metals and conjugated organic molecules. *J. Phys.: Condens. Matter*, 20(18):184008, 2008.

[165] Norbert Koch, Steffen Duhm, Jürgen P. Rabe, Antje Vollmer, and Robert L. Johnson. Optimized hole injection with strong electron acceptors at organic-metal interfaces. *Phys. Rev. Lett.*, 95(23):237601–, 2005.

[166] Norbert Koch, Georg Heimel, Jishan Wu, Egbert Zojer, Robert L. Johnson, Jean-Luc Brédas, Klaus Müllen, and Jürgen P. Rabe. Influence of molecular conformation on organic/metal interface energetics. *Chem. Phys. Lett.*, 413(4–6):390–395, 2005.

[167] Martin Körner, Felix Loske, Mario Einax, Angelika Kühnle, Michael Reichling, and Philipp Maass. Second-layer induced island morphologies in thin-film growth of fullerenes. *Phys. Rev. Lett.*, 107:016101, 2011.

[168] S Kowarik, A Gerlach, and F Schreiber. Organic molecular beam deposition: fundamentals, growth dynamics, and in situ studies. *J. Phys.: Condens. Matter*, 20(18):184005, 2008.

[169] S. Kowarik, A. Gerlach, S. Sellner, F. Schreiber, L. Cavalcanti, and O. Konovalov. Real-time observation of structural and orientational transitions during growth of organic thin films. *Phys. Rev. Lett.*, 96:125504, 2006.

[170] Stefan Kowarik, Alexander Gerlach, Stefan Sellner, Leide Cavalcanti, and Frank Schreiber. Dewetting of an organic semiconductor thin film observed in real-time. *Adv. Eng. Mater.*, 11(4):291–294, 2009.

[171] A. Kraft, R. Temirov, S. K. M. Henze, S. Soubatch, M. Rohlfing, and F. S. Tautz. Lateral adsorption geometry and site-specific electronic structure of a large organic chemisorbate on a metal surface. *Phys. Rev. B*, 74:041402, 2006.

[172] B. Krause, A. C. Durr, F. Schreiber, H. Dosch, and O. H. Seeck. Thermal stability and partial dewetting of crystalline organic thin films: 3,4,9,10-perylenetetracarboxylic dianhydride on Ag(111). *J. Chem. Phys.*, 119(6):3429–3435, 2003.

[173] B. Krause, F. Schreiber, H. Dosch, A. Pimpinelli, and O. H. Seeck. Temperature dependence of the 2D-3D transition in the growth of PTCDA on Ag(111): A real-time X-ray and kinetic Monte Carlo study. *Europhys. Lett.*, 65(3):372–378, 2004.

[174] Stefan Krause, Matthias Stolte, Frank Würthner, and Norbert Koch. Influence of merocyanine molecular dipole moments on the valence levels in thin films and the interface energy level alignment with Au(111). *J. Phys. Chem. C*, 117(37):19031–19037, 2013.

[175] C. Krellner, S. Haas, C. Goldmann, K. P. Pernstich, D. J. Gundlach, and B. Batlogg. Density of bulk trap states in organic semiconductor crystals: Discrete levels induced by oxygen in rubrene. *Phys. Rev. B*, 75:245115, 2007.

[176] J. Kröger, H. Jensen, R. Berndt, R. Rurali, and N. Lorente. Molecular orbital shift of perylenetetracarboxylic-dianhydride on gold. *Chem. Phys. Lett.*, 438(4–6):249–253, 2007.

[177] Jérôme Lagoute, Kiyoshi Kanisawa, and Stefan Fölsch. Manipulation and adsorption-site mapping of single pentacene molecules on Cu(111). *Phys. Rev. B*, 70:245415, 2004.

[178] I. Langmuir. Vapor pressures, evaporation, condensation and adsorption. *JACS*, 54(7):2798–2832, 1932.

[179] Penelope A. Lewis, Christina E. Inman, Francisco Maya, James M. Tour, James E. Hutchison, and Paul S. Weiss. Molecular engineering of the polarity and interactions of molecular electronic switches. *JACS*, 127(49):17421–17426, 2005.

[180] Lothar Ley, Yaou Smets, Christopher I. Pakes, and Jürgen Ristein. Calculating the universal energy-level alignment of organic molecules on metal oxides. *Adv. Funct. Mater.*, 23(7):794–805, 2012.

[181] Chen Li, Zhihong Liu, Jan Schöneboom, Felix Eickemeyer, Neil G Pschirer, Peter Erk, Andreas Herrmann, and Klaus Müllen. Perylenes as sensitizers in hybrid solar cells: how molecular size influences performance. *J. Mater. Chem.*, 19(30):5405–5415, 2009.

[182] Linfeng Li, Rongliang Wu, Shanyi Guang, Xinyan Su, and Hongyao Xu. The investigation of the hydrogen bond saturation effect during the dipole-dipole induced azobenzene supramolecular self-assembly. *Phys. Chem. Chem. Phys.*, 15:20753–20763, 2013.

[183] L. S. Liao and K. P. Klubek. Power efficiency improvement in a tandem organic light-emitting diode. *Appl. Phys. Lett.*, 92(22):223311, 2008.

[184] L. S. Liao, W. K. Slusarek, T. K. Hatwar, M. L. Ricks, and D. L. Comfort. Tandem organic light-emitting diode using hexaazatriphenylene hexacarbonitrile in the intermediate connector. *Adv. Mater.*, 20(2):324–329, 2008.

[185] Linda Lindell, Deniz Çakir, Geert Brocks, Mats Fahlman, and Slawomir Braun. Role of intrinsic molecular dipole in energy level alignment at organic interfaces. *Appl. Phys. Lett.*, 102(22):223301, 2013.

[186] Linda Lindell, Mikael Unge, Wojciech Osikowicz, Sven Stafström, William R. Salaneck, Xavier Crispin, and Michel P. de Jong. Integer charge transfer at the tetrakis(dimethylamino)ethylene/Au interface. *Appl. Phys. Lett.*, 92(16):163302, 2008.

[187] S.Å. Lindgren and L. Walldén. Adsorbate-induced angle averaging of Cu(111) photoemission spectra. *Phys. Rev. Lett.*, 43(6):460–463, 1979.

[188] Xianjie Liu, Yinying Wei, Janice E. Reutt-Robey, and Steven W. Robey. Dipole-dipole interactions in TiOPc adlayers on Ag. *J. Phys. Chem. C*, 118(7):3523–3532, 2014.

[189] J. Christopher Love, Lara A. Estroff, Jennah K. Kriebel, Ralph G. Nuzzo, and George M. Whitesides. Self-assembled monolayers of thiolates on metals as a form of nanotechnology. *Chem. Rev.*, 105(4):1103–1170, 2005.

[190] X. Lu, M. Grobis, K.H. Khoo, S.G. Louie, and M.F. Crommie. Charge transfer and screening in individual C_{60} molecules on metal substrates: A scanning tunneling spectroscopy and theoretical study. *Phys. Rev. B*, 70(11):115418–1–115418–8, 2004.

[191] Shin'ichi Machida, Yusuke Ozawa, Jun ichi Takahashi, Hiroshi Tokairin, Yasuo Nakayama, and Hisao Ishii. Low-energy photoemission study of C_{60}/rubrene/Au interfaces in practical device thickness. *Appl. Phys Express*, 6(2):025801, 2013.

[192] Roberto Macovez, Andrea Goldoni, Luca Petaccia, Ingrid Marenne, Paul A. Brühwiler, and Petra Rudolf. Reversible phase transformation and doubly charged anions at the surface of simple cubic rbc_{60}. *Phys. Rev. Lett.*, 101:236403, 2008.

[193] Peter Maksymovych, Dan C. Sorescu, and John T. Yates. Gold-adatom-mediated bonding in self-assembled short-chain alkanethiolate species on the Au(111) surface. *Phys. Rev. Lett.*, 97:146103, 2006.

[194] S. Mannsfeld, M. Toerker, T. Schmitz-Hübsch, F. Sellam, T. Fritz, and K. Leo. Combined LEED and STM study of PTCDA growth on reconstructed Au(111) and Au(100) single crystals. *Org. Electron.*, 2(3–4):121–134, 2001.

[195] Hong Ying Mao, Fabio Bussolotti, Dong-Chen Qi, Rui Wang, Satoshi Kera, Nobuo Ueno, Andrew Thye Shen Wee, and Wei Chen. Mechanism of the fermi level pinning at organic donor-acceptor heterojunction interfaces. *Org. Electron.*, 12(3):534–540, 2011.

[196] J.I. Martínez, E. Abad, F. Flores, J. Ortega, and G. Brocks. Barrier height formation for the ptcda/au(111) interface. *Chem. Phys.*, 390(1):14–19, 2011.

[197] Gerhard Meyer. A simple low-temperature ultrahigh-vacuum scanning tunneling microscope capable of atomic manipulation. *Rev. Sci. Instrum.*, 67(8):2960–2965, 1996.

[198] Johannes Mielke, Sofia Selvanathan, Maike Peters, Jutta Schwarz, Stefan Hecht, and Leonhard Grill. Molecules with multiple switching units on a Au(111) surface: self-organization and single-molecule manipulation. *J. Phys.: Condens. Matter*, 24(39):394013, 2012.

[199] W. Mizutani, M. Shigeno, K. Kajimura, and M. Ono. Tunneling through a deformed potential. *Ultramicroscopy*, 42-44, Part 1(0):236–241, 1992.

[200] S. Müllegger, I. Salzmann, R. Resel, G. Hlawacek, C. Teichert, and A. Winkler. Growth kinetics, structure, and morphology of para-quaterphenyl thin films on gold(111). *J. Chem. Phys.*, 121(5):2272–2277, 2004.

[201] O. V. Molodtsova and M. Knupfer. Electronic properties of the organic semiconductor interfaces CuPc/C_{60} and C_{60}/CuPc. *J. Appl. Phys.*, 99(5):053704, 2006.

[202] M. Mura, X. Sun, F. Silly, H. T. Jonkman, G. A. D. Briggs, M. R. Castell, and L. N. Kantorovich. Experimental and theoretical analysis of H-bonded supramolecular assemblies of PTCDA molecules. *Phys. Rev. B*, 81:195412, 2010.

[203] Yuki Nagata. Polarizable atomistic calculation of site energy disorder in amorphous Alq_3. *ChemPhysChem*, 11(2):474–479, 2010.

[204] Yasuo Nakayama, Shin'ichi Machida, Yukimasa Miyazaki, Tatsuhiko Nishi, Yutaka Noguchi, and Hisao Ishii. Electronic structures at organic heterojunctions of N,N'-bis(1-naphthyl)-N,N'-diphenyl-1,1'-biphenyl-4,4'-diamin (NPB)-based organic light emitting diodes. *Org. Electron.*, 13(12):2850–2855, 2012.

[205] A. Natan, L. Kronik, H. Haick, and R. T. Tung. Electrostatic properties of ideal and non-ideal polar organic monolayers: Implications for electronic devices. *Adv. Mater.*, 19(23):4103–4117, 2007.

[206] J. B. Neaton, Mark S. Hybertsen, and Steven G. Louie. Renormalization of molecular electronic levels at metal-molecule interfaces. *Phys. Rev. Lett.*, 97:216405, 2006.

[207] David Nečas and Petr Klapetek. Gwyddion: an open-source software for SPM data analysis. *Cent. Eur. J. Phys.*, 10:181–188, 2012.

[208] Miloslav Nic, Jiri Jirat, and Bedrich Kosata. IUPAC compendium of chemical terminology, (the "gold book"), online version, 2014.

[209] Nicoleta Nicoara, Elisa Román, José M. Gómez-Rodríguez, José A. Martín-Gago, and Javier Méndez. Scanning tunneling and photoemission spectroscopies at the PTCDA/Au(111) interface. *Org. Electron.*, 7(5):287–294, 2006.

[210] J. Niederhausen, P. Amsalem, J. Frisch, A. Wilke, A. Vollmer, R. Rieger, K. Müllen, J. P. Rabe, and N. Koch. Tuning hole-injection barriers at organic/metal interfaces exploiting the orientation of a molecular acceptor interlayer. *Phys. Rev. B*, 84:165302, 2011.

[211] J. Niederhausen, P. Amsalem, A. Wilke, R. Schlesinger, S. Winkler, A. Vollmer, J. P. Rabe, and N. Koch. Doping of C_{60} (sub)monolayers by Fermi-level pinning induced electron transfer. *Phys. Rev. B*, 86:081411, 2012.

[212] Jens Niederhausen, Steffen Duhm, Georg Heimel, Christoph Bürker, Qian Xin, Andreas Wilke, Antje Vollmer, Frank Schreiber, Satoshi Kera, Jürgen P. Rabe, Nobuo Ueno, and Norbert Koch. Seleno groups control the energy-level alignment between conjugated organic molecules and metals. *J. Chem. Phys.*, 140(1):014705, 2014.

[213] Tomoaki Nishino, Takahito Ohshiro, and Yoshio Umezawa. Molecular tips for intermolecular tunneling microscopy. *Jpn. J. Appl. Phys.*, 46(8S):5519, 2007.

[214] Martin Oehzelt, Leonhard Grill, Stephen Berkebile, Georg Koller, Falko P. Netzer, and Michael G. Ramsey. The molecular orientation of para-sexiphenyl on Cu(110) and Cu(110) p(2×1)O. *ChemPhysChem*, 8(11):1707–1712, 2007.

[215] Martin Oehzelt, Norbert Koch, and Georg Heimel. Organic semiconductor density of states controls the energy level alignment at electrode interfaces. *Nat. Commun.*, 5:4174, 2014.

[216] Kamiya Koji Okudaira, Shinji Hasegawa, Hisao Ishii, Kazuhiko Seki, Yoshiya Harada, and Nobuo Ueno. Structure of copper- and H_2-phthalocyanine thin films on MoS_2 studied by angle-resolved ultraviolet photoelectron spectroscopy and low energy electron diffraction. *J. Appl. Phys.*, 85(9):6453–6461, 1999.

[217] Andreas Opitz. As yet untitled paper. In preparation, 2000.

[218] W. Osikowicz, M. P. de Jong, and W. R. Salaneck. Formation of the interfacial dipole at organic-organic interfaces: C_{60}/polymer interfaces. *Adv. Mater.*, 19(23):4213–4217, 2007.

[219] Kazunari Ozasa, Hiromi Ito, Mizuo Maeda, and Masahiko Hara. Photoinduced evolution of surface-potential undulation observed on vacuum-deposited thin films of tris(8-hydroxyquinolinato) aluminum. *Appl. Phys. Lett.*, 98(1):013301, 2011.

[220] Kazunari Ozasa, Shigeyuki Nemoto, Takashi Isoshima, Eisuke Ito, Mizuo Maeda, and Masahiko Hara. Measurement of photo-patterned surface potential of Alq_3 thin films by kelvin-force microscope together with near-field optical stimulation. *Surf. Interface Anal.*, 40(3–4):810–813, 2008.

[221] Kazunari Ozasa, Shigeyuki Nemoto, Takashi Isoshima, Eisuke Ito, Mizuo Maeda, and Masahiko Hara. Photoinduced reduction and pattern preservation of giant surface potential on tris(8-hydroxyquinolinato) aluminum(iii) thin films. *Appl. Phys. Lett.*, 93(26):263304, 2008.

[222] R. Paniago, R. Matzdorf, G. Meister, and A. Goldmann. Temperature dependence of Shockley-type surface energy bands on Cu(111), Ag(111) and Au(111). *Surf. Sci.*, 336(1–2):113–122, 1995.

[223] L. Patrone, S. Palacin, J. Charlier, F. Armand, J. P. Bourgoin, H. Tang, and S. Gauthier. Evidence of the key role of metal-molecule bonding in metal-molecule-metal transport experiments. *Phys. Rev. Lett.*, 91:096802, 2003.

[224] Rémy Pawlak. *Auto-assemblage et polymérisation 2D de molécules organiques en surface.* PhD thesis, Aix-Marseille Université, 2009.

[225] N. Pertaya, K.-F. Braun, and K.-H. Rieder. On the stability of Besocke-type scanners. *Rev. Sci. Instrum.*, 75(8):2608–2612, 2004.

[226] N.V. Petrova and I.N. Yakovkin. Lateral interaction and CO adlayer structures on the Pt(111) surface. *Surf. Sci.*, 519(1–2):90–100, 2002.

[227] J. Pflaum, J. Niemax, and A.K. Tripathi. Chemical and structural effects on the electronic transport in organic single crystals. *Chemical Physics*, 325(1):152–159, 2006.

[228] Oksana Plekan, Andrew Cassidy, Richard Balog, Nykola C. Jones, and David Field. A new form of spontaneously polarized material. *Phys. Chem. Chem. Phys.*, 13:21035–21044, 2011.

[229] Oksana Plekan, Andrew Cassidy, Richard Balog, Nykola C. Jones, and David Field. Spontaneous electric fields in films of cis-methyl formate. *Phys. Chem. Chem. Phys.*, 14:9972–9976, 2012.

[230] Hongwei Qu, Wei Yao, T. Garcia, Jiandi Zhang, A. V. Sorokin, S. Ducharme, P. A. Dowben, and V. M. Fridkin. Nanoscale polarization manipulation and conductance switching in ultrathin films of a ferroelectric copolymer. *Appl. Phys. Lett.*, 82(24):4322–4324, 2003.

[231] P. Rahe, R. Bechstein, and A. Kühnle. Vertical and lateral drift corrections of scanning probe microscopy images. *J. Vac. Sci. Technol., A*, 28(3):C4E31–C4E38, 2010.

[232] Philipp Rahe, Robert Lindner, Markus Kittelmann, Markus Nimmrich, and Angelika Kühnle. From dewetting to wetting molecular layers: C_{60} on $CaCO_3(10\bar{1}4)$ as a case study. *Phys. Chem. Chem. Phys.*, 14:6544–6548, 2012.

[233] Erin L. Ratcliff, Brian Zacher, and Neal R. Armstrong. Selective interlayers and contacts in organic photovoltaic cells. *J. Phys. Chem. Lett.*, 2(11):1337–1350, 2011.

[234] Jascha Repp, Gerhard Meyer, Sladjana M. Stojković, André Gourdon, and Christian Joachim. Molecules on insulating films: Scanning-tunneling microscopy imaging of individual molecular orbitals. *Phys. Rev. Lett.*, 94:026803, 2005.

[235] G.E. Rhead, M.-G. Barthès, and C. Argile. Determination of growth modes of ultrathin films from Auger electron spectroscopy : An assessment and commentary. *Thin Solid Films*, 82(2):201–211, 1981.

[236] J. Riga, J. J. Verbist, F. Wudl, and A. Kruger. The electronic structure and conductivity of tetrathiotetracene, tetrathionaphthalene, and tetraselenotetracene studied by ESCA. *J. Chem. Phys.*, 69(7):3221–3231, 1978.

[237] Ferdinand Rissner, Gerold M. Rangger, Oliver T. Hofmann, Anna M. Track, Georg Heimel, and Egbert Zojer. Understanding the electronic structure of metal/SAM/organic - semiconductor heterojunctions. *ACS Nano*, 3(11):3513–3520, 2009.

[238] M. L. M. Rocco, M. Haeming, D. R. Batchelor, R. Fink, A. Schöll, and E. Umbach. Electronic relaxation effects in condensed polyacenes: A high-resolution photoemission study. *J. Chem. Phys.*, 129(7):074702, 2008.

[239] Lorenz Romaner, Georg Heimel, Jean-Luc Brédas, Alexander Gerlach, Frank Schreiber, Robert L. Johnson, Jörg Zegenhagen, Steffen Duhm, Norbert Koch, and Egbert Zojer. Impact of bidirectional charge transfer and molecular distortions on the electronic structure of a metal-organic interface. *Phys. Rev. Lett.*, 99(25):256801–, 2007.

[240] Frédéric Rossel, Pierre Brodard, François Patthey, Neville V. Richardson, and Wolf-Dieter Schneider. Modified herringbone reconstruction on Au(111) induced by self-assembled azure a islands. *Surf. Sci.*, 602(14):L115–L117, 2008.

[241] V. M. Rozenbaum, Vladimir M. Ogenko, and A. A. Chuĭko. Vibrational and orientational states of surface atomic groups. *Sov. Phys. Usp.*, 34(10):883, 1991.

[242] P. C. Rusu, G. Giovannetti, C. Weijtens, R. Coehoorn, and G. Brocks. Work function pinning at metal-organic interfaces. *J. Phys. Chem. C*, 113(23):9974–9977, 2009.

[243] Paul C. Rusu and Geert Brocks. Work functions of self-assembled monolayers on metal surfaces by first-principles calculations. *Phys. Rev. B*, 74:073414, 2006.

[244] Ingo Salzmann, Steffen Duhm, Georg Heimel, Martin Oehzelt, Rolf Kniprath, Robert L. Johnson, Jürgen P. Rabe, and Norbert Koch. Tuning the ionization energy of organic semiconductor films: The role of intramolecular polar bonds. *JACS*, 130(39):12870–12871, 2008.

[245] Ingo Salzmann, Georg Heimel, Steffen Duhm, Martin Oehzelt, Patrick Pingel, Benjamin M. George, Alexander Schnegg, Klaus Lips, Ralf-Peter Blum, Antje Vollmer, and Norbert Koch. Intermolecular hybridization governs molecular electrical doping. *Phys. Rev. Lett.*, 108:035502, 2012.

[246] Paolo Samorí and Jürgen P. Rabe. Scanning probe microscopy explorations on conjugated (macro)molecular architectures for molecular electronics. *J. Phys.: Condens. Matter*, 14(42):9955, 2002.

[247] G. A. Samorjai. *Introduction to surface chemistry and catalysis*. Wiley: NewYork, 1994.

[248] Naoki Sato, Hiroo Inokuchi, and Edger A. Silinsh. Reevaluation of electronic polarization energies in organic molecular crystals. *Chem. Phys.*, 115(2):269–277, 1987.

[249] Naoki Sato, Kazuhiko Seki, and Hiroo Inokuchi. Polarization energies of organic solids determined by ultraviolet photoelectron spectroscopy. *J. Chem. Soc., Faraday Trans. 2*, 77:1621–1633, 1981.

[250] Jay D. Sau, J. B. Neaton, Hyoung Joon Choi, Steven G. Louie, and Marvin L. Cohen. Electronic energy levels of weakly coupled nanostructures: C_{60}-metal interfaces. *Phys. Rev. Lett.*, 101:026804, 2008.

[251] Maya Schöck, Roberto Otero, Sladjana Stojkovic, Frauke Hümmelink, André Gourdon, Erik Lægsgaard, Ivan Stensgaard, Christian Joachim, and Flemming Besenbacher. Chiral close-packing of achiral star-shaped molecules on solid surfaces. *J. Phys. Chem. B*, 110(26):12835–12838, 2006.

[252] J. Schiessling, L. Kjeldgaard, T. Käämbre, I. Marenne, J.N. O'Shea, J. Schnadt, C.J. Glover, M. Nagasono, D. Nordlund, M.G. Garnier, L. Qian, J.-E. Rubensson, P. Rudolf, N. Mårtensson, J. Nordgren, and P.A. Brühwiler. Bulk and surface charge states of K_3C_{60}. *Phys. Rev. B*, 71(16), 2005.

[253] Martin Schmid, Andre Kaftan, Hans-Peter Steinrück, and J. Michael Gottfried. The electronic structure of cobalt(II) phthalocyanine adsorbed on Ag(111). *Surf. Sci.*, 606(11–12):945–949, 2012.

[254] Heiko Schmidle, Carol K. Hall, Orlin D. Velev, and Sabine H. L. Klapp. Phase diagram of two-dimensional systems of dipole-like colloids. *Soft Matter*, 8:1521–1531, 2012.

[255] T. Schmitz-Hübsch, T. Fritz, F. Sellam, R. Staub, and K. Leo. Epitaxial growth of 3,4,9,10-perylene-tetracarboxylic-dianhydride on Au(111): A STM and RHEED study. *Phys. Rev. B*, 55:7972–7976, 1997.

[256] F. Schreiber, A. Gerlach, N. Koch, E. Zojer, M. Sokolowski, F. S. Tautz, M. Rohlfing, and E. Umbach. Comment on "electron core-hole interaction and its induced ionic structural relaxation in molecular systems under x-ray irradiation". *Phys. Rev. Lett.*, 99:059601, 2007.

[257] Frank Schreiber. Structure and growth of self-assembling monolayers. *Prog. Surf. Sci.*, 65(5–8):151–257, 2000.

[258] M. P. Seah and W. A. Dench. Quantitative electron spectroscopy of surfaces: A standard data base for electron inelastic mean free paths in solids. *Surf. Interface Anal.*, 1(1):2–11, 1979.

[259] M. P. Seah, I. S. Gilmore, and G. Beamson. XPS: binding energy calibration of electron spectrometers 5 – re-evaluation of the reference energies. *Surf. Interface Anal.*, 26(9):642–649, 1998.

[260] C. Seifert, D. Skuridina, X. Dou, K. Müllen, N. Severin, and J. P. Rabe. Tomography of molecular nanographene double layers using scanning tunneling microscopy. *Phys. Rev. B*, 80:245429, 2009.

[261] Sofia Selvanathan, Maike V. Peters, Stefan Hecht, and Leonhard Grill. Island formation and manipulation of prochiral azobenzene derivatives on Au(111). *J. Phys.: Condens. Matter*, 24(35):354013, 2012.

[262] A. Shaporenko, M. Brunnbauer, A. Terfort, L. S. O. Johansson, M. Grunze, and M. Zharnikov. Odd-even effects in photoemission from terphenyl-substituted alkanethiolate self-assembled monolayers. *Langmuir*, 21(10):4370–4375, 2005.

[263] A. Shaporenko, P. Cyganik, M. Buck, A. Terfort, and M. Zharnikov. Self-assembled monolayers of aromatic selenolates on noble metal substrates. *J. Phys. Chem. B*, 109(28):13630–13638, 2005.

[264] Kai Sheng, Qiang Sun, Chi Zhang, and Qinggang Tan. Steering on-surface supramolecular nanostructures by tert-butyl group. *J. Phys. Chem. C*, 118(6):3088–3092, 2014.

[265] I. Y. Shevyakova, L. I. Buravov, La Kushch, E. B. Yagubskii, S. S. Khasanov, L. V. Zorina, R. P. Shibaeva, N. V. Drichko, and I. Olejniczak. Radical cation salts of tetrathiotetracene and tetraselenotetracene with photochromic anion $[Fe(NO)(CN)_5]^{2-}$. *Russ. J. Coord. Chem.*, 28(7):487–495, 2002.

[266] D.A. Shirley. Many-electron and final-state effects: Beyond the one-electron picture. In M. Cardona and L. Ley, editors, *Photoemission in Solids I*, volume 26 of *Topics in Applied Physics*, pages 165–195. Springer Berlin Heidelberg, 1978.

[267] I. Shirotani, Y. Kamura, H. Inokuchi, and T. Hirooka. Electrical-conductivity, photoemission and absorption-spectrum of tetraselenonaphthacene, $C_{18}H_8Se_4$. *Chem. Phys. Lett.*, 40(2):257–260, 1976.

[268] William Shockley. On the surface states associated with a periodic potential. *Phys. Rev.*, 56:317–323, 1939.

[269] John G. Simmons. Generalized formula for the electric tunnel effect between similar electrodes separated by a thin insulating film. *J. Appl. Phys.*, 34(6):1793–1803, 1963.

[270] Nadja Sändig, Gilberto Teobaldi, and Francesco Zerbetto. Polymorphism and isomerisation of an azobenzene derivative on gold. *Chem. Commun.*, 47:8662–8663, 2011.

[271] Hans Wolfgang Spiess. Probing macromolecular and supramolecular structure, dynamics, and function by magnetic resonance. In Virgil Percec, editor, *Hierarchical Macromolecular Structures: 60 Years after the Staudinger Nobel Prize I*, volume 261 of *Advances in Polymer Science*, pages 295–320. Springer International Publishing, 2013.

[272] Christoph Stadler, Sören Hansen, Ingo Kröger, Christian Kumpf, and Eberhard Umbach. Tuning intermolecular interaction in long-range-ordered submonolayer organic films. *Nat. Phys.*, 5(2):153–158, 2009.

[273] R. Staub, M. Toerker, T. Fritz, T. Schmitz-Hübsch, F. Sellam, and K. Leo. Scanning tunneling microscope investigations of organic heterostructures prepared by a combination of self-assembly and molecular beam epitaxy. *Surf. Sci.*, 445(2–3):368–379, 2000.

[274] Hans-Peter Steinrück. Angle-resolved photoemission studies of adsorbed hydrocarbons. *J. Phys.: Condens. Matter*, 8(36):6465, 1996.

[275] Tomoki Sueyoshi, Hirohiko Fukagawa, Masaki Ono, Satoshi Kera, and Nobuo Ueno. Low-density band-gap states in pentacene thin films probed with ultrahigh-sensitivity ultraviolet photoelectron spectroscopy. *Appl. Phys. Lett.*, 95(18):183303, 2009.

[276] Tomoki Sueyoshi, Haruya Kakuta, Masaki Ono, Kazuyuki Sakamoto, Satoshi Kera, and Nobuo Ueno. Band gap states of copper phthalocyanine thin films induced by nitrogen exposure. *Appl. Phys. Lett.*, 96(9):093303, 2010.

[277] Yoshi-ichi Suzuki, Tadaaki Isozaki, Shigeharu Hashimoto, Tetsuo Kusumoto, Tamejiro Hiyama, Yoichi Takanishi, Hideo Takezoe, and Atsuo Fukuda. Stability of the antiferroelectric phase in dimeric liquid crystals having two chiral centres with CF_3 or CH_3 groups; evaluation of conformational and electric interactions. *J. Mater. Chem.*, 6:753–760, 1996.

[278] S. M. Sze. *Physics of Semiconductor Devices*. Wiley, New York, 1981.

[279] Oren Tal, Yossi Rosenwaks, Yohai Roichman, Yevgeni Preezant, Nir Tessler, Calvin K. Chan, and Antoine Kahn. Threshold voltage as a measure of molecular level shift in organic thin-film transistors. *Appl. Phys. Lett.*, 88(4):043509, 2006.

[280] I. Tamm. On the possible bound states of electrons on a crystal surface. *Physik. Z. Soviet Union*, 1:733, 1932.

[281] Sovirith Tan and Pui-Man Lam. Monte Carlo simulation of three-dimensional islands. *Phys. Rev. B*, 60:8314–8320, 1999.

[282] S. Tanaka, E. Kawabe, K. Kanai, T. Iwahashi, T. Nishi, Y. Ouchi, and K. Seki. n-type doping effect on the electronic structure of organic semiconductor: doping of tetrathianaphthacene (TTN) into hexadecafluorophthalocyaninatozinc (F_{16}ZnPc) by co-evaation. *J. Electron. Spectrosc. Relat. Phenom.*, 144(Sp. Iss. SI):533–536, 2005.

[283] Nikos Tasios, Christos Grigoriadis, Michael Ryan Hansen, Henrike Wonneberger, Chen Li, Hans W. Spiess, Klaus Müllen, and George Floudas. Self-assembly, dynamics, and phase transformation kinetics of donor-acceptor substituted perylene derivatives. *JACS*, 132(21):7478–7487, 2010.

[284] F.S. Tautz. Structure and bonding of large aromatic molecules on noble metal surfaces: The example of PTCDA. *Prog. Surf. Sci.*, 82(9–12):479–520, 2007.

[285] J. Tersoff and D. R. Hamann. Theory and application for the scanning tunneling microscope. *Phys. Rev. Lett.*, 50:1998–2001, 1983.

[286] J. Tersoff and D. R. Hamann. Theory of the scanning tunneling microscope. *Phys. Rev. B*, 31:805–813, 1985.

[287] Giulia Tomba, Massimiliano Stengel, Wolf-Dieter Schneider, Alfonso Baldereschi, and Alessandro De Vita. Supramolecular self-assembly driven by electrostatic repulsion: The 1D aggregation of rubrene pentagons on Au(111). *ACS Nano*, 4(12):7545–7551, 2010.

[288] Benjamin J. Topham, Manoranjan Kumar, and Zoltan G. Soos. Profiles of work function shifts and collective charge transfer in submonolayer metal-organic films. *Adv. Funct. Mater.*, 21(10):1931–1940, 2011.

[289] Isabel Fernández Torrente, Katharina J Franke, and Jose Ignacio Pascual. Spectroscopy of C_{60} single molecules: the role of screening on energy level alignment. *J. Phys.: Condens. Matter*, 20(18):184001, 2008.

[290] Kenji Toyoda, Ikutaro Hamada, Kyuho Lee, Susumu Yanagisawa, and Yoshitada Morikawa. Density functional theoretical study of pentacene/noble metal interfaces with van der Waals corrections: Vacuum level shifts and electronic structures. *J. Chem. Phys.*, 132(13):134703, 2010.

[291] Kenji Toyoda, Ikutaro Hamada, Kyuho Lee, Susumu Yanagisawa, and Yoshitada Morikawa. Density functional theoretical study of perfluoropentacene/noble metal interfaces with van der Waals corrections: Adsorption states and vacuum level shifts. *J. Phys. Chem. C*, 115(13):5767–5772, 2011.

[292] E. V. Tsiper, Z. G. Soos, W. Gao, and A. Kahn. Electronic polarization at surfaces and thin films of organic molecular crystals: PTCDA. *Chem. Phys. Lett.*, 360(1–2):47–52, 2002.

[293] Jun'ya Tsutsumi, Hiroyuki Yoshida, Richard Murdey, and Naoki Sato. Spontaneous buildup of surface potential with a thin film of a zwitterionic molecule giving noncentrosymmetric crystal structure. *Appl. Phys. Lett.*, 95(18):182901, 2009.

[294] Jun'ya Tsutsumi, Hiroyuki Yoshida, Richard Murdey, and Naoki Sato. Decay mechanism of spontaneously built-up surface potential in a thin film of a zwitterionic molecule having noncentrosymmetric crystal structure. *J. Phys. Chem. C*, 115(5):2356–2359, 2011.

[295] H. Vázquez, W. Gao, F. Flores, and A. Kahn. Energy level alignment at organic heterojunctions: Role of the charge neutrality level. *Phys. Rev. B*, 71:041306, 2005.

[296] Elena Y. Vedmedenko and Nikolai Mikuszeit. Multipolar ordering in electro- and magnetostatic coupled nanosystems. *ChemPhysChem*, 9(9):1222–1240, 2008.

[297] Stijn Verlaak, David Beljonne, David Cheyns, Cedric Rolin, Mathieu Linares, Frederic Castet, Jerome Cornil, and Paul Heremans. Electronic structure and geminate pair energetics at organic/organic interfaces: The case of pentacene/C_{60} heterojunctions. *Adv. Funct. Mater.*, 19(23):3809–3814, 2009.

[298] A. Vollmer, O. D Jurchescu, I. Arfaoui, I. Salzmann, T. T. M Palstra, P. Rudolf, J. Niemax, J. Pflaum, J. P Rabe, and N. Koch. The effect of oxygen exposure on pentacene electronic structure. *Eur. Phys. J. E*, 17:339–343, 2005.

[299] H. Vázquez, Y. J. Dappe, J. Ortega, and F. Flores. Energy level alignment at metal/organic semiconductor interfaces: Pillow effect, induced density of interface states, and charge neutrality level. *J. Chem. Phys.*, 126(14):144703, 2007.

[300] H Vázquez, F Flores, R Oszwaldowski, J Ortega, R Pérez, and A Kahn. Barrier formation at metal-organic interfaces: dipole formation and the charge neutrality level. *Appl. Surf. Sci.*, 234(1–4):107–112, 2004.

[301] H. Vázquez, R. Oszwaldowski, P. Pou, J. Ortega, R. Pérez, F. Flores, and A. Kahn. Dipole formation at metal/PTCDA interfaces: Role of the Charge Neutrality Level. *Europhys. Lett.*, 65(6):802, 2004.

[302] Willard R. Wadt and P. Jeffrey Hay. Ab initio effective core potentials for molecular calculations. potentials for main group elements Na to Bi. *J. Chem. Phys.*, 82(1):284–298, 1985.

[303] C. Wagner, D. Kasemann, C. Golnik, R. Forker, M. Esslinger, K. Müllen, and T. Fritz. Repulsion between molecules on a metal: Monolayers and submonolayers of hexa-peri-hexabenzocoronene on Au(111). *Phys. Rev. B*, 81:035423, 2010.

[304] Julia Wagner, Mark Gruber, Alexander Hinderhofer, Andreas Wilke, Benjamin Bröker, Johannes Frisch, Patrick Amsalem, Antje Vollmer, Andreas Opitz, Norbert Koch, Frank Schreiber, and Wolfgang Brütting. High fill factor and open circuit voltage in organic photovoltaic cells with diindenoperylene as donor material. *Adv. Funct. Mater.*, 20(24):4295–4303, 2010.

[305] A. Wan, A. Mäkinen, P. Lane, and P. Kushto. Photoemission study of direct hole injection into Alq_3 by PEDOT:PSS polymer anode. *Chem. Phys. Lett.*, 446:317–322, 2007.

[306] Haibo Wang, Patrick Amsalem, Georg Heimel, Ingo Salzmann, Norbert Koch, and Martin Oehzelt. Band-bending in organic semiconductors: the role of alkali-halide interlayers. *Adv. Mater.*, 26(6):925–930, 2014.

[307] Rui Wang, Hong Ying Mao, Han Huang, Dong Chen Qi, and Wei Chen. Scanning tunneling microscopy and photoelectron spectroscopy investigation of the sexithiophene:C_{60} donor-acceptor nanostructure formation on graphite. *J. Appl. Phys.*, 109(8):084307, 2011.

[308] D. Wasserfallen, I. Fischbach, N. Chebotareva, M. Kastler, W. Pisula, F. Jäckel, M. D. Watson, I. Schnell, J. P. Rabe, H. W. Spiess, and K. Müllen. Influence of hydrogen bonds on the supramolecular order of hexa-peri-hexabenzocoronenes. *Adv. Funct. Mater.*, 15(10):1585–1594, 2005.

[309] J.H. Weaver. Electronic structures of C_{60}, C_{70} and the fullerides: Photoemission and inverse photoemission studies. *J. Phys. Chem. Solids*, 53(11):1433–1447, 1992.

[310] Tobias Weidner, Andrey Shaporenko, Jan Müller, Martin Schmid, Piotr Cyganik, Andreas Terfort, and Michael Zharnikov. Effect of the bending potential on molecular arrangement in alkaneselenolate self-assembled monolayers. *J. Phys. Chem. C*, 112(32):12495–12506, 2008.

[311] Christian Weiss, Christian Wagner, Ruslan Temirov, and F. Stefan Tautz. Direct imaging of intermolecular bonds in scanning tunneling microscopy. *JACS*, 132(34):11864–11865, 2010.

[312] Stacey D. Wetmore, Robyn Schofield, David M. Smith, and Leo Radom. A theoretical investigation of the effects of electronegative substitution on the strength of C–H$\cdots$N hydrogen bonds. *J. Phys. Chem. A*, 105(38):8718–8726, 2001.

[313] A. Wilke, P. Amsalem, J. Frisch, B. Bröker, A. Vollmer, and N. Koch. Electric fields induced by energy level pinning at organic heterojunctions. *Appl. Phys. Lett.*, 98(12):123304, 2011.

[314] A. Wilke, J. Endres, U. Hörmann, J. Niederhausen, R. Schlesinger, J. Frisch, P. Amsalem, J. Wagner, M. Gruber, A. Opitz, A. Vollmer, W. Brütting, A. Kahn, and N. Koch. Correlation between interface energetics and open circuit voltage in organic photovoltaic cells. *Appl. Phys. Lett.*, 101(23), 2012.

[315] Andreas Wilke. *Electronic properties of interfaces in molecular organic solar cells*. PhD thesis, HU Berlin, 2014.

[316] Stefanie Winkler. private communication.

[317] Stefanie Winkler, Johannes Frisch, Patrick Amsalem, Stefan Krause, Melanie Timpel, Matthias Stolte, Frank Würthner, and Norbert Koch. Impact of molecular dipole moments on Fermi level pinning in thin films. *J. Phys. Chem. C*, 118(22):11731–11737, 2014.

[318] Stefanie Winkler, Johannes Frisch, Raphael Schlesinger, Martin Oehzelt, Ralph Rieger, Joachim Räder, Jürgen P. Rabe, Klaus Müllen, and Norbert Koch. The impact of local work function variations on Fermi level pinning of organic semiconductors. *J. Phys. Chem. C*, 117(43):22285–22289, 2013.

[319] B. Winter, S. Berkebile, J. Ivanco, G. Koller, F. P. Netzer, and M. G. Ramsey. Oxygen induced molecular reorientation on aluminum. *Appl. Phys. Lett.*, 88(25):253111, 2006.

[320] Gregor Witte, Simon Lukas, Paul S. Bagus, and Christof Wöll. Vacuum level alignment at organic/metal junctions: "cushion" effect and the interface dipole. *Appl. Phys. Lett.*, 87(26):263502, 2005.

[321] Sang-Yeon Won, Ji-Hoon Kim, Howon Kim, Jong Keon Yoon, Se-Jong Kahng, Young-Kyun Kwon, and Yongsup Park. Linear and hexagonal porous structures of an organic charge acceptor hexaaza-triphenylene-hexacarbonitrile on Au(111) with CN$\cdots$CN dipolar interactions. *J. Phys. Chem. C*, 117(41):21371–21375, 2013.

[322] S. N. Yaliraki, M. Kemp, and Mark A. Ratner. Conductance of molecular wires: Influence of molecule-electrode binding. *JACS*, 121(14):3428–3434, 1999.

[323] H. Yamane, K. Kanai, Y. Ouchi, N. Ueno, and K. Seki. Impact of interface geometric structure on organic-metal interface energetics and subsequent films electronic structure. *J. Electron. Spectrosc. Relat. Phenom.*, 174(1–3):28–34, 2009.

[324] H. Yamane, S. Nagamatsu, H. Fukagawa, S. Kera, R. Friedlein, K. K. Okudaira, and N. Ueno. Hole-vibration coupling of the highest occupied state in pentacene thin films. *Phys. Rev. B*, 72:153412, 2005.

[325] Susumu Yanagisawa, Kyuho Lee, and Yoshitada Morikawa. First-principles theoretical study of Alq_3/Al interfaces: Origin of the interfacial dipole. *J. Chem. Phys.*, 128(24):244704, 2008.

[326] Susumu Yanagisawa and Yoshitada Morikawa. Theoretical investigation of the electronic structure of the Alq_3/Mg interface. *J. Phys.: Condens. Matter*, 21(6):064247, 2009.

[327] Yuhsuke Yasutake, Zujin Shi, Toshiya Okazaki, Hisanori Shinohara, and Yutaka Majima. Single molecular orientation switching of an endohedral metallofullerene. *Nano Lett.*, 5(6):1057–1060, 2005.

[328] Kazumichi Yokota, Masateru Taniguchi, and Tomoji Kawai. Control of the electrode-molecule interface for molecular devices. *JACS*, 129(18):5818–5819, 2007.

[329] Kazumichi Yokota, Masateru Taniguchi, and Tomoji Kawai. Metal-molecule interfaces formed by noble-metal-chalcogen bonds for nanoscale molecular devices. *J. Phys. Chem. C*, 114(9):4044–4050, 2010.

[330] Takashi Yokoyama, Tomonori Takahashi, Kazuteru Shinozaki, and Masakuni Okamoto. Quantitative analysis of long-range interactions between adsorbed dipolar molecules on Cu(111). *Phys. Rev. Lett.*, 98:206102, 2007.

[331] Hiroyuki Yoshida, Eisuke Ito, Masahiko Hara, and Naoki Sato. Core level energy differences between the surface and bulk of organic semiconductor films: The effect of electrostatic polarization energy. *Synth. Met.*, 161(23–24):2549–2553, 2012.

[332] Harold J.W. Zandvliet and Arie van Houselt. Scanning tunneling spectroscopy. *Annu. Rev. Anal. Chem.*, 2(1):37–55, 2009.

[333] Christopher D. Zangmeister, Laura B. Picraux, Roger D. van Zee, Yuxing Yao, and James M. Tour. Energy-level alignment and work function shifts for thiol-bound monolayers of conjugated molecules self-assembled on Ag, Cu, Au, and Pt. *Chem. Phys. Lett.*, 442(4–6):390–393, 2007.

[334] Ulrich Zerweck, Christian Loppacher, and Lukas M Eng. Ordered growth and local workfunction measurements of tris(8-hydroxyquinoline) aluminium on ultrathin KBr films. *Nanotechnology*, 17(7):S107, 2006.

[335] Hong Liang Zhang, Wei Chen, Lan Chen, Han Huang, Xue Sen Wang, Junji Yuhara, and Andrew Thye Shen Wee. C_{60} molecular chains on alpha-sexithiophene nanostripes. *Small*, 3(12):2015–2018, 2007.

[336] Lei Zhang, Sami M. Fakhouri, Feng Liu, Justin C. Timmons, Niva A. Ran, and Alejandro L. Briseno. Chalcogenoarene semiconductors: new ideas from old materials. *J. Mater. Chem.*, 21(5):1329–1337, 2011.

[337] Qing Zhao, Jason Coult, and Gerald H. Pollack. Long-range attraction in aqueous colloidal suspensions. In *Proc SPIE*, volume 7376, pages 73761C–73761C–13, 2010.

[338] Jian Qiang Zhong, Hong Ying Mao, Rui Wang, Dong Chen Qi, Liang Cao, Yu Zhan Wang, and Wei Chen. Effect of gap states on the orientation-dependent energy level alignment at the DIP/F_{16}CuPc donor-acceptor heterojunction interfaces. *J. Phys. Chem. C*, 115(48):23922–23928, 2011.

[339] Mi Zhou, Rui-Qi Png, Siong-Hee Khong, Sankaran Sivaramakrishnan, Li-Hong Zhao, Lay-Lay Chua, Richard H. Friend, and Peter K. H. Ho. Effective work functions for the evaporated metal/organic semiconductor contacts from in-situ diode flatband potential measurements. *Appl. Phys. Lett.*, 101(1):013501, 2012.

[340] Rajendra R. Zope, Tunna Baruah, Mark R. Pederson, and B. I. Dunlap. Static dielectric response of icosahedral fullerenes from C_{60} to C_{2160} characterized by an all-electron density functional theory. *Phys. Rev. B*, 77:115452, 2008.

Selbständigkeitserklärung

Hiermit erkläre ich, die Dissertation selbständig und nur unter Verwendung der angegebenen Hilfen und Hilfsmittel angefertigt zu haben.

Ich habe mich anderwärts nicht um einen Doktorgrad beworben und besitze nicht einen entsprechenden Doktorgrad.

Ich erkläre die Kenntnisnahme der dem Verfahren zugrunde liegenden Promotionsordnung der Mathematisch-Naturwissenschaftlichen Fakultät der Humboldt-Universität zu Berlin.

Jens Niederhausen
Berlin, 16. September 2014